Northumbria Research Link

STUDY OF Cu(In,Al)Se$_2$ THIN FILMS PREPARED BY SELENISATION OF SPUTTERED METALLIC PRECURSORS FOR APPLICATION IN SOLAR CELLS

Rémi Aninat

Ph.D

2012

STUDY OF Cu(In,Al)Se$_2$ THIN FILMS PREPARED BY SELENISATION OF SPUTTERED METALLIC PRECURSORS FOR APPLICATION IN SOLAR CELLS

Rémi Aninat

A thesis submitted in partial fulfilment
of the requirements of the
University of Northumbria at Newcastle
for the degree of
Doctor of Philosophy

Research undertaken in the
Faculty of Engineering and Environment

School of Computing, Engineering and
Information Sciences

November 2012

Abstract

Cu-In, Cu-Al and Cu-In-Al metallic precursor layers were deposited using radio-frequency magnetron sputtering and selenised to produce thin films of $CuInSe_2$ (CIS), $CuAlSe_2$ (CAS) and $CuIn_{1-x}Al_xSe_2$ (CIAS), respectively. The selenisation stage of this 2-stage process was carried out in a tube furnace (TF) or a rapid thermal processor (RTP) in the presence of elemental Se, either deposited on top of the precursor film or provided from an external source in the chamber, in order to fabricate the chalcopyrite material. The aim was to produce single phase, device quality CIS, CAS and CIAS for use as an absorber layer material in thin film photovoltaic solar cells. Profilometry performed on the as-deposited Cu-In-Al metallic precursors showed an important increase in surface roughness compared to the Cu-In and Cu-Al precursors. This was found to be due to the preferential formation of $Cu_9(In,Al)_4$, which stoichiometry led the excess In to form island-shaped In phases at the surface of the bulk, while only Cu_2In and $CuIn_2$ formed in Cu-In precursors. Regarding the selenisation, temperatures ranging from 250°C to 550°C were used, and the resulting samples were investigated using scanning electron microscopy (SEM), energy dispersive X-ray spectroscopy (EDS), X-ray diffraction (XRD), secondary ion mass spectroscopy (SIMS) and glow-discharge optical emission spectroscopy (GD-OES). Thin films of single phase CIS and CAS were successfully produced with energy band gaps of 0.99 eV and 2.68 eV, respectively. However the incorporation of Al proved to be difficult. The results showed that no incorporation of the Al into the chalcopyrite lattice was achieved in the samples selenised in the RTP, which was believed to be due to the oxidation of the element Al into amorphous Al_2O_3. In the tube furnace, possibly due to lower levels of oxidation, incorporation occurred more readily but Al and In segregated

towards the back and front of the layer, respectively. The causes of the segregation were studied and solutions to avoid it developed, resulting under certain conditions in successful production of $CuIn_{1-x}Al_xSe_2$. Samples were tested in a photoelectrochemical cell and showed (apparent) external quantum efficiency values comparable to a $CuInSe_2$ (CIS) sample used as a standard.

Acknowledgements

Declaration

I declare that the work contained in this thesis has not been submitted for any other award and that it is all my own work. I also confirm that this work fully acknowledges opinions, ideas and contributions from the work of others.

Work done in collaboration with others

The work presented in this thesis was undertaken by the author with the exception of the following:

- The wavelength-dispersive spectroscopy and cathodoluminescence measurements (sections 6.3.5 and 6.3.6) were performed by Dr F. Luckert from Strathclyde University.

- Secondary ion mass spectroscopy measurements and e-beam evaporation of the front contacts of the solar cells were performed by Dr G. Zoppi, from the same group as the author. The thickness uniformity measurements used in Figure 57 were also provided by Dr G. Zoppi.

- The glow discharge-optical emission spectroscopy depth profiles were measured by J. Cooper and P. Chapon at Horiba Jobin Yvon (UK and French branch, respectively).

List of acronyms

Acronym	Full name
AM	Air Mass
CAS	$CuAlSe_2$
CBD	Chemical bath deposition
CIAS	$CuIn_{1-x}Al_xSe_2$
CIGS	$CuIn_{1-x}Ga_xSe_2$
CIGSSe	$CuIn_{1-x}Ga_x(S_{1-y}Se_y)_2$
CIS	$CuInSe_2$
c-Si	Crystalline silicon
EDS	Energy dispersive X-ray spectroscopy
EQE	External quantum efficiency
FWHM	Full width at half maximum
GD-OES	Glow discharge-optical emission spectroscopy
GIXD	Grazing incidence X-ray diffraction
ITO	Indium tin oxide
I-V	Current-voltage
LED	Light-emitting diode
ODC	Ordered defect compound
PV	Photovoltaics
RTP	Rapid thermal processor
SCR	Space charge region
SEL	Stacked elemental layers
SEM	Scanning electron microscope
SIMS	Secondary ion mass spectroscopy
SRH	Shockley-Read-Hall
TCO	Transparent conductive oxide
TF	Tube furnace
UPS	Ultraviolet photoelectron spectroscopy
WDS	Wavelength dispersive spectroscopy
XPS	X-ray photoelectron spectroscopy
XRD	X-ray diffraction

List of symbols

Symbol	Description	Unit
[A]	Composition in element A	at% or wt%
k_B	Boltzmann constant	$m^2.kg.s^{-2}$
n_{id}	Ideality factor	-
b	Bowing coefficient	-
I	Current	A
J	Current density	$A.cm^{-2}$
V	Voltage	V
E_g	Band gap	eV
η	Photovoltaic conversion efficiency	%
FF	Fill factor	-
V_{OC}	Open-circuit voltage	V
I_{SC}	Short-circuit current	A
J_{SC}	Short-circuit current density	$A.cm^{-2}$
R_s	Series resistance	Ω
R_{sh}	Shunt resistance	Ω
V_A	Atom *A* vacancy	-
A_B	Atom *A* on antisite *B*	-
A_M	Atom *A* on metallic antisite	-
$A^{\bullet\bullet}$	Double relative positive charge on atom A	-
$\{A_x - B_y\}$	Complex between defects A_x and B_y	-
P_{MP}	Maximum power output of the solar cell	W
P_{in}	Power shone on the solar cell	W
E_{pe}	World's primary energy consumption in a year	Q or Btu
$E_{s/l}$	Solar energy received by the land area of the Earth per year	Q or Btu
d_{hkl}	Orthogonal distance between two {hkl} planes	Å
<hkl>	Texture perpendicularly to the (hkl) plane	-
{hkl}	Family of equivalent (hkl) planes	-

Table of contents

CHAPTER 1 INTRODUCTION

This thesis reports on the investigation of the 2-stage fabrication of a thin $CuIn_{1-x}Al_xSe_2$ (CIAS) absorber layer[1], with possible applications in both single junction and multi-junction solar cells [1].

1.1 Need for photovoltaics

There is increasing need for clean, renewable sources of energy in today's geopolitical and environmental context. The reserves of coal, oil and gas, which have been the dominant sources of energy since the industrial revolution, are running low. The price of oil, in particular, is subject to important variations associated with the geopolitics of the principal regions of extraction. Besides the undeniable pollution caused by the use of fossil fuels, concerns are also growing as to the role that the products of combustion of such fuels could play in the recent changes of the world's climate. Nuclear energy, which was initially meant as a temporary solution to contemporary energy crises, has now developed to a scale where waste management, risks of accidents and even acts of terrorism, have made it a poor alternative to fossil fuels. If the costs of de-commissioning are taken into account it is also a costly alternative. The growing population of the world and the fast development of countries such as China and India will require the supply of abundant, clean and cheap sources of energy over the coming decades. Photovoltaics, combined with other 'green' technologies such as wind, hydroelectric, solar thermal and geothermal power generation, is now generally recognised to be a solution to these problems. The energy available from the Sun at the surface of the Earth is more than sufficient to provide for our present and future energy needs (see section 2.2). The main challenge is to design devices that are efficient in converting the sunlight into

---

[1] Also written $Cu(In,Al)Se_2$.

electricity, made of sustainable and cheap elements, and that can be fabricated using low cost processes.

1.2 Thin-film photovoltaics

Although up to the present most photovoltaic solar cells are made using crystalline silicon (c-Si), much cheaper devices can be made using thin film technologies based on the use of direct energy band gap semiconductors. c-Si, with its indirect energy band gap, requires thicknesses of several hundreds of microns to absorb most of the sunlight. Also, the photogenerated carriers need to diffuse this distance back to the junction without being lost by recombination, which can only be achieved by purifying the silicon to a high level and growing crystals free from defects. In thin films, on the other hand, their direct band gap allow a similar absorption of the sunlight with only a few microns of material, and the carriers are generated very close to or within the junction, minimising the need for a long minority carrier diffusion length. Thin films can therefore be made cheaper and of comparable efficiencies to c-Si. The most successful thin film materials used at present are cadmium telluride (CdTe), hydrogenated amorphous Si (a-Si), and copper indium gallium diselenide (CIGS). Figure 1 shows the market share of the different technologies currently produced. Although CdTe is the dominant thin film technology at present, the share of CIGS is expected to grow rapidly in the near future, thanks to recent module efficiency breakthroughs by companies such as Solar Frontier [2] and Miasolé [3]. A 20.3% efficient solar cell, the current record for any single junction thin film device, has also been recently achieved with this material [4], which demonstrates a still larger potential for efficiency improvement.
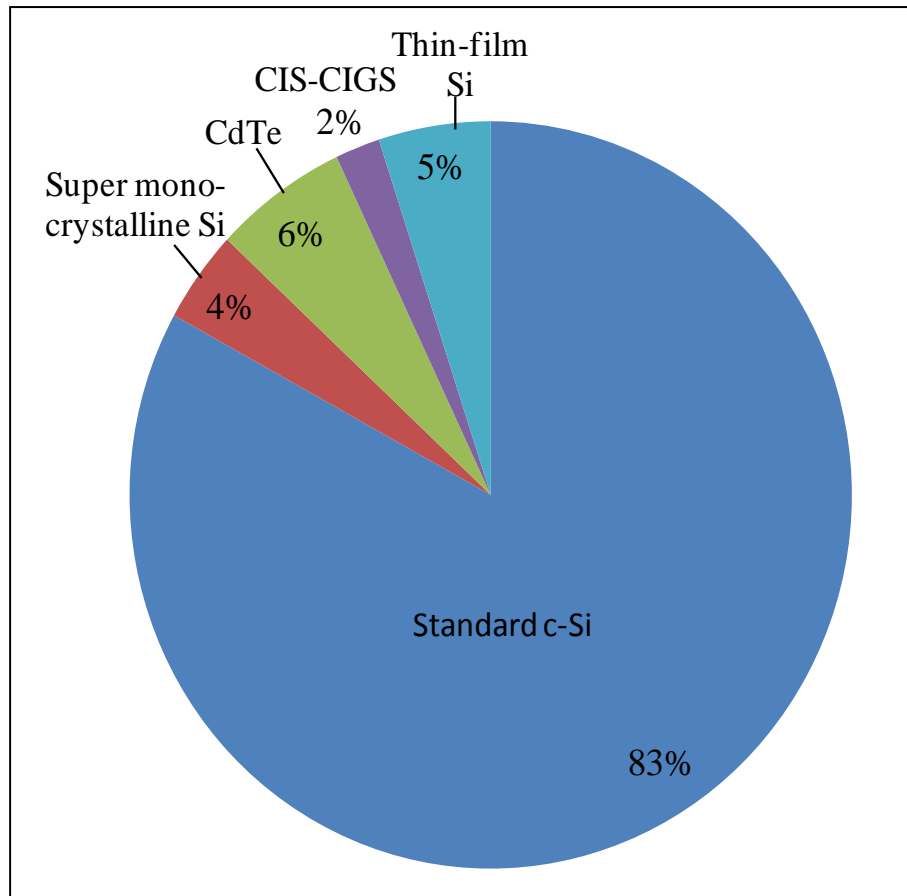
Figure 1: 2010 cell production by technology (in MW of DC current). Total production: 23,889 MW [5].

1.3 Reasons governing the choice of the material and the fabrication technique

$CuIn_{1-x}Al_xSe_2$ (CIAS) is derived from CIGS. The substitution of Ga for Al yields two interesting properties. First of all, it allows for a wider range of band gaps, that is 1.0-2.7 eV (against 1.0-1.7 eV in CIGS), to be attained by altering the ratio $x=[Al]/([Al]+[In])$ from 0 to 1. This could lead to applications of CIAS in multi-junction devices. The simplest device would use a CIS lower cell with a CIAS upper cell ($Eg(CIS)<Eg(CIAS)$). A corollary of this wider accessible range is that less alloying of Al with $CuInSe_2$ (CIS) is required to yield the same band gap as CIGS, therefore reducing the stresses and associated lattice defects. This should permit the production of CIAS cells with wider energy band gaps than CIGS devices as the

latter are found to degrade in efficiency for energy band gaps > 1.2 eV [6]. As the optimum energy band gap of a single junction solar cell is estimated at 1.4 eV [7], the high efficiencies achieved with CIGS could be improved in CIAS. The higher V_{OC} (and therefore lower current) resulting from the wider energy band gap would also reduce the resistive losses ($\propto RI^2$) in modules.

1.4 History of Cu(In,Al)Se$_2$

$CuIn_{1-x}Al_xSe_2$ (CIAS), like its parent materials $CuInSe_2$ (CIS) and $CuIn_{1-x}Ga_xSe_2$ (CIGS), is based on the chalcogen element Se and crystallizes into the chalcopyrite structure. The use of chalcogen elements for photovoltaics can be traced back to 1883, when Fritts fabricated a photovoltaic device constituted of a Se sheet sandwiched between a metal plate and a gold sheet. He was also the first one to foresee the modern application of the photovoltaic effect, concluding his report by "the current, if not wanted immediately, can be either stored where produced, in storage batteries or transmitted a distance and there used" [8]. Other chalcogen-based materials were later developed, including a CdS/Cu_2S heterojunction in 1954 [9] and $CuInSe_2/CdS$ in 1971 [10].

Although references to CIAS can be found as far back as the late 1980s [11, 12], its potential as an alternative to CIGS was only demonstrated in 2002 when Marsillac and co-workers from Delaware [1] produced a high performance CIAS device which showed improved properties in comparison to a similarly deposited CIGS device. Both absorbers were deposited by co-evaporation, and the solar cell layout was the following: Mo back contact, CIAS or CIGS absorber layer, CdS buffer layer, indium tin oxide window layer, Ni/Al front contact grid and MgF_2 anti-reflective coating. Both absorbers had a single, uniform band gap of 1.16 eV. The efficiency of the

CIAS device, $\eta = 16.9\%$, was 0.4 points higher than that obtained from the CIGS absorber ($\eta = 16.5\%$). This was a proof of principle that CIAS could be a good alternative to the record-breaking material CIGS.

1.5 2-stage process

A **2-stage process** for the fabrication of CIAS, where the first stage is the deposition of the metallic precursor (i.e. Cu, In and Al) and the second stage is the annealing in a Se atmosphere, was chosen for this project over multi-source co-evaporation. In particular, the first stage can be made cheaper and more controllable over large areas than co-evaporation, making the technique more suitable for large scale production. Sputtering was used for the work of this thesis, because it meets the requirements of large scale production, with attested uniformity over large areas, allowing important throughput, and good controllability. This is a process derived from the 2-stage, called 'sulphurisation after selenisation' (SAS), that Solar Frontier, currently the biggest CIGSSe manufacturer[2], uses to fabricate its absorber material. Solar Frontier achieved a GW-scale production capacity in 2011 [13] and has produced some of the highest efficiency thin-film module efficiencies (17.8% on 900 cm^2 [2]).

1.6 Use of elemental Se

The selenium was deposited by evaporation in its elementary form on top of the metallic precursor before annealing in order to form the chalcopyrite phase. This way of providing the Se was chosen over the flowing of H$_2$Se, which in spite of good reported results [14, 15], is toxic and highly flammable.

Zoppi and co-workers have previously obtained single phase CIAS [16], but faced important issues with the reproducibility of this result.

---

[2] CIGSSe consists in sulphurised $CuIn_{1-x}Ga_xSe_2$.

1.7   Aims of this work

The aims of this work are the following:

- Determine the optimal precursor deposition parameters and growth conditions for $CuInSe_2$ and $CuAlSe_2$ absorbers. These two materials correspond to the two extreme compositions of $CuIn_{1-x}Al_xSe_2$, x=0 and x=1, respectively, and are simpler to analyse, due to their ternary nature, than the quaternary compound $CuIn_{1-x}Al_xSe_2$.

- Fabricate full devices based on CIS, in order to practice the different steps of the fabrication and be able to apply them to CIAS once the absorber fabrication process is optimised. The structuring layers of the CIS cell was indeed expected to be suitable, if not ideal, to $CuIn_{1-x}Al_xSe_2$ as well, at least in the limit of low x values.

- Determine the optimum conditions of deposition of the Cu-In-Al metallic precursor. This involved studying the uniformity of composition and thickness of the films deposited, and the stability of the deposition rate from the different sputtering targets used for the deposition.

- Assess the optimal conditions of selenisation to obtain, as far as possible, single phase CIAS. This included testing three different levels of alloying between Al and In in the precursor ($x \approx 0.11$, $x \approx 0.32$ and $x \approx 0.51$) and studying the possible phenomena hindering the formation of the single phase.

- Make complete devices from the most promising samples.

1.8 Structure of the thesis

This report is structured according to the following plan. After this introduction follow two theoretical chapters, the first one exposing the theoretical considerations underlying the studies (CHAPTER 2) and the second summarising the results of the literature relevant to this work (CHAPTER 3). CHAPTER 2 contains the essential definitions and theoretical bases underlying the work. In complement to this chapter, the detailed balance calculation of the highest achievable band gap is reported in APPENDIX 1, and some aspects of XRD are detailed in APPENDIX 2. After CHAPTER 3 are described the experimental methods and setups used (CHAPTER 4), and then the results. Five results chapters are presented. Preliminary calibrations of the sputtering targets, not essential to the discussion of the results, can be found in APPENDIX 4. The properties of different types of Cu-In, Cu-Al and Cu-In-Al metallic precursors are dealt with in 0. CHAPTER 6 describes the fabrication and characterisation of CIS and CAS absorber layers. The next study (CHAPTER 7) comprises a comparison of annealed Cu-In-Al precursors and selenised CIAS absorber layers prepared by rapid thermal processing at four different temperatures, as well as a related study in a tube furnace. Following the results of CHAPTER 7, alternative layouts were designed and their respective qualities assessed (0). Results regarding photoelectrochemical selection of the CIAS absorbers and the fabrication of CIS and CIAS cells are reported in CHAPTER 9, and conclusions are drawn on the different studies and suggestions are made for exploring further the different findings (CHAPTER 10).

CHAPTER 2   ELEMENTS OF THEORY UNDERLYING THE STUDIES

2.1   Photovoltaic conversion efficiency

The most important figure of merit of a solar cell is its **photovoltaic conversion efficiency η**. This is defined [17] as the ratio between the maximum power output P_{MP} generated by the solar cell, and the power input received from the sun P_{in}:

$$\eta = \frac{P_{MP}}{P_{in}} \tag{2.1}$$

An accurate knowledge of the solar irradiance spectrum (i.e. power received per unit area and per unit wavelength) is therefore a prerequisite to calculate P_{in} and then η.

2.2   Energy available from the sun

The sun is an extremely abundant source of energy. A detailed assessment of the yearly insolation and its comparison to energy consumption can be found in [18]. If 1 Q= 1.055×10^{21} J=10^{18} Btu, then every year, 5160 Q of the energy emitted from the Sun reach the Earth. Of these, part is absorbed and part reflected by the atmosphere, clouds and oceans such that 2490 Q remain available for use at the Earth's surface. Only considering the land area, this is still $E_{s/l} \approx 1100$ Q. Let us compare these figures with the world annual primary energy consumption, i.e. all non-processed energy, such as oil, coal, natural gas, but also solar and wind energy for example. An update of [18] on the world primary energy consumption for 2006 can be found in the database of the American Energy Information Administration (EIA) [19]. The world data on primary energy consumption was last compiled during the 2006 International Energy Annual, where a world consumption of $E_{pe.}=0.472$ Q was reported. Therefore, the sun provides approximately $E_{pe.}/E_{s/l} \approx 2330$ times the

2006 world primary energy consumption. Considering electricity needs only, E_{el} ≈0.06 Q were consumed that same year [20], or about 18000 times less than the potential PV energy available.

Solar spectrum

The radiation of the sun is produced by the nuclear fusion taking place in its core, and reaches its surface via successive absorptions and re-emissions by layers of gas constituting the star. As a result, it can be considered to a reasonable approximation as black body radiation. The sun's surface temperature is ≈5800 K. Once the light has left the sun's surface, it travels through space with negligible losses and reaches the Earth's atmosphere. There, it undergoes reflection or absorption at wavelengths specific to the atoms and molecules present in the atmosphere. The spectrum of the sun measured from the surface of the earth is the fraction of the spectrum measured in outer space that is transmitted to the Earth surface (Figure 2). The solar energy is usually expressed in terms of irradiance, in W.m^{-2}, which depends on the zenith angle of the sun θ. A figure of merit named "air mass" (AM) is used in photovoltaics to characterize the sun position. The air mass is defined as the path length of light through the atmosphere, normalized to the path length from the zenith (Figure 3):

$$AM = \frac{1}{\cos \theta} \qquad (2.2)$$

The standard solar spectrum used for efficiency measurements is the one at AM 1.5 (i.e. for a zenith angle θ≈48°) [21].
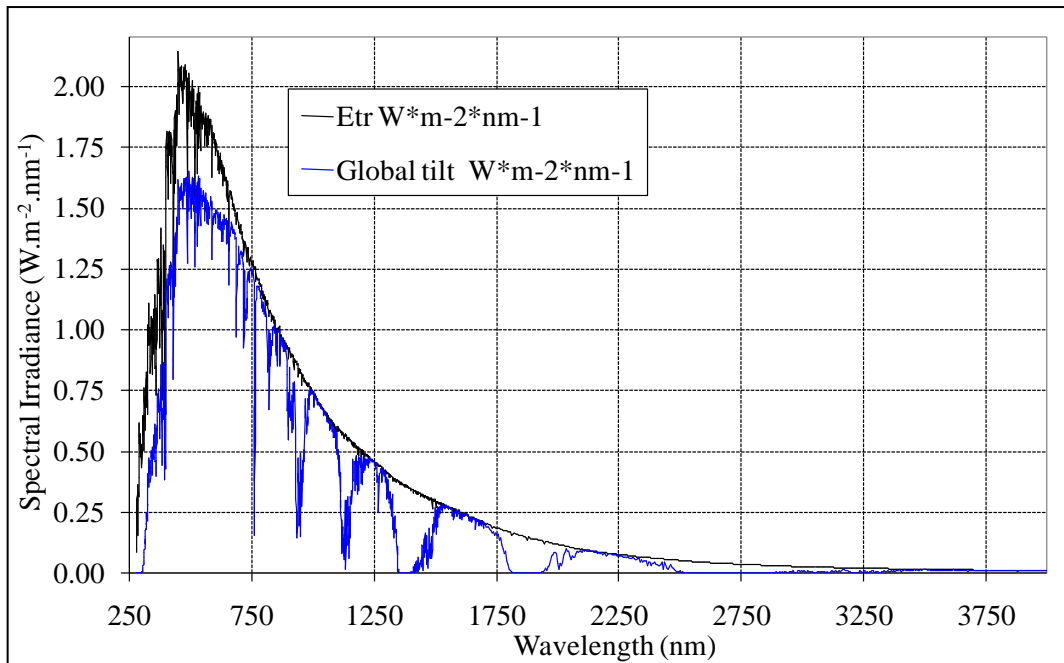
Figure 2: ASTM G173-03 Reference Spectra for the solar irradiation. The air Mass 0 spectrum is in *black* and the global tilt air mass 1.5 spectrum is in *blue*. *Source: [21].*
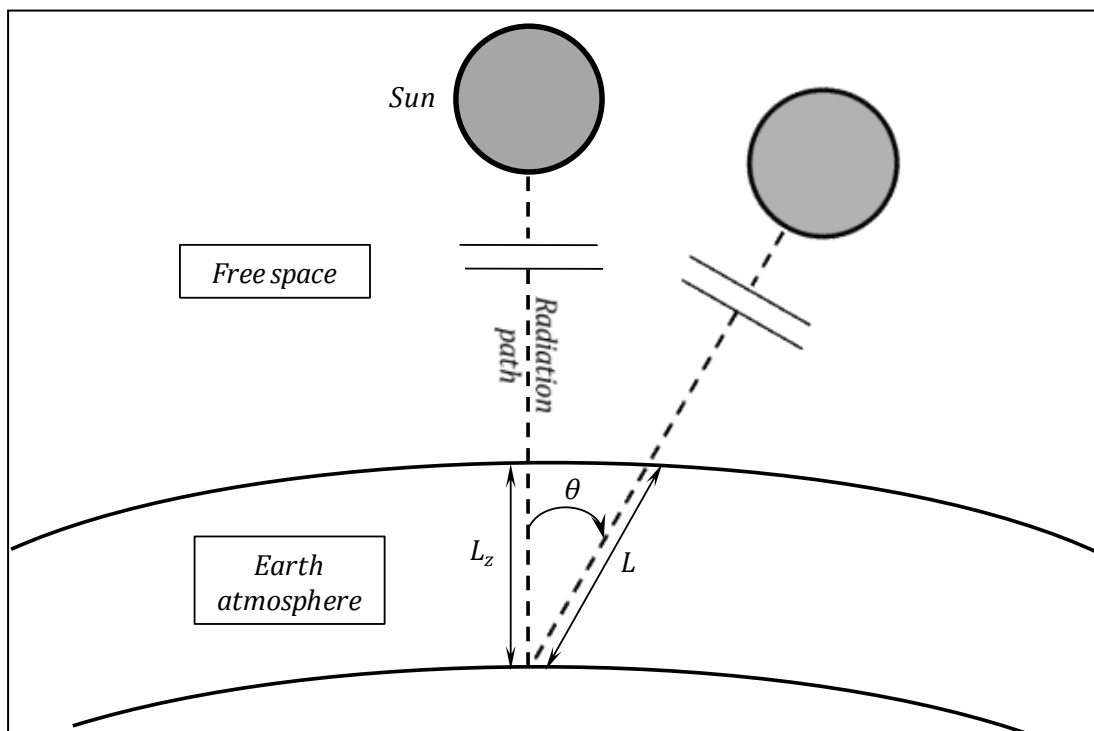
Figure 3: Diagram illustrating the variation of the solar radiation path length through the Earth atmosphere with the zenith angle θ. *Adapted from [22].*

2.3 p-n junction, Schottky and ohmic contacts

2.3.1 p-n junction

The electrons of the valence band of a semiconductor can, under illumination for example, be promoted to the conduction band, leaving a vacancy called a **hole**. The hole can be satisfactorily described as a positively-charged particle possessing an effective mass. When an electron-hole pair is created, the two types of particles can recombine after a certain time, emitting a photon of equivalent energy. However, in the presence of an electric field, electrons and holes are driven in opposite directions, and can be separated before they recombine. An effective way to create such an electric field in a semiconductor is by making a **p-n junction**. A p-n junction is formed when two semiconductor materials of opposite conductivities (p-type and n-type) are put in contact. The **p-type** material has an excess of holes in its valence band, and the **n-type** material an excess of electrons in its conduction band. When p-type and n-type semiconductors are put in contact, excess electrons on the n-type side of the interface feel the electrostatic attraction of the p-type side and diffuse in this direction. Reciprocally, holes diffuse from the p-side towards the n-side. There is therefore a region near the interface, called **space-charge region** (SCR), which is depleted in carriers, and the donors (or acceptors), no longer screened by the carriers around them, are stripped off (or given) an electron, turning into cations (anions). As a consequence, cations are left near the n-side and anions near the p-side [17]. These unscreened charges generate an electric field in the SCR (Figure 4), which drives electrons and holes in opposite directions and helps to separate them before they recombine. Note that, once the thermodynamic equilibrium is established between the two semiconductors, the **Fermi level** (E_F) must be constant throughout the junction, which translates into band bending in the space-charge region. The Fermi

11

level, is defined as the energy at which the probability of occupation by an electron is ½ in the Fermi-Dirac distribution.
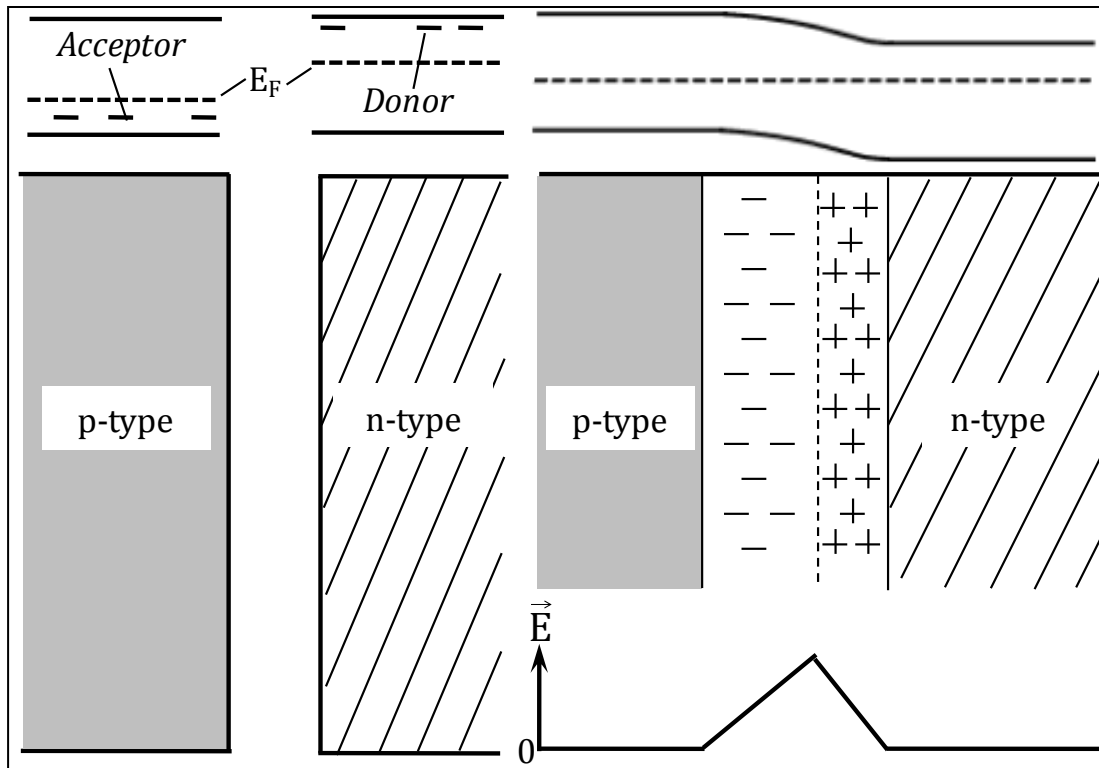
Figure 4: Diagram summarizing (*left*) the individual band diagrams for two p and n materials not in contact; (*right*) the band bending (*top right*), ions formation (*middle right*) and resulting electric field (*bottom right*) at a p-n junction. *Adapted from [17].*

In CuInSe$_2$ (CIS) devices, the p-n junction is formed between a p-type CIS and an n-type CdS (section 3.4.3).

2.3.2 Schottky and ohmic contacts

Beside the light-absorbing semiconductor, other layers are required to make a functioning solar cell. In particular, metal contacts are used to collect the carriers at both ends. The losses at the various contacts must be considered and minimized. The **band diagram** description of metal-semiconductor interfaces was studied by Schottky in the first half of the 20th century [23].

Work function

The **work function** Φ of a material is defined as the energy necessary to extract[3] an electron from its Fermi level E_F to a point immediately outside the material, i.e. just far enough for the electron to have the same energy V_0 it has in vacuum [24]. For a semiconductor, this is:

$$\Phi_S = \chi_S + (E_C - E_F) \tag{2.3}$$

with χ_S the electron affinity and E_C the conduction band energy. In a metal, the Fermi level is located in the conduction band, so that the work function is the same as the ionization energy. When a metal and a semiconductor are put in contact [25], the electronic properties of the contact made can be of mainly two sorts: Schottky contact or ohmic contact.

Schottky Contact

They are characterised by a diode-like I-V curve if measured across the contact. In a Schottky contact, an energy barrier, called **Schottky barrier** (Figure 5), is formed at the interface between the semiconductor and the metal. The height of this barrier is $q.V_{bi} = \Phi_M - \Phi_S$. The best way for the carriers to pass the barrier is to possess an energy higher than the barrier (hence the diode-like behaviour), but tunnelling through Schottky barriers can also occur. The transmission of the carriers at the junction was initially modelled as a barrier lowering and is therefore referred to as the **Schottky barrier lowering** [24]. When a Schottky contact is established, a depletion region is created near the interface between metal and semiconductor, but unlike the p-n junction, only on the semiconductor side. This is because no depletion region can form in the metal, where there is a much larger number of carriers

---

[3] The theoretical calculation is actually done for the opposite action, i.e. to bring the electron from immediately outside the surface to the surface.

available, which immediately compensate the loss of any carrier to the semiconductor. The depletion layer at the semiconductor contact surface is populated with cations if the semiconductor is n-type, or anions if it is p-type. It results in a bending of the semiconductor bands near the contact. Since a Schottky contact has a rectifying action, I-V measurements across the contact will show a diode-like curve. If the I-V curve of a PV device with a Schottky contact is measured, its shape will integrate the effect of the two diodes: the Schottky contact and the p-n junction.
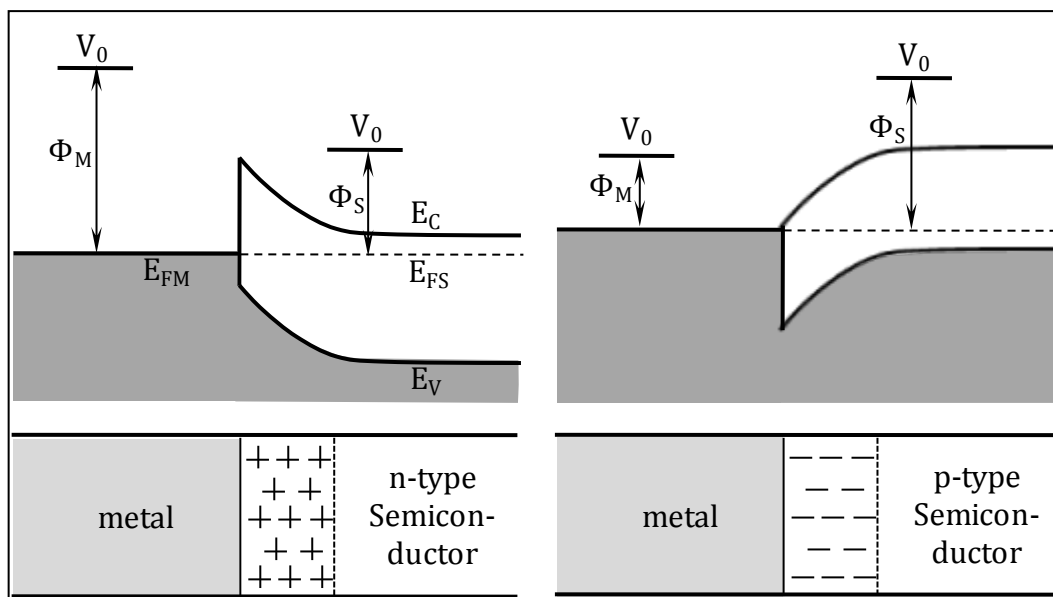
Figure 5: Diagrams illustrating the Schottky contact between a metal and *(a)* **an n-type semiconductor or** *(b)* **a p-type semiconductor. The vacuum energy levels and the work functions are represented to justify the band bending. Note that for clarity of the diagram the bending is not to scale.** *Adapted from [24].*

Ohmic contact

Ohmic contacts are non-rectifying. This means that there is a linear relationship between I and V across the contact. In terms of circuit equivalent, the ohmic contact is equivalent to a resistor. Ohmic contacts are usually defined into two types:

- Tunnelling Ohmic contact, where the majority carriers cross the contact by tunnelling through the potential barrier (see Figure 6, *left*).

- Metal-like Ohmic junction, where the work functions of metal and
semiconductor are such that there is no potential barrier, but instead a
favourable band bending for the carriers to cross the contact (see Figure 6,
r*ight*).
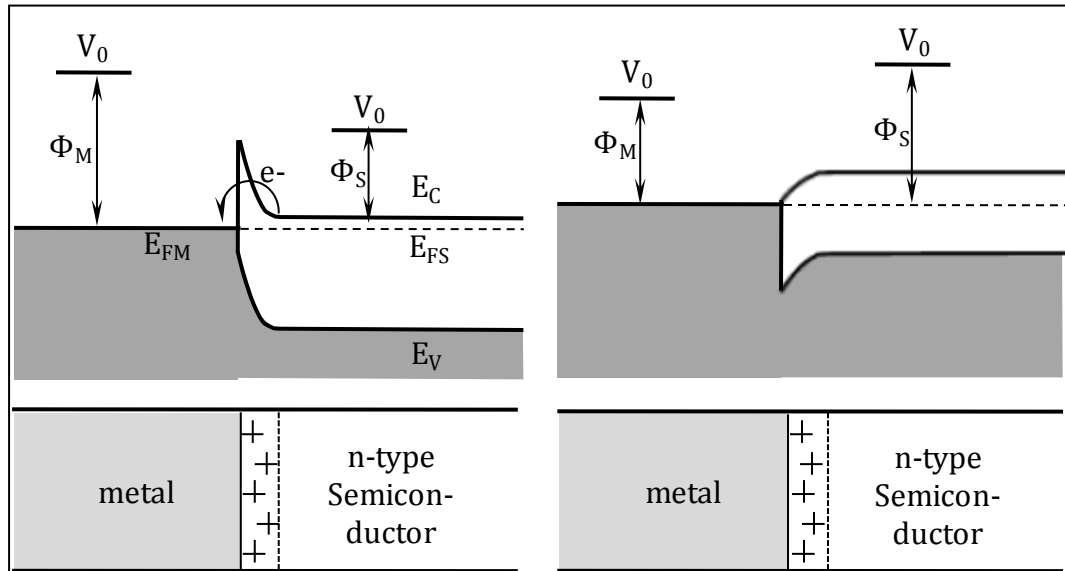
Figure 6: Diagram illustrating *(a)* **the tunnelling and** *(b)* **the metal-like Ohmic contact between a metal and an n-type semiconductor (bending not to scale for clarity).**
Adapted from [24].

In the first type of contact, the semiconductor must be heavily doped, so that the
band bending is sharp enough for the tunnelling to occur. As a consequence, the
depletion region at the interface is small. In a metal-like ohmic junction, the
semiconductor only needs to be moderately doped.

Note that we referred so far to the work functions as decisive factors for the nature of
the contact. In practice however, it is often little dependent on the work function of
the metal, due to the so-called *Fermi-level pinning*. This phenomenon will not be
discussed here, but it is satisfactorily described by modelling of interface bonding
[26, 27].

2.4 J-V characteristic

The **Shockley-Queisser detailed balance model** (APPENDIX 1) is the model generally used to assess the maximum theoretical efficiency that can be expected from a material of given band gap. However, this model corresponds to a perfect device, and real devices usually depart in several respects from the founding assumptions of the model [28]:

(a) The absorptance *A(E)* has generally not a sharp but rather a relatively smooth step near the band edge, due to the limited thickness of the film.

(b) In polycrystalline thin-films, charge extraction can be an issue, especially when there are resistive losses in the bulk of the n and p-type regions and at the different contacts of the cell.

(c) In addition to radiative recombinations (i.e. from conduction band to valence band), non-radiative recombination processes must also be taken into account. For example, absorbers can present defects with energetic levels deep within the band gap. These can cause **Shockley-Read-Hall** (SRH) recombination.

Losses (b) and (c) can be classified as resistive losses and shunt losses, respectively. The conversion efficiency of devices and the magnitude of the three types of losses (a), (b) and (c) can be extracted from the **current-voltage** (J-V) characteristics of a device. Let us focus on the example of a junction between a thicker (typically 2 µm) p-type bulk, with a thinner ($\approx$200 nm) n-type layer on top, such as the typical CIS/CdS junction.

2.4.1 Modelling of J-V characteristics

To better visualise the effect that the different types of losses occurring in photovoltaic devices may have on the efficiency, the cell can be treated as a relatively simple electrical circuit. The equivalent circuit to the device used for the Shockley-Queisser detailed balance calculation is shown in Figure 7 (a).
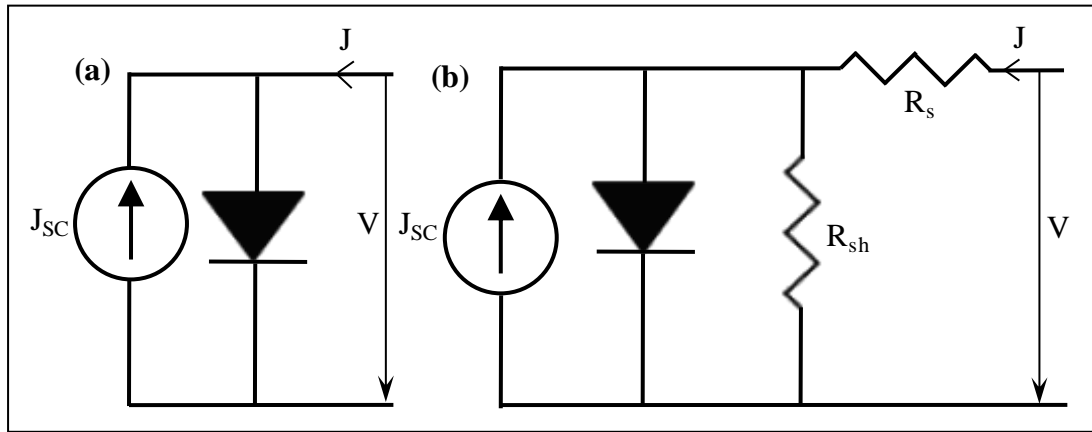
Figure 7: Circuit model associated with (a) the ideal photovoltaic device under illumination used in the Shockley-Queisser detailed balance model and (b) a more realistic illuminated device where the possible types of losses are represented by a series resistance Rs and a shunt resistance Rsh. Adapted from [29].

In this model, the absorber layer is a perfect diode, and the photocurrent I_L (due to the illumination from the sun for example) provides current to the circuit. The ideal case represented by the circuit of Figure 7 (a) can be described by the following equation:

$$J(V) = J_0 \cdot \left[e^{\frac{qV}{n_{id} k_B T}} - 1 \right] - J_{SC} \tag{2.4}$$

with $J(V)$ the density of current (i.e. current per unit area), V the applied voltage, J_0 the **reverse saturation current**, k_B the Boltzmann constant ($\approx 1.38 \times 10^{-23}$ m^2.kg.s^{-2}.K^{-1}, or 8.62×10^{-5} eV.K^{-1}), J_{SC} the **short-circuit current density**, n_{id} the **ideality factor** of the device and T its temperature. An alternative circuit providing a potentially

17

better fit to real J-V measurements is shown in Figure 7 (b). It is described by equation 2.5:

$$J(V) = J_0 \left[e^{\frac{q.(V - J R_s)}{n_{id} k_B . T}} - 1 \right] + \frac{V - J.R_s}{R_{sh}} - J_{sc} \qquad (2.5)$$

with R_s the **series resistance** of the device, associated with carrier losses by resistive dissipation, and R_{sh} the **shunt resistance**, which by becoming lower than infinity reflects the recombination losses in the device (e.g. SRH recombinations), represented in the equivalent circuit by an alternative path for the current.
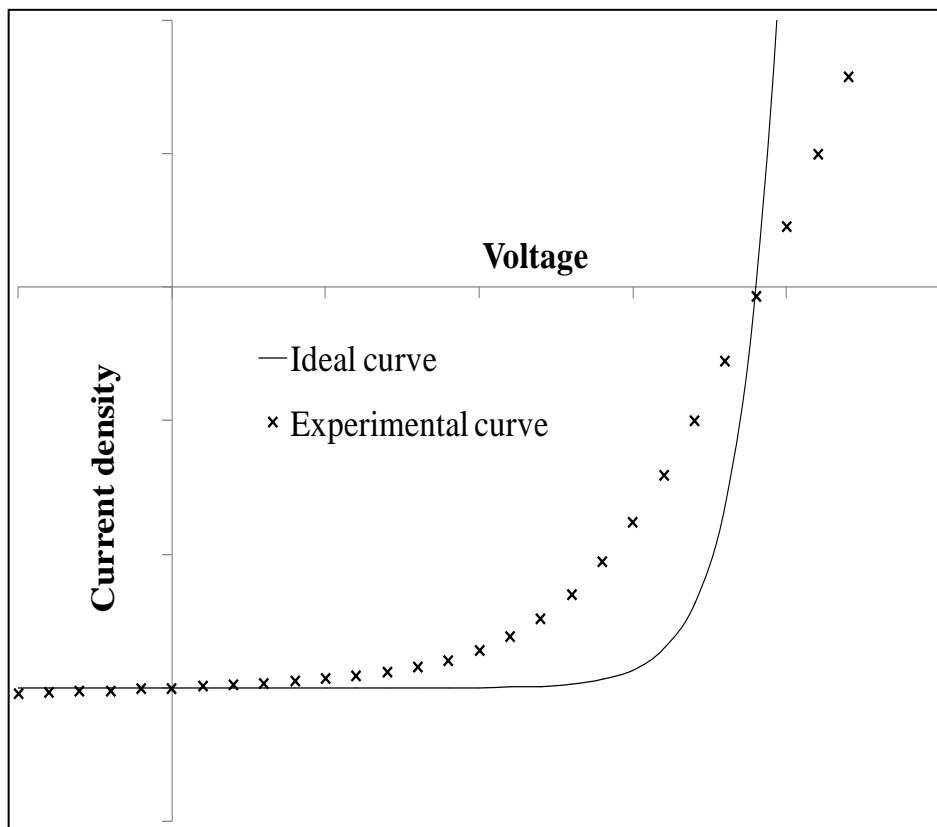
Figure 8: Comparison of an experimental J-V curve (*crosses*) and the ideal curve of a perfect diode (n=1) with R_s=0 and R_{sh}=∞ (*full line*).

In Figure 8 are shown the ideal J-V curve generated by the equivalent circuit (a), and a real J-V curve measured on a ≈5% efficient CIS cell. The main obvious differences are the increased slope of the curve in the [V<0; J<0] quadrants and decreased slope in the [V>0; J>0] quadrant.

2.4.2 Analysis of experimental J-V characteristics

Device conversion efficiency

In Figure 9 is shown the I-V characteristic of the real device already shown in Figure 8.
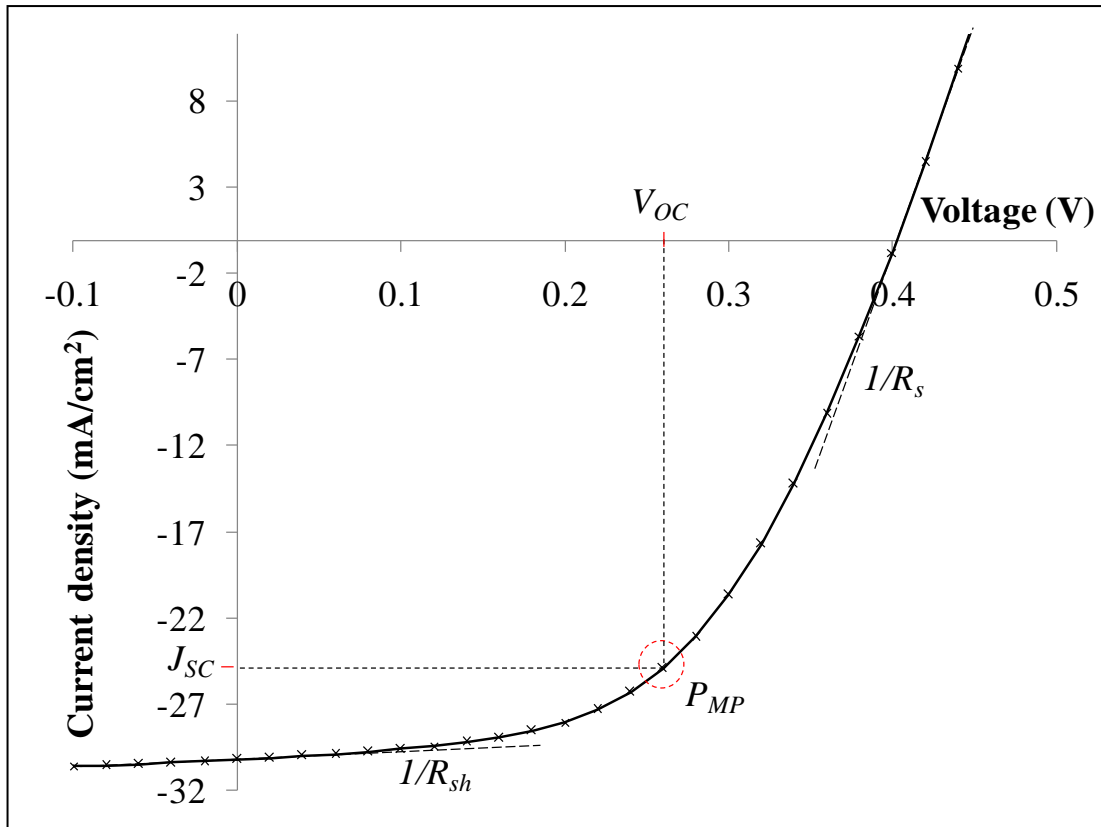
Figure 9: Experimental J-V curve illustrating the concepts of short-circuit current I_{SC}, open-circuit voltage V_{OC} and maximum power point P_{MP}. The slopes in the [V<0; J<0] and [V>0; J>0] quadrants are due to non-infinite shunt resistance R_{sh} and non-nil series resistance R_s, respectively.

The passage from current density J to current I is done by the simple operation $J=I/A$, with A the active area of the device. In Figure 9 are indicated the three most important electrical parameters of a solar cell: short-circuit current I_{SC}, **open-circuit voltage** V_{OC} and **maximum power output** P_{MP}. These three parameters are defined by:

$$I_{SC} = I(V)|_{V=0} \qquad\qquad (2.6)$$

$$V_{OC} = V(I)|_{I=0} \qquad\qquad (2.7)$$

$$P_{MP} = \text{Max}(I.V) \qquad\qquad (2.8)$$

For calculating the device efficiency, only the maximal power output P_{MP} and the power shone by the source P_{in} are required (see section 2.1 relation 2.1). However, another informative parameter is the **fill factor** FF, defined as:

$$FF = \frac{P_{MP}}{V_{OC}.I_{SC}} \qquad\qquad (2.9)$$

The fill factor quantifies the deviation from the ideal diode behaviour, where P_{MP} is very close to the product $V_{OC}.I_{SC}$. It can easily be shown from geometrical considerations that for a linear relationship between I and V, type V=R.I (implying that the device behaves like a simple resistor), FF=1/4. The fill factor of high efficiency CIGS devices produced today are typically in the range 70-80% (81.2% in the 19.9% CIGS device reported in [30]). Equations 2.1 and 2.9 show that high I_{SC}, V_{OC} and FF are required to obtain high efficiency. The energy band gap is the main factor limiting V_{OC} (see APPENDIX 1), but R_{sh} also has an important impact, since recombinations reduce the open circuit voltage. In the ideal case, I_{SC} depends linearly on the area of the device that is illuminated, and is also affected by R_s. The diode ideality factor, which can help determine whether SRH recombinations are predominantly taking place in the SCR, or in the bulk or the contacts, is also a valuable parameter.

Ideally, the experimental curve must therefore be fit with a model to extract device parameters.

Series resistance

If the shunt resistance is considered high enough in equation 2.5 the expression becomes:

$$J(V) = J_0 \left[e^{\frac{q.(V-JR_S)}{n_{id}k.T}} - 1 \right] - J_{sc} \tag{2.10}$$

V as a function of J can then be calculated:

$$J_0 \left[e^{\frac{q.(V-JR_S)}{n_{id}k.T}} - 1 \right] = J + J_{sc} \tag{2.11}$$

$$e^{\frac{q.(V-JR_S)}{n_{id}k.T}} = \frac{J + J_{sc}}{J_0} + 1 = \frac{J + J_{sc} + J_0}{J_0} \tag{2.12}$$

$$V - JR_s = \frac{n_{id}k.T}{q.} . ln \left[\frac{J + J_{sc} + J_0}{J_0} \right] \tag{2.13}$$

$$V = \frac{n_{id}k.T}{q.} . ln \left[\frac{J + J_{sc} + J_0}{J_0} \right] + JR_s \tag{2.14}$$

The derivative of 2.14 is:

$$\frac{dV}{dJ} = \frac{n_{id}.k.T}{q} . \left(\frac{1}{J + J_{sc} + J_0} \right) + R_s \tag{2.15}$$

Now, let us estimate the first term on the RHS of equation 2.15 when the slope *dV/dJ* is measured near $V=V_{OC}$. In this region of the curve, $J \ll J_{SC}$. Besides, J_0 is given by:

$$J_0 = \frac{J_{SC}}{e^{\frac{q.V_{OC}}{n_{id}.k.T}} - 1} \approx J_{SC} . e^{\frac{-q.V_{OC}}{n_{id}.k.T}} \ll J_{SC} \tag{2.16}$$

The second equality arises from the fact that for reasonably high V_{OC} values, for example $\frac{q.V_{OC}}{n_{id}.k.T} > 6$ (this lower value obtained for V_{OC}=300mV, n_{id}=2 and T=298K), $e^{\frac{q.V_{OC}}{n_{id}.k.T}} \gg 1$. It ensues:

$$\left.\frac{dV}{dJ}\right|_{V \approx V_{OC}} \approx \frac{n_{id}.k.T}{q}.\frac{1}{J_{SC}} + R_s \tag{2.17}$$

If for example J_{SC}=20 mA.cm^{-2} and the other conditions are the ones enounced before, this results in $\frac{n_{id}.k.T}{q}.\frac{1}{J_{sc}} \approx 2.5 \times 10^{-3}$ Ω, which is considered as negligible in this work, and therefore:

$$\left.\frac{dV}{dJ}\right|_{V \approx V_{OC}} \approx R_s \tag{2.18}$$

As a consequence, assuming the simple one-diode model and neglecting the shunt resistance, the measurement of the inverse of the slope of the J-V curve near $V=V_{OC}$ can be used to determine the series resistance with a reasonable accuracy. Note that the approximation becomes even more valid when J>0, since it makes the denominator of the RHS of equation 2.17 bigger and therefore the fraction smaller. The slope dV/dJ should therefore be measured in the [J>0; V>0] quadrant using at least one point far from V=V$_{OC}$.

Shunt resistance

Following a similar line of reasoning as for the series resistance, the shunt resistance can be found as:

$$\left.\frac{dV}{dJ}\right|_{J \approx J_{SC}} \approx R_{sh} \tag{2.19}$$

Therefore, an approximation of R_s and R_{sh} can be extracted from the J-V curve by taking the inverse of the slope near $V=V_{OC}$ and $J=J_{SC}$, respectively.

2.5   X-Ray diffraction

X-ray diffraction (XRD) is a characterisation technique which consists in reflecting a monochromatic beam off a crystal and analysing the resulting diffraction pattern. From the diffraction pattern can be extracted, among other parameters, the crystal structure and the lattice parameters of the crystal. These two pieces of information make it possible, provided the existence of powder diffraction standards, to identify the crystal analysed. This technique is one of the most direct ways to identify the crystalline phase $CuIn_{1-x}Al_xSe_2$, focus of this work, and therefore of great importance for this thesis.

2.5.1   Bragg diffraction

To understand why X-rays diffract on a crystal, the crystal must be visualised as a series of atomic planes, formed by the periodically arranged atoms of the material. When a radiation of wavelength λ hits the crystal at an angle θ_i, part of this radiation is reflected by the first atomic plane it encounters without a change in λ. The radiation reflects from the atomic plane at an angle θ_r, where $|\theta_r|=|\theta_i|$. Another part of the beam is transmitted and then reflects from the second plane, and so on. If λ is of the same order of magnitude as the orthogonal distance between a family of atomic planes d_{hkl}, the radiations reflected by the successive layers interfere when they meet after reflection from the crystal (Figure 10). Geometric considerations show that constructive interference occurs when:

$$n.\lambda = 2.d.sin\theta \tag{2.20}$$

with d the interplanar spacing. This simple representation of the diffraction phenomenon in terms of an interaction with atomic planes was first presented by W.L. and W.H. Bragg in 1913, and the relation 2.20 is referred to as the Bragg's diffraction law. Among electromagnetic radiation, X-rays are an attractive choice since they possess a short enough wavelength to obtain a highly resolved diffraction pattern from a crystal. A high degree of monochromatism is also required to obtain high resolution of d and this is best achieved using a synchrotron radiation source. An alternative to the XRD is the diffraction of neutrons. Since neutrons have a mass, their associated De Broglie wavelength is small, and therefore they provide a higher degree of resolution compared to X-rays.

Bragg's diffraction law:

$$L = n.\lambda = 2.d.\sin\theta$$

L=optical path difference
n=order of interference
λ=wavelength of incident light
d=distance between atomic planes
θ= angle between incident beam and plane of the sample
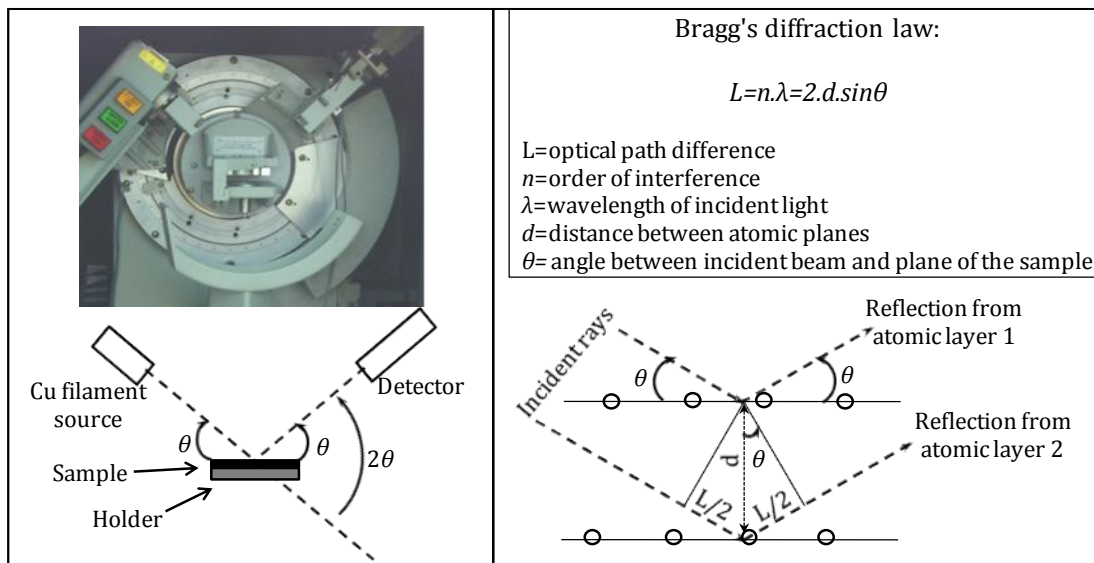
Figure 10: Diagram illustrating the θ-2θ X-ray diffraction setup (*left*) and Bragg's diffraction (*right*).

2.5.2 Crystallography of CuInSe$_2$, CdS and Cu$_{2-x}$Se

The main material of interest for the work of this thesis is CuInSe$_2$ (CIS), since it is the base of the absorber material prepared. It usually crystallizes with the chalcopyrite structure, space group $I\bar{4}2d$ in the international notation. Other crystalline phases of some importance are Cu$_{2-x}$Se and CdS. CdS is the buffer layer

24

used in this work and most CIS-based devices. It can be formed in one of two crystalline forms: either with the **sphalerite** crystal structure ($F\bar{4}3m$) or with the **wurtzite** crystal structure ($P6_3mc$), represented in Figure 11.
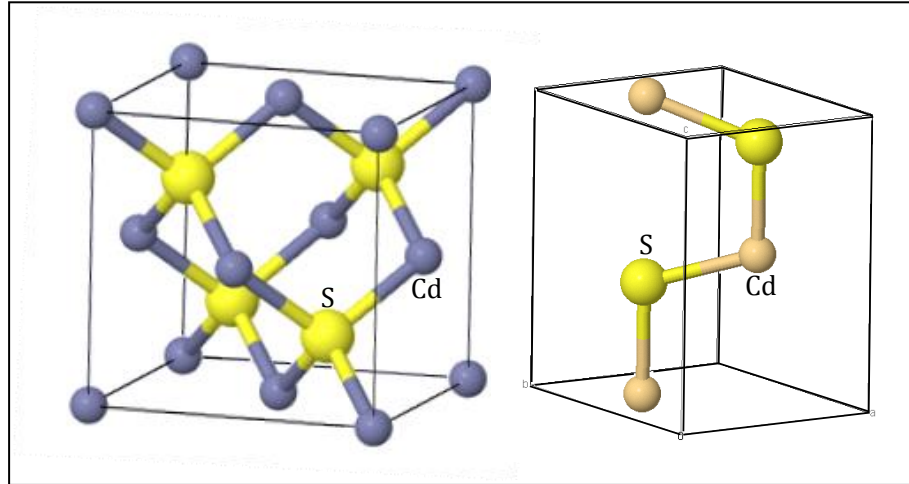
Figure 11: Two forms of CdS. *Left*: **sphalerite ($F\bar{4}3m$). Smaller blue balls:** *Cd;* **bigger yellow balls:** *S. Right*: **wurtzite ($P6_3mc$). Smaller beige ball:** *Cd;* **bigger yellow ball:** *S.* **Drawn with** *Jmol* **from [31].**

The **chalcopyrite** crystal structure is derived from the sphalerite structure, which is the structure of most II-VI semiconductors including CdS and CdTe. If the sites initially occupied by group II (e.g. Cd) elements are alternately replaced by a group I element (e.g. Cu) and a group III element (e.g. In), then the new crystal structure formed is the chalcopyrite crystal structure (Figure 12, *left*). The chalcopyrite compounds have a tetragonal structure, and the difference in bond length between In-Se and Cu-Se introduces a distortion along the *c* axis. This distortion, called the *tetragonal distortion*, is characterised by the quantity $2 - \frac{c}{a}$. The tetragonal distortion observed in CuInSe$_2$ is -0.01 and that in CuGaSe$_2$, +0.04. In the absence of In, and depending on the Cu to Se ratio, Cu and Se can crystallize in a Cu$_2$Se cubic face-centered lattice[4] (Figure 12, *right*), $F\bar{3}m$. CIS and Cu$_{2-x}$Se display very similar

---

[4]To which the Cu$_{2-x}$Se structure is closely related.

structures, and therefore the XRD patterns of those two phases are hard to distinguish. Only the tetragonal distortion, observed in CIS and most chalcopyrites, makes it possible to tell between the two, but it is only visible for sufficiently high intensity peaks.
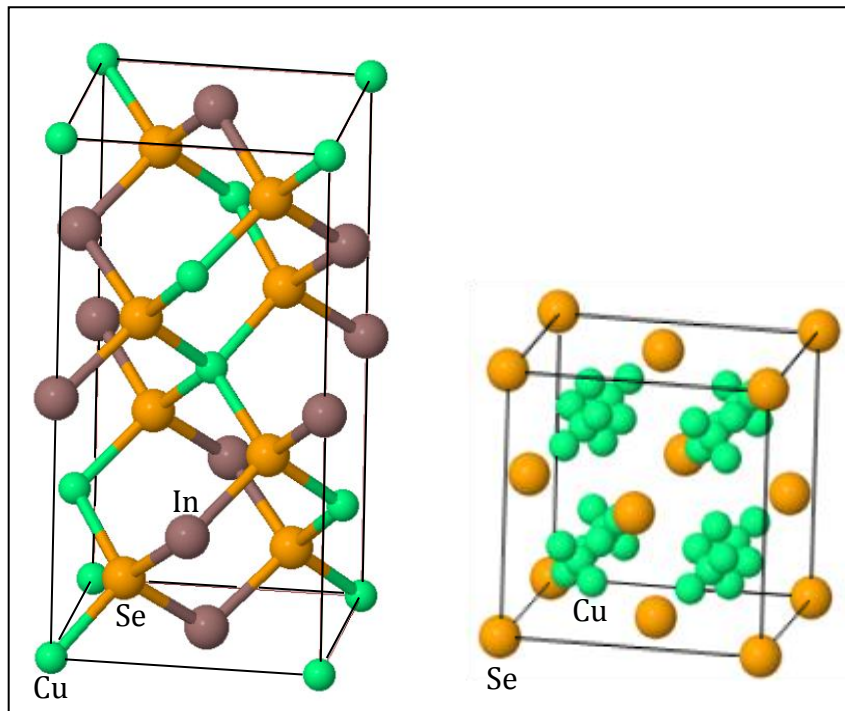
Figure 12: Crystal structure of l*eft* CuInSe$_2$ ($I\bar{4}2d$) and r*ight* Cu$_2$Se ($F\bar{3}m$) (the bonds are not displayed for clarity). In Cu$_2$Se, the smaller balls are the possible locations of the Cu atoms. *Drawn with Jmol from the Chemical Database Service [31].*

CHAPTER 3　　　CuInSe$_2$-BASED SOLAR CELLS: EVOLUTION

AND STATE OF THE ART

This chapter describes the development of CuInSe$_2$ (CIS) and then CuIn$_{1-x}$Ga$_x$Se$_2$ (CIGS), the most commonly used CIS-based material today, and finally CuIn$_{1-x}$Al$_x$Se$_2$ (CIAS). The state of the art device structure, the progress made in the theoretical understanding of the material properties and the evolution of the fabrication technologies are reviewed.

3.1　CuInSe$_2$-based solar cells: state of the art

Today, several chalcopyrites and related materials are being investigated. The most successful material in laboratory is CuIn$_{1-x}$Ga$_x$Se$_2$ (CIGS). At the time of redaction, the record efficiency for a thin films solar cell is held by Zentrum für Sonnenenergie- und Wasserstoff-Forschung Baden-Württemberg (ZSW) [4, 32] with a 20.3±0.6% efficient CIGS device. In their layout, the substrate was soda-lime-glass (SLG), the back contact sputtered Mo, and the CIGS absorber was deposited by co-evaporation. A CdS buffer layer was deposited by chemical bath deposition on top, followed by a sputtered thin i-ZnO layer and a thicker Al-doped ZnO transparent conductive oxide. The front contact grid was made of a thin Ni layer and a thick Al layer. The National Renewable Energy Laboratory in Colorado has produced devices of efficiencies close to 20% with the same cell layout [30].

It appears interesting to start from these high efficiency cells to trace back the progress made since the first CIS devices, fabricated and studied in the Bell Laboratories in the mid 70s [33-35]. First of all, regarding our fundamental understanding of the material, several important steps were taken. Cheap soda-lime-glass (SLG) substrates have now replaced the more expensive high purity substrates

27

used in the early days (section 3.2.1). The introduction of the element Ga has also been found to yield improvements in the device characteristics (3.2.2). The intrinsic doping of CIS and CIS-based absorbers, usually made p-type for use as absorber in solar cells, was thoroughly investigated [6] and found to be due the presence of native defects (3.2.3). A type inversion, from p to n-type, was discovered at the surface of CIS and CIGS, and its causes partially elucidated (3.2.4). The performance degradation due to the presence of a copper selenide phase at the surface of Cu-rich absorbers and its removal by potassium cyanide (KCN) etch were also studied (3.2.5).

Regarding the fabrication techniques for the absorber, the Boeing (section 3.3.1) and the 3-stage co-evaporation processes (3.3.3) were developed, the latter yielding the record efficiency cells to date. The so-called 2-stage process was also created (3.3.2), mainly for scaling up purposes.

On top of the absorber is still deposited an intrinsically n-type CdS buffer layer (section 3.4.3), but the In-doped CdS of the early technologies was replaced by a transparent conductive oxide (TCO) such as ZnO:Al (section 3.4.4). An important factor in high efficiency was the addition of a thin ($\approx$50 nm), resistive, undoped ZnO (i-ZnO) layer between the CdS and the TCO.

3.2   Progress in the understanding of the physics of CIS and CIGS absorber layers

3.2.1 The role of Na

Hedström *et al.* were the first group to report on the improved performance provided by soda-lime-glass (SLG) over other substrates [36]. They compared the performance of CIS and CIGS films grown on SLG, sapphire, alumina and

borosilicate, and noticed a considerably higher open-circuit voltage for the cells grown on SLG, as well as bigger grains in the absorber films. Even today the reasons behind the improvements brought by Na have not all been clarified. However the models detailed below have been proposed.

Defects passivation

The most important model concerns the role of Na in reducing the activity of the film surface and grain boundaries (GB) by oxygen passivation of the defects. This was first presented by Kronik *et al.* [37]. An evidence of this passivation is the drastic decrease in the film resistivity of Na-containing absorbers compared to Na-free absorbers. Ruckh *et al.* [38] reported for example an increase of conductivity by one order of magnitude in Na-containing films compared to Na-free ones, whereas Virtuani *et al.* observed an increase by two orders of magnitude [39]. Activation energies extracted from temperature-dependant conductivity measurements also indicated a reduced band bending at the grain boundaries in the presence of Na [37]. The model suggested by Kronik *et al.* to explain this passivation was based on the observation that Na is preferentially located at the film surface and grain boundaries. It builds on an earlier model from Cahen *et al.* [40] regarding oxidation of Se vacancies at the surface and grain-boundaries (GB) when the films are annealed in air. The model of Kronik *et al.* combines this to the well-established oxidising effect of alkali in Si and in GaAs. The model postulates that Na acts as a catalyst, polarising the O_2 adsorbed at the film's surface and GB and lowering their work function. This results in the formation of O_2^-, which then breaks down into individual atoms that in turn attach themselves to the In atoms who lost their Se partner.

The general reaction can be summarized as follows:

(a) Na-assisted adsorption (i.e. chemical bonding) of O^{2-} onto the surface

$$\frac{1}{2}O_{2\ physisorbed} + 2e_{cb}^{-} \xrightarrow[Na]{} O^{2-}{}_{adsorbed} \tag{3.1}$$
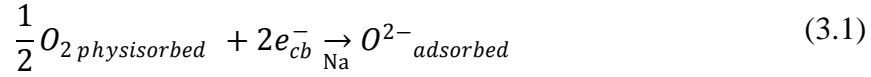
(b) Creation of a charged Se vacancy V_{Se}

$$\{In_M - Se_{Se}\}_{surface} \leftrightarrow \{In_M - V_{Se}^{\bullet\bullet}\}_{surface} + 2e_{cb}^{-} + Se \tag{3.2}$$
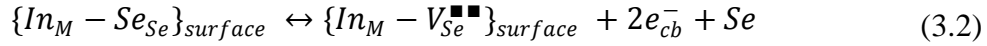
with $^{\bullet\bullet}$ a double relative positive charge, $_M$ a metal site (In or Ga in CIGS) and $_{Se}$ a Se site.

(c) Finally, neutralisation of the $\{V_{Se}^{\bullet\bullet}\}$ by bonding with O:

$$\{In_M - V_{Se}^{\bullet\bullet}\}_{surface} + O^{2-}{}_{adsorbed} \leftrightarrow \{In_M - O_{Se}\}_{surface} \tag{3.3}$$

Note that in the absence of Na, reaction 3.1 does not readily occur, leaving the products of reaction 3.2 at the surface in the end. The donor defect states associated with $\{In_M - V_{Se}^{\bullet\bullet}\}$ have the double negative effect of decreasing the effective p-type doping and acting as recombination centres for photogenerated carriers.

Other Na effects

Na also causes a texturing towards a (112) preferred orientation in the co-evaporation process, and an increase in grain size [36], especially in the 2-stage process with rapid thermal processing (RTP). This latter observation was made by Probst *et al.* [41] and the authors suggested it was due to the effect of Na on the kinetics of formation of CIS. Indeed, it is believed that CIS-based chalcopyrites form at low temperatures by consumption of $Cu_{2-x}Se$ in solid phase, whereas at higher temperatures the $Cu_{2-x}Se$ becomes liquid, segregates at the film surface and acts as a flux agent (see [42] and section 3.3.1). If Na slows down the reaction of formation of

CIS, the consumption of Cu and Se is slowed down as well, and $Cu_{2-x}Se$ is still present when the process temperature reaches 523°C, and starts to act as a flux agent. However, Probst *et al.* noted that even with Na, only rapid thermal processing allows sufficiently high ramping rates to reach the high temperatures required for big grains formation before complete consumption of the $Cu_{2-x}Se$.

It is also possible that part of the sodium is actually incorporated into the lattice [43], as supported by some X-ray diffraction (XRD) and X-ray photoelectron spectroscopy (XPS) data, showing respectively an increased cell volume and the presence of Na-Se bonds in Na containing films. In this assumption, Na_{In} and Na_{Ga} acceptor defects could be responsible for an increase in the p-conductivity of the film.

Finally, Na is associated with a reduction in the defect compensation in CIGS, possibly by re-ordering of the defects into electrically passive clusters [44].

The sodium distribution in SLG can be non uniform and vary from substrate to substrate. To ensure a better Na uniformity across large–area modules, the company Siemens introduced an alkali-barrier layer on top of the SLG (such as SiO_x or Al_2O_3), and added a uniform Na-compound coating on top [41]. This is now common practise in the industry.

3.2.2 The role of Ga

Two types of Ga distributions in CIS are commonly used today:

- A uniform $CuIn_{1-x}Ga_xSe_2$ composition throughout the depth, for which the band gap ranges between 1.0 eV (CIS band gap) at x=0 and 1.7 eV (CGS band gap) at x=1.

- A Ga composition varying with depth (graded composition).

The uniform distribution allows a tuning of the band gap for a better match to the solar spectrum, and can be used as a single junction or be inserted into a multiple junction device. This type of distribution is more readily obtained from co-evaporation.

The graded composition can have a variety of effects on the device characteristics. One typical example is a layout where the Ga content increases near the back contact. This type of layout was first investigated in 1988, in one of the early papers on CIGS, by Tuttle *et al.* [11]. The authors investigated among other things the effect Ga could have if inserted at the back of the space charge region (SCR), in a configuration they called "electron-mirror". Indeed, this Ga gradient, if properly incorporated into the lattice, is associated with a band gap gradient, which for CIGS is mainly a shift of the conduction band [45, 46]. This gradient corresponds physically to an in-built electrical field that pushes electrons away from the back contact where they would otherwise recombine (Figure 13), and increase the number of them reaching the SCR. The authors anticipated that this reduced electron losses would cause an increase in J_{sc}, but did not observe it and therefore could not conclude positively on the experiment. In 1993, Jensen *et al.* [47] reported a V_{oc} increase in Ga-containing CIS films prepared by the 2-stage process, where the Ga had accumulated (unintentionally) at the back. Dullweber *et al.* [48] also found the introduction of Ga at the back to lead to a significant increase in V_{oc}[5], with small improvement in J_{sc}, and no change in the optical band gap of the bulk. These results fit the model of reduced recombination losses at the back.

---

[5] up to $E_G \approx 1.2$ eV, i.e. $x \approx 0.3$
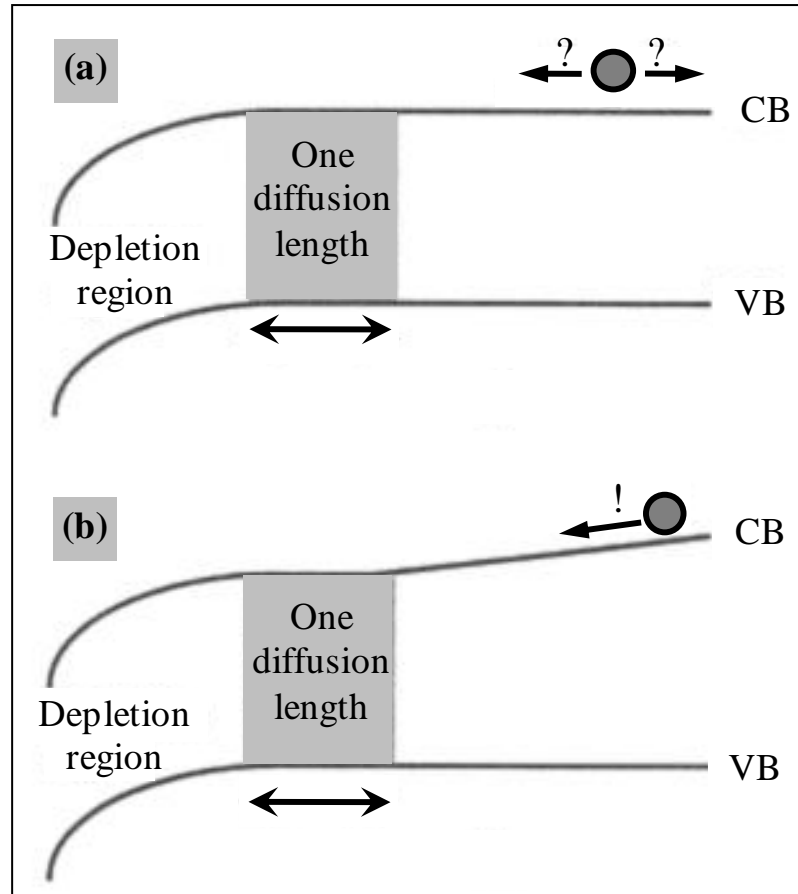
Figure 13: Band diagram of (a) a non-graded band gap absorber and (b) an increasing band gap towards the back. *Source: [49].*

Another typical graded design, that can be seen as an improvement on the previous one, is the so-called "notch profile", usually deposited by co-evaporation. It consists in an increased amount of Ga both at the back and the front of the film, and a lower band gap in the bulk (Figure 14). The deposition procedure is referred to as the 3-stage process. The notch profile yields the highest efficiency thin film solar cells produced by NREL and ZSW (up to 20.3%) [4, 30]. The additional benefit of the band gap increase near the front surface is yet another improvement in the V_{oc} and can be attributed to lower recombination losses at the front, thanks to a better band line up with CdS.
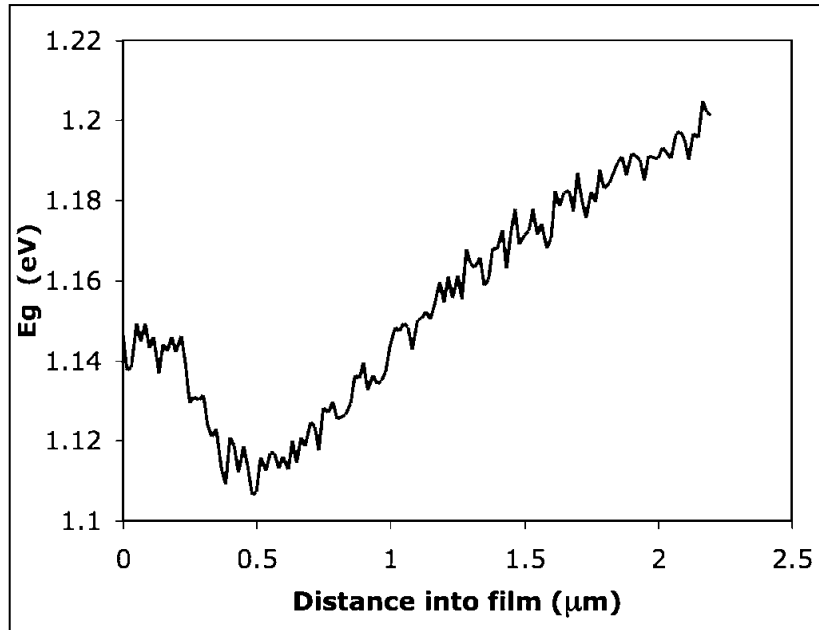
Figure 14: Band gap profile of the CIGS absorber used in a 20% efficient device, obtained from Ga/(Ga+In) in Auger electron spectroscopy. *Source: [50].*

3.2.3 Native doping defects and deep recombination centres in CIS and CIGS

Defects play a determinant role in the properties of CIS-based absorbers. They are responsible for their intrinsic doping as well as for the Shockley-Read-Hall (SRH) recombination centres that limit this material's efficiency [51]. Although the discussion below is valid for all CIS-based materials unless explicitly indicated otherwise, only CIS will be mentioned for clarity.

Doping defects

The defect chemistry of CIS is mainly dictated by its composition. The intrinsic doping of CIS is known to be p-type when grown from Cu-poor (i.e. Cu/In<1) material under an overpressure of Se, whereas a too low Se pressure associated with a Cu-rich composition produces n-type material. A copper vacancy V_{Cu} is the main acceptor (p-type) in Cu-poor CIS [51]. It lies $\approx$30meV above the Valence Band Maximum (VBM) [44] and has a negative formation energy in Cu-poor and

34

stoichiometric material, which accounts for the intrinsic and relatively strong ($\approx 1.10^{16} cm^{-3}$) p-type doping of Cu-poor CIS. Selenium vacancy V_{Se}, on the other hand, is a donor defect located $\approx 110 meV$ [51] below the Conduction Band Minimum (CBM), and is responsible for the n-type conductivity of Cu-rich, Se-deficient CIS. In summary, the relative populations of V_{Cu} and V_{Se} determine the conductivity type of CIS.

Other defects

Besides those doping defects, which are shallow (a few tens of meV from the CBM for the donor and VBM for the acceptor), other defects lie deep within the band gap and can cause recombination of the electron-hole pairs, leading to performance degradation. Some of these defects can be more or less detrimental depending on the band structure where they are inserted (e.g. CIS or CIGS with a given composition).

A defect found at $\approx 300 meV$ above the VBM in CuInSe$_2$ was used to measure the valence band shifting when alloying CuInSe$_2$ with Ga. The absolute energy of this defect remained stable with Ga alloying, the measurement of the energy difference between this energy state and the VBM allowed Turcu *et al.* [46] to measure the band shifting with Ga alloying. The authors observed no shift of the valence band with Ga alloying, and therefore deduced a shift of the conduction band towards higher energy, in agreement with theoretical predictions of Wei and Zunger [45]. This property explains the increased performance of CIGS devices including a Ga increase near the back surface (see section 3.2.2). The defect $\{2V_{Cu}\text{-}In_{Cu}\}$, which has a very low formation energy, is believed to be responsible for the surprisingly high tolerance of CIS-type absorbers with respect to the Cu/In ratio. This defect has no transition within the band gap, and helps accommodating with Cu-poor compositions

without performance degradation. It is most likely the building block of the ordered defect complexes such as $CuIn_3Se_5$ and $CuIn_5Se_8$, important for the junction formation mechanism (see section 3.2.4).

V_{Se} can form with V_{Cu} the divacancy complex $\{V_{Se}\text{-}V_{Cu}\}$ [52].$\{V_{Se}\text{-}V_{Cu}\}$ is one of two types of metastable defects believed to limit the V_{oc} beyond $E_g > 1.15eV$ in CIGS by forming an acceptor state for recombination of the electrons, 0.9 eV and 1.0 eV above the VBM in CIS and CGS, respectively. This metastable defect is particularly harmful to CIGS, because, as the band gap increases, the CBM shifts away from the defect, and the defect level becomes an active recombination centre. The other type of metastable defects affecting Cu poor CIGS comprise the two antisite defects In_{Cu} and Ga_{Cu}, which are double donors and have a deep energy state at ≈0.5 eVabove the VBM [52].

3.2.4 Ordered defect compound and surface defect layer

The first important insight into the process of formation of the p-n junction in CIS devices was brought by Schmid *et al.* in 1993 [53], who showed that a thin n-type $CuIn_3Se_5$ layer was present at the surface of Cu-poor (albeit slightly) $CuInSe_2$ absorbers. It is important to point out that the samples were grown on Na-free substrates. $CuIn_3Se_5$ is an **ordered defect compound** (ODC) of $CuInSe_2$. It is obtained for Cu as-deposited compositions lower than 50 at%. The composition of the ODC was determined by XRD on a bulk layer of the stoichiometric 1:3:5 composition and by XPS at the surface of a slightly Cu-deficient $CuInSe_2$ absorber. The p-n junction was shown by electron beam induced current (EBIC) to be buried, and ultraviolet photoelectron spectroscopy (UPS) revealed that the valence band of the ODC layer was of lower energy than that of $CuInSe_2$, and that the Fermi level

36

energy was located in the conduction band. This meant that the ODC was strongly n-type. The formation of a p-n junction between CIS and the ODC was also directly proved by making a cell lacking the buffer and window layers, i.e. comprising only the stack "back contact/CIS/ODC/semi-transparent front contact". The cell showed a relatively good I-V curve in spite of the important optical absorption due to the semi-transparent metallic contacts on top. The authors assumed that the n-type ODC was probably the cause of the p-n junction formation.
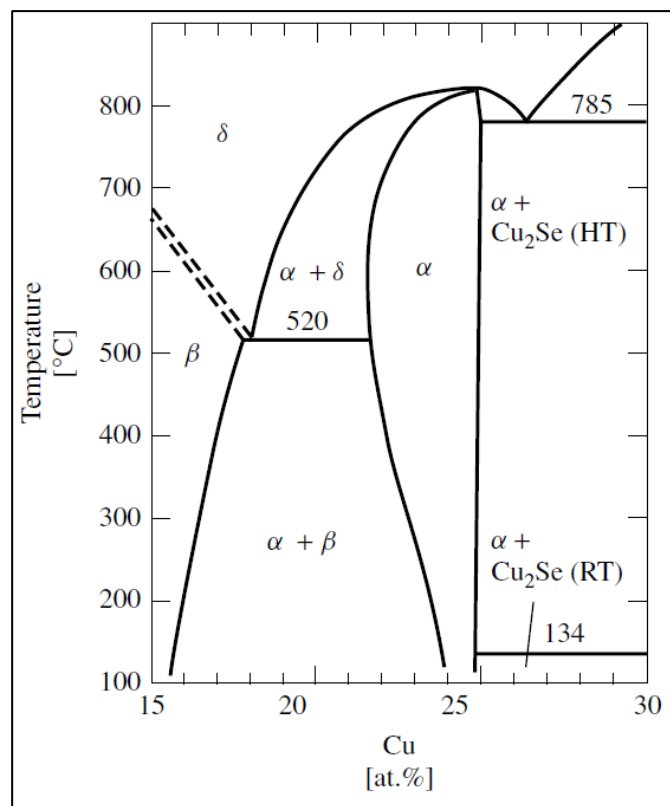
Figure 15: Pseudo-binary phase diagram along the tie line Cu2Se-In2Se3 on Na-free substrate as presented in [54]. Here, the α phase is the chalcopyrite CuInSe2 and the β phase the ordered defect compound CuIn3Se5.

This model, initially established for CIS on Na-free substrates (i.e. not on SLG), was later revised and applied to CIGS by Herberholtz *et al.* The authors presented an alternative model explaining the junction formation in CIS on Na-free substrate, CIS on SLG, and in CIGS [55]. The main finding was a broadening of the existence

range of the phase CuInSe$_2$ in the pseudo-binary phase diagram presented in Figure 15. The model was built on the following results:

(a) CIS grown on soda lime glass (therefore containing Na) showed a wider existence range of the α-CuInSe$_2$ phase in the Cu$_2$Se-In$_2$Se$_3$ pseudo-binary phase diagram. This implies that the ODC corresponding to the β phase in Figure 15 will form for more Cu-poor compositions than in Na-free CIS. For slightly Cu-poor CIS samples in the existence range of pure α, a disordered surface defect layer forms, where the Cu content is graded, from more Cu-poor at the surface to less Cu-poor in the bulk.

(b) In CIGS, the introduction of Ga also causes a widening of the existence range of the α phase. The reasons are not totally elucidated. Ga enhances the oxidation of the surface and hence its passivation. Furthermore, the formation energy of Ga$_{Cu}$ is higher than that of In$_{Cu}$, meaning that the defect complex $\{2V_{Cu} - Ga_{Cu}\}$ is less likely to form and therefore β is less likely to form too. Let us point out that this last explanation is only applicable for high Ga content, which could possibly exclude the record efficiency devices where $x = \frac{Ga}{Ga+In} < 0.3$.

(c) The model of a positively charged surface assisting the junction formation was also applied to CIS on Na-free substrate. The authors noted that to achieve a conductivity type inversion the phase present at the surface of the film should have a carrier density much higher (3 orders of magnitude) than that actually observed in bulk β phase. Therefore, the β phase alone could not account for the type inversion observed by Schmid *et al.* Instead, the best way to explain this type inversion was by invoking the presence of the same positively charged surface states mentioned in section 3.2.1. The electromigration of the Cu away from the surface, would then be a

consequence rather than a cause, of the presence of these positive charges at the surface.

3.2.5 Effect of a superficial $Cu_{2-x}Se$ layer

In samples made with an excess of Cu (i.e. where Cu/III>1), a superficial layer of $Cu_{2-x}Se$ usually remains at the end of the absorber fabrication stage, which is a degenerate semiconductor. In a degenerate p-type (n-type) semiconductor, the hole (electron) doping density is so high that its Fermi level lies less than $3k_BT$ above (below) its valence (conduction) band [56]. This high doping density causes its allowed energy levels to overlap, causing band gap narrowing [17] and providing the material with metallic properties, that tend to dominate the opto-electronic properties of the finalised devices. This $Cu_{2-x}Se$ layer must therefore be prevented or removed before subsequent layers can be deposited [42].

Detrimental effect of $Cu_{2-x}Se$ / importance of potassium cyanide etch

An early paper from Klenk *et al.* [57] reported on the performance degradation in CIS devices due to the presence of $Cu_{2-x}Se$ at the interface with the buffer layer. In their experiment, they compared the open circuit voltages (V_{oc}), short circuit current densities (J_{sc}) and fill factors (FF) of $CuGaSe_2$/(Zn,Cd)S heterojunctions made from unetched Cu-rich absorbers, against identical heterojunctions made from potassium cyanide (KCN) etched absorbers. They observed an important increase of V_{oc} ($\approx$50%), Jsc (>300%), and FF ($\approx$20% relative) after etching with a solution of KCN. Similar results were also obtained with CIGS samples [58]. Etching in a KCN solution is the most common way to remove the superficial $Cu_{2-x}Se$ phase [57-61]. KCN has the interesting property that it etches $Cu_{2-x}Se$ much faster than the other possible phases present in the absorber, namely, for CIGS, the phases $CuGaSe_2$,

CuInSe$_2$, Ga$_2$Se$_3$ and In$_2$Se$_3$ [57]. A too long etching, on the other hand, results in a degradation of the fill factor. Klenk *et al.* also measured an increase in absorption of the absorber layer within the band gap of CGS when the Cu$_{2-x}$Se layer was etched away. The same authors also observed a conductivity at the surface of the films two to three orders of magnitudes higher on unetched Cu-rich samples than on the etched ones [62], as well as a hole density orders of magnitude higher [57]. This fits with the degenerate p-type conductivity of Cu$_{2-x}$Se. The degradation of opto-electronic properties of the heterojunction suggests that this superficial Cu$_{2-x}$Se layer dominates the properties of the absorber.

Other properties of Cu$_{2-x}$Se

Considering the very high conductivity of Cu$_{2-x}$Se, if it happened to percolate along the grain boundaries for example, one would expect it to create shunting paths between back contact and TCO. This would result in a reduction of the shunt resistance. However, no decrease of the shunt resistance was observed in Cu-rich absorbers [39]. That suggests that Cu$_{2-x}$Se must remain at the surface of the grains only, and is not a factor in the shunting in CIS-based absorbers.

3.3 CuInSe$_2$ and CuInSe$_2$-based absorber layer fabrication

3.3.1 The Boeing process

From the early studies of the Bell Laboratories, an important step up in the fabrication of CIS cells was taken in 1980 with the **Boeing process**, developed by a team of the company Boeing [63, 64]. This process consisted in growing, by co-evaporation from elemental sources and onto a heated substrate, a bottom CIS film with a Cu composition higher than the stoichiometric 1:1:2, followed by another layer with this time less Cu than stoichiometry. The overall composition used in the

early devices was Cu-rich [64]. This fabrication process is sometimes referred to as the "bilayer process". An n-type CdS layer was deposited on top, and followed by an n^+ CdS:In to collect the electrons[6]. The substrate used by Mickelsen *et al.* was Al_2O_3 [64], since the beneficial effect of Na had not yet been discovered. The Boeing process was mostly empirical, and the underlying reasons for its success in yielding high efficiency cells, was not well understood at the time. These reasons, some of which only valid for the particular experimental setup used, have been elucidated since.

The Cu-poor part of the film was reported by several authors [53, 55, 65] to turn into a bulk phase with a Cu:In ratio of $\approx$1:1 and a phase at the nearest surface of lower Cu composition. The Cu:In ratio depends on the initial precursor bulk composition. This superficial phase can for example be the ODC $CuIn_3Se_5$ discussed in section 3.2.4.

A good reason also motivates the use of a Cu-rich stage. A Cu-rich composition leads to the formation, at high temperatures (see Figure 16), of Cu_2Se and $Cu_{2-x}Se$ at the surface of the film, from combination of CuSe and Se[7]. This phase, although undesirable in its solid state at the end of the process, has been suggested by Klenk *et al.* [42, 62] to act as a "flux agent" at the surface of the grains at high temperature, improving their growth. The advantage of growing big grains is that it minimizes the total area of the grain boundaries, where accumulated defects can yield deep level traps or potential barriers, causing recombination and impeding carrier diffusion. Klenk *et al.* also found that this $Cu_{2-x}Se$ layer is present as long as the overall composition of the film is Cu-rich, and independently of the composition of the

---

[6] The In-doped CdS is denoted n^+ because it has higher n-type conductivity than undoped CdS, allowing a better collection of the photogenerated carriers.
[7]$Cu_{2-x}Se$, although not explicitly mentioned in Figure 16, accounts for the stoichiometries allowed for the phase labeled "Cu_2Se" in the phase diagram.

particular layer being deposited. Therefore, in the bilayer process of Boeing, the growth is assisted by the presence of liquid $Cu_{2-x}Se$ not only during the Cu-rich stage but also during part of the Cu-deficient stage, as long as the overall composition is still Cu-rich. The consequence is that, by adjusting the deposition times for the Cu-rich and Cu-deficient stages, it is possible to obtain a film made of large grains and free of $Cu_{2-x}Se$
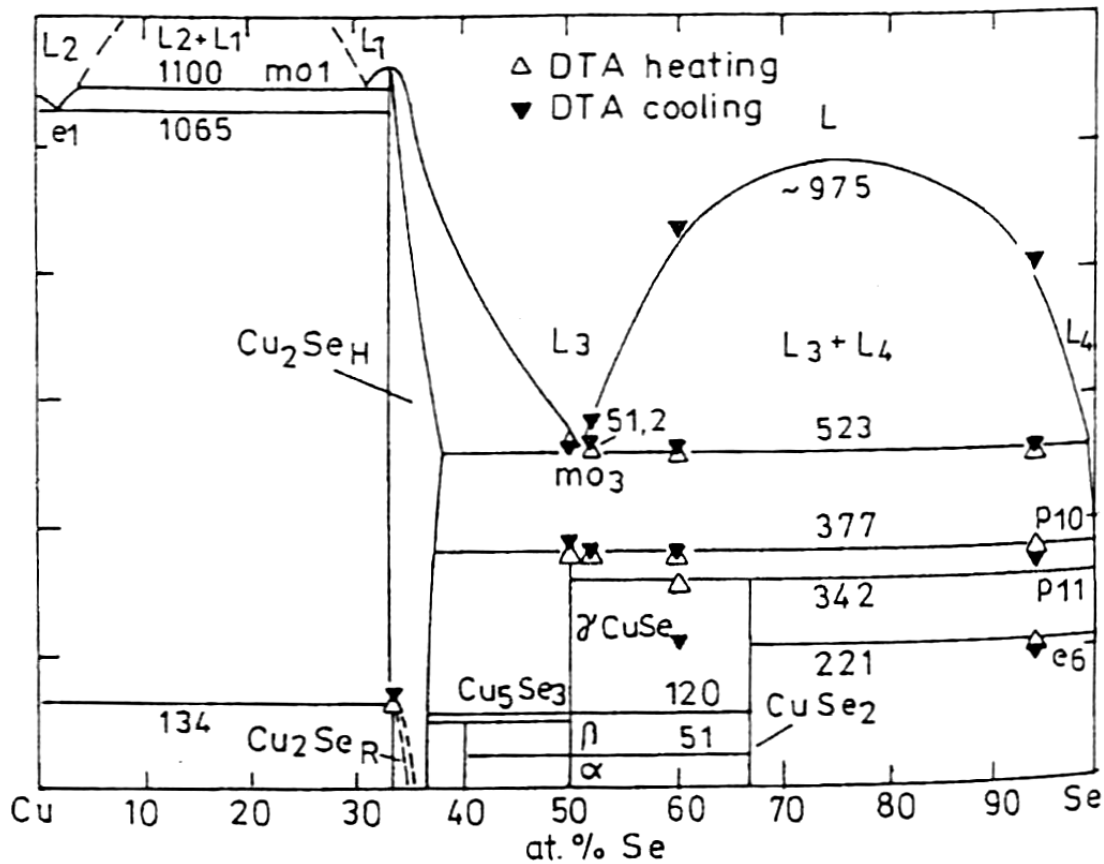
Figure 16: Binary phase diagram of Cu-Se [66]. The temperatures are indicated in °C.

3.3.2   The 2-stage process

Another process of special importance is the so-called 2-stage process. Already studied in some detail on a laboratory scale, notably by Binsma *et al.* in Netherlands in 1982 [67], it was developed into a scalable manufacturing process for $CuInSe_2$ by the PV branch of the Atlantic Richfield Company, ARCO Solar inc. [68] in the early and mid-1980s. The process consisted in:

(a) A first stage where metallic precursors (i.e. a layer comprising all the elements except for the chalcogen Se) were deposited. The early deposition process was the electroplating of Cu and In.

(b) A second stage where Se was incorporated into the metallic precursor to form the chalcopyrite compound, in a step called **selenisation**. This step was achieved by annealing the metallic precursors in a 50 sccm Ar flow containing 1.5% of H_2Se.

Modern 2-stage fabrication techniques

The techniques used for depositing the metallic precursors have diversified since the 1980s. The most successful ones are sputtering and evaporation of stacked elemental layers, which are relatively easy to apply uniformly on large surfaces. However, some non-vacuum deposition routes, reviewed in [69], could lead to important cost reduction and higher throughput. Electrodeposition is still investigated notably because it makes an optimal usage of the material, and reasonably high efficiencies (up to ≈14%) have been achieved, although the co-deposition of several elements of different standard potentials in the same bath is an important challenge. Another relatively successful non-vacuum technique is the deposition of nanoparticles of the precursor elements. The nanoparticles can be deposited as an ink for example, as done by Nanosolar. Deposition of hydrazine-based precursors in solution is a recent technique that has shown promising results, with up to 12.1% efficiency [70], but the presence of the hazardous hydrazine gas in the by-products makes its use delicate [69].

Regarding the second stage of the 2-stage process, the main improvement is the replacement of traditional furnaces by rapid thermal processing furnaces (RTP), which allow much faster heating and cooling rates (see section 4.1.4.2).

One particularly successful method of depositing the metallic precursors is what is called the stacked elemental layers (SEL) layout, whereby the total amount of each element is deposited at once, followed by the next element, and so on until all the elements have been deposited. For CIS for example, the SEL could be a $x\ nm$ thick layer of Cu, followed by a $y\ nm$ thick In layer, where x and y are adjusted to obtain the desired stoichiometry.

The chalcogenisation (selenisation or sulphurization) step converts the metallic precursors into a semiconductor with the chalcopyrite structure. The source of chalcogen used in the early days, was a carrier gas of H_2Se (or H_2S). Although this route yields high efficiency devices, the toxicity of these gases led some PV companies to investigate less hazardous ways of providing the chalcogen element for the chalcogenisation. The main alternative is to anneal the metallic precursor with solid Se or S, either by depositing a solid layer of the chalcogen on top of it or by placing solid Se (or S) in the reaction chamber. The solid Se then interacts with the film during annealing, in solid and vapour phase, and combines to form the chalcopyrite material.

Probst *et al.* reported in reference [41] two different grain size regions, bigger grains at the top and smaller grains at the bottom, in SEL films grown via a 2-stage rapid thermal process in the presence of Na (process summarized in Figure 17). The authors concluded that the grain size enhancement observed in the Boeing and 3-stage processes could also take place in the 2-stage process. However, this requires a ramping speed high enough for some solid $Cu_{2-x}Se$ to remain at the melting temperature of this phase, 523°C, and form the liquid phase mentioned earlier.
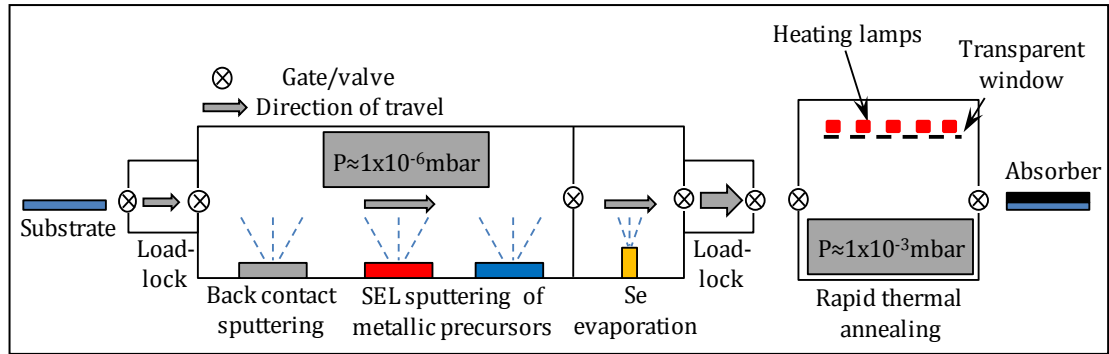
Figure 17: Example of 2-stage deposition with stacked elemental layer, used by Probst *et al.* in [41].

Phase segregation in 2-stage process

One major drawback of the 2-stage process is an observed tendency for the different elements of the absorber to migrate within the film. In particular, a segregation of Ga at the back and In at the front is often reported [14, 47, 71]. As mentioned in section 3.2.2, this migration does not necessarily lead to a degradation of the device performance. However, for high performance and process stability it is important to control precisely the depth profile of the different elements present.

Manufacturing companies using a 2-stage process

AVANCIS, Solar Frontier and Sulfurcell are examples of companies manufacturing CIS-based modules via a 2-stage process. AVANCIS use CIGS as the absorber. They also deposit a Na barrier layer (SiO_2 or Al_2O_3) on top of the SLG, and then add a uniform Na-containing layer on top of it. The barrier layer blocks the Na from the SLG substrate and prevents potential impurities from diffusing from the substrate into the absorber. The use of this barrier layer therefore allows a better control of the Na amounts introduced and of its distribution uniformity. Sulfucell utilizes a $CuInS_2$ absorber layer, which has a band gap of 1.5 eV [72], closer to the optimal band gap for single junction solar cells. Solar Frontier, a Japanese subsidiary of Showa Shell Sekiyu, claims a 17.8% efficient 30 cm by 30 cm $CuIn_{1-x}Ga_x(S_{1-y}Se_y)_2$ (CIGSSe or

45

CIGSS) submodule deposited by 'sulfurisation after selenisation' (SAS) 2-stage process [2]. This company also currently has the biggest CIGS production capacity with over 1 GW [13]. Nanosolar developed a deposition system that allows non-vacuum deposition of a CIGS ink followed by annealing, which yields higher throughput and lower production costs than vacuum-based processes [73].

3.3.3 The 3-stage process

An important improvement was made to the Boeing process in the 1990s, notably by Gabor *et al.*. They moved towards the so-called "3-stage process", which is today the base fabrication process for the best performing, "notch-profiled" devices (see section 3.2.2). An example of the 3-stage process, reported by [49] is shown in Figure 18 and detailed next:

(a) Interaction of In, Ga and Se at a substrate temperature $T_s = 260°C$ to form $(In,Ga)_2Se_3$.

(b) Addition of Cu, still in presence of Se, at $T_s = 560°C$ to form slightly Cu-rich CIGS.

(c) Introduction of In and Ga once again, still at $T_s = 560°C$ and in presence of Se, in order to re-establish an overall Cu-poor composition. Between the previous step and this one, a dwell at temperature in Se vapour only is performed, in order to recrystallize the film under a Cu-rich composition (bigger grains).

Se is provided with a constant flux throughout the process, as well as during the cooling down stage until the substrate temperature reaches Ts $=350°C$, when both controlled cooling and Se flux are switched off. In comparison to the Boeing process, the growth is here first performed under Cu-poor composition, up until

some point near the end of step (b), then Cu-rich from (b) to (c), and finally Cu-poor again. Even though best devices are still obtained with films of relatively large grain size (>1µm), Shafarman *et al.* [74] found that the presence of Na, which was absent in the Boeing process, reduced the need for big grains.
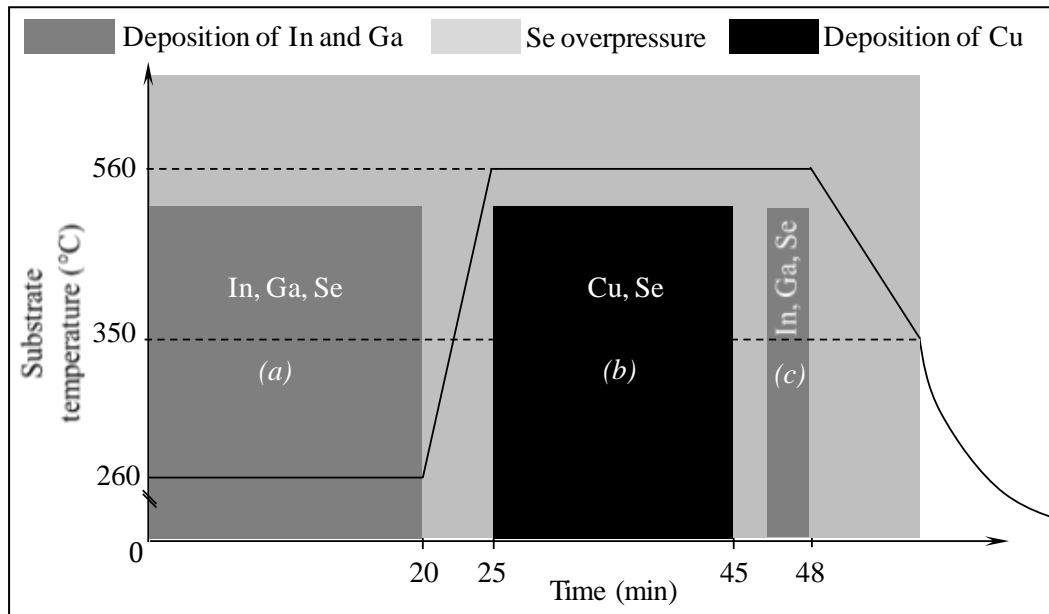
Figure 18: Schematic representation of a 3-stage process used by NREL. Adapted from [49].

The authors compared the performance of a film deposited with one single deposition step of slightly Cu-poor composition all the way through, with the performance of a film obtained from the bilayer process. The measurements showed that, even though the grain size of the Cu-poor film was smaller in the Cu-poor sample, the performances were almost identical. This is due to the passivation of the grain boundaries by the Na from the SLG, reported in section 3.2.1. With the activity of the grain boundaries drastically reduced, the advantage of a big-grained film (i.e. grown Cu-rich) over a smaller-grained one (Cu-poor) becomes much less important.

Comparison between 3-stage and 2-stage process

47

On the laboratory scale, devices prepared via a 3-stage co-evaporation process usually yield higher efficiencies than those prepared by 2-stage process, but both fabrication routes show very similar performance on the module scale. Indeed, one important challenge for scaling up co-evaporation is to tackle the relative instability of the evaporation rates from each crucible, which can affect the overall composition. Even though chalcopyrites have a surprisingly large tolerance to variations in composition (see section 3.2.3), they are thin films and a good control is needed to ensure stable performances. The live in-situ monitoring of these evaporation rates becomes critical to ensure process stability and reproducibility [75]. The 2-stage process, on the other hand, lends itself more readily to large-scale fabrication. Techniques like sputtering or electrodeposition can be performed over large areas and stacked elemental layers can be deposited by an in-line process, such as the one described in Figure 17.

Manufacturing companies using a 3-stage process

In spite of the difficulties to scale up, some companies have moved to large-area manufacturing of CIGS by co-evaporation. ZSW's industrial partner Würth Solar for example uses downward co-evaporation from line sources, disposed in such a way to provide a composition gradient (Figure 19). The substrates are heated to ≈600°C during deposition [76] and the deposition rates are controlled by atomic absorption spectrometry (AAS). Solibro produced an attested 17.4% efficient 16 cm^2 CIGS submodule [77] using a similar setup. Other companies use the more conventional upward evaporation. In the latter deposition setup, the glass substrate temperature has to be limited to 510°C to avoid substrate bending due to gravity [78]. Global Solar deposits on barrier-coated stainless steel flexible substrates. Miasolé uses co-sputtering on heated flexible substrates [79] which is affiliated with the 3-stage

process, and the company has achieved a record certified 15.7% efficiency with a 1 m^2 module [80].
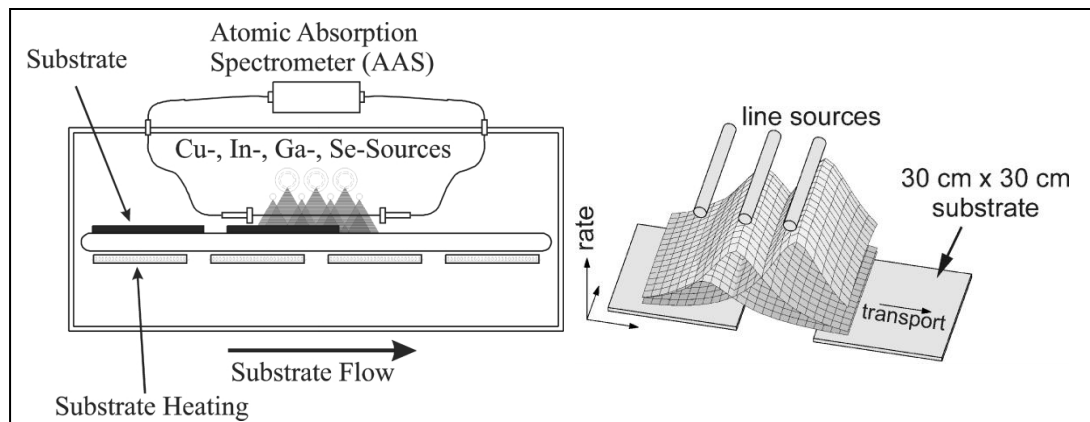
Figure 19: Large-area CIGS co-evaporation system used by Würth Solar. *Left:* **deposition setup with live monitoring of the evaporation rates;** *right:* **Deposition rate profiles of the elements Ga, In and Cu, respectively, in the evaporation chamber.** *Source: [76].*

3.3.4   CuIn$_{1-x}$Ga$_x$(S$_{1-y}$Se$_y$)$_2$

Alloys based on CIGS by partial substitution of Se by S, to form CuIn$_{1-x}$Ga$_x$(Se$_{1-y}$S$_y$)$_2$, have also been studied. They are currently used by manufacturing companies [81] to passivate the front of the film. Indeed, the band gap of CuGaS$_2$ is ≈2.4 eV, against 1.7 eV for CuGaSe$_2$, and that of CuInS$_2$ 1.5 eV against 1.0eV for CuInSe$_2$. The presence of S at the front therefore causes an increase of the band gap of Cu(In,Ga)(S,Se)$_2$ at the front, by both lowering of the valence band and raising the conduction band [46]. This type of alloying allows reproducing something similar to the "notch profile" (see section 3.2.2) in a 2-stage manufacturing process, where the precursor is a stacked elemental layer of Cu and Ga together followed by In, selenized and then sulphurized. The Ga at the back and sulphur at the front help to reduce back surface and front surface recombinations, respectively. The sulphurization step is also believed to passivate the surface of the absorber [82].

49

3.3.5 Summary

Some of the manufactured layouts mentioned in the sections above are summarized in Figure 20. This chart is an adaptation of [81]. In Table 1 are listed the best CIGS efficiencies obtained with different fabrication routes on lab scale and module scale.

Fabrication process	In-line co-evaporation		Selenisation and/or sulphurization			In-line co-sputtering
n-type window	ZnO:Al	ZnO:Al	ZnO:Al	ZnO:B	ZnO:Al	ZnO:Al
Buffer (50-100nm)	CdS	CdS	CdS	$Zn(S,OH)_x$	CdS	ZnS
p-type absorber (2-3 μm)	$CIGSe_2$	$CIGSe_2$	$CIG(SSe)_2$	$CIG(SSe)_2$ / $CIGSe_2$	CIS_2	$CIGSe_2$
Metallic back contact (0.5-1 μm)	Mo	Mo / barrier	Mo / barrier	Mo / barrier	Mo	barrier / Ag / barrier / Cu
Substrate	SLG	Stainless steel foil	SLG	SLG	SLG	Stainless steel foil
	Würth Solar	Global Solar	AVANCIS	Showa Shell Sekiyu	Sulfurcell	Miasolé

Figure 20: Different module layouts used by some major CIGS manufacturing companies, grouped by fabrication process. *Adapted from [81].*

The best cell efficiencies for some of the fabrication routes are believed to have been obtained by companies, since some of them achieved high efficiencies on the module scale. However, these companies generally publish only the results obtained from large-area devices, so that cell-scale efficiencies are missing for some technologies.

Table 1: Review of the best efficiencies achieved by CIGS cells and modules fabricated via different routes.

Absorber fabrication technique	Highest reported cell efficiency			Highest reported module/ submodule efficiency		
	Effi-ciency	Device area	Lab/Co.	Efficiency	Area	Lab/Co.
3-stage co evaporation	20.3% [4]	0.5 cm^2	ZSW	17.4%[83] 14.7%[84]	16 cm^2 6840 cm^2	Solibro
3-stage co-sputtering				17.3%*[3] 15.7%[80]	N/S 1m^2	Miasolé
2-stage sputtering				17.8%*[a] [2]	900 cm^2	Solar Frontier
2-stage printing	17.1%* [85]	N/S	Nano-solar	11.6% [86]	N/S	Nano-solar
2-stage electroplating	14.7% [87]	11.8 cm^2	Solo-power	11.2% [87]	3709 cm^2	Solo-power
2-stage hydrazine	15.2% [88]	0.45 cm^2	IBM	N/A	N/A	N/A
* Not independently certified [a] CIGSSe						

3.4   Component layers of high performance CIS-based solar cells

The layers of the complete solar cell structure typically used in high-performance CIS-based devices are summarized in Table 2.

Table 2: Typical cell structure of CIS-based devices and the techniques commonly used for their deposition.

Layer (typical thickness)	Common deposition technique
MgF_2 AR coating	Evaporation
Ni/Al front contact grid	Evaporation
i-ZnO/ZnO:Al window (100-200nm)	Sputtering
CdS buffer (50-100nm)	Chemical bath deposition
CIS-based absorber (2-3 μm)	Evaporation, sputtering
Mo back contact (0.5-1 μm)	Sputtering
SLG Substrate	

3.4.1 Mo back contact

Molybdenum is currently the most widely used back contact metal. It is used in high efficiency devices such as those described in [4, 30]. The thickness commonly deposited ranges from 500 nm to 1.5 μm. Several reasons explain why Mo is chosen over other metals:

(a) First of all, it does not diffuse into the absorber up to 650^0C, and is stable at the processing temperatures generally used (i.e. lower than 550^0C) [89]. Indeed, Mo recrystallises at temperatures greater than 900°C. Only marginal changes in structural and electrical properties are therefore expected at the annealing temperatures used for CIS-based materials, typically below 600°C [90, 91].

(b) Another positive aspect of Mo is that Na can easily diffuse through it from the soda lime glass (SLG) to the absorber [51, 92], which is required for good device performance (see section 3.2.1). Schmid *et al.* [92] for example observed by XPS the presence of Na at the surface of Mo on SLG after 1 hour air anneal at 200^0C only.

(c) Mo forms, during annealing and in presence of Se, the compound $MoSe_2$ at its surface, which is a semiconductor of band gap 1.3 eV [51]. It results in the formation

of a back surface field, which prevents local electrons from recombining, in the same way an increased amount of Ga at the back does in CIGS (see section 3.2.2).

(d) The CIS/MoSe$_2$/Mo contact was also found to be ohmic [93-95], whereas CIS/Mo is Schottky. Therefore losses are reduced at the back interface.

(e) A good adhesion between MoSe$_2$ and CI(G)S, compared to other back contact metals, was also reported [44].

3.4.2 Absorber layer

The absorber layer is the most critical part of the device, since this is where the photovoltaic conversion is realised. This layer is generally between 2 μm and 3 μm thick. The properties of the CIS and CIGS absorbers (section 3.2) and their fabrication routes (section 3.3) have been described earlier on. All the other component layers of the solar cell must be chosen to be compatible with the absorber.

3.4.3 CdS buffer layer

A relatively thin (typically ≈50 nm), n-type CdS buffer layer, is commonly used for creating or improving the p-n junction with the absorber. The best performing CdS buffers are deposited by chemical bath deposition (CBD) [4, 30]. The technical details of the CBD process are exposed in section 4.1.5. CBD of CdS also has other positive properties besides the junction formation [51]:

(a) CdS smoothens the surface of the absorber, which is usually rough.

(b) CdS acts as a "buffer", protecting the surface of the absorber from plasma damage caused by the sputtering of the next layer, the window layer (e.g. ZnO). The

i-ZnO layer deposited on top of the CdS is also expected to reinforce this protective effect (see next section).

(c) The CBD process itself was shown to remove the native oxides (e.g. In_2O_3) from the film surface. This restores positively charged surface states which, as mentioned in section 3.2.1, increase the type inversion near the CIS/CdS interface, because of the Cu migration that accompanies the positively charged surface.

(d) Cd ions are also thought to remove remaining Se atoms from the surface.

(e) Cd ions diffuse to some degree into the absorber, and possibly form Cd_{Cu} which are donor defects. This would result in a further enhancement of the type inversion at the interface [43].

(f) The chemical bath itself could also be responsible for a passivation of defects present at the absorber surface, thus reducing the surface recombination velocity.

(g) Finally, CdS displays a favourable lattice match with CIS [50].

All the above points explain why CdS is by far the most used buffer layer and yields the best efficiencies. However, it also suffers some important drawbacks, namely:

(a) Its toxicity. Cd is a heavy metal, in the same way as arsenic for example, and therefore, for environmental considerations, alternative, less hazardous buffer layers such as ZnS or In_2S_3 have been sought. Companies like First Solar, who deposits CdS on CdTe, developed effective waste recycling and treatment procedures to meet international regulations on toxic waste.

(b) The use of chemical bath deposition as a deposition process hampers throughput in in-line deposition processes because it is not vacuum compatible. As a

consequence, the vacuum has to be broken for the CdS deposition stage and re-established for the depositions of ZnO and contacts.

(c) CdS, with a band gap of 2.42 eV, absorbs the short wavelength part of the spectrum that could be used by the absorber (below ≈500 nm). This limits the photocurrent by ≈2% [7].

3.4.4 i-ZnO/ZnO:Al window layer

The front electrodes of the most efficient devices are realised with a transparent conductive oxide (TCO), usually an Al-doped ZnO layer (noted ZnO:Al, or AZO), such as in [4] for example, or indium tin oxide (ITO) [30]. This layer must allow a more efficient collection of the photogenerated carriers than the bare p-n junction could provide, and therefore needs to have relatively high, n-type conductivity. However, it also stands between the sun and the absorber, and therefore needs to be transparent to the wavelengths useful for the absorber. ZnO:Al offers a good compromise between electrical conductivity and optical transparency.

Prior to ZnO:Al deposition, a thin undoped ZnO (i-ZnO) layer is deposited on top of the buffer layer. The importance of this layer is especially high when the ZnO:Al layer is deposited by DC magnetron sputtering. Indeed, this type of sputtering is faster than RF, which is desirable for industrial scale production, but also causes more surface damage. The inclusion of a thin (typically 50 nm) i-ZnO layer by RF sputtering helps to protect the CdS against such damage [96]. However, i-ZnO is also highly resistive, and the right thickness has to be found to provide surface protection without much increase in the resistive losses.

ITO, a mixture of SnO_2 (≈90 wt%) and In_2O_3 (10 wt%), has also been shown to yield high efficiencies. Its use pre-dates that of ZnO:Al, the latter being developed to

reduce the need for In, which is an expensive element, and to get a better lattice match with the underlying i-ZnO, in industrial production. The ZnO:Al band gap is ≈ 3.3eV [97], against typically >3.8 for ITO [98]. However, deposition conditions can help to increase its band gap towards more suitable values. ZnO on its own is highly resistive, and a small amount of Al (≈ 2 wt%) must therefore be alloyed, uniformly, to obtain acceptable conductivity and preserve a good transparency.

3.4.5 Front contact grid

The carriers are collected for electrical transportation by a highly conductive metallic grid. The geometry and size of the grid fingers must be tuned to obtain both a good conductivity and a minimum coverage ("shadowing") of the active area of the device [50]. The shape of the grid is defined by the application of a mask onto the TCO during the deposition. Electron-beam (e-beam) evaporation is usually used for depositing the front contact grid, since it allows fast deposition of good-quality, thick metallic layers. The contact usually consists of a thin Ni layer (50 nm) followed by a thick 2-6 μm Al layer. The Ni helps to prevent oxidation of the Al from the TCO.

3.4.6 Anti-reflection coating

The final layer used is an anti-reflection (AR) coating. This layer is made of a dielectric material, and its thickness and refraction index must be chosen based on the refractive index of the underlying layer and the light spectrum, to minimize reflections at its surface.

3.5 $CuIn_{1-x}Al_xSe_2$ absorber layer

3.5.1 Properties of $CuIn_{1-x}Al_xSe_2$

CIAS, finally, is the focus of this work. It has been investigated by several laboratories [99-104]. It is, like CIS, a I-III-VI$_2$ semiconductor, and like CIGS a

quaternary chalcogenide crystallizing in the chalcopyrite structure. This material has several potential advantages over CIGS.

The first one is a larger accessible range of band gaps obtainable by varying $x = \frac{Al}{Al+In}$ (Figure 21), which makes CIAS potentially suitable for monolithically integrated multi-junction solar cells. Quite generally, the evolution of E_g vs x for any alloy of two semiconductors A and B present in the ratio $x = \frac{A}{A+B}$ obeys a relationship derived from Vegard's law:

$$E_g(A, B, x) = E_g(A) + xE_g(B) - bx(1 - x) \tag{3.4}$$

where, $E_g(A)$ is the band gap of semiconductor A, $E_g(B)$ is the band gap of semiconductor B, $E_g(A, B, x)$ is the band gap of the alloy semiconductor, and b is the bowing parameter, characterising the deviation from a linear relationship. The relationships E_g vs x for CuIn$_{1-x}$Al$_x$Se$_2$ (equation 3.5) and for CuIn$_{1-x}$Ga$_x$Se$_2$ (equation 3.6), as reported in [99] and [105] respectively, are plotted in Figure 21:

$$E_g(x)[eV] = 1.04 + 1.01x + 0.62x^2 \tag{3.5}$$

$$E_g(x)[eV] = 1.04 + 0.56x + 0.11x^2 \tag{3.6}$$

Therefore, one can see that the range of band gaps accessible is 1.0 eV to 2.7 eV for CIAS and 1.0 eV to 1.7 eV for CIGS. The transmittance of CIAS below the energy gap is >85% [99], which is a necessary condition for a material to qualify as top junction in a tandem junction cell. A second consequence of the relationships 3.5 and 3.6 is the fact that, to reach a given band gap, less lattice strain is induced by the introduction of Al than by that of Ga (Figure 22).
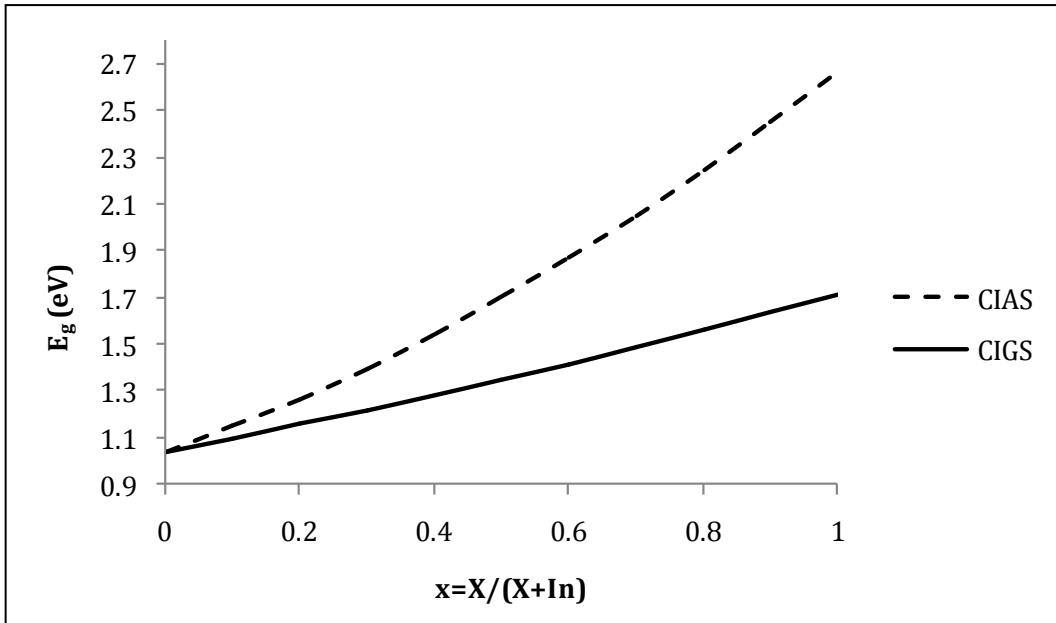
Figure 21: E_g vs $x=X/(X+In)$**, where** $X{\equiv}Al$ **or** $X{\equiv}Ga$**. Plotted from the equation found in ref [105] for CIGS and ref [99] for CIAS.**
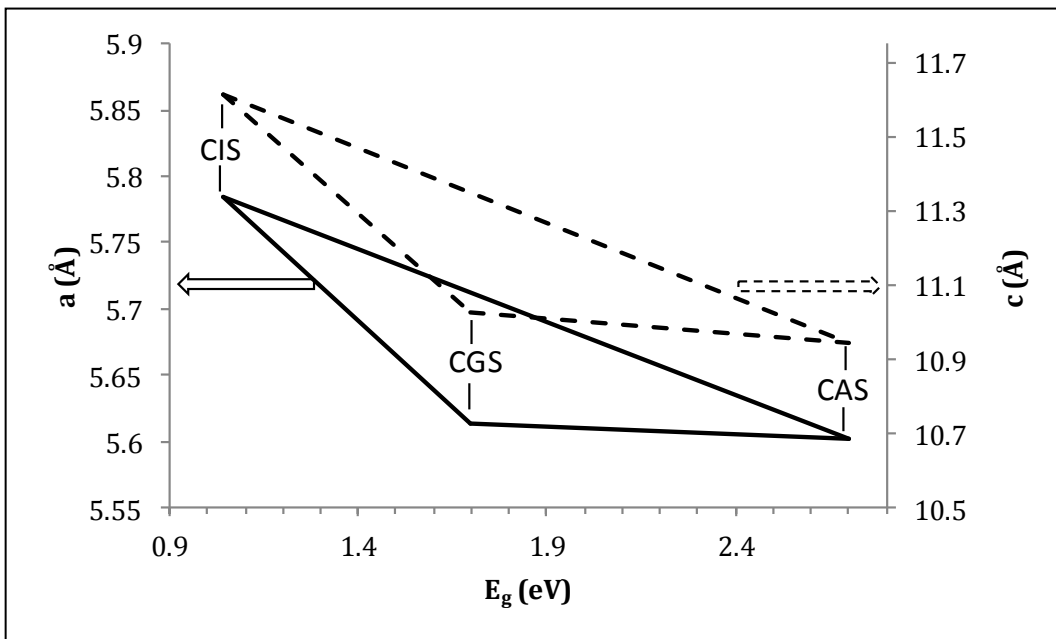
Figure 22: Variation of the lattice parameters a **and** c **with band gap. Extrapolated from** E_g **vs** x **for** $b=0$**, and Vegard's law.**

Since the chalcopyrite structure is tetragonal, only two lattice parameters are relevant. The reduced change in lattice parameters in CIAS compared to CIGS should result in fewer defects associated with dislocation or lattice mismatch. As mentioned in section 3.2.3, the performance of CIGS tends to degrade beyond a band

58

gap E_g>1.2 eV because of the presence of deep energy levels in the mid-band gap region, acting as recombination centres [6, 51]. These deep recombination centres are a characteristic of the specific band diagram of CIGS and CIAS should avoid them. Thanks to this potentially better behaviour at band gaps >1.2 eV, band gaps closer to the theoretical optimum can be explored. This theoretical optimum was calculated to be around 1.35 eV for a single junction device, with a 33% efficiency limit (see [7] and Figure 23). A higher band gap would also means a higher V_{oc} and a lower J_{sc}, and therefore less power losses due to the cable resistivity ($\propto R \times I^2$) in interconnected modules [99].
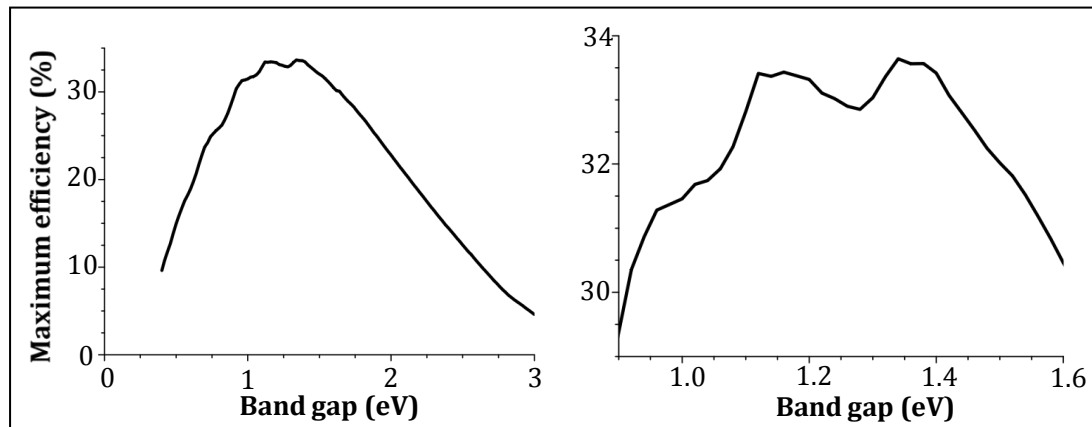
Figure 23: Shockley-Queisser limit calculated from the measured solar spectrum. *Left:* **large range of band gaps.** *Right:* **zoom on the highest efficiency range.**

3.5.2 2-stage processed CuIn$_{1-x}$Al$_x$Se$_2$

The preparation route investigated in this thesis is the 2-stage process. As mentioned earlier (section 3.3.2), this process is more suited for upscaling than co-evaporation, but tends to cause Ga migration in CIGS. CIAS is not spared this problem.

Zoppi *et al.* [16] reported a similar migration of the Al towards the back, and Olejnícek *et al.* [106] observed that Al did not incorporate into the CIS phase under certain conditions. Dwyer *et al.* [107] found some Al in the phase Al$_2$O$_3$ near the interface with the Mo. Umezawa *et al.* [108] also obtained a graded Al composition

in $CuIn_{1-x}Al_xSe_2$ grown using a carrier gas [$(C_2H_3)_2$, Se] to provide the Se. This phase segregation between In and Al is supported by the reported reaction path for CIAS formation. According to Jost *et al.* [100] who used live, in-situ XRD to study the different crystalline phases forming at different stages of a RTP selenisation process, CIAS forms at ≈490°C, shortly after $(In,Al)_2Se_3$ $(T_f≈430^0C)$:

$$\frac{1}{2}Cu_2Se + \frac{1}{2}(In, \text{Al})_2Se_3 \rightarrow Cu(In, Al)Se_2 \qquad (3.7)$$
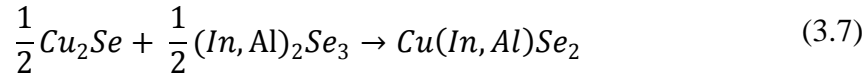
The formation of CIS, on the other hand, starts in RTP with the reaction path reported in [109] by Hegert *et al.*:

$$CuSe + InSe \rightarrow CuInSe_2 \qquad (3.8)$$

Reaction path 3.8 starts at the melting temperature of Se, 221^0C, which means that CIS starts forming well before the CIAS. If the ramping is not fast enough, all the indium will be consumed before the temperature of formation of CIAS is reached. CIAS can therefore only form by interdiffusion between CIAS (or CAS) and CIS. This is somehow similar to the CIGS formation path, which proceeds via Ga_2Se_3 and In_2Se_3, instead of $(In, Al)_2Se_3$ in equation 3.7, and starts forming at ≈425°C [110].

The works of Dwyer *et al.* and Olejnícek *et al.* showed dissimilar results regarding the optimal growth conditions to form single phase, uniformly distributed CIAS. Olejnícek *et al.* observed incorporation of the Al into the CIAS lattice only for $x = \frac{Al}{(Al+In)}$ higher than 0.64 and for a 550°C annealing temperature. Dwyer *et al.*, on the other hand, found that the best temperature for their process was 500°C, and the incorporation better at very low Al content ($x = 0.09$). The cause of the discrepancy between these results is not clear from the published data. The

fabrication processes used by the two groups were fairly similar, with sputtered precursors (co-sputtering for Dwyer *et al.*, sputtering from an alloy CuInAl target for Olejníček *et al.*) followed by rapid thermal selenisation in presence of elemental Se. The metallic precursor layouts were different, with a single matrix of the mixed elements in the case of Olejníček *et al.*, and a CuIn/CuInAl/Cu stacked precursor for Dwyer *et al.* However, there is no obvious reason why the different precursor layouts would cause the differences observed.

Both papers however agree on the presence of Al_2O_3 in the samples. This oxide forms extremely quickly and its high resistivity was proposed by Dwyer *et al.* to be the cause of the poor device performance the authors obtained in most of their CIAS-based devices. Another group [111] noted on the other hand a higher conductivity in some of their samples, and associated this result with possible remaining metallic phases. To date, the only 2-stage processed CIAS device efficiency reported in the literature was 5.2%, with V_{OC}=465 mV and J_{SC}=33mA.cm^{-2} [107]. These parameters suggest a fill factor of 34%, which the authors attribute to the high resistivity of the Al-Al_2O_3 phase present at the interface with the back contact. The other devices prepared by this group were not active. Similar results were obtained internally in NPAC in the past.

3.5.3 Summary

To summarize, the determining parameters for the growth of CIAS via the 2-stage process are not yet fully elucidated, and unlike the 3-stage co-evaporation process, no high efficiency devices have been obtained by this route. The films also show a migration of the Al similar to that of Ga in CIGS.

CHAPTER 4   EXPERIMENTAL METHOD AND SETUP

In the first part of this chapter the processes for fabricating each component layer of a solar cell are described. In the second part, the techniques used to determine the chemical and physical properties of the layers synthesised are discussed.

4.1   Fabrication

The substrate configuration (as opposed to superstrate configuration) was used throughout this work. In this configuration, a substrate is first coated with the back contact, followed by the absorber layer. The p-n junction is then formed by depositing a buffer layer on top of the absorber, and the device is terminated by a transparent conductive oxide (TCO) layer and a metallic grid as a front contact. The light is shone through the TCO layer before entering the other layers. The cell structure used in this work, along with the typical thickness of each of its constitutive layers and the fabrication technique used, are summarised in Table 3.

Table 3: Structuring layers of the cells fabricated in this work.

Layer (typical thickness)	Fabrication technique
Ni (50 nm)	e-beam evaporation
Al (4 μm)	e-beam evaporation
Ni (50 nm)	e-beam evaporation
InO:Sn (ITO) TCO (180nm)	Sputtering
i-ZnO (55 nm)	Sputtering
CdS buffer (60 nm)	Chemical bath deposition
CIS-based absorber (2-3μm)	Sputtering/selenisation
Mo back contact (850 nm)	Sputtering
Soda lime glass ($\approx$1 mm)	

4.1.1   Soda Lime Glass substrate cleaning

Commercial microscope slides of soda lime glass (SLG), of dimensions 26 mm by 76 mm and about 1 mm thick, were used as a substrate for all the layers and structures grown in this work. The cleaning of the SLG was essential since the

surface of an unclean glass substrate can contain particles and debris of sizes orders of magnitude bigger than the film thickness, and therefore greatly affect the performance of the final devices built upon it. In particular, these particles can result in the formation of pinholes through to the back contact. Although their effect on the structure of full cells was not studied in detail, it was observed that many cells contained pinholes and exhibited poor performances when grown on back contacts displaying many pinholes themselves, whereas all cells grown on Mo containing less pinholes were generally active and had similar characteristics. Two water purification systems were used for the cleaning:

- An ELGA PURELAB option-S15, which produced a water resistivity[8] of $\rho > 1$ MΩ.cm and contained a total organic carbon (TOC) level <30ppb.

- An ELGA PURELAB Ultra, which produced water resistivity of $\rho=18.2$ MΩ.cm with a TOC level < 15ppb.

The PURELAB Ultra water was used in the final stage of the cleaning because its purity ensures that a minimum amount of contaminants is left on the slides after the drying stage.

The standardized cleaning procedure used for the SLG substrate was the following:

- Mechanical cleaning of the surface with a nylon toothbrush dipped in a diluted detergent solution of Decon 90, to remove any grease and particles from the surface.

- Rinsing with deionised PURELAB S15 water (lower purity).

- Rinsing with deionised PURELAB Ultra water (higher purity).

- Drying by blowing pressurised N_2.

---

[8]The resistivity of water is used to assess its purity. Most of the impurities in water are present as ions that decrease its resistivity. Therefore purer water shows higher resistivity.

To prevent further dust contamination from the air, the slides were loaded into the deposition system within minutes after cleaning.

4.1.2 Molybdenum back contact deposition

Molybdenum (Mo) was used as back contact and deposited by sputtering. Some substrates were not coated with Mo in order to be able to perform absorbance measurement or test the effect of the substrate on the crystalline structure of the absorber. Sputtering is a physical vapour deposition (PVD) technique consisting in bombarding, with ions, plates ("targets") which are made of the element(s) to deposit. The ions that possess enough energy will eject ("sputter") the constituting atoms of the targets, which will then deposit onto the samples. The sputtering system used for this work was a Nordiko 2000, which was designed for radio frequency (RF) magnetron down-sputtering. Its principle of operation is shown in Figure 24. The targets used in this system were all 6'' in diameter. The steps taken for sputtering deposition in this machine are the following:

- The samples, up to 20 (4 platens of 5 samples each), were first loaded and the deposition chamber was evacuated to a base pressure of typically 1×10^{-6} mbar prior to deposition.

- Argon was then circulated in the chamber throughout the deposition to feed a plasma. The typical pressure during the deposition was $\approx 2.5 \times 10^{-3}$ mbar.

- A voltage was applied between the targets and the substrate table that caused the Argon atoms to be ionised. The ions, positively charged, were then attracted towards the targets and, when a target was hit with sufficient momentum, atoms were sputtered away from the targets and deposited onto the back plate below.

A rotation of the substrate table was essential to obtain higher uniformity, especially along the width of the slides (Figure 25). Indeed, the magnetic field located between the inner and the outer part of the magnetron, causes the Ar^+ particles to sputter preferentially the zone of the target directly underneath the magnetic field. As a result, in static deposition a target placed directly on top of a platen would deposit over an area that is the projection of this ring-shaped sputtered zone onto the platen. When the substrate table is rotated, the non uniformity along the direction of rotation is reduced, while that perpendicular to this remains.
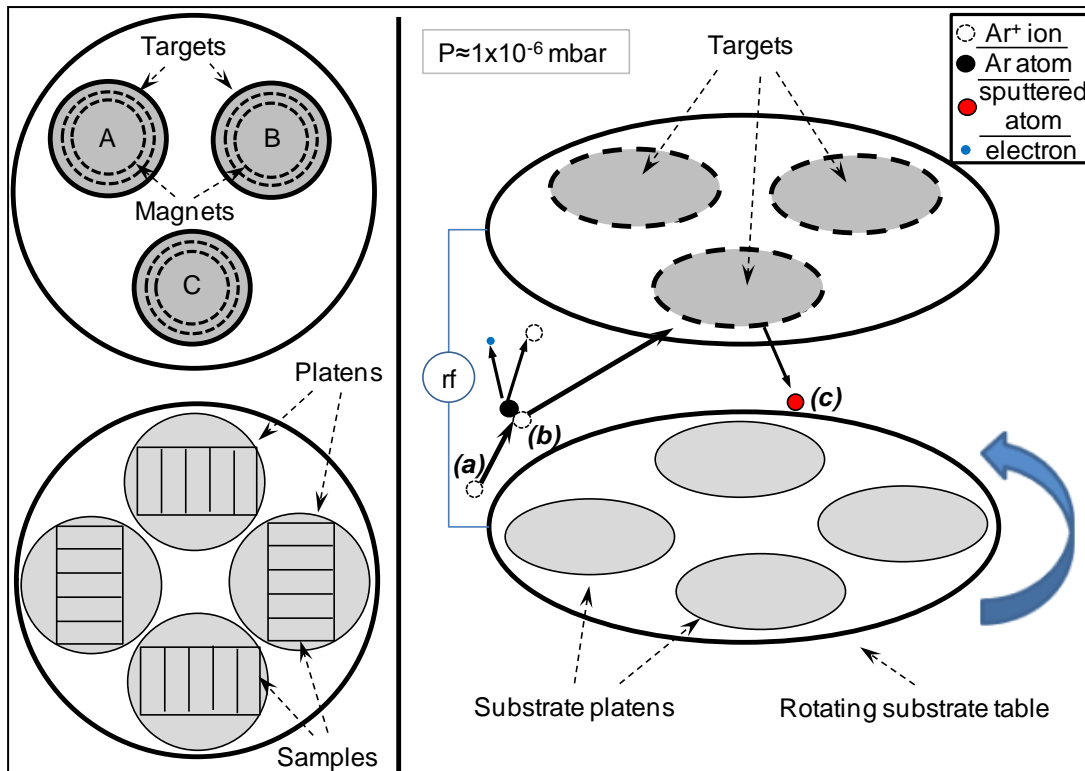
Figure 24: Explanatory diagram of the sputtering operation in a Nordiko 2000. (a) Ionised atoms of Argon are drawn towards the negatively charged targets; (b) When accelerated ions or generated electrons meet neutral Ar atoms, they ionise them; (c) When Ar$^+$ ions hit the target, they sputter its constituent atoms, which in turn deposit on the table underneath. A permanent ring-shaped magnet was present behind each target to curve the path of the ions and enhance the ionisation of residual gas atoms.

The Mo back contact used was typically 850 nm thick, corresponding to a 2 hours deposition at 300 W. The table rotation speed was set on 2 rotations per minute, the flow of Argon during the depositions at 30 sccm.
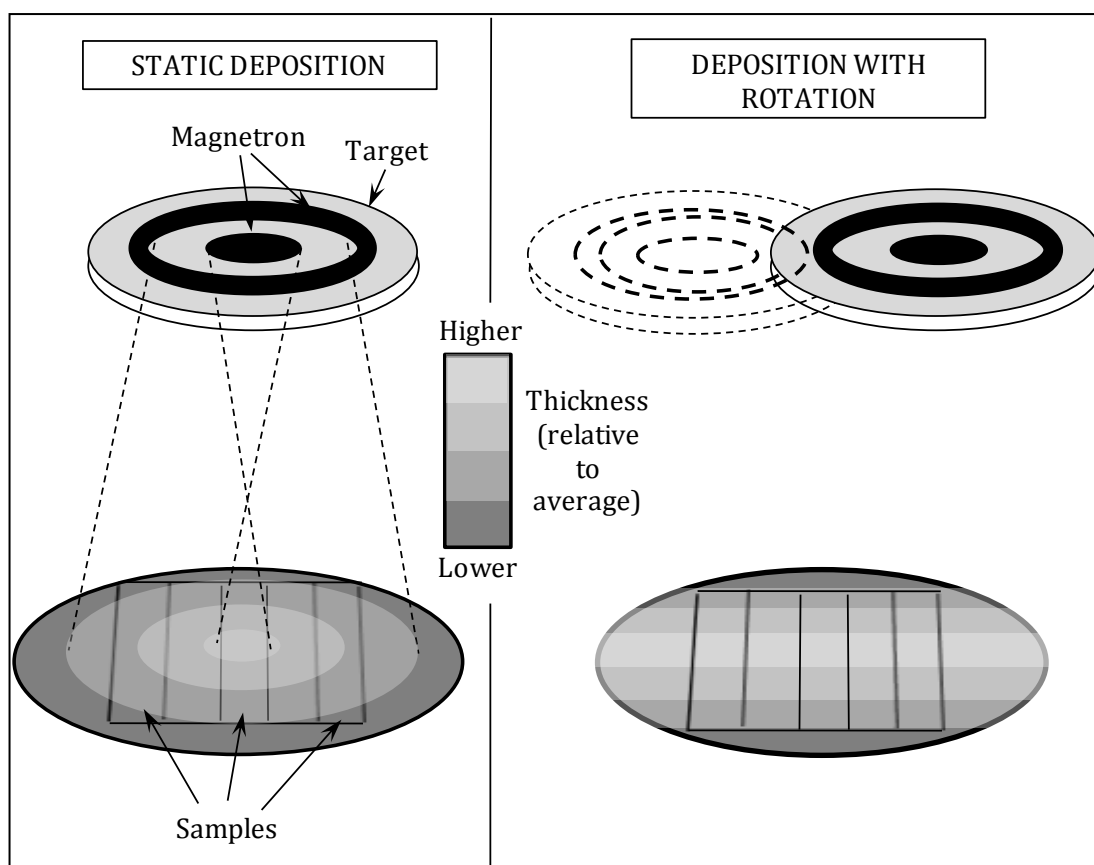
Figure 25: explanatory diagram of the thickness uniformity deposited in static and in rotation. The target is preferentially sputtered in the zone above which is the magnet. In static deposition (*left*), that results in a concentric thickness gradient pattern. In rotation (*right*) the non uniformity is greatly reduced in the direction of the rotation.

4.1.3 Metallic precursor deposition

CIS, CIAS and CAS were grown by a variant of the 2-stage process:

- Depositing precursor layers of the metallic elements using r.f. sputtering.

- Depositing a selenium capping layer on top of the metallic precursor layers.

- Annealing in a selenium environment to react the metallic layers with the selenium to form the selenide compound or alloy.

4.1.3.1 Precursors for CuInSe$_2$

The Cu-In precursor layers were formed by either:

- Sputtering the Cu-In alloy directly from a target of atomic composition 48 at% copper and 52 at% indium (to get slightly Cu-poor absorbers).

- Or, sputtering alternate layers of Cu and In using 2 elemental targets of Cu and In.

The power applied to the alloy target was 100 W, while that applied to the elemental targets was in the range 70 W-80 W for the Cu target and 170 W-180 W for the In target. The deposition time was tuned to obtain the desired thickness. During the deposition, the substrate table was rotated at a speed of 2 to 5 rotations per minute (rpm). When two elemental targets were used, the deposition was a sequence of short alternative depositions of Cu and In. At a rotation speed of 5 rpm, the amount of material deposited from each elemental target corresponded on average to an equivalent of five ≈1.0 nm-thick In layers and five ≈1.0 nm-thick Cu layer, per minute. The deposition rate for each element had to be calibrated to obtain the desired composition (APPENDIX 4).

4.1.3.2 Precursor for CuAlSe$_2$

For depositing the metallic precursor for CAS, either an alloy target of atomic composition 50 at% Cu and 50 at% Al, or elemental targets of Cu and Al, were used. The powers applied to the alloy target or elemental targets were 180 W for 90 min, or 120 to 150 W for sputtering the Cu and 300 W for 80 to 100 min for sputtering the Al. The substrate table was rotated at 5 rpm.

4.1.3.3 Precursors for CuIn$_{1-x}$Al$_x$Se$_2$

The metallic precursors for the preparation of CIAS films were deposited from 3 elemental targets of Cu, In and Al using a rotation speed of 5 rpm. To obtain the compositions required, the power applied to the targets of Cu, In and Al, were

determined by plotting calibration curves for the 3 targets. The details of these plots are reported in APPENDIX 4. For each required composition, a couple of long depositions on clean substrates were first performed with applied powers extracted from the calibration curves. This allowed both cleaning of the targets from possible oxides and to refinement of the values of power and time to get the composition and thickness required.

4.1.4 Selenisation

The conversion of metallic precursors into the chalcogenide absorbers (selenisation) was realised by first evaporating selenium (Se) on top of the metallic precursor and then annealing the sample.

4.1.4.1 Selenium evaporation

Se was evaporated on top of the metallic precursor in a Nano 38 evaporation system. The chamber was evacuated to a vacuum of typically 1×10^{-6} mbar and the Se was evaporated at a rate of 30 to 35 Å.s^{-1} to obtain a final thickness of 1 to 2 μm, depending on the amount of metallic precursor. No intentional heating was provided to the samples. A quartz crystal oscillator was used to record the thickness deposited *in situ*.

4.1.4.2 Annealing

Annealing processes were performed to convert the Se-coated metallic precursors into chalcopyrites, or to study the phase changes with temperature in the metallic precursors. Two different types of furnaces were used for annealing samples: an AS-One 100 rapid thermal processor (RTP), and a 3-zone large Bore Carbolite GHC 12/450 tube furnace (TF).

Rapid thermal processor

69

In the RTP (Figure 26), the heat was provided by 12X1200 W halogen lamps (144V each).
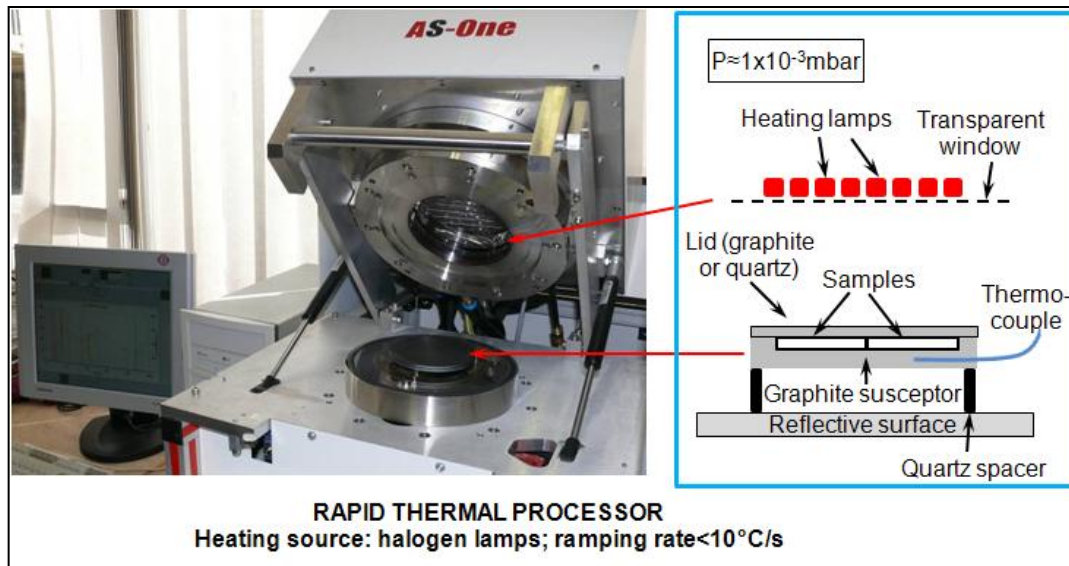
Figure 26: Picture and explanatory diagram of the Rapid Thermal Processor used for annealing and selenisation.

This heating process allowed fast temperature ramping, up to ≈9°C/s in average for reaching 550°C from room temperature. The cool down rate was also relatively fast (≈ 0.4°C/s) due to the small chamber size and the use of a water cooling system. The chamber of the RTP system was first mechanically pumped down to a base pressure of $1x10^{-3}$ mbar and then either Ar or H_2/N_2 (forming gas) was admitted into the chamber; the resulting pressure was in the range 100 mbar and 800 mbar. The substrates were placed on a graphite susceptor, 10 cm in diameter, which could hold up to 2 microscope slide substrates. However, it was found difficult to control the uniformity of heating over such large samples and therefore only single substrates of ½ or ¾ size were used in most cases, placed in the middle of the susceptor. The process temperature was monitored by a thermocouple inserted in a hole in the susceptor. The annealing process could be controlled either by the temperature

profile provided by the thermocouple or alternatively by the power profile applied to the lamps. In Figure 27 is shown an example of power controlled annealing profile.
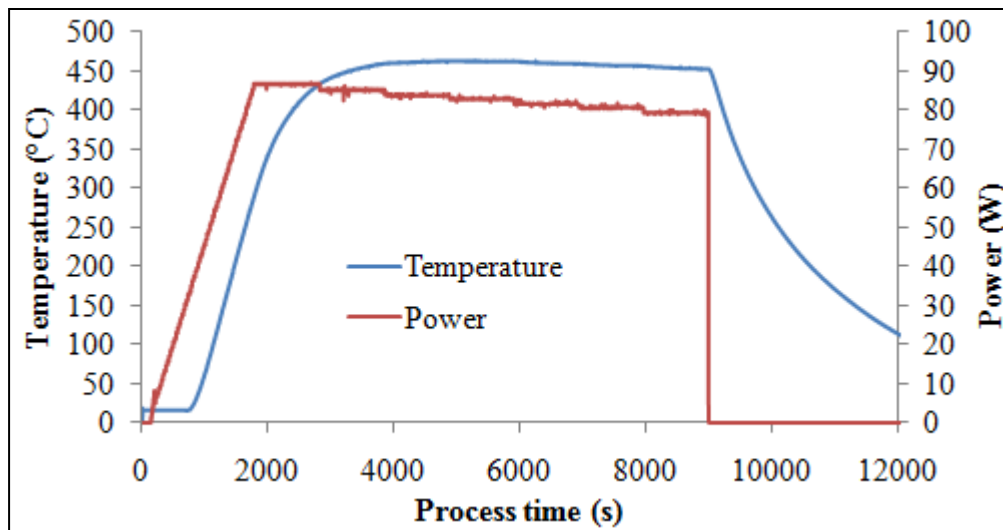
Figure 27: Example of a power-controlled annealing recipe in the rapid thermal processor. *red line*: **power applied to the heating lamps;** *blue line*: **temperature measured by the thermocouple.**

Tube furnace annealing

The TF (Figure 28) had a much bigger chamber compared to the RTP. The chamber was a 10 cm diameter quartz tube sealed on both ends. The heating was provided by cylindrical coils located around the chamber, which makes it slower than the RTP, both in terms of ramping rate (<18°C/min in average to 550°C) and cooling rate (<1°C/min in average from 550°C). The TF yields relatively good temperature uniformity with a maximum temperature variation of ±5°C across a 30 cm domain (Figure 29). The holders used were two graphite holders, each one capable of containing two samples side by side, so that four samples could be mounted in total. The base pressure was typically 1×10^{-3} mbar, and the working pressure either 6 mbar of Argon or 10 mbar of forming gas.
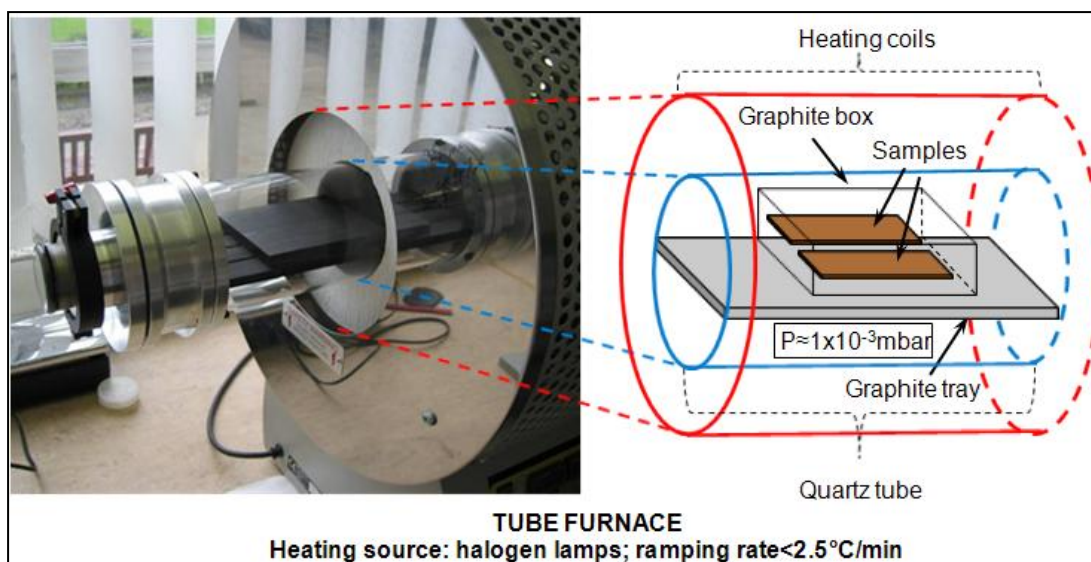
Figure 28: Photograph and explanatory diagram of the tube furnace used for annealing and selenisation.
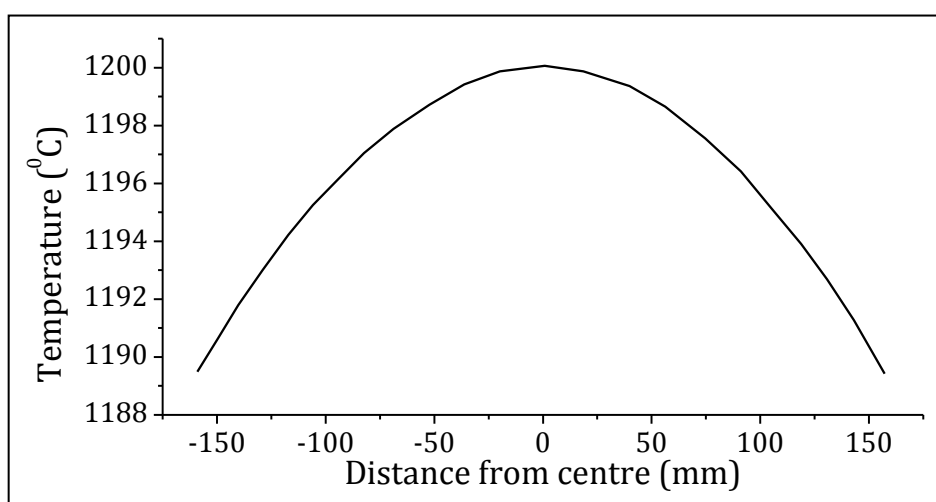
Figure 29: Uniformity profile in the tube furnace 12/450 as provided by the manufacturer. *Digitized from* **[112].**

Both systems went through two series of Ar or forming gas flush and pumping, before starting and before unloading the samples, to remove any residual atmospheric gases, and to clean the chamber from remaining gaseous Selenium, respectively.

72

4.1.5   KCN etching and CdS buffer layer

The absorber layers grown in the stages described earlier were generally of p-type conductivity. CdS, known as a good n-type buffer layer for CIS-based devices (for reasons described in section 3.4.3), was used to establish the junction. It was deposited using a chemical bath deposition.

Surface preparation by KCN etching

Prior to the CdS deposition, some samples needed etching of superficial phases with potassium cyanide (KCN, see section 3.2.5).

A 5 wt% KCN solution was prepared by weighing KCN powder and diluting it in the appropriate amount of water. Samples were immersed in the KCN and then rinsed abundantly with deionised water. The duration of the KCN etch was typically varied between 10 s and 45 s to follow the specific needs of each type of sample, assessed by measuring the photocurrent response.

CdS deposition

For the CdS deposition itself, a solution of cadmium sulphate ($CdSO_4$) and ammonia (NH_4OH) was heated up at 65°C by flowing hot water between the walls of the reaction vessel, and the samples immersed in it for 10 minutes with a gentle stirring, for the cadmium treatment (see section 3.2.5). Thiourea ($SC(NH_2)_2$) was then added to start the CdS deposition. N_2 was bubbled during the deposition to homogenize the solution and obtain a uniform thickness. A schematic of the setup is shown in Figure 30.
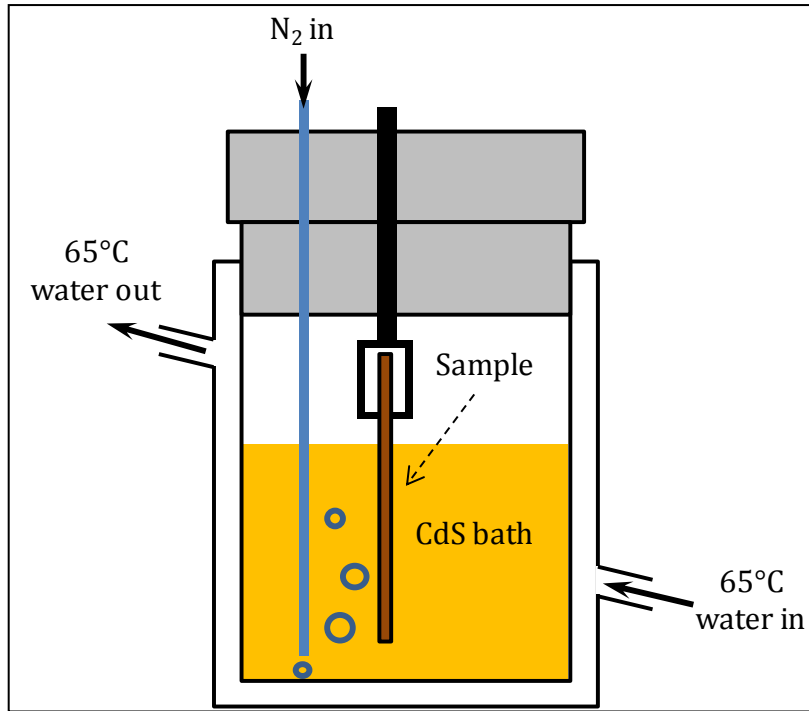
Figure 30: Diagram of principle of CdS chemical bath deposition setup. The solution is kept at a temperature of 65°C by flowing water between the walls of the vessel. The stirring of the solution is provided by bubbling N_2 at regular intervals.

The hydrolysis of $CdSO_4$ yields the ion Cd^{2+} which reacts with thiourea according to the following reactions:

$$Cd^{2+} + nNH_3 \leftrightarrow Cd(NH_3)_n^{2+} \tag{4.1}$$

$$(NH_2)_2SC \leftrightarrow H_2S + CN_2H_2 \; ; \; H_2S + 2OH^- \leftrightarrow S^{2-} + 2H_2O \tag{4.2}$$

$$Cd^{2+} + S^{2-} \rightarrow CdS \tag{4.3}$$
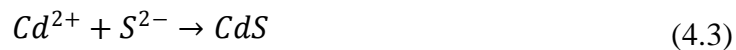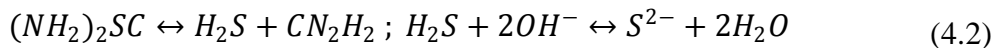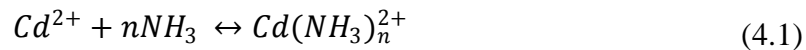
The molarities of the different elements in the bath before deposition were the following:

- CdSO$_4$: M=1.97x10^{-3} mol.L^{-1}

- SC(NH$_2$)$_2$: M=12.37x10^{-3} mol.L^{-1}

- NH$_3$: M=147.77x10^{-3} mol.L^{-1}

A 20 min deposition was used, corresponding to a thickness of ≈60 nm. After the deposition, the samples were rinsed abundantly and dried by blowing nitrogen.

4.1.6 i-ZnO /Indium tin oxide window layer

The electrons are generally collected at the front by a transparent conductive oxide (TCO), deposited on top of the CdS. The TCO used in this project was indium tin oxide (ITO). Additionally, a thin i-ZnO layer was deposited before the ITO. This thin insulating layer was reported to improve the electrical properties of the devices, for reasons mentioned in section 3.4.4). Both layers were sputtered in a Teer Coating UDP 350 system by pulse DC magnetron sputtering and RF magnetron sputtering for i-ZnO and ITO, respectively. The chamber was first pumped down to a base pressure $<1 \times 10^{-5}$ mbar. The i-ZnO layer was ≈ 55 nm thick. It was deposited with gas flows of 50 sccm of Ar and 2 sccm of O_2. The material was sputtered from an alloy ZnO target at a 1000 kHz pulse DC power of ≈ 110 W. No intentional heating was provided during the deposition of this layer. The ITO layer deposited was 180 nm thick. The composition of the target used was ≈ 90 wt% in In_2O_3 and ≈ 10 wt% in SnO_2 and the power applied 200 W. The deposition was performed at a substrate temperature of $\approx 160°C$, under a gas flow of 20 sccm of Argon ($P \approx 5 \times 10^{-3}$ mbar), for 90 minutes.

4.1.7 Ni/Al/Ni front contacts

The devices were then terminated by depositing a front metallic grid contact through a mask. This contact was deposited in a Tec Vac ECU 700 electron beam (e-beam) evaporation system. It comprised a bottom 50 nm thick Nickel layer, followed by a 4 μm thick Aluminium layer and another 50 nm thick Nickel layer at the top. The Al layer was the contact itself, whereas the two thin Ni layers were designed to prevent the oxidation of the Al layer by both the ITO and the air. A mask was clamped onto the sample prior to evaporating the front contact to create a grid. The specific pattern

chosen for the grid is commonly used in photovoltaic devices because of its relatively low shading and good electrical properties (used for example in the PV laboratory of Uppsala University [113]). A picture of a finalised sample is shown in Figure 31.
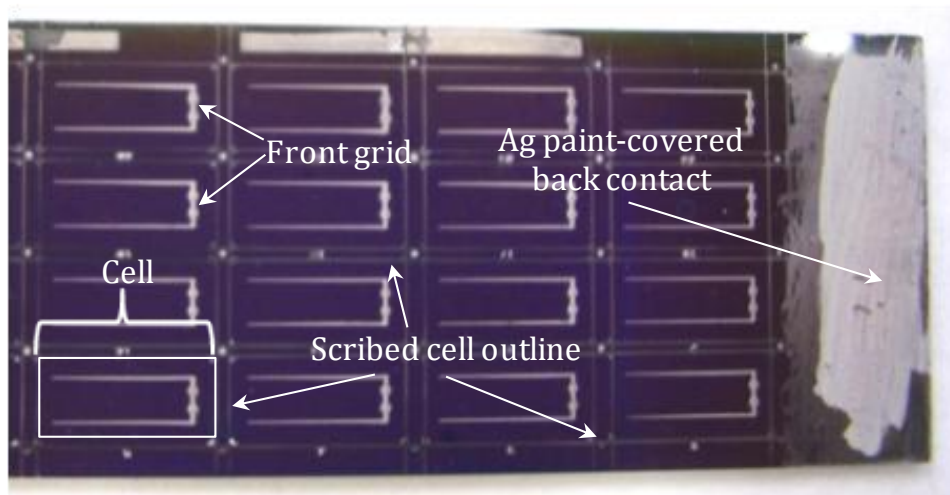
Figure 31: Photograph of complete CuInSe$_2$ cells. The front contact can be contacted from the two dots on the grid pattern and the back from the Ag paint-covered Mo back contact. The lines of scribing separating the cells can be seen in lighter grey.

4.1.8 Scribing of the outline of the cell

Finally, cells had to be isolated electrically from one another, so that the active area of each cell was well defined. This was done by scribing through the film, down to the Mo layer. To perform this task a mechanical scriber was used in which a needle was mounted on a sliding frame. The force of the needle onto the sample could be adjusted with a spring to adapt to the thickness of the layers to scribe through.

4.2 Characterisation

4.2.1 X-ray diffraction

In thin polycrystalline films, the crystallites can *a priori* be considered as randomly oriented, and therefore powder diffraction is used, whereby the samples are

compared with powder diffraction standards. These standards are made from very fine powders in order to obtain a random orientation of the crystallites. Different X-ray diffraction setups can be used, such as θ-2θ diffraction and grazing incidence X-ray diffraction (GIXD).

XRD setup

Analyses of the bulk phases were done by θ-2θ diffraction. The presence of shallow phases such as $Cu_{2-x}Se$, usually located at the surface of the film, was studied by GIXD. The analyses were performed in a Brüker D5000 diffractometer. The source was a copper filament, supplied with a voltage of 40 kV and a current of 40 mA. This source presents a strong doublet of peaks of emission, $K\alpha_1$ and $K\alpha_2$, at the wavelengths 1.540596 Å and 1.544493 Å, respectively. The Brüker EVA software was used to deduct the effect of $K\alpha_2$, in order to model a more monochromatic emission, and to match the phases of the patterns with the powder diffraction files in the Joint Committee for Powder Diffraction Standards (JCPDS) database.

4.2.2 Secondary Electron Microscope and composition analysis

Both imaging and composition analysis were performed in a FEI Quanta 200 scanning electron microscope (SEM), by secondary electron detection and energy dispersive spectroscopy (EDS) respectively. Wavelength dispersive spectroscopy (WDS) was also used in the cases where Al and Se were present in the sample. EDS and WDS were performed in Oxford Instruments INCA ENERGY and INCA WAVE X-ray spectrometers, respectively.

Secondary electron generation and detection

Secondary electrons are electrons ejected from the sample as a result of electrons from the SEM gun hitting the specimen. They are detected with an Everhart-Thornley detector, and their mapping provides an image of the surface of the sample.

X-ray generation from the sample and Energy dispersive Spectroscopy

In the SEM, a beam of electrons is generated by an electron gun and focused and directed by a series of coils onto the sample positioned below. The incident electrons may then interact with the electrons or the nuclei of the sample in various ways and the products of these interactions can be analysed with specific techniques (Auger, backscatter, etc). One type of detection of particular interest to us is the one detected by EDS, described in Figure 32. In practice, in an EDS detector the intensity and the energy of the X-rays emitted by the sample are measured. Each X-ray wavelength detected corresponds to a transition (i.e. K_α, K_β, L_α, L_β, etc) of an element present in the sample. In EDS, all the X-rays in the detection range are measured in parallel, which makes it a fast characterisation technique. Depending on the parameters of detection, a composition measurement can take a few seconds to a few minutes. The X-ray detection is limited by the smallest difference in energy ΔE_m that can be resolved in the EDS. If ΔE_m is bigger than the difference in energy between two transitions, the detected peaks will overlap and the composition measured will no longer be reliable.
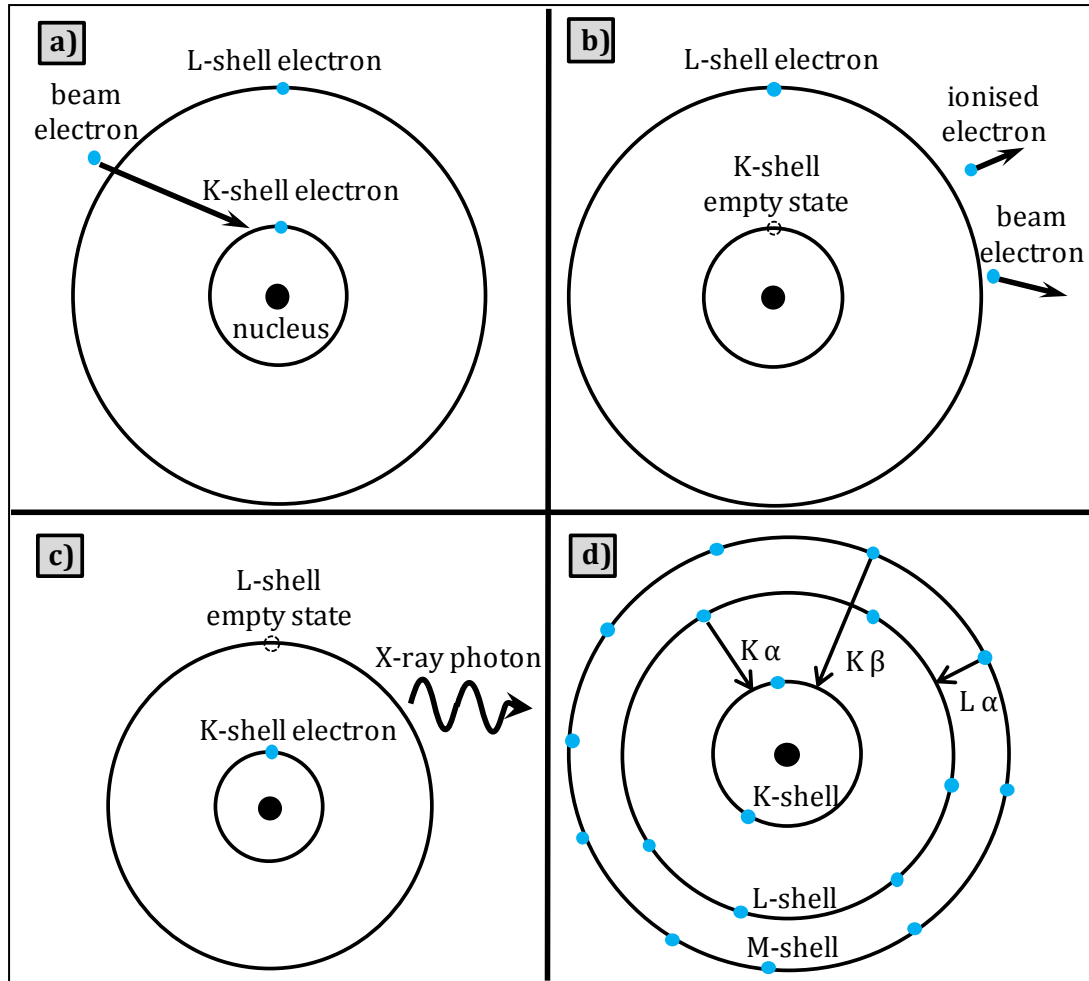
Figure 32: Principle of X-ray generation by atoms in secondary electron microscope. a) an electron from the electron beam transfers energy to an electron of the sample; b) the sample's electron is ionised and leaves an empty energy state; c) this empty state is filled by an electron from an outer shell, giving away its excess energy in the form of an X-ray photon; d) different transitions are allowed, each one yielding X-rays of energies characteristic to the nature of the atom.

The EDS detector used in this work was a Lithium drifted Si detector with a ΔE_m of 133 eV at 5.9 keV. For standard measurements, the accelerating voltage was set on 20 kV and the beam size on 5 (arbitrary unit). Except for analysing particular features, the composition measurements were performed at a magnification of x100. It is important to point out two sources of error when measuring compositions in converted films containing Al and Se. First of all, the energy difference between the K series of Al and the L series of Se is less than 90 eV, i.e. lower than the 133 eV

limit of resolution of the instrument, which affects the composition measurement. Besides, the program assessing the composition relies on the assumption that the film is of uniform composition along the depth, which does not stand if some species have migrated either towards the top or the bottom of the film.

Note that a short study was undertaken at an early stage of this thesis to assess the error on the EDS measurements (APPENDIX 3).

Wavelength dispersive spectroscopy

The problem of the resolution between peaks can be addressed by using wavelength dispersive spectroscopy (WDS) to separate the unresolved peaks. WDS, like EDS, is also a type of X-ray detector, which allows much higher resolution than the latter: typically ≈5 eV against 133 eV for EDS. Unlike EDS, which integrates in parallel the X-rays emitted at all the energies lower than the beam energy, WDS detects individually each wavelength. The wavelength selection is done by diffracting the emitted X-rays off a crystal, and the diffracted light is then measured by a gas proportional counter. Measuring the composition in different elements by WDS is much slower than EDS, so that WDS is usually used for resolving elements for which peaks overlap while the other elements are detected in parallel by EDS.

4.2.3 Photocurrent response to LED illumination in electrolytic solution

One important characterisation step is to determine whether an absorber is photoactive or not, that is whether it generates carriers when exposed to light. At this stage the absorber is p-type but no junction is formed and therefore no built-in voltage is present to separate the photogenerated carriers. However, a setup, described in Figure 33, can be used to overcome the problem and check the

photoactivity in a qualitative way. This early stage characterisation allows spotting the possible issues with the absorber itself, whereas a poor or absent photoactivity in a full device could not easily be attributed to one particular layer.
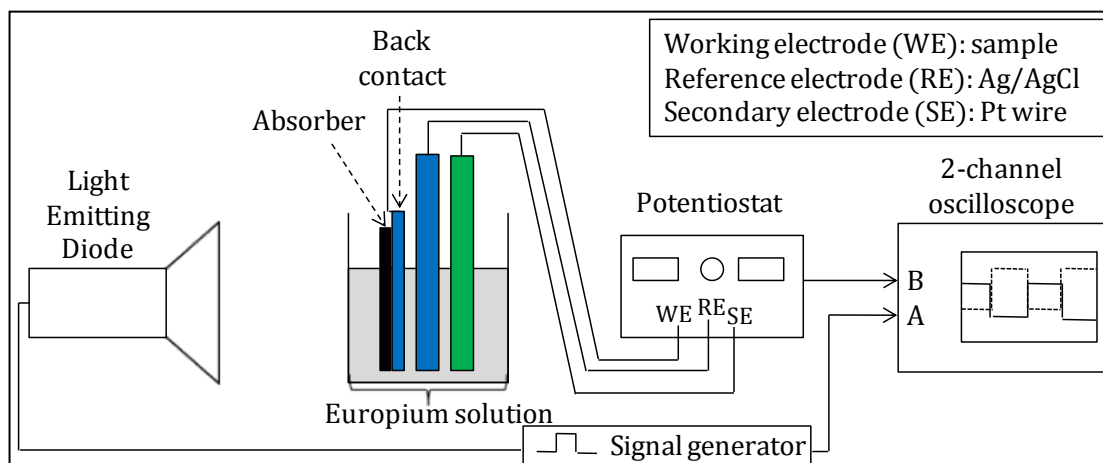
Figure 33: Diagram of principle of the photocurrent response measurement setup.

Its principle of operation is the following. The sample is placed in a photoelectrochemical cell containing an electrolytic solution of $Eu^{3+/2+}$, where are immersed the sample (the working electrode), a reference electrode and a counter electrode. Thanks to its electrochemical potential of -0.557 V vs Ag|AgCl, this electrolyte, under the appropriate bias, will form with the sample a Schottky junction and help to separate the carriers and collect the electrons. When the light is shone, the sample generates carriers; the electrons are drawn towards the absorber/electrolyte interface, stripped off the surface of the absorber by the electrolytic solution and finally conveyed to the counter electrode where they are collected. A detailed explanation of the absorber/electrolyte interface and carrier collection processes can be found in the references [114, 115]. A reverse bias between the reference electrode and the sample can be applied by the potentiostat. This bias results in the Fermi level to shift, and, as a consequence, the band bending at the Schottky contact between semiconductor and electrolyte to change. Since the

band bending affects in turn the width of the space charge region, the bias applied between the sample and the reference can be adjusted to obtain the maximum photocurrent, corresponding to an optimal separation of the carriers. In order to make the contact with the Mo at the back of the sample, the film was scraped off with a scalpel and the back was cleaned mechanically with a piece of paper dipped in alumina (Al_2O_3), a powerful abrasive agent. The photoelectrochemical cell used in this work comprised the sample as the working electrode, an Ag/AgCl reference electrode and a platinum wire as the counter electrode. The electrolyte was a diluted solution of 99.9% pure Alfa Aesar Europium ($Eu(NO_3)_3$, $6H_2O$). All three electrodes were connected to a potentiostat, the output of which was fed to one of the 2 channels of an oscilloscope.

A Thorlabs MCWHL2 white LED (emission spectrum in Figure 34), supplied with a 6-7 Hz rectangular signal, was shone onto the sample which was immersed in the electrolytic solution.
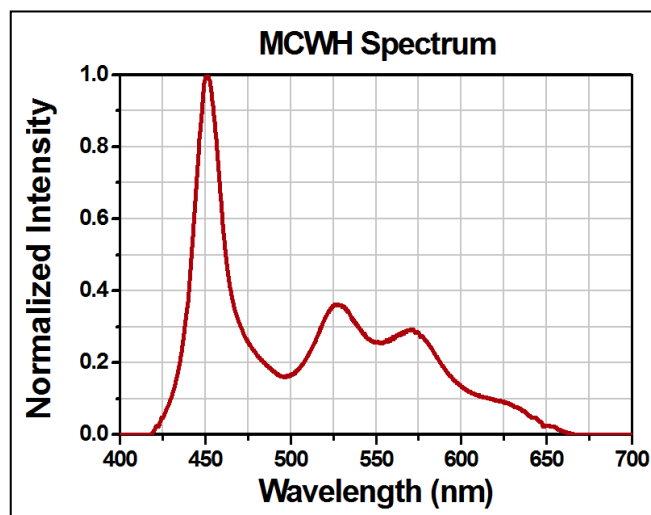
Figure 34: Spectrum emitted by the white phosphor-based LED used for photoresponse characterisation. Source: [116].

The input signal of the LED was also displayed on one channel of the oscilloscope. Finally, a reverse potential was applied between the sample (the working electrode in

this setup) and the reference electrode. The voltage applied in the measurements was kept lower than 0.80 V, except for the early trials where the bias was raised up to 1.15 V, which led to sample degradation.

4.2.4 Photocurrent spectroscopy in solution and External Quantum Efficiency

To get a quantitative characterisation of the opto-electronic properties of the film, a similar setup to that described in the previous section can be used. From this latter type of characterisation, called photocurrent spectroscopy, the external quantum efficiency (EQE) of the absorber in solution can be extracted. The EQE of the system can be defined as

$$EQE = \frac{J_e}{J_\gamma} \tag{4.4}$$

with J_e the current of electrons collected by the Pt wire and J_γ the flux of incident photons. The main difference with the photocurrent response under LED illumination is that the photocurrent generated was in this case measured for each individual wavelength. However, as a consequence of the monochromation the intensity of the incident light was very low and, to overcome the low signal to noise ratio generated by such a low light intensity, a light chopper was used in conjunction with a lock-in amplifier. The basic operation principle of the lock-in amplifier is the following: as a consequence of the chopping of the light, the sample generates carriers with a frequency equal to the chopping frequency of the light. The lock-in amplifier then selects only the generated signals within a narrow bandwidth around the chopping frequency, using a phase-sensitive detector (PSD). Note that the effect of the applied reverse bias is to widen the space-charge region, and therefore the

EQE measured is an apparent quantum efficiency, which cannot be directly compared with the EQE in short-circuit conditions measured in the finalised devices.

A Bentham EQE setup was used for the measurements in solution. The photoelectrochemical cell and the connections to the potentiostat were those described for the photocurrent measurement under LED illumination.
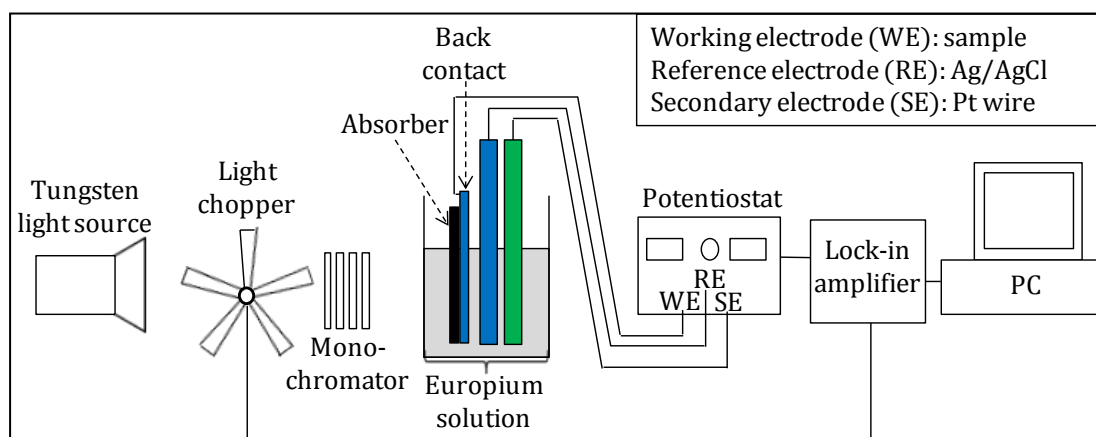
Figure 35: Diagram of principle of the external quantum efficiency measurement setup in solution.

The output of the potentiostat was connected to the lock-in amplifier unit, which was itself connected to a DC amplifier. Calibrated silicon and germanium photodetectors were used to determine the exact spectrum of the source and, by comparing the response of the calibrated detectors to that of the sample, the sample's EQE values could be extracted. Because of the detectors' specific ranges of sensitivity, the silicon detector was used for the range 400 nm - 800 nm and the germanium detector for the range 800 nm - 1300 nm.

4.2.5 External quantum efficiency on finalised device

The EQE was also measured on full solar devices. As compared to the EQE in solution, this measurement is affected by additional loss factors, such as the additional reflections or recombinations of photogenerated carriers at the interfaces

between layers and the shadowing of the contact pads. The setup used for this measurement (Figure 36) was very much the same as for EQE in solution, with the difference that the potentiostat was no longer required.
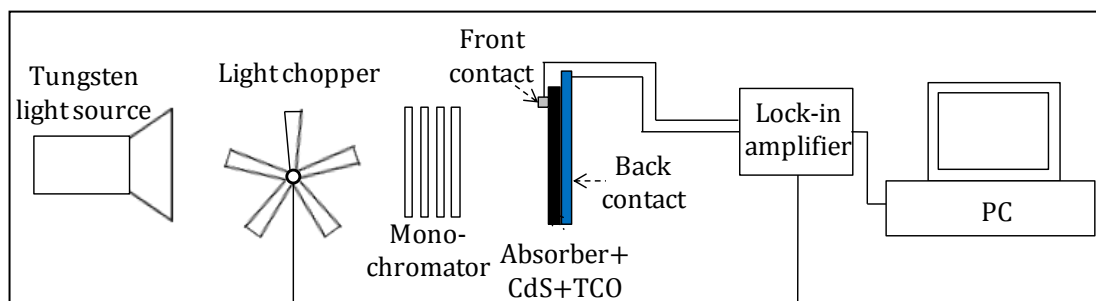
Figure 36: Diagram of principle of the External Quantum Efficiency measurement setup on cells.

4.2.6 Spectrophotometry

Spectrophotometry was used to characterize the reflectance and transmittance of the films deposited. The measurements were performed in a Shimadzu SolidSpec-37000 UV-VIS-NIR spectrophotometer. It was equipped with an integrating sphere, which allows measurement of both the diffuse reflectance (i.e. light scattered by the sample in every direction) and the specular reflectance (mirror-like reflection) by collecting light emitted in a large solid angle. The sample holder had a 5° tilt to the normal to the incident beam, so that the light of the specularly reflected beam would be collected. The light is generated by a deuterium and a halogen lamp. Three detectors are in use in this machine: a photomultiplier tube, sensitive to the ultra-violet and visible regions, an InGaAs detector and a PbS detector for the near infrared. Transmittance was measured by a direct detection unit.

4.2.7 Secondary Ion Mass Spectroscopy

Secondary ion mass spectroscopy (SIMS) was used in the characterisation of the distribution of the elements as a function of the depth. This technique consists in

bombarding the film to be analysed with an ion beam. As the beam ions hit the sample, they sputter ions of sample species from it and these secondary ions are collected by a mass spectrometer. The area of the sample sputtered forms a crater. Since the depth of the centre of this crater depends on the sputtering time, a depth profile of the abundance of each element present in the sample can be established. SIMS requires an ultra high vacuum to ensure consistent secondary/primary ion ratio and a better accuracy of detection by the mass spectrometer.

A SIMS equipped with a Hiden Analytical IG 20 ion gun and a quadrupole mass spectrometer was used for this measurement. The base pressure before operation was systematically lower than 1×10^{-9} mbar. A beam of O_2 ions could be used for sputtering positive ions from the sample, whereas Ar ions made it possible to analyse both positive and negative sample ions.

4.2.8 Current-voltage measurement under AM 1.5 illumination

To measure the I-V characteristic of the completed cells, the front and back contacts were connected to a Keithley 2400 2-channel sourcemeter. An ABET Sun 2000 solar simulator, equipped with a 500 W Xe lamp and filters, was used to provide the AM 1.5 illumination to the devices. 2 and 4-wire measurements were undertaken (Figure 37). The 4-wire measurement setup was introduced towards the end of this work. Compared to 2-wire, it eliminates the effect of the resistance of the leads on the measurements.

2-wire measurements were performed by contacting front and back with one lead each, whereas in the 4-wire configuration the voltage was measured in a separate branch of low current (typically a few nA).
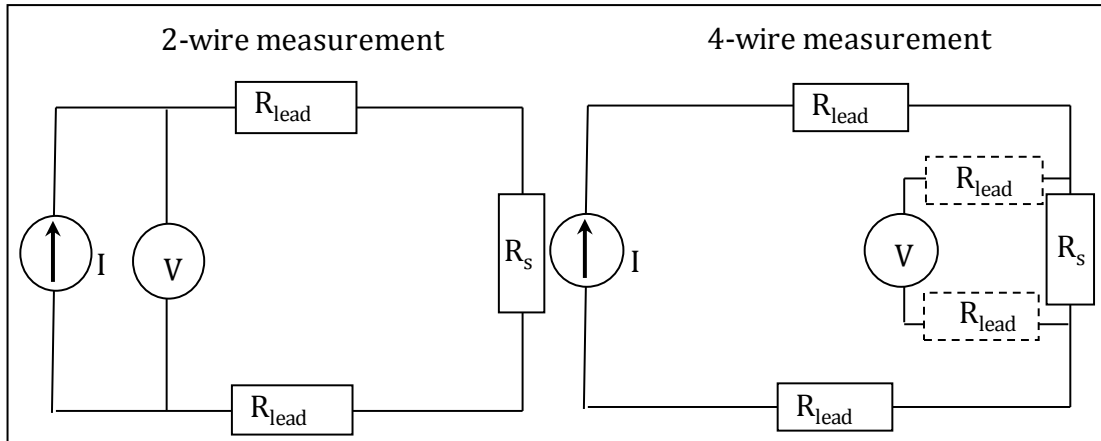
Figure 37: diagram illustrating the 2-wire (left) and 4-wire (right) I-V measurements in the configuration where the current is the input and the voltage the output. In the 2-wire configuration the voltage is affected by the leads' resistance R_{lead} because a high current is flowing through them. In the 4-wire measurement the voltage is measured in a branch of very low current, and is therefore not affected by R_{lead}.

CHAPTER 5 METALLIC PRECURSOR PREPARATION AND CHARACTERISATION

In this section the focus is on the crystalline phases present in the as-deposited metallic precursors.

5.1 Fabrication data on the samples of the chapter

Table 4 summarises the fabrication data for the samples of this chapter.

Table 4: Deposition data for the samples of chapter 5.

Page	ID	Substrate	Target	Layout	Comp. (at%)		
					Cu	In	Al
88-90	N255C4	SLG/Mo	elem.	Cu-In	57.0	43.0	0.0
88-89	N258D4	SLG/Mo	elem.	Cu-In	54.0	46.0	0.0
88-89,134-135	N623E6	SLG/Mo	alloy	Cu-In	48.0	52.0	0.0
89-90	N535Y	SLG/Mo	elem.	Cu-In	37.5	62.5	0.0
90	N202C	SLG/Mo	elem.	Cu-Al	59.0	0.0	41.0
90-91	N205S4	SLG/Mo	elem.	Cu-Al	52.0	0.0	48.0
91-92	#556	SLG/Mo	elem.	Cu-In	49.5	50.5	0.0
91-92	N548G	SLG/Mo	elem.	Cu-In-Al	51.0	45.0	4.0
91-92,9	N611E	SLG/Mo	elem.	Cu-In-Al	49.0	36.0	15.0
93	N561F	SLG/Mo	elem.	Cu-In-Al	46.0	38.0	16.0
92,94	N392I	SLG/Mo	elem.	Cu-In-Al	47.0	43.0	10.0
92,94,189	N428Y	SLG	elem.	Cu-In-Al	50.0	22.0	28.0
94	N366A	SLG/Mo	elem.	Cu-In	44.0	56.0	0.0

5.2 Cu-In precursors

Four Cu-In precursors of increasing indium content were deposited and characterised. All samples were sputter-deposited from elemental targets except for N623E6, which was deposited from an alloy target of atomic composition ratio [Cu]/[In]=0.92.

5.2.1 Data

The XRD patterns (Figure 38) show that the same two crystalline phases are present throughout the four compositions: Cu_2In (PDF 00-042-0475) and $CuIn_2$ [117]. The Cu_2In (110) reflection is very broad for N255C4 ([Cu]/[In]=1.33) and N258D4

([Cu]/[In]=1.17), indicating poor crystallinity, and becomes somehow sharper in the two In-rich samples. The area under the peak decreases between N623E6 ([Cu]/[In]=0.92) and N535Y ([Cu]/[In]=0.60). The intensity of the $CuIn_2$ (112) reflection increases with increasing indium ratio, and the (310)/(266) doublet of this same phase resolves when an In-rich composition is reached.
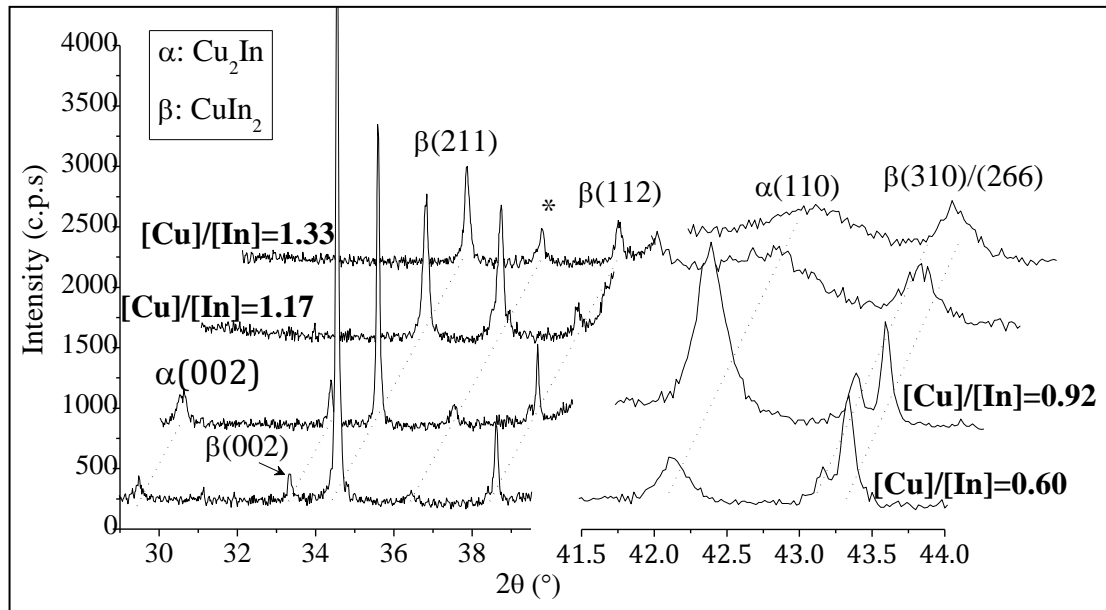
Figure 38: XRD patterns of four Cu-In precursors, deposited on Mo, of increasing indium composition, [Cu]/[In]=1.33 (N255C4), [Cu]/[In]=1.17 (N258D4), [Cu]/[In]=0.92 (N623E6) and ([Cu]/[In]=0.60 (N535Y). The peak marked * is an artefact from the XRD machine.

5.2.2 Discussion

The phases Cu_2In and $CuIn_2$ can be combined in different ratios to produce any of the four different EDS compositions measured in the samples. The apparent change in crystallinity of the Cu_2In phase between In-poor samples and In-rich samples cannot be satisfactorily explained from the data available. However, the decrease in area observed between the two In-rich films is consistent with a decreasing presence of Cu_2In. The trend of increasing area of the $CuIn_2$ (211) reflection from the In-poor

precursor N255C4 to the very In-rich N535Y is also consistent with an increasing presence of this phase.

5.3   Cu-Al precursors

5.3.1   Data

The XRD patterns of two precursors sputter-deposited from Cu and Al elemental targets, N202C ([Cu]/[Al]=1.44) and N205S4 ([Cu]/[Al]=1.08), are presented in Figure 39. N202C contains the crystalline phases Cu_9Al_4 (PDF 01-071-0307), Cu_4Al (PDF 00-028-0006) and a weak reflection corresponding to $CuAl_2$ (PDF 00-003-1079). N205S4 contains Cu_4Al, $CuAl_2$ and Al (PDF 00-001-1100).
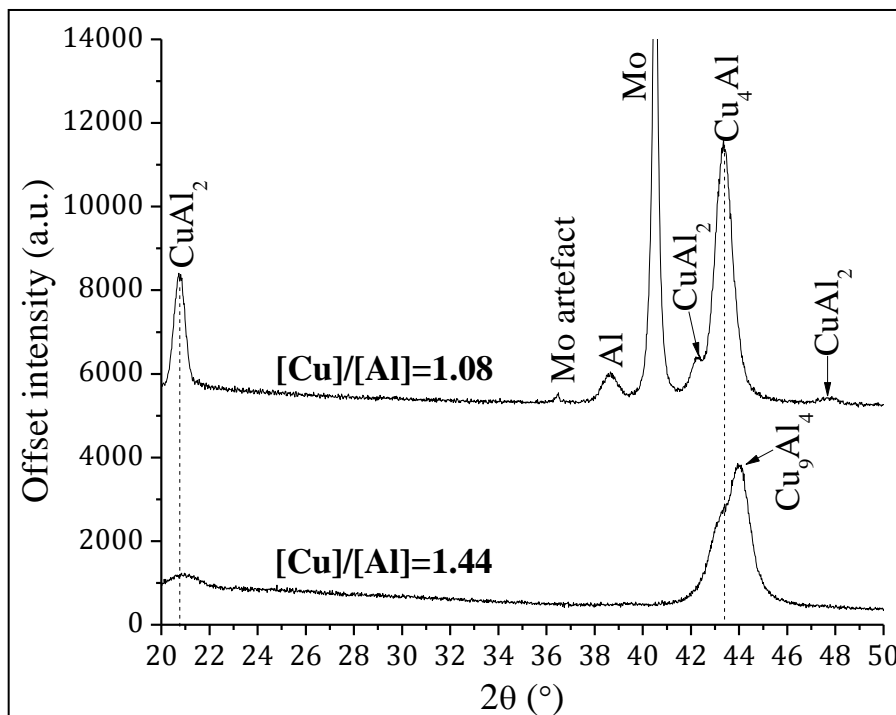
Figure 39: XRD patterns of N202C ([Cu]/[Al]=1.44) and N205S4 ([Cu]/[Al]=1.08), reported with the relevant standard powder diffraction files.

5.3.2   Discussion

The presence in N202C of the crystalline phases Cu_4Al, Cu_9Al_4 and only a small amount of $CuAl_2$ (the only Al-rich phase) is consistent with the overall Cu-rich

90

composition measured by EDS. N205S4, on the other hand, shows an important presence of $CuAl_2$, as well as elemental Al, which fits with the overall composition measured by EDS, [Cu]/[Al]=1.08.

5.4 Cu-In-Al precursor

5.4.1 Data

One particularly striking feature of the Cu-In-Al precursors was their marked surface roughness compared to that for Cu-In and Cu-Al precursors. This roughness appears in the thickness measurements performed with the Talystep profilometer. The typical amplitude of the roughness observed for Cu-In and Cu-Al precursors was around 10-30 nm, while that of Cu-In-Al precursors was 80 nm to 200 nm. Figure 40 shows the features at the surface of a Cu-In film (a) and two Cu-In-Al films of increasing Al content (b)-(c). In this figure, the features on the surface of N611E (x=[Al]/([Al]+[In])=0.29) are bigger than those on #556 (CuIn). In N548G (x=0.08), the small features present in the Cu-In precursor are present, but some bigger features are also present (circled in white).
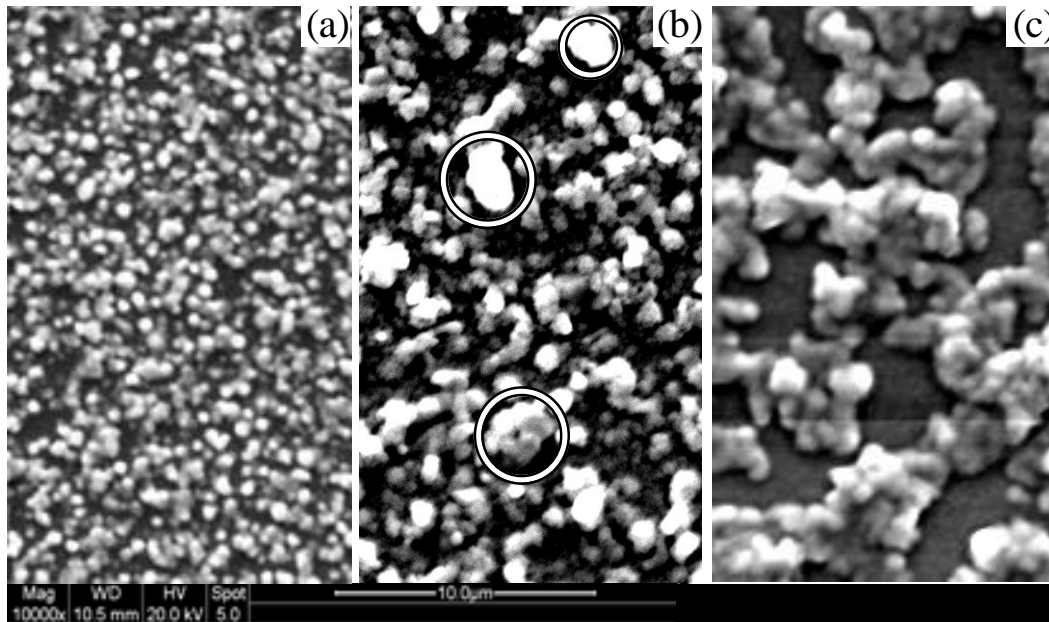
Figure 40: SEM micrograph of three samples deposited from elemental targets, a Cu-In precursor, *(a)* #556 ([Cu]/[In]≈0.98) and two Cu-In-Al precursors, *(b)* N548G (x=[Al]/([Al]+[In])=0.08), and *(c)* N611E (x=0.29).

Localised EDS analyses were performed in fixed point mode on the surface features (red circle) and bulk of the film (green circle). The results are shown in the inset table of Figure 41 and show a higher abundance of indium in the features than the bulk. Note that the beam energy was kept at 20 kV, which was too high to interact with the surface features alone (see dotted lines in Figure 41).

The XRD patterns of three Cu-In-Al samples with different Al content were analysed and compared to the spectrum of a Cu-In sample (Figure 42). All samples were grown on Mo apart from N428Y, which was grown directly onto the SLG substrate. A crystalline phase of indium (PDF 00-005-0642) is present in all Cu-In-Al precursors, but absent from Cu-In. In N392I (10.0 at% Al), the Al is incorporated into $Cu_{11}In_9$ (PDF 00-041-0883) by partial substitution of In; At 15.0 at% Al (N611E), it incorporates into Cu_9In_4 (PDF 00-042-1476); At 28.0 at% (N428Y), finally, it forms Cu_4Al (PDF 00-028-0006).

Location	[Cu] (%)	[In] (%)	[Al] (%)
feature	35.5	54.5	10
bulk	54	26.5	19.5
large scale	46	38	16
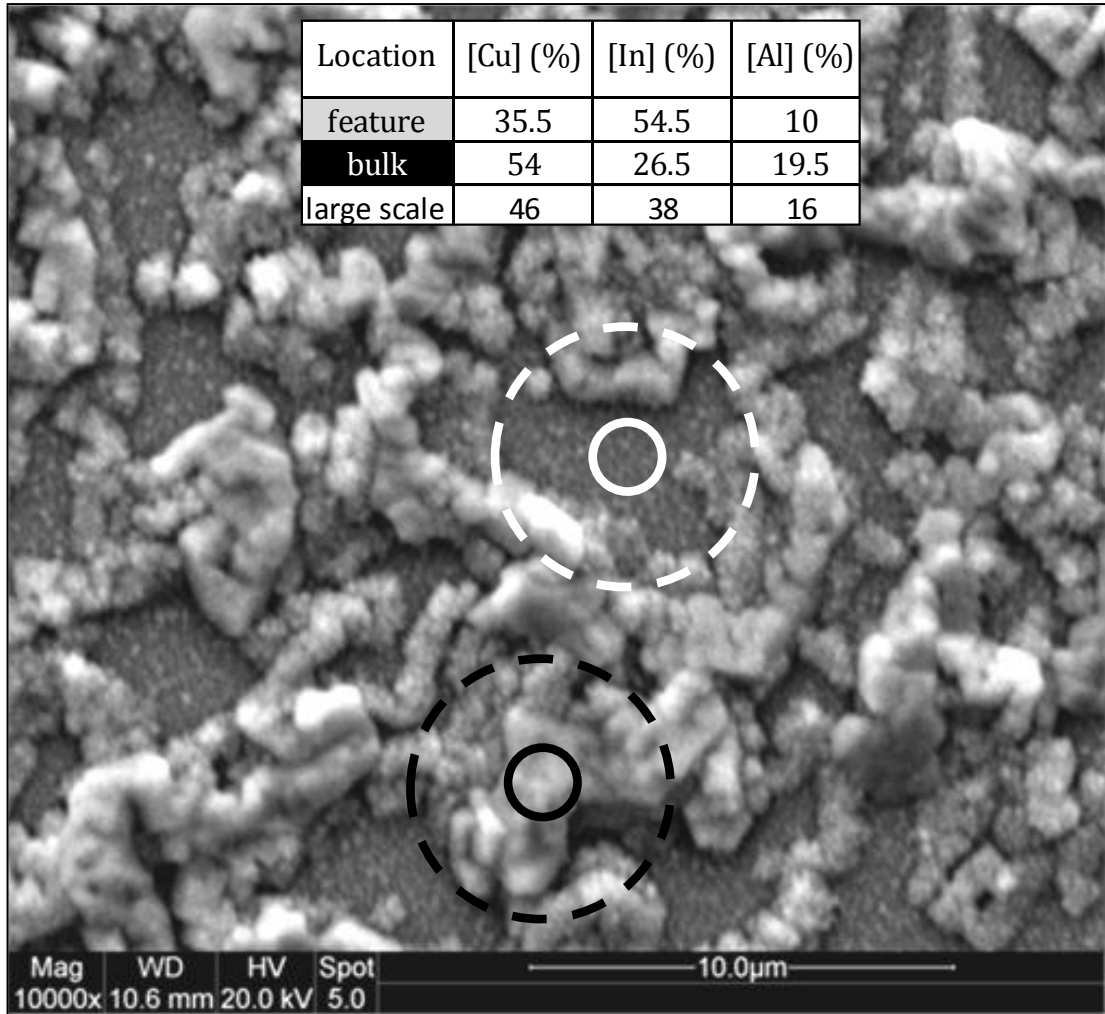
Figure 41: Surface image by Scanning Electron Microscope of N561F (Cu-In-Al precursor). Embedded is a table listing the EDS compositions measured on one of the smoother features (*black circle*) and on a region of the bulk free of such features (*white circle*). The plain circles represent the incoming electron beam and the dashed lines the projected radius of the volume emitting the X-rays analysed.
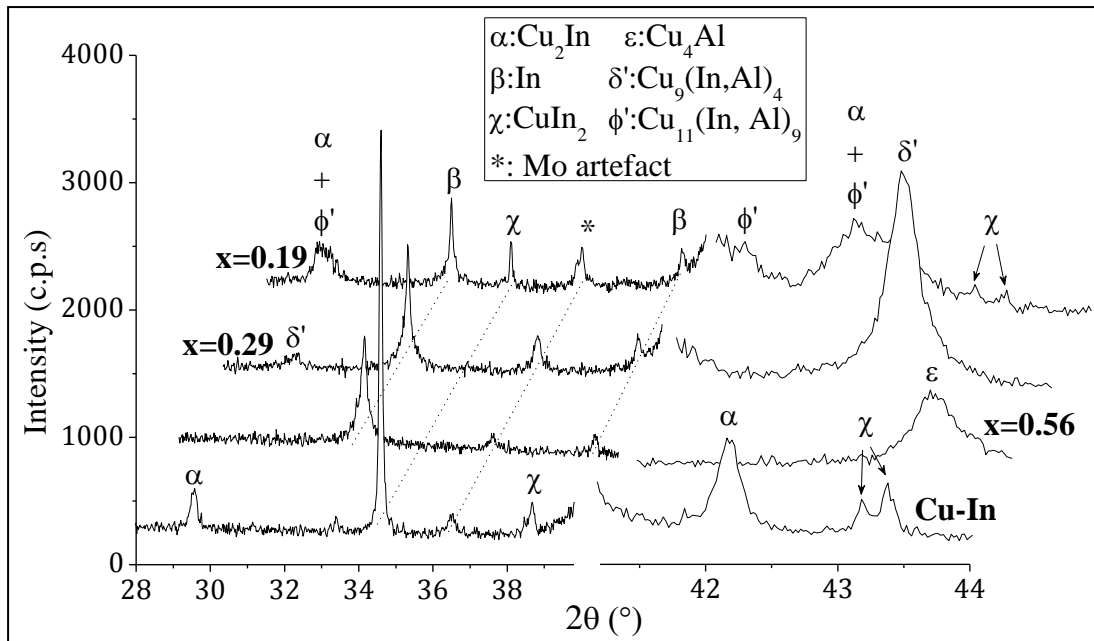
Figure 42: XRD patterns of 3 different Cu-In-Al precursors of increasing Al content, N392I (x=0.19), N611E (x=0.29), N428Y (x=0.56) and one CI precursor, N366A. Note that all samples were deposited on SLG/Mo apart from N428Y, deposited on SLG only.

5.4.2 Discussion

The bigger features found at the surface of Cu-In-Al were more abundant on the more Al-rich samples tested, and more indium-rich than the bulk of the samples (Figure 41, *insert*). The roughness found in profilometry therefore arises from the concomitance of the two elements In and Al. Besides, the XRD patterns of the Cu-In-Al samples all contain an indium phase, absent from the Cu-In precursor. It is likely that the bigger features observed at the surface of Cu-In-Al are pure indium. Figure 42 makes it possible to suggest a cause behind the formation of an indium phase. Indeed, whereas $Cu_{11}In_9$ and $CuIn_2$ are the dominant phases in the Cu-In precursor, the phases $Cu_9(In,Al)_4$ and Cu_4Al are seen in the Cu-In-Al precursors. $Cu_9(In,Al)_4$ is obtained from Cu_9In_4, by partial substitution of In with Al [66]. However, the overall composition dictates that some indium will not be incorporated into $Cu_9(In,Al)_4$ (or Cu_4Al if the Al content is high enough), and this indium therefore has to form a phase of its own. The presence of such superficial indium

94

features was reported on very In-rich Cu-In precursors [118]. This reference also identifies the small features visible on the surface of the Cu-In precursor as CuIn$_2$ (Figure 40 (a)), which is indeed detected by XRD.

CHAPTER 6   SELENISATION OF CuInSe$_2$ AND CuAlSe$_2$ PRECURSORS

6.1 Experimental

The absorbers were prepared in the rapid thermal processor (RTP) via the procedure described in section 4.1. They were characterised by XRD and EDS. Wavelength dispersive spectroscopy (WDS) and cathodoluminescence (CL) were also performed, at Strathclyde University, on one CuAlSe$_2$ sample. WDS can resolve the Al K-transitions from the Se L-transitions and CL helps determine the electronic transitions in the energy band gap.

The fabrication data for the samples of this chapter is summarise in Table 5 (next section).

6.2 Fabrication data on the samples of the chapter

Table 5: Deposition and processing data summary for the samples of chapter 6.

Page	ID	Substrate	Target	Layout	Comp. (at%)			Se?	Fur-nace	P^{re} (mbar)	Gas	Dwell T^{re} (°C)	Dwell dur. (s)	Ramp dur. (s)
					Cu	In	Al							
99,101,104-106,108,110	N205R1	SLG/Mo	elem.	Cu-Al	52.0	0.0	48.0	Yes	RTP	600	Ar	550	60	45
99	N205O4	SLG/Mo	elem.	Cu-Al	52.0	0.0	48.0	Yes	RTP	600	Ar	550	60	45
100-101,104	N205R4	SLG/Mo	elem.	Cu-Al	52.0	0.0	48.0	Yes	RTP	800	Ar	550	60	45
101-103,105-107	N234C1	SLG	alloy	Cu-Al	50.0	0.0	50.0	Yes	RTP	800	Ar	550	60	45
104-107	N236C1	SLG	alloy	Cu-Al	50.0	0.0	50.0	Yes	RTP	800	Ar	600	60	50
104-107	N205Q1	SLG/Mo	elem.	Cu-Al	52.0	0.0	48.0	Yes	RTP	800	Ar	520	60	40
110-115,122	N332C1	SLG/Mo	elem.	Cu-In	49.0	51.0	0.0	Yes	RTP	100	H_2/N_2	530	300	70
110-115,122	N332C4	SLG/Mo	elem.	Cu-In	49.0	51.0	0.0	Yes	RTP	100	H_2/N_2	530	60	70
110-115	N332R1	SLG/Mo	elem.	Cu-In	49.0	51.0	0.0	Yes	RTP	100	H_2/N_2	530	300	900
110-115	N332R4	SLG/Mo	elem.	Cu-In	49.0	51.0	0.0	Yes	RTP	100	H_2/N_2	530	900	900
115-117, 122	N328P1	SLG/Mo	elem.	Cu-In	42.0	58.0	0.0	Yes	RTP	100	H_2/N_2	530	900	900
115-118, 122	N328P4	SLG/Mo	elem.	Cu-In	42.0	58.0	0.0	Yes	RTP	100	H_2/N_2	530	900	900
119-121	N622C4	SLG/Mo	alloy	Cu-In	48.0	52.0	0.0	Yes	RTP	10	H_2/N_2	250	1400	300
119-121	N622C3	SLG/Mo	alloy	Cu-In	48.0	52.0	0.0	Yes	RTP	10	H_2/N_2	350	1400	400
119-121	N622C2	SLG/Mo	alloy	Cu-In	48.0	52.0	0.0	Yes	RTP	10	H_2/N_2	450	1400	630
119-120,148-149	N622C1	SLG/Mo	alloy	Cu-In	48.0	52.0	0.0	Yes	RTP	10	H_2/N_2	530	1400	750
124-128	N687R	SLG/Mo	alloy	Cu-In	48.0	52.0	0.0	Yes	RTP	10	H_2/N_2	530	500	600
124-128	N687S	SLG/Mo	alloy	Cu-In	48.0	52.0	0.0	Yes	RTP	800	H_2/N_2	530	500	600

6.3 CuAlSe$_2$

The RTP selenisation process used aimed at forming single phase CuAlSe$_2$ (CAS).

6.3.1 Reproducibility

6.3.1.1 Data

The reproducibility in the RTP was assessed by selenising consecutively two precursors of the same batch, deposited from Cu and Al elemental targets, with an identical annealing process. The as-deposited composition was [Cu]/[Al]=1.08. The corresponding XRD patterns are displayed in Figure 43.

Both XRD patterns indicate the presence of the same crystalline phases[9]: CuAlSe$_2$ (PDF 01-075-0101), CuAl [119] and several copper selenides, including Cu$_{2-x}$Se (PDF 00-006-0680) and α-CuSe (PDF 00-027-0184). The peak areas are similar for both samples.

---

[9]When the PDF number could not be found, the reference to a publication is indicated
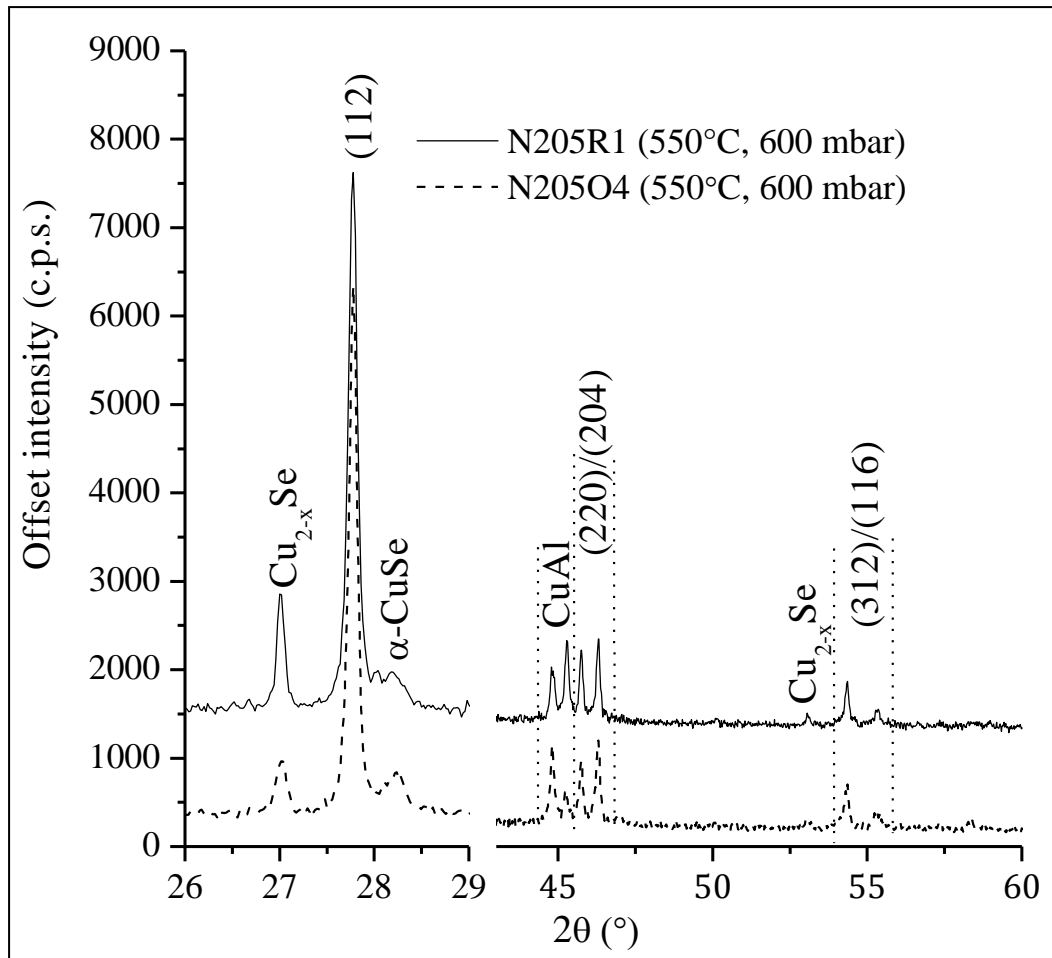
Figure 43: Comparison of the XRD patterns of two identical precursors, N205O4 and N205R1 ([Cu]/[Al]=1.08), selenised in the same conditions (RTP, 550°C, 60 s dwell, 600mbar Ar). The Miller indices refer to CuAlSe₂.

6.3.1.2 Discussion

The presence of CuAl and copper selenide phases suggests an incomplete conversion of the Cu-Al metallic precursor into CuAlSe$_2$, possibly because of the short dwell at maximum temperature (60 s) or alternately a lack of Se. CuAl was not observed in the metallic precursor, which contained CuAl$_2$ and Cu$_9$Al$_4$ (section 5.3). Since the precursors used were slightly Cu rich ([Cu]/[Al]≈1.08), the formation of CuAl can be interpreted as a result of intermixing of the phases CuAl$_2$ and Cu$_9$Al$_4$ and the loss of some of the excess Cu to the copper selenide phases. The presence of CAS at such a

temperature was expected, since this compound was reported to form from Cu_2Se and the only known compound of Al and Se, Al_2Se_3 (T_f=490°C) [100] via:

$$Cu_2Se + Al_2Se_3 \rightarrow 2\ CuAlSe_2 \qquad (6.1)$$
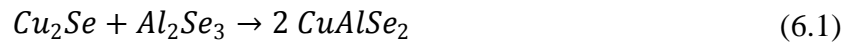
Optimal growth temperatures around 580°C have been reported in the literature [120, 121]. However, the samples used for this study were deposited on soda lime glass, which was often observed to bend when subjected to temperatures above or in the range of 550°C. This is believed to be due to the conjunction of stresses in the films and the softening of the glass around this temperature.

The results point at good reproducibility between consecutive annealing runs. This justifies the study below, where the effects of varying different parameters (pressure, maximum temperature etc) are investigated.

6.3.2 Pressure

Ar pressures of 600 mbar and 800 mbar were compared. The XRD patterns (Figure 44) do not show significant differences, apart from a slightly more intense CAS (112) reflection in sample N205R4 (800 mbar). Therefore, pressures of 600 mbar and 800 mbar do not yield discernable differences in the structural properties of the films. This result will be used in section 6.3.4, where one sample was grown in a pressure of 600 mbar when all the others were grown at 800 mbar.
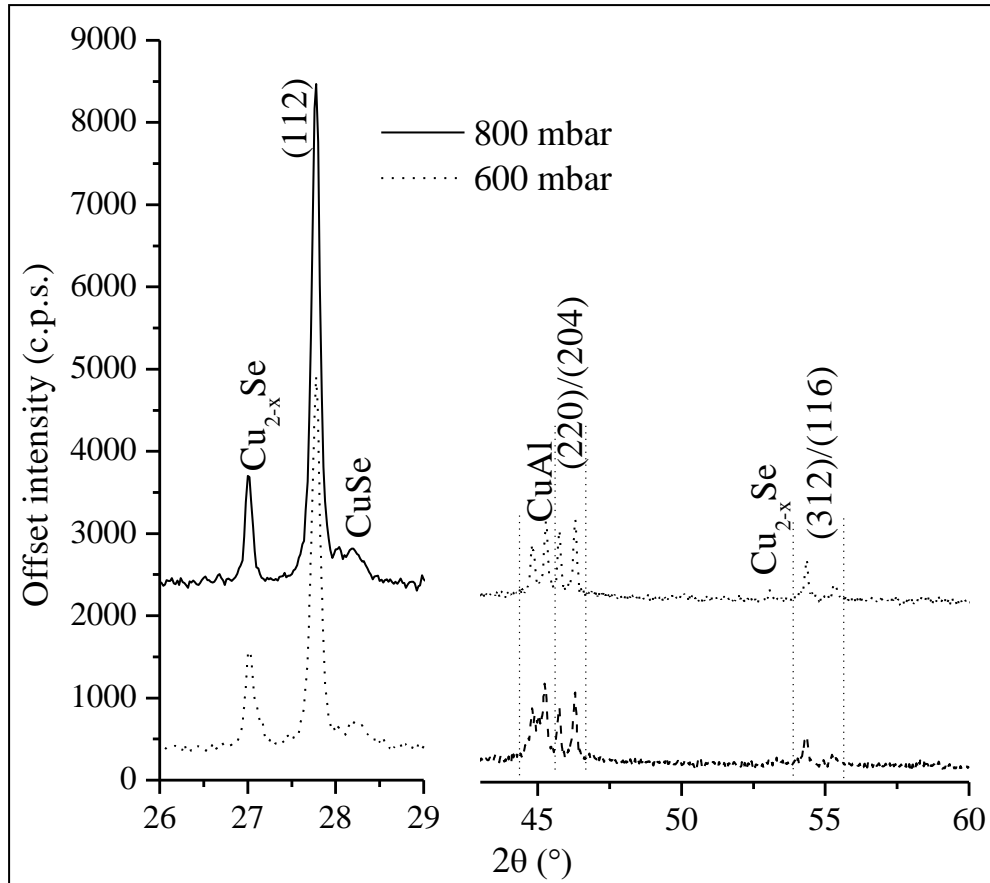
Figure 44: XRD patterns of two samples selenised at 550°C under different pressures of Ar, N205R1 (600 mbar) and N205R4 (800 mbar).

6.3.3 Copper excess and KCN etching

6.3.3.1 Data

X-ray diffraction

N234C1 ([Cu]/[Al]≈1.00), deposited from the alloy target, was selenised in the RTP at 550°C for 60 seconds in 800 mbar of argon, and its XRD pattern recorded (Figure 45, *dashed line*). The unetched sample contained CAS (PDF 01-075-0101), traces of CuAl [119] and the copper selenides $Cu_{2-x}Se$ (PDF 00-006-0680) and α-CuSe (PDF 00-027-0184). To remove the copper selenides, KCN etch was then performed for 5 minutes in a solution of KCN of mass composition 5 wt% (Figure 45 *solid line*). The reflections corresponding to copper selenides disappeared after the KCN etching,

and the area of the CAS reflections after etching is also lower than before by approximately a half [10].
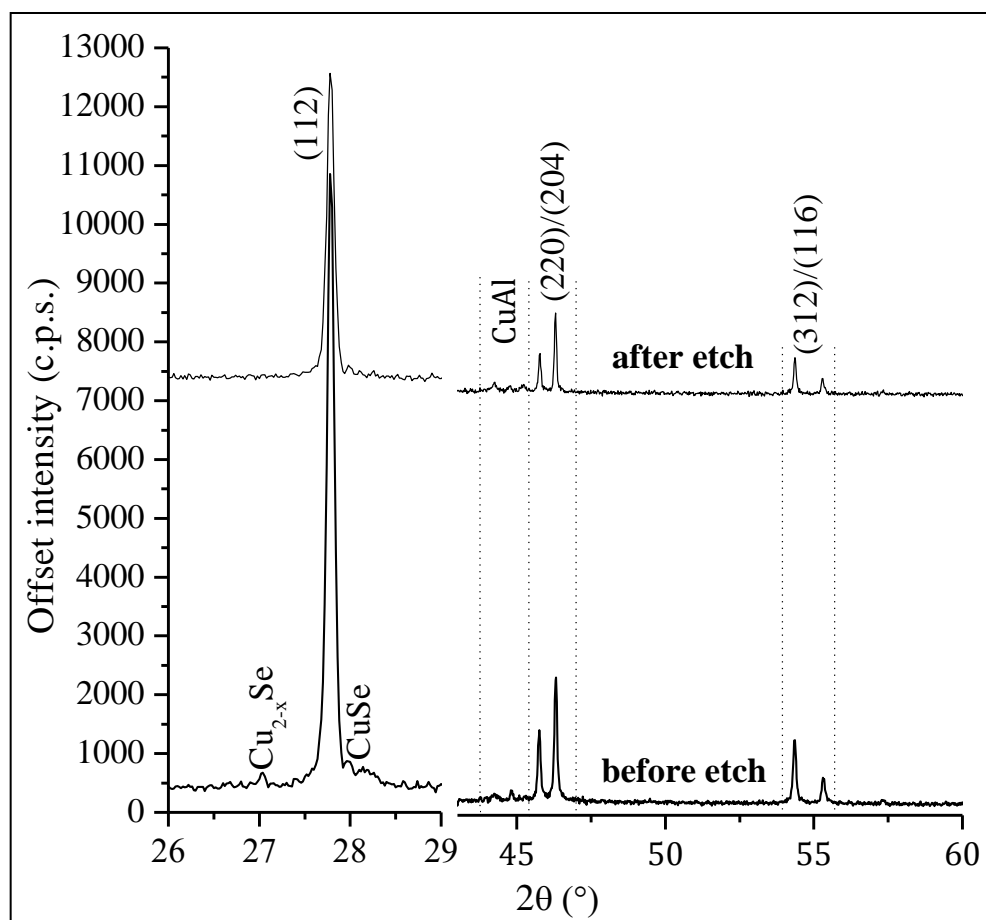
Figure 45: XRD pattern of N234C1 (550°C, 60 s, 800 mbar Ar) before and after KCN etch.

Scanning electron microscopy/Energy dispersive spectroscopy

The SEM micrographs of the film surface before and after etching are displayed in Figure 46. The surface of the unetched film is covered by bristle-shaped features which aggregate into balls in some places (Figure 46 (a)), removed by KCN etching (Figure 46 (c)). EDS composition of these features was 4 at% Al, 36 at% Cu and 53 at% Se. However, this composition is affected by the EDS overlapping of Al and Se (see section 6.3.5) and the fact that the beam interacts with part of the bulk.

---

[10] Established by peak fitting.

Furthermore, the colour of the film was grey before the etching process and yellow afterwards (Figure 46 (b)).
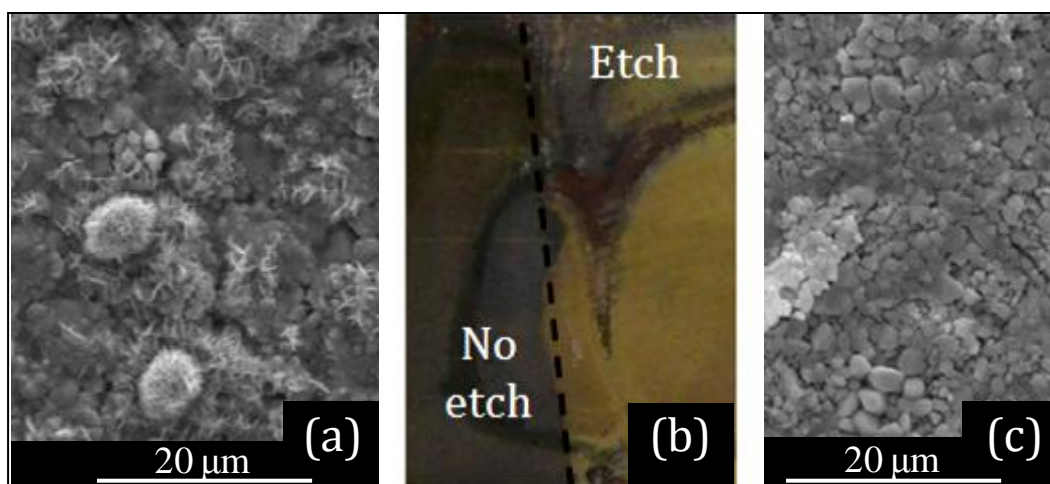
Figure 46: SEM micrographs of N234C1 (550°C, 60 s dwell, 800 mbar Ar) *(a)* before and *(c)* after 5 minutes etching from a 5 wt% concentration solution. *(b)* is a photograph of the surface of N234C1, where the left half was left unetched and the right half was etched.

6.3.3.2 Discussion

The presence of residual amounts of copper selenides and CuAl in unetched N234C1 indicates that these phases have not been entirely consumed to form CAS. This can be explained by the briefness of the dwell at 550°C, or by a slightly Cu-rich composition. The surface features (Figure 46 **(a)**) were most likely copper selenide, since they disappeared after etching. The decrease of area of CAS peaks after etching is believed to arise from a thinning of the film following the KCN etch. Indeed, the area under the peaks relates to the abundance of the phase. This thinning could mean that the etching process was too long. Although KCN etching was reported to have only little effect on CIS and CIGS, it is possible that the etching rate of $CuAlSe_2$ by this agent is higher than for CIS and CIGS. Alternately, copper selenides might have been present in the bulk, and their removal caused part of the film to delaminate. The change of the film colour from grey before etch to yellow after etch indicates less

absorption in the visible spectrum, and potentially a higher band gap material. $Cu_{1.8}Se$, one of the possible compositions of $Cu_{2-x}Se$, was reported to absorb photons with wavelength $\lambda < 550$ nm [122] (i.e. the part of the visible spectrum ranging from green to violet), while CAS, with a band gap of 2.7 eV, absorbs $\lambda \leq 450$ nm (violet only). The removal of $Cu_{2-x}Se$ would therefore explain why the etched part exhibits a brighter and more yellow colour while copper selenides yield in the unetched part a higher overall absorption (i.e. darker tone) and a shift towards gray taints (Figure 46 **(b)**).

6.3.4 Dwell Temperature

6.3.4.1 Data

Three samples selenised at different dwelling temperatures (Figure 47) were compared. The other parameters were kept constant apart for N205R1, which was converted at 600 mbar instead of 800 mbar for the other two. However, the results of section 6.3.2 suggest that such a variation does not cause noticeable variations on the structural properties. The Cu-Al metallic precursor of N236C1 was deposited from the alloy target, with the composition ratio $[Cu]/[Al] \approx 1.00$, while N205R1 and N205Q1 were deposited from elemental targets with the ratio $[Cu]/[In] \approx 1.08$. Like N205R4 presented earlier (section 6.3.2), all three samples contained copper selenides and CuAl phases. The CAS (112) reflection is most intense in N205R1 (550°C).

Since the composition of the Cu-Al target used for depositing N236C1 was different from that of the other two, the XRD pattern of this film was compared to another film from the same alloy target, but selenised at 550°C (Figure 48). N236C1 (600°C)

presents higher copper selenides and CuAl peak areas and weaker CAS reflections than N234C1 (550°C).
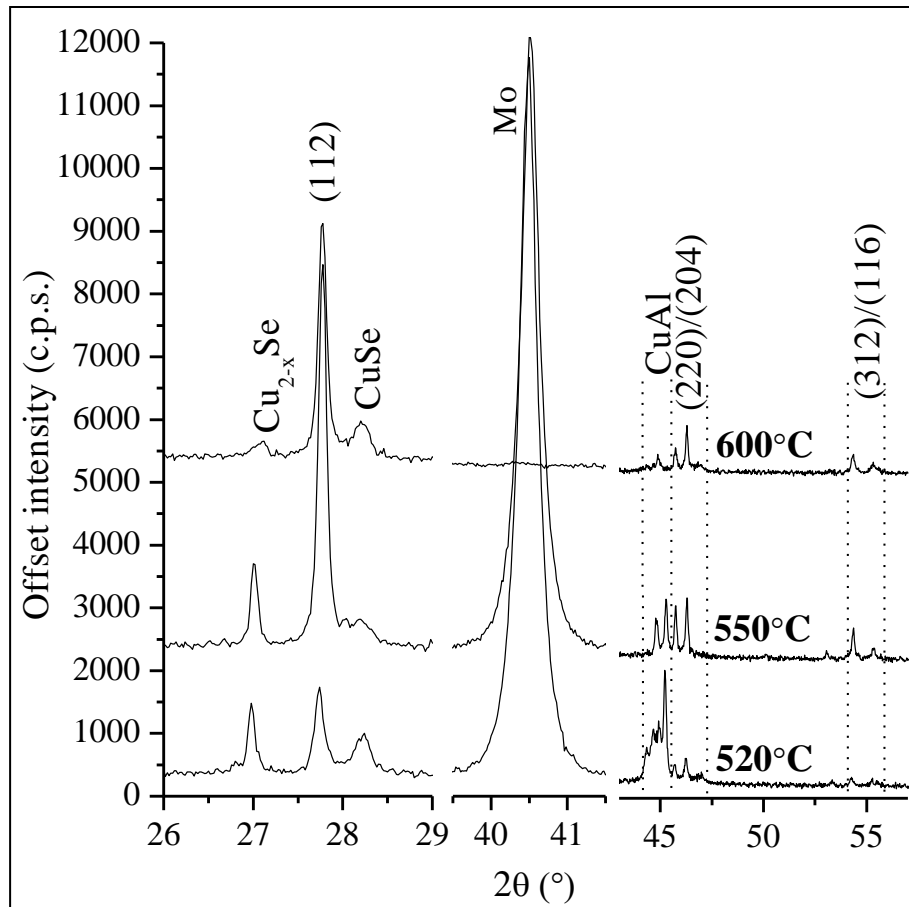
Figure 47: XRD patterns of three selenised Cu-Al precursors N205Q1 (elemental targets, 520°C, 800 mbar), N205R1 (elemental targets, 550°C, 600 mbar) and N236C1 (alloy target, 600°C, 800 mbar).
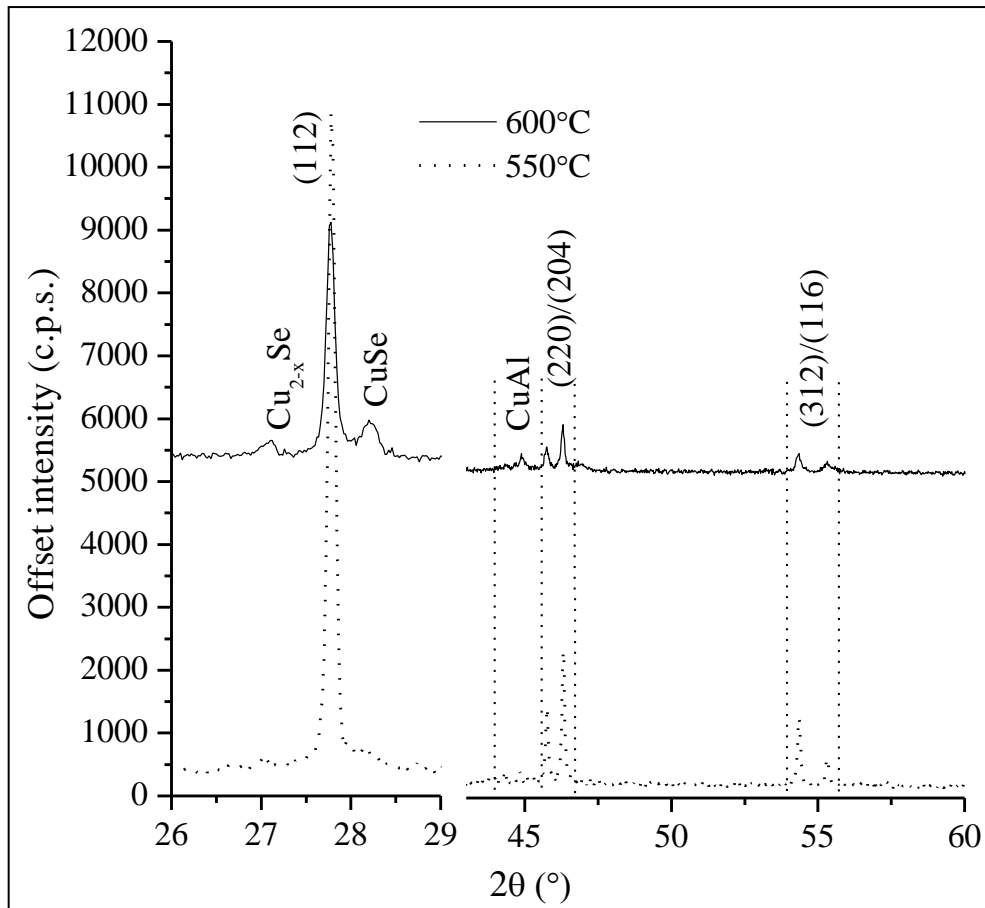
Figure 48: XRD patterns of N234C1 (550°C) and N236C1 (600°C). The Miller indices correspond to CuAlSe₂.

6.3.4.2 Discussion

The relatively strong copper selenide reflections in N236C1 (600°C) are surprising since N234C1, grown from the same alloy target, contains only traces. A metallic phase of CuAl is also detected, which suggests incomplete conversion. The reason for the lesser conversion of N236C1 could be a faster evaporation of Se at higher temperature. More Se would then escape the chamber before it could be captured by the precursor (see section 6.4.4). It was also noticed that N236C1 showed zones of evaporation at the film surface, which is coherent with the smaller intensity of all the reflections detected in this sample compared to the others. The comparison of the CAS peaks of N205Q1 (520°C) and N205R1 (550°C) indicates a better growth of CAS at 550°C (Figure 47). More of the CuAl phase has been consumed in N205R1

106

than in N205Q1, which explains the better growth of the chalcopyrite phase. The comparison between N236C1 (600°C) and N234C1 (550°C), shown in Figure 48, indicates that CAS is more abundant (larger peak areas) in N234C1. Therefore, among the three temperatures tested, 550°C is the most suitable. Finally, the soda lime glass substrate was slightly bent in N236C1. This bending can induce stresses in the film and makes it difficult to characterise by XRD since a good measurement requires the surface of the sample to be flat and level with the plane of reference of the system detector-source. SLG was seen in several other occasions to soften and bend when the process temperature was taken above 550-560°C. Therefore, temperatures of 530-540°C were more commonly used in the studies below.

6.3.5 Uniformity across the surface

Additional characterisation was performed on one of the absorbers showing a CAS phase in order to determine the composition of film surface features and study its luminescence. The uniformity of composition across the surface of a selenised sample containing the phase CAS was assessed by WDS (5 eV resolution), as it can resolve the Al K-transitions from the Se L-transitions ($\Delta E \approx 90$ eV). In Figure 49 **(a)** is shown an SEM micrograph of a sample containing CAS, as well as the WDS linescan performed twice on this sample. For the first series of points the electron beam was focused on surface features (Figure 49 **(b)**), while the second series focused on the bulk (Figure 49 (c)).
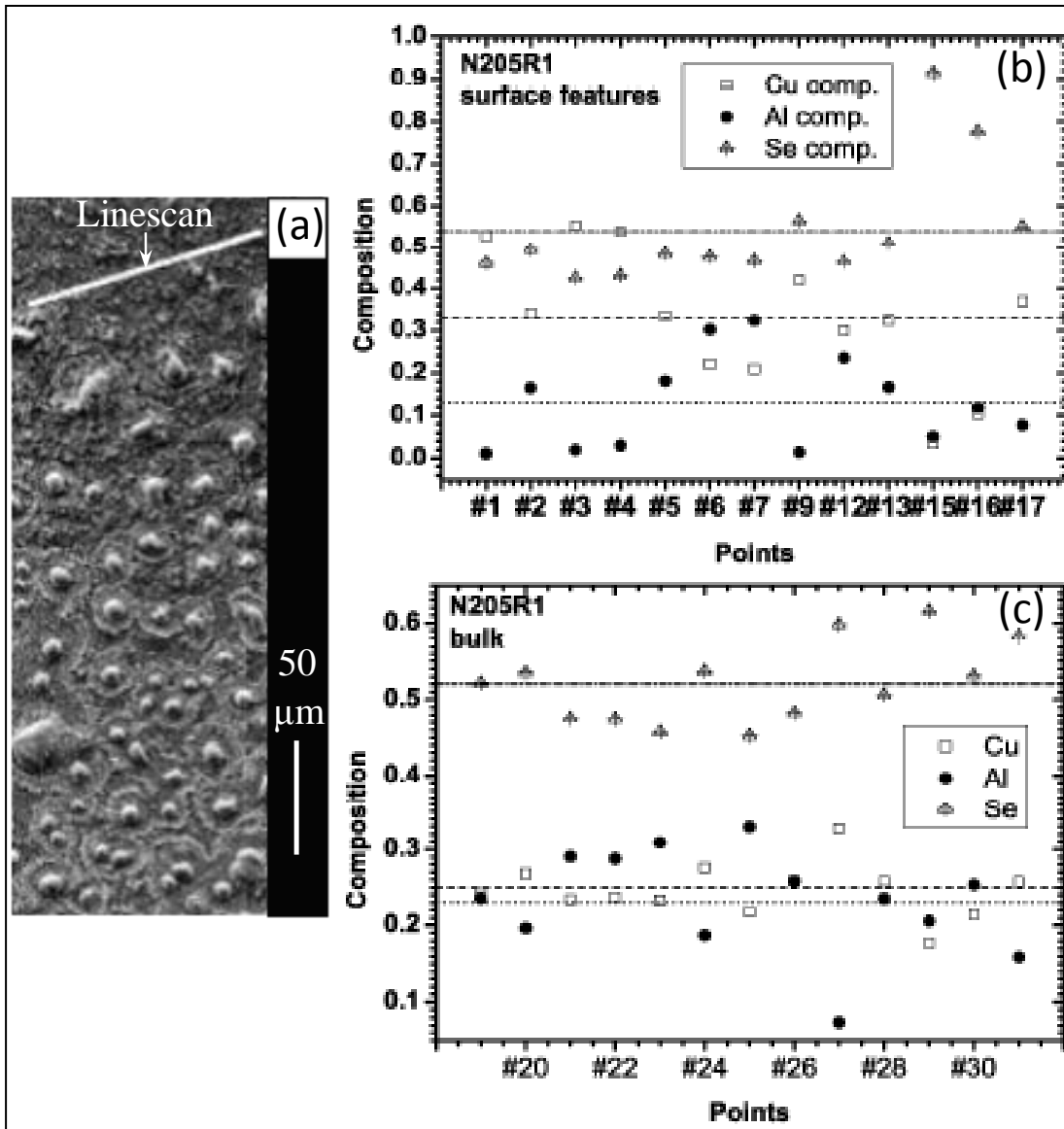
Figure 49: *(a)* **SEM micrograph of N205R1 (RTP, 550°C, 60 s dwell, unetched),** *(b)* **WDS composition of surface features and** *(c)* **bulk across a linescan. The horizontal lines in the WDS composition plots represent the composition in Cu (dashed), Al (dotted) and Se (dashed-dotted) averaged over the entire linescan.**

The compositions given must only be taken as a rough indication, since the beam also interacted with a shallow depth of film underneath the features. The surface linescan shows features of compositions consistent with CuSe and/or $Cu_{2-x}Se$ (e.g. points #1, #3 and #4), others with $CuAlSe_2$ (#6, #7, #12) and some made of almost pure Se (#15, #16). Se was not observed in the XRD pattern (Figure 44), and these features are therefore thought to be very localised.

The linescan of the bulk is consistent with $CuAlSe_2$ across the entire scan, except for point #27, where the composition corresponds to $CuSe_2$. $CuSe_2$ has also a very weak reflection in the XRD of this sample (not shown), but with only one occurrence in the linescan no correlation can be made.

This study therefore shows that most copper selenides are located at the surface and are local features, while the bulk is uniform and mainly CAS.

6.3.6 Cathodoluminescence

Cathodoluminescence was also performed (Figure 50) in order to determine the energies of the radiative transitions in the film. The spectrum at room temperature shows a dominating luminescence peak at 2.68 eV, which is in very good agreement with the band gap generally reported in the literature for single crystal CAS [121, 123], 2.67 eV.
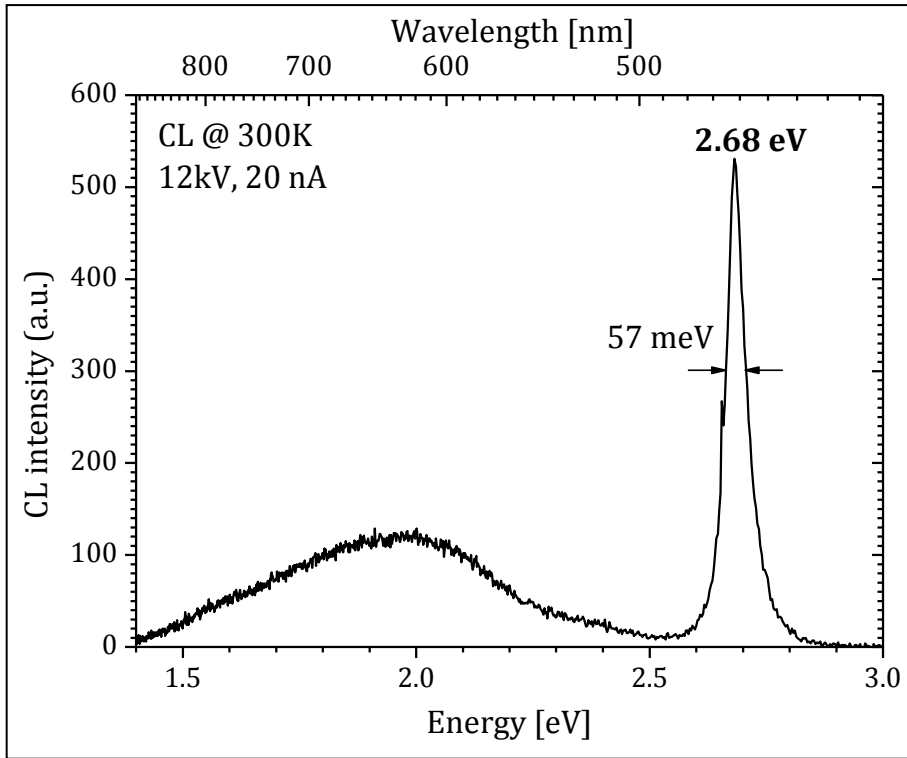
Figure 50: Room temperature cathodoluminescence spectrum of N205R1 (RTP, 550°C, 60 s dwell) [124].

6.4   CuInSe$_2$

As for CAS, the optimal growth parameters were assessed for CIS in the RTP. The as-deposited Cu-In metallic precursors, already studied in section 5.2, contained exclusively the binary phases CuIn$_2$ and Cu$_2$In, independently of the [Cu]/[In] ratio, and XRD could not detect any oxide. Selenisation of these precursors under different conditions is studied in this section.

6.4.1   Ramping rate/dwell time

6.4.1.1   Data

In Figure 51 are plotted the XRD patterns of four Cu-In precursors ([Cu]/[In]≈0.85) selenised at 530°C, for 60 s (N332C4), 300 s (N332C1), 450 s (N332R1) and 900 s (N332R4) dwelling periods.
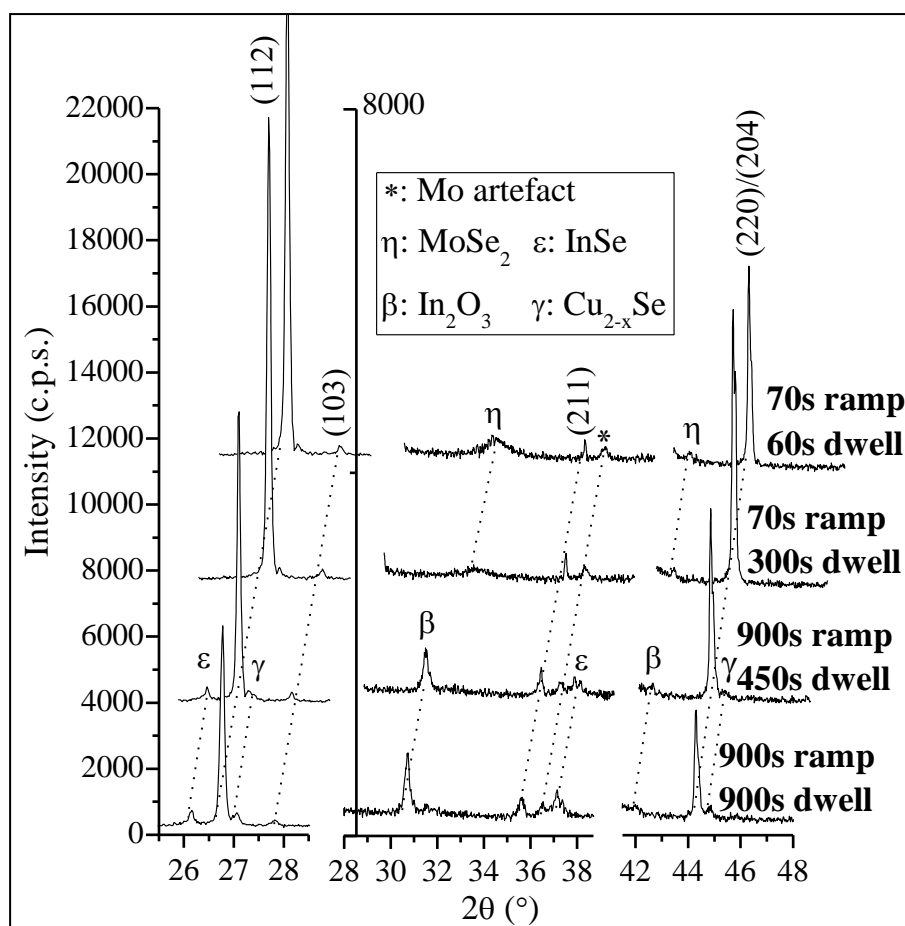
Figure 51: XRD patterns of four Cu-In precursors ([Cu]/[In]=0.96) selenised at 530°C in 100 mbar of H_2/N_2, N332C4 (70 s ramp, 60 s dwell); N332C1 (70 s ramp, 300 s dwell); N332R1 (900 s ramp, 450 s dwell); and N332R4 (900 s ramp, 900 s dwell). The symbol * designs an artefact associated with the molybdenum. The Miller indices correspond to $Cu_{0.938}InSe_2$.

N332C1 and N332C4 were selenised with a faster ramping rate ($\approx$8°C/s in average, or 70 s to reach 530°C) than N332R1 and N332R4 (0.6°C/s or 900 s). All four samples contain $Cu_{0.938}InSe_2$ (PDF 01-078-2001)[11], although the reflections are stronger for N332C1 and N332C4 than for N332R1 and N332R4. The two samples ramped up faster contain the phase $MoSe_2$ (PDF 01-072-1420), while the ones ramped up more slowly contain In_2O_3 (PDF 01-071-2195) and possibly traces of $MoSe_2$. Finally, N332R1 and N332R4 also contained InSe and $Cu_{2-x}Se$.

---

[11] This PDF is the best match for the position of the strongest reflections and the tetragonal distortion observed in the samples.

The crystallite sizes[12], calculated from the full-widths at half maximum (FWHM) of the (112) reflection using the Scherrer formula, were found to be 84 nm for N332C1 and N332C4, 79 nm for N332R1 and 74 nm for N332R4.

A shift of the CIS and Mo peaks was observed in N332C1 and N332C4, compared to the relevant PDF standards. The strain along the film depth was therefore calculated using the following formula [125]:

$$\varepsilon_z = \frac{d_s - d_0}{d_0} \qquad\qquad (6.2)$$

Strains measured on CIS were -0.007 (N332C1), -0.006 (N332C4), -0.003 (N332R4), and less than -0.001 (N332R1) and those calculated from the Mo shifts -0.003, -0.020, 0.000 and +0.002, respectively. The XRD setup used did not permit a tilting of the sample itself, so that the "$\sin^2\psi$ method" could not be applied to extract the stress parameters from the strain.

The texture coefficients C_{hkl} of the samples were assessed from the XRD patterns and the the formula used to calculate them is presented in APPENDIX 2. The standard deviation with respect to random orientation (in which case $C_{hkl}=1$), σ, was also calculated and is reported in the last column to the right. This figure of merit, also presented in APPENDIX 2, provides a single figure to estimate the degree of preferred orientation of the sample, $\sigma(C_{hkl})$. In theory, the maximum possible texture coefficient would be 9 in this example, and the maximal $\sigma\approx2.67$. In practice however, the formula used for the calculation of texture coefficients is only valid for moderate textures. For the four samples studied here, σ seems to increase with increasing dwell time, but this trend does not correlate with any simple trend in the

---

[12] The Scherrer formula used for the calculation only provides a lower limit for the crystallite size, because other factors (notably instrumental ones) can be responsible for an increase of the FWHM.

individual texture coefficients. All four samples show a slight texturing perpendicular to the crystal planes (103), (112) and (211). The faster ramp up (N332C4 and N332C1) led to a stronger preferred orientation perpendicularly to the (112) planes than the slower one (N332R1 and N332R4). However, C_{211} is also significantly smaller, leading to a lower σ for N332R1 and N332R4.

Table 6: Texture coefficients of N332C4 (70 s ramp, 60 s dwell), N332C1 (70 s ramp, 300 s dwell), N332R1 (900 s ramp, 450 s dwell) and N332R4 (900 s ramp, 900 s dwell), and their standard deviation.

	C_{101}	C_{112}	C_{103}	C_{211}	C_{204}	C_{312}	C_{008}	C_{400}	C_{316}	$\sigma(C_{hkl})$
N332C4	0.73	2.07	2.27	1.58	0.63	0.40	0.81	0.21	0.31	**0.73**
N332C1	0.67	1.90	2.19	1.99	0.82	0.46	0.50	0.22	0.26	**0.75**
N332R1	0.73	1.35	2.26	2.60	0.65	0.35	0.59	0.22	0.27	**0.83**
N332R4	0.56	1.42	2.29	2.87	0.56	0.28	0.55	0.22	0.25	**0.92**

6.4.1.2 Discussion

The presence of In_2O_3 in N332R1 and N332R4 is not due to oxidation during storage, since N332C1 and N332C4 were stored in the same dessicator in a N_2 atmosphere, and selenised at one day interval. Besides, the evolution of the XRD phases in a similar deposition batch was checked over a period of three weeks and showed no presence of In_2O_3. The longer ramping step is the most likely cause. At this stage of the discussion the data presented is insufficient to determine the modalities of this oxidation. A better understanding will come with additional data presented in section 6.4.3.

Effect of ramping rate

The presence of $Cu_{2-x}Se$ and InSe binaries in N332R1 and N332R4 indicate incomplete conversion of the films, in agreement with the lower abundance of CIS in those samples compared to N332C1 and N332C4. CIS is believed to form (from ≈370°C) in RTP processes, mainly via the reaction [109]:

113

$$Cu_2Se + 2InSe + Se \rightarrow 2CuInSe_2 \qquad\qquad (6.3)$$
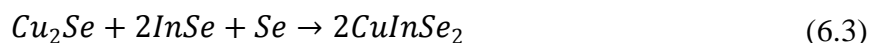
Two of the reactants of this reaction, InSe and $Cu_{2-x}Se$ (which forms during cooling down of Cu_2Se [126]), were present in N332R1 and N332R4, even after a long anneal (up to 900 s for N332R4). Therefore the absence of elemental Se must have blocked reaction 6.3. The stronger presence of $MoSe_2$ in N332C1 and N332C4, on the other hand, suggests that more Se is present throughout the films ramped faster. The fast ramp up therefore allowed the precursor to capture more Se (by formation of selenide compounds). A reasonable explanation is that slower ramping allows for better crystallization of either InSe or In_4Se_3 (from which InSe forms). Indeed, it is a known fact that the surface area of the reactants is an important factor in the kinetics of a reaction, and since formation of larger crystallites of In_4Se_3 or InSe make their effective surface area (i.e. number of sites) for interaction with Se smaller, their crystallization can be expected to slow down the incorporation of Se into the matrix of the film. This argument was also reported in [109] to impede the formation of CIS. Furthermore, the Se evaporated leaves the RTP graphite box after a few minutes only (see section 6.4.4). Therefore, the Se already incorporated into the film is slowly consumed to form InSe, and by the time this is done, no more elemental Se is available for the reaction of CIS formation described by reaction 6.3. The slightly higher crystallite size in N332C1 and N332C4 compared to N332R1 and N332R4 seems to indicate a somehow better crystallinity in the samples ramped-up faster. Finally, a compressive strain in the samples ramped up faster suggests more important stresses were present.

Effect of dwell time

Comparing only the patterns of the samples grown with the same ramping rate but a different dwell time (900 s for N332R1 and N332R4; 70 s for N332C1 and N332C4), the impact of dwell time seems low. This is not surprising in the case of N332C1 and N332C4, where the CIS growth is complete, but more so in N332R1 and N332R4, where unconverted material is still present as binary selenides after 900 s. However, this can be explained by the fact, mentioned in the previous paragraph, that Se evaporates away from the sample surface quickly. Indeed, additionally to reaction 6.3, another high temperature reaction ($\approx$430°C) can occur in this system [109]:

$$Cu_2Se + In_2Se_3 \rightarrow 2CuInSe_2 \qquad (6.4)$$

This reaction also requires Se to react with InSe and form In_2Se_3.

6.4.2 Selenium source

6.4.2.1 Data

Two routes were tested for providing the selenium necessary for converting a Cu-In metallic precursor ([Cu]/[In]$\approx$0.72) into the chalcopyrite compound (inset of Figure 52). In the first one, 5 μm of selenium were evaporated on a SLG substrate, which was cut into two equal pieces. These pieces were then placed symmetrically around the metallic precursor before starting the annealing process (N328P4, inset of Figure 52). The second method consisted in evaporating the 5 μm of selenium directly on top of the metallic precursor (N328P1, inset diagram of Figure 52).
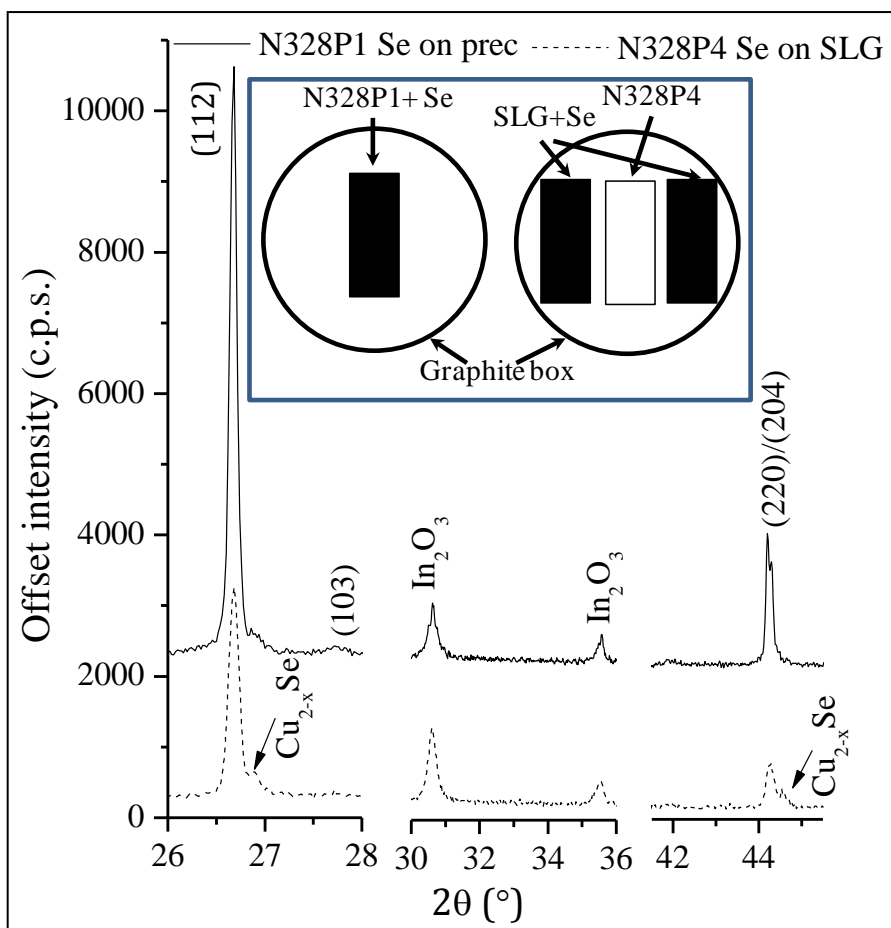
Figure 52: XRD patterns of two samples selenised together at 530°C with different selenisation routes (*inset*), N328P1 (Se on SLG) and N328P4 (Se on precursor).

N328P1 (Se on precursor) and N328P4 (Se on SLG) both contain In_2O_3. $Cu_{2-x}Se$ is also present in N328P4, and possibly as traces in N328P1 too. Finally, $Cu_{0.938}InSe_2$ reflections are visible in both, but less abundant in N328P4. The crystallite sizes calculated from the FWHM are 97 nm for N328P1 and 66 nm for N328P4. EDS data before and after selenisation is reported in Table 7. The selenisation seems to lead in both samples to a loss of Cu, more pronounced in N328P4. The composition ratio [Se]/[Cu] is also higher in N328P1 ($\approx$1.49) than N328P4 (1.15), but in both cases lower than the stoichiometry of $CuInSe_2$, i.e. [Se]/[Cu]=2. Note that [Se]/[Cu] was preferred to [Cu]/([Cu]+[In]) because Cu was the limiting reactant in these samples.

Table 7: EDS composition of N328P1 (Se on SLG) and N328P4 (Se on metallic precursor), in the metallic precursor and after selenisation.

Sample ID		Composition (at %)				
		Cu	In	Se	[Cu]/[In]	[Se]/[Cu]
N328P1	Precursor	42.0	58.0	0.0	0.72	0.00
	Absorber	25.5	36.5	38.0	0.70	1.49
N328P4	Precursor	42.0	58.0	0.0	0.72	0.00
	Absorber	27.5	41.0	31.5	0.67	1.15

6.4.2.2 Discussion

The more abundant $Cu_{2-x}Se$ (XRD), the lower intensity of the CIS peaks (XRD) and the smaller Se content (EDS) in N328P4 point towards incomplete conversion. A major difference between the two routes tested is the fact that, in the case where Se is deposited on top of the precursor (N328P1), the growth can start as soon as the temperature reaches Se melting point ($T_m=221°C$), whereas when the Se is on separate slides (N328P4), the chalcogenides can only start forming when some Se evaporates and passes near the sample. The relationship between saturated vapour pressure P^{sat} and the temperature T for the element Se is reported in [127] as follows:

$$\log(P^{sat}[mmHg]) \approx 8.054 - \frac{4949}{T[K]} \tag{6.5}$$

The pressure established in the chamber prior to deposition was 100 mbar (or 75 mmHg). Boiling of an element or compound occurs when its saturated vapour pressure equals the ambient pressure P^{amb}, so that equation 6.5 yields $T_b^{100\ mbar} \approx 527°C$. The glass slides used for providing the Se in N328P4 has no more Se after selenisation, indicating that the boiling point had indeed been reached. Hence, the selenisation of the precursor N328P4 must have started a little before 530°C, while the selenisation of N328P1 started around 220°C. Furthermore, only a portion of the Se vapours emitted in N328P4 could have passed near the precursor surface, before

escaping the susceptor. The delayed CIS growth in N328P4 therefore explains the poor crystallinity.

The presence of In_2O_3 is again discussed in section 6.4.3. The decrease in Cu content between as-deposited precursor and selenised sample (especially in N328P4) has found no satisfactory explanation.

6.4.3 Effect of temperature

Four different dwelling temperatures for the selenisation process were tested on four pieces of the same sample. The dwell time at temperature was 1400 s, the pressure established before selenisation 10 mbar of H_2/N_2. Note that for the experiments below, the RTP process was controlled by the power applied to the heating lamps rather than by the temperature, as was the case for the previous samples presented. This change was motivated by punctual issues encountered with the temperature-controlled processes. In the temperature-controlled processes, a thermocouple inserted into the base of the graphite susceptor monitored the temperature. Although the reproducibility between runs was shown to be good for most annealing processes, very punctual variations were sometimes observed. They were attributed to the thermocouple which sometimes came to be partially dislodged from its hole in the susceptor, leading to a change in the temperature measured. The power applied was therefore used as the governing parameter for the process.

6.4.3.1 Data

X-ray diffraction

The XRD patterns are reported in Figure 53.
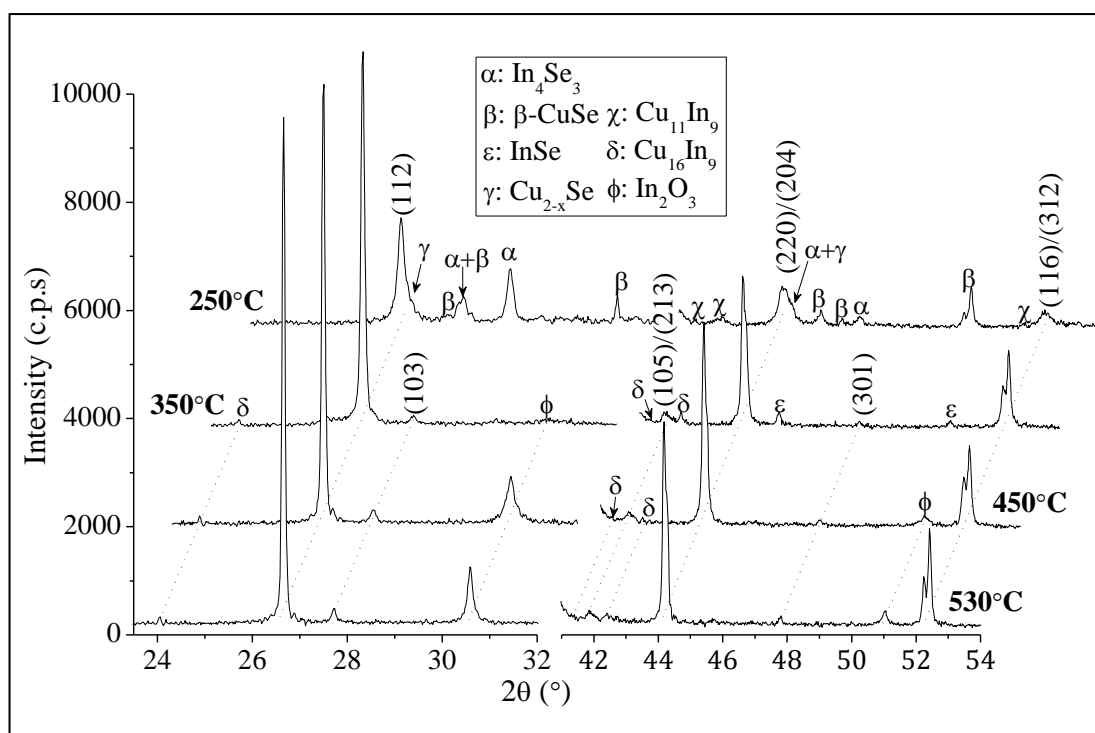
Figure 53: XRD patterns of four pieces of N622C ([Cu]/[In]=0.92), N622C1 (530°C), N622C2 (450°C), N622C3 (350°C) and N622C4 (250°C). The Miller indices correspond to Cu$_{0.938}$InSe$_2$.

The sample selenised at 250°C (N622C4) contains the phases Cu$_{0.938}$InSe$_2$ (PDF 01-078-2001), In$_4$Se$_3$ (PDF 01-083-0039), β-CuSe (PDF 00-027-0184) and traces of Cu$_{11}$In$_9$ (PDF 00-041-0883). Deconvolution of the CIS peaks suggests the presence of an overlapping phase, best matched with Cu$_{1.8}$Se [128].

At 350°C (N622C3), the intensity of the Cu$_{0.938}$InSe$_2$ reflections increases and the FWHM decreases. InSe (PDF 01-073-0609), traces of Cu$_{16}$In$_9$ (PDF 00-026-0523) and low crystallinity In$_2$O$_3$ (PDF 00-006-0416) are also present.

At 450°C (N622C2), the intensity of the CIS peaks increases further. Higher crystallinity In$_2$O$_3$ and traces of Cu$_{16}$In$_9$ (small amount) are also found.

The same phases are present at 530°C (N622C1), with however a modifid Cu$_{16}$In$_9$ phase (PDF 00-026-0522). The crystallinity of the CIS grows steadily with increasing temperature, with crystallite sizes of 48 nm at 250°C, 85 nm at 350°C,

119

105 nm at 450°C and 115 nm at 540°C. The (112) peak area is multiplied by two between 250°C and 350°C, and then stays stable.

Energy dispersive spectroscopy

EDS was performed on the four samples (Table 8).

Table 8: EDS compositions after selenisation of N622C4 (250°C), N622C3 (350°C), N622C2 (450°C), and N622C1 (530°C).

Sample ID	EDS composition (at %)					Cu/In	Se/(Cu+In)
	Cu	In	Se	Mo	O		
N622C4 (250°C)	32.7	13.9	47.2	0.4	5.7	2.36	1.01
N622C3 (350°C)	19.7	20.4	35.9	0.1	24.0	0.97	0.90
N622C2 (450°C)	12.4	19.4	18.4	0.3	49.6	0.64	0.58
N622C1 (530°C)	13.4	19.7	21.8	0.1	45.0	0.68	0.66

The O content increases greatly from 250°C ($\approx$6 at%) to 450°C ($\approx$50 at%), and then decreases slightly at 530°C (45 at%). [Cu]/[In] and [Se]/([Cu]+[In]), on the contrary, decrease from 250°C (1.01) to 450°C (0.58) and increase slightly again at 530°C (0.66). [Cu]/[In] goes from 2.36 at 250°C (i.e. well above the as-deposited ratio of 0.92) to 0.64 at 450°C, and then increases slightly again at 530°C. The Se content is below stoichiometry at 450°C and 530°C. However, non uniform depth distribution could also explain this observation.

6.4.3.2 Discussion

The stoichiometry of $Cu_{0.938}InSe_2$ ties in with the ratio [Cu]/[In]=0.92 of the metallic precursor selenised. The presence of CIS at temperatures as low as 250°C (N622C4) is explained in [109] by the low temperature reaction:

$$CuSe + InSe \rightarrow CuInSe_2 \tag{6.6}$$

This reaction starts at the melting temperature of selenium, 221°C (at 1 bar), and is relatively slow, which explains the incomplete consumption of $Cu_{11}In_9$, In_4Se_3, β-

CuSe and $Cu_{2-x}Se$, in spite of the long dwell (1400 s). At 250°C, many copper selenide phases are present (XRD) and the oxygen content is low (≈ 5.7 at% in EDS). The [Cu]/[In] ratio also suggests a non uniform distribution of Cu and In, with more Cu present at the surface. At 350°C (N622C3), the kinetics of CIS growth increase, and the phase becomes more crystalline, as emphasised by the dissociation of the (116)/(312) doublet. The change of stoichiometry from In_4Se_3 in N622C4 to InSe in N622C3 seems due to a higher presence of Se in the bulk. The disappearance of copper selenides is accompanied with a decrease of [Cu]/[In], which is very close to the value in the as-deposited precursor. The O content also shoots up, associated with the low crystallinity In_2O_3 (XRD). At 450°C (N622C4), all the InSe has been consumed to form CIS, and In_2O_3 keeps growing. No substantial difference is observed at 530°C except for a further improvement of crystallinity. The fact that the CIS peak area increases between 250°C and 350°C, and forms a plateau between 350°C and 530°C indicates that most of the CIS forms at 350°C. The traces of $Cu_{16}In_9$ remaining after the process, even at temperatures as high as 530°C, are most likely due to lack of Se (EDS), possibly near the back since no $MoSe_2$ is detected using XRD.

In_2O_3 formation

Regarding the formation process of In_2O_3, the fact that it only appears in the samples selenised above 450°C (N622C2) gives an important clue as to the modalities of this oxidation, and ties in with the results of sections 6.4.1 and 6.4.2. Indeed, the pressure established before selenisation is this time 10 mbar. Using equation 6.5, the expected boiling point of Se at this pressure is found to be ≈ 416°C. This means that for dwelling temperatures higher than 416°C, the Se will evaporate quickly and leave the sample surface. Figure 53, on the other hand, shows that between 350°C and

121

450°C, a phenomenon occurs that causes oxidation of In. Connecting these two observation, it seems plausible that, because of the Se deficiency resulting from Se evaporation, the In atoms are no longer bound to Se and are therefore free to bond with O to form In_2O_3. In section 6.4.1, the faster ramping rate of N332C1 and N332C4 led to a better capture of Se, so that the formation of In_2O_3 was not favoured. N328P1 and N328P4 (section 6.4.2) contained such an excess of In that, even after all the copper selenides had been consumed to form CIS, some In still remained. By then, the atmosphere around the sample was Se deficient and In_2O_3 could form. Indeed, even though the standard heat (or enthalpy) of formation of In_2O_3 is $\Delta H_f \approx$ -922 kJ.mol^{-1} [129], against $\Delta H_f \approx$ -65 kJ.mol^{-1} for InSe [130], the concentration of the species must be taken into account. The effective heat of formation model (EHF) states that the relevant parameter to predict formation reactions is the effective heat of formation $\Delta H'$, defined as [130]:

$$\Delta H' = \Delta H \times \frac{Effective\ concentration\ of\ limiting\ element}{Compound\ concentration\ of\ limiting\ element} \tag{6.7}$$

with ΔH the standard heat of formation (i.e. with unlimited source of reactant). Equation 6.7 shows that if O is present in much lower concentration than Se, $\Delta H_{In_2O_3} < \Delta H_{InSe}$, but if Se becomes deficient, the situation is reversed.

Origin of the oxygen

Four potential sources of oxygen can be suggested to account for the formation of this oxide:

(a) Impurity in the H_2/N_2 gas injected before the process.

(b) Oxygen remaining in the chamber after pumping.

(c) Oxygen from the soda lime glass substrate.

(d) Oxygen trapped or released by the cooling system of the RTP.

Supporting hypothesis **(a)** is a the study led by Marsillac *et al.* [120]. The authors applied a constant flow of Ar during the selenisation of $CuInAlSe_2$ and reported an increasing oxidation of the samples with increasing gas flow, which were attributed to the trace amounts of oxygen in the Ar bottle. The impurities in the H_2/N_2 gas used for this work included O_2 (5 ppm), CO_2 (3 ppm), CO (1 ppm) and H_2O (5 ppm), while the Ar bottle used for some other experiments contained O_2 (4ppm). However, the gas was not the same as in [120], but instead, a pressure (10 mbar here) was established beforehand. Therefore, less oxygen would be fed to the sample in our setup. Hypothesis **(b)** could also explain the oxidation, since the vacuum established in the chamber before injecting H_2/N_2 was typically 1.10^{-3} mbar. Besides, elements present in the chamber could be outgasing. It must be pointed out that similar experiments carried out in a tube furnace (section 7.5) did not lead to the formation of In_2O_3. Nevertheless, many differences exist between the RTP and the tube furnace (chamber size, pumping time, etc), which make a strict comparison difficult. Hypothesis **(c)** is partly invalidated by the argument of the absence of In_2O_3 in the tube furnace. The cooling (hypothesis **(d)**) could also be the cause:

(i) When the chamber is opened, the water present in the air could condense onto the cooled metal pieces surrounding the lamps.

(ii) A small leak of water from the cooling system into the chamber could be taking place.

Hypotheses **(b)** and **(d)** seem the most likely explanations.

6.4.4 Effect of pressure on Se incorporation

An extra series of experiments was motivated by the results above on the effect of temperature and pressure on the incorporation of selenium.

6.4.4.1 Data

N687R and N687S were deposited together from an alloy target ([Cu]/[In]=0.92) and selenised in the RTP in H_2/N_2 at 530°C for 500 s. Prior to this the RTP reactor was thermally cleaned at 550°C under constant pumping for 240 min. The ramp up stage lasted 600 s and the dwelling stage 500 s in both cases. The pressure established prior selenisation was 10 mbar for N687R and 800 mbar for N687S. Photographs of the samples after selenisation are shown in Figure 54. The surface of N687R is a very dark brown/black taint, while N687S is a brighter grey. N687S shows traces of evaporation locally on the film. The precursors coated with Se were weighed before and after selenisation on the high precision balance. Additionally, each sample was weighed along with the susceptor in the RTP, before and after selenisation.

The mass variations observed are summarized in Table 9. The error was assessed from the amplitude of oscillation of the readout on the balance. The error proved to vary mainly with the magnitude of the mass measured.
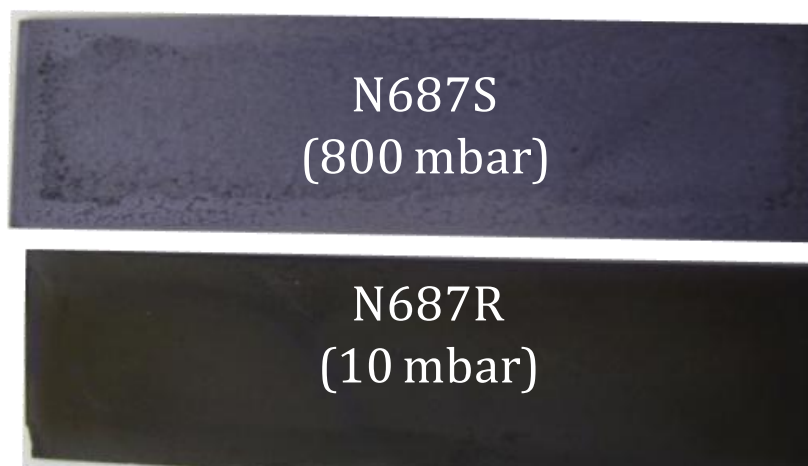
Figure 54: Photographs of N687R (10 mbar) and N687S (800 mbar) after selenisation.

Table 9: Masses and mass variations measured on N687R (10 mbar) and N687S (800 mbar), and for the sets sample + susceptor.

	Mass (g)	Error (g)	Δm (g)	Error (g)
N687R+3μm Se	5.16789	3.E-05	0.01535	4.E-05
N687R+ after selenisation	5.15254	3.E-05		
N687R+3μm Se+susceptor	77.0281	2.E-04	0.0154	3.E-04
N687R+susceptor after selenisation	77.0127	2.E-04		
N687S+3μm Se	5.10778	3.E-05	0.01121	4.E-05
N687S+ after selenisation	5.09657	3.E-05		
N687S+3μm Se+susceptor	76.9685	2.E-04	0.0120	3.E-04
N687S+susceptor after selenisation	76.9565	2.E-04		

The weight losses from the samples are in good agreement with those of the sets "sample + graphite susceptor", with however a more important difference for N687S between the sample loss and the susceptor loss. It was besides noticed that Se deposits formed around the susceptor in the annealing chamber (Figure 55). EDS measurements were also performed on the selenised samples and compared (Table 10). The ratios [Se]/([Cu]+[In]) after selenisation are 0.72 for N687R and 0.96 in N687S. A higher presence of oxygen is also noted in N687R.
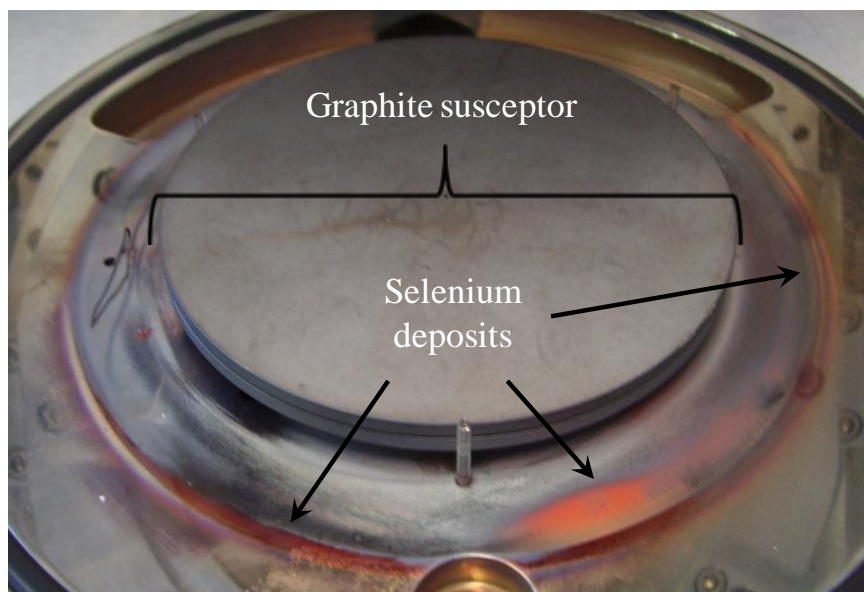
Figure 55: Photograph of the RTP deposition chamber after selenisation.

Table 10: EDS composition of the absorbers N687R (10 mbar) and N687S (800 mbar).

The most important changes are in bold.

Sample ID	EDS composition (at %)					Cu/In	Se/(Cu+In)
	Cu	In	Se	Mo	**O**		
N687R	15.8	21.8	27.1	0.3	**35.1**	0.73	**0.72**
N687S	23.9	25.0	46.7	1.1	**3.4**	0.95	**0.96**

Finally, the XRD patterns of the selenised samples were also recorded (Figure 56), and show the phases $Cu_{0.938}InSe_2$ (PDF 01-078-2001) and In_2O_3 (PDF 01-071-2195) in the lower pressure sample (N687R), while the higher pressure one (N687S) contains $Cu_{0.938}InSe_2$ and $MoSe_2$ (PDF 01-072-1420).
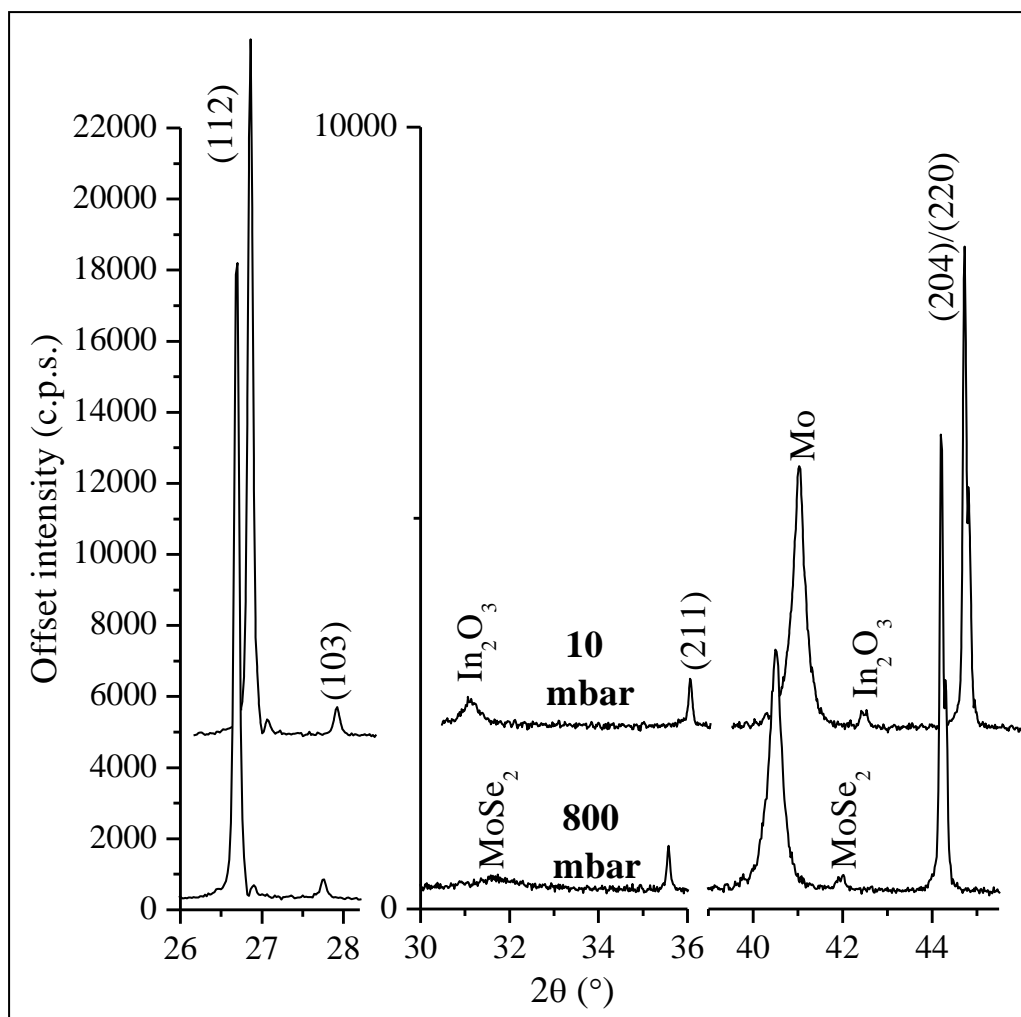
Figure 56: XRD patterns of N687R (10 mbar) and N687S (800 mbar).

6.4.4.2 Discussion

Table 9 and Table 10 indicate that the weight losses resulting from the annealing are at least in part Se losses. They are mainly losses of the sample rather than the susceptor. Practically all (within the error of the measurement) that is lost by the sample leaves the susceptor as well. N687S (800 mbar) shows a lower weight loss than N687R (10 mbar), which indicates a better capture and incorporation of the Se into the film. However, the weight loss of the system "N687S+susceptor" exceeds that of the sample alone by $\approx 8.10^{-4}$g, which is higher than the estimated error of the measurement, 3.10^{-4}g. It is possible that a small residual amount of selenium was already present on the inside walls of the susceptor before selenisation, and was

127

removed by the process. Indeed, N687S was selenised after N687R, without performing an extra thermal cleaning in between runs. The EDS data (Table 10) clearly shows that more Se was retained by the sample selenised under higher pressure, which ties up with the weight loss and confirms Se as the material being lost. EDS data also shows that much more oxygen is present in the lower pressure sample (N687R) than in the higher pressure one (N687S). XRD data shows that this higher presence of oxygen in N687R is mainly due to formation of In_2O_3, while the higher presence of Se in N687S results from a deeper diffusion of Se, visible by the formation of $MoSe_2$. This is in agreement with the results reported earlier in sections 6.4.1, 6.4.2 and 6.4.3 regarding the inverse correlation between Se incorporation and oxide formation. The higher pressure therefore yielded a better incorporation of the Se and a lower formation of oxides. The visual aspect of N687S however suggests a slight evaporation of the sample, possibly due to the high pressure. A suggested reason for the beneficial effect of high pressure is that it prevents the boiling point of Se from being reached, whereas a low pressure allows evaporation and favours oxidation. Another possibility is that by establishing a pressure close to atmospheric, possible air leakage into the chamber was limited.

CHAPTER 7   ANNEALING AND SELENISATION OF CuIn$_{1-x}$Al$_x$Se$_2$ PRECURSORS

7.1   Experimental

SLG microscope slide substrates coated with ≈850 nm of Mo and Cu-In, Cu-In-Al and Cu-In-Al with a copper cap (Cu-In-Al/Cu), were cut into five smaller pieces, four of which sized approximately 1.0 cm along the length of the slide by 2.6 cm along the width (inset diagram Figure 57).
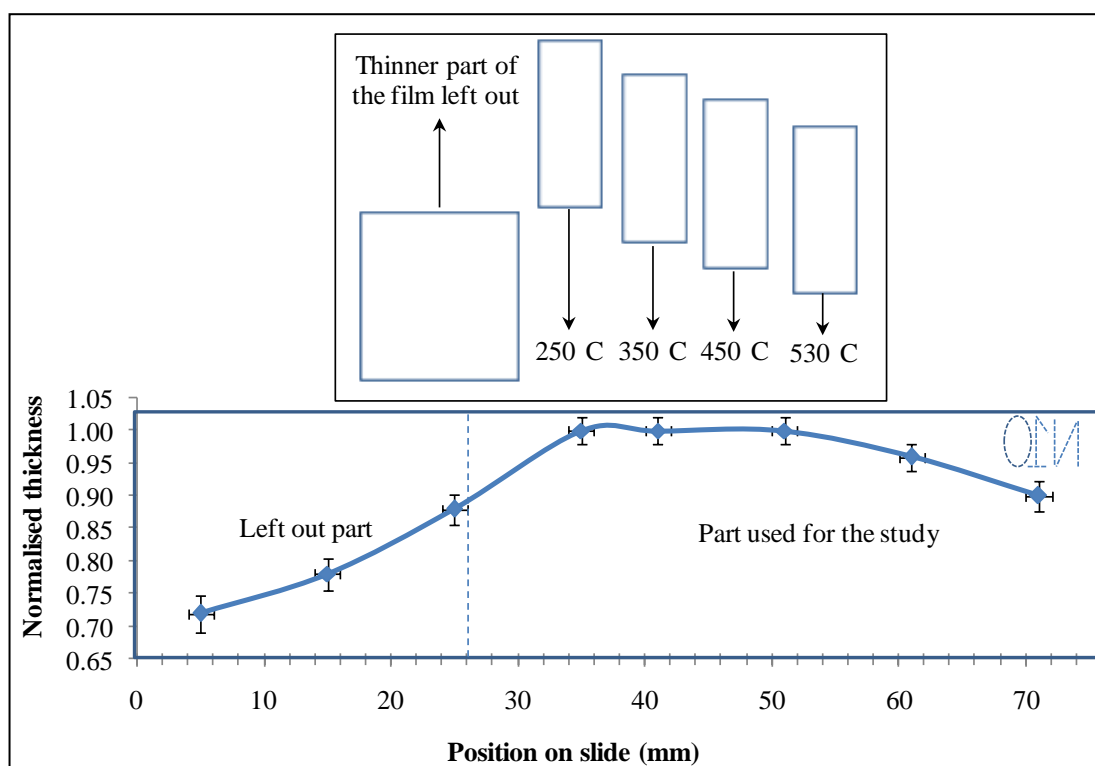
Figure 57: Thickness variation across a 26 mm by 76 mm slide, deposited in the Nordiko 2000. The inset diagram summarizes how the different pieces are processed. *Data for the plot was provided by Dr Zoppi.*

The remaining bigger piece (≈2.6 cm by 2.6 cm) of each slide was left out because thickness measurements showed that the thickness deposited in the Nordiko 2000 can vary by up to 30% across the entire length of the slide, most of this variation occurring near the edge of the slide that was left out (Figure 57). One piece of each

of the three types of precursors was loaded into the RTP and the three pieces were subsequently annealed together, without selenium, in one single ramp at a ramping rate of 0.8-0.9°C/s to maximum temperature followed by a 20 minutes dwell and a 1800 s cooling stage. 10 mbar of H_2/N_2 were established in the chamber before starting the process. Four processes with similar ramping rates but different maximum temperatures (250°C, 350°C, 450°C and 530°C) were tested.

Finally, the depth profile distribution of the different elements in the samples was studied by secondary ion mass spectroscopy (SIMS). For the precursor annealing study (section 7.3), Ar was used for the ion beam, and the same beam parameters were applied for extracting positive (Cu, In, Al, Mo) and negative (O, AlO) ions. For the selenisation study, an O ion beam was used for analysing positive ions, Ar for negative ions, and the sputtering rates were therefore different. Therefore a normalisation of the x-axis was necessary to plot together and compare positive and negative ions. This is equivalent to normalising the depth of the film, in the assumption of a constant ratio between the sputtering rate of the oxygen ion beam and the sputtering rate of the argon ion beam. Since the Mo signal was not very sharp, however, a slight error in the normalised axis must be considered. For the precursor annealing study (section 7.3.1), an Ar beam of 400 nA current and 4 keV energy was used to sputter the sample and create the ions. The crater formed was 500 nm by 500 nm, and the gate area was 10% of the crater size.

The aims of this study were:

(a) To minimize the possible variations in process between Cu-In and Cu-In-Al samples (by annealing them together).

(b) To determine the sequence of metallic compounds formation with increasing temperature.

(c) To compare these metallic compounds with the phases formed in presence of selenium.

(c) could for instance help to locate metallic phases (without Se) corresponding to unconverted (but annealed) precursor in the selenised samples. Indeed, if part of a selenised sample has not incorporated any Se, it might still have undergone certain changes due to the annealing, that should be similar to the precursor annealed at the same temperature.

The fabrication data for the samples of this chapter is summarised in Table 11 (section 7.2).

7.2 Fabrication data on the samples of the chapter

Table 11: Sample deposition and processing data for chapter 7. In the "layout" column, the layers are indicated by order of deposition. Compositions in italics are calculated from bulk compositions.

Page	ID	Substrate	Target	Layout	Comp. (at%) Cu	In	Al	Se?	Fur-nace	P^{re} (mbar)	Gas	Dwell T^{re} (°C)	Dwell dur. (s)	Ramp dur. (s)
134-137,139-141	N623E5	SLG/Mo	alloy	Cu-In	48.0	52.0	0.0	Yes	RTP	10	H_2/N_2	250	1400	300
135-137	N623E4	SLG/Mo	alloy	Cu-In	48.0	52.0	0.0	Yes	RTP	10	H_2/N_2	350	1400	400
135-137	N623E3	SLG/Mo	alloy	Cu-In	48.0	52.0	0.0	Yes	RTP	10	H_2/N_2	450	1400	630
135-137,144,147	N623E2	SLG/Mo	alloy	Cu-In	48.0	52.0	0.0	Yes	RTP	10	H_2/N_2	530	1400	750
139-143,147,152,155	N591K5	SLG/Mo	elem.	Cu-In-Al	47.0	36.0	17.0	No	RTP	10	H_2/N_2	250	1400	300
140-143	N591K4	SLG/Mo	elem.	Cu-In-Al	47.0	36.0	17.0	No	RTP	10	H_2/N_2	350	1400	400
141-143	N591K3	SLG/Mo	elem.	Cu-In-Al	47.0	36.0	17.0	No	RTP	10	H_2/N_2	450	1400	630
141-144,147-148	N591K2	SLG/Mo	elem.	Cu-In-Al	47.0	36.0	17.0	No	RTP	10	H_2/N_2	530	1400	750
146-148	N548L5	SLG/Mo	elem.	Cu-In-Al/Cu	*50.0*	*34.0*	*16.0*	No	RTP	10	H_2/N_2	250	1400	300
146-147	N548L4	SLG/Mo	elem.	Cu-In-Al/Cu	*50.0*	*34.0*	*16.0*	No	RTP	10	H_2/N_2	350	1400	400
146-148	N548L3	SLG/Mo	elem.	Cu-In-Al/Cu	*50.0*	*34.0*	*16.0*	No	RTP	10	H_2/N_2	450	1400	630
146-148	N548L2	SLG/Mo	elem.	Cu-In-Al/Cu	*50.0*	*34.0*	*16.0*	No	RTP	10	H_2/N_2	530	1400	750
149-157	N591R4	SLG/Mo	elem.	Cu-In-Al	47.0	36.0	17.0	Yes	RTP	10	H_2/N_2	250	1400	300
149-150,152-154,156	N591R3	SLG/Mo	elem.	Cu-In-Al	47.0	36.0	17.0	Yes	RTP	10	H_2/N_2	350	1400	400
149-150,152-153,156,162	N591R2	SLG/Mo	elem.	Cu-In-Al	47.0	36.0	17.0	Yes	RTP	10	H_2/N_2	450	1400	630

Page	ID	Substrate	Target	Layout	Comp. (at%)			Se?	Fur-nace	P^{re} (mbar)	Gas	Dwell T^{re} (°C)	Dwell dur. (s)	Ramp dur. (s)
					Cu	In	Al							
149-150,152-153,162-163	N591R1	SLG/Mo	elem.	Cu-In-Al	47.0	36.0	17.0	Yes	RTP	10	H_2/N_2	530	1400	750
157-161,166,169-170	N582L4	SLG/Mo	elem.	Cu-In-Al/Cu	50.0	34.0	16.0	Yes	RTP	10	H_2/N_2	250	1400	300
157-161,166	N582L3	SLG/Mo	elem.	Cu-In-Al/Cu	50.0	34.0	16.0	Yes	RTP	10	H_2/N_2	350	1400	400
157-162,166	N582L2	SLG/Mo	elem.	Cu-In-Al/Cu	50.0	34.0	16.0	Yes	RTP	10	H_2/N_2	450	1400	630
157-161,166,172	N582L1	SLG/Mo	elem.	Cu-In-Al/Cu	50.0	34.0	16.0	Yes	RTP	10	H_2/N_2	530	1400	750
165-171	N582O	SLG/Mo	elem.	Cu-In-Al/Cu	52.5	32.5	15.0	Yes	TF	6	Ar	130-250	1800	≈800
165-168,171	N582Q	SLG/Mo	elem.	Cu-In-Al/Cu	52.5	32.5	15.0	Yes	TF	6	Ar	130-250-350	1800	≈1200
165-168,171	N582K	SLG/Mo	elem.	Cu-In-Al/Cu	52.5	32.5	15.0	Yes	TF	6	Ar	130-250-450	1800	≈1500
166-168,171-173,200-202	N535W	SLG/Mo	elem.	Cu-In-Al/Cu	52.5	32.5	15.0	Yes	TF	6	Ar	130-250-530	1800	≈1800
								No	PSA	10	Ar	573	3600	≈1900
172-173	N591W	SLG/Mo	elem.	Cu-In-Al	46.0	48.0	6.0	Yes	TF	10	H_2/N_2	530	1800	≈1800
172-173	N587H	SLG/Mo	elem.	Cu-In-Al	48.0	38.0	14.0	Yes	TF	10	H_2/N_2	530	1800	≈1800
172-175	N394B4	SLG/Mo	elem.	Cu-In-Al	49.0	31.5	19.5	Yes	TF	10	H_2/N_2	530	1800	≈1800
172-173,190-192,194	N783D1	SLG/Mo	elem.	Cu-In-Al	48.0	25.0	27.0	Yes	TF	10	Ar	540	1800	≈1800
174-176	N394C1	SLG/Mo	elem.	Cu-In-Al	49.0	31.5	19.5	Yes	TF	10	H_2/N_2	530	1800	≈1800

7.3 Precursor annealing study (RTP): effect of temperature

7.3.1 Cu-In precursor annealing

The effect of the annealing temperature was first studied on a Cu-In metallic precursor deposited from the alloy target ([Cu]/[In]=0.92). Since only Cu and In are initially present in this precursor, the XRD identification is unambiguous. These patterns were later used as a support to identify the phases in Al-containing samples (sections 7.3.2 and 7.3.3). For SIMS analyses, an Ar ion beam was used to extract both positive (i.e. ionised Cu, In, Al and Mo) and negative (O, Se) ions from the sample.

7.3.1.1 Data

X-ray diffraction

Figure 58 shows the evolution with temperature of the XRD phases in the Cu-In precursor. The as-deposited precursor N623E6 was analysed in section 5.2, and contained only the crystalline phases Cu_2In and $CuIn_2$. N623E5 (250°C) is made of $Cu_{11}In_9$ (PDF 00-041-0883), Cu_2In (PDF 00-042-1475), In in abundance (PDF 00-005-0642) and traces of In_2O_3 (PDF 00-006-0416). The In phase possesses a very strong texture perpendicular to the (002) plane, an attenuated (110) reflection and an extinguished (101) reflection, with C_{002}=2.42, C_{110}=0.54 and C_{101}=0.05, respectively (maximum of three for a single crystal[13]). This texture is in fact too high to be adequately measured in the θ-2θ setup, designed for powder diffraction.

---

[13] Only three In peaks exist in the range of 2θ angles measured.
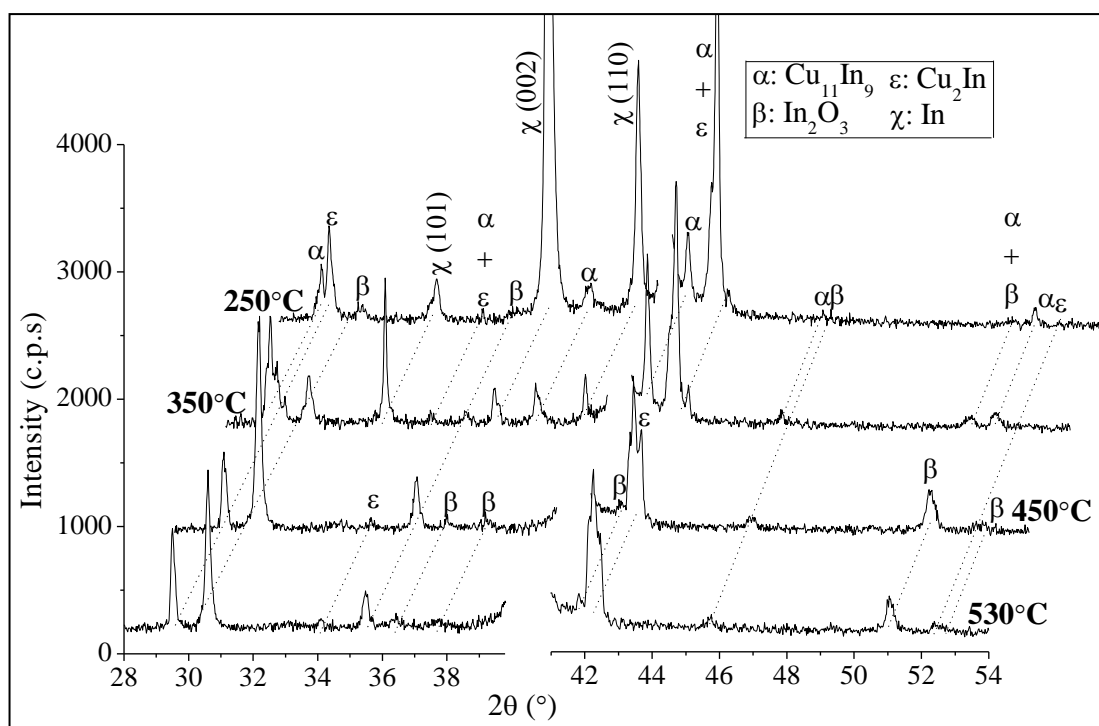
Figure 58: XRD patterns of four pieces of N623E ([Cu]/[In]=0.92, from alloy target) annealed without Se, N623E5 (250°C), N623E4 (350°C), N623E3 (450°C) and N623E2 (530°C).

N623E4 (350°C) contains the same phases as N623E6, but In_2O_3 has larger crystallites (40 nm against 27 nm) and the phase more abundant (peak area four times larger), while the $Cu_{11}In_9$ phase grows and the Cu_2In phase decreases. The indium phase, finally, is much less textured than in N623E5 (C_{101}=0.75, C_{002}=1.32, C_{110}=0.93). N623E3 (450°C) contains more In_2O_3 than at lower temperatures and $Cu_{11}In_9$ has disappeared, while Cu_2In endures and becomes more crystalline. N623E2 (530°C) contains the same phases as N623E3, with slightly less In and In_2O_3 and an increased Mo reflection intensity (not shown), indicating an overall loss of material.

Energy dispersive spectroscopy and scanning electron microscopy

In Table 12 are reported the EDS compositions of the four samples.

Table 12: EDS compositions of N623E5 (250°C), N623E4 (350°C), N623E3 (450°C) and N623E2 (530°C).

Sample ID	EDS composition (at %)				Cu/In	O/(Cu+In)
	Cu	In	Mo	O		
N623E5 (250°C)	35.0	40.3	7.0	17.7	0.87	0.22
N623E4 (350°C)	28.8	34.7	5.0	31.5	0.83	0.46
N623E3 (450°C)	15.7	25.8	2.0	56.5	0.61	1.30
N623E2 (530°C)	18.7	24.7	3.6	53.0	0.76	1.13

The oxygen content of the film, measured by the figure of merit [O]/([Cu]+[In]), increases with increasing temperature between 250°C and 450°C (0.22 to 1.30), and then decreases slightly between 450°C and 530°C (1.30 to 1.13). The ratio [Cu]/[In], on the other hand, decreases between 250°C and 450°C (0.87 to 0.61), and increases between 450°C and 530°C (0.61 to 0.76). The Mo layer is located underneath the Cu-In layer, and therefore the presence or lack of Mo in the measured composition relates directly to the film thickness[14]. Indeed, the thicker the film, the less Mo will be included in the volume of interaction between the electron beam and the sample, and therefore the less Mo will be detected.

The decreasing presence of Mo between 250°C and 450°C therefore indicates a thickening of the film, while its increase between 450°C and 530°C shows a thinning out.

Secondary ion mass spectroscopy (SIMS)

SIMS was performed on the samples (Figure 59). The average oxygen intensity detected in the bulk increases from 250ºC (≈1000) to 450ºC (≈20000), and then decreases at 530ºC (≈4000). Two to three regions are found in the depth profiles and discussed in the next paragraph.

---

[14] Note that, the fact that two stacked layers are included in the interaction volume with the electron beam induces an error on the EDS measurement, since the EDS software calculates the compositions on the assumption of a uniform layer throughout. However, the error induced for such samples where less than 10% Mo was detected, was assessed and found negligible.
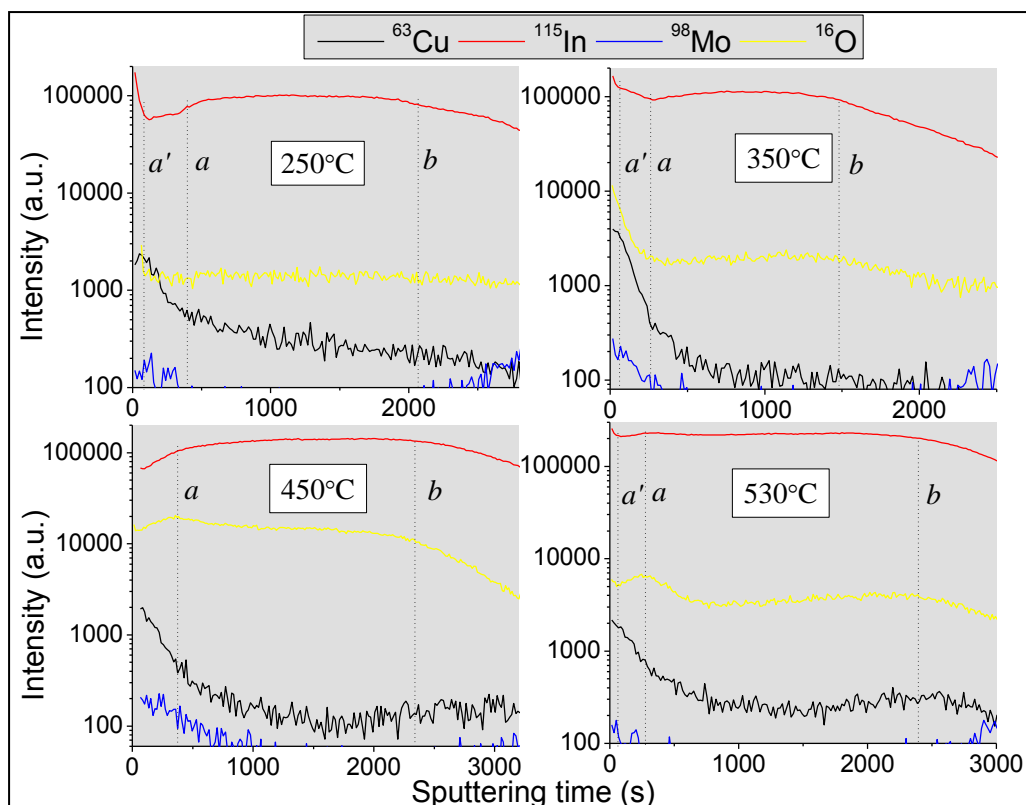
Figure 59: SIMS depth profiles of four pieces of the Cu-In precursor N623E ([Cu]/[In]=0.92) annealed for 1500 s, N623E5 (250°C), N623E4 (350°C), N623E3 (450°C) and N623E2 (530°C). In superscript after the elements in the legend are the isotopes used for the detection.

7.3.1.2 Discussion

XRD data shows that the In and the Cu_2In phases are first consumed to form $Cu_{11}In_9$ and In_2O_3 between 250°C and 350°C. This is attested by the weakening of the In and Cu_2In reflections and the parallel increase of the In_2O_3 and $Cu_{11}In_9$ reflections. Above 350°C, $Cu_{11}In_9$ totally disappears and In dwindles, consumed to form In_2O_3 and the more In-poor phase Cu_2In. Indeed, Cu_2In can accommodate a lower In content than $Cu_{11}In_9$, and has most likelyformed as a response to the oxidation of part of the indium. EDS indicates an increase in oxygen content from 250°C to 450°C, which ties in with the increased presence of In_2O_3. XRD indicates that In_2O_3 is the main oxide present, and the main source of oxygen in the film. Regarding the SIMS data (Figure 59), the increasing intensity, with temperature, of the oxygen

signal in the bulk (**a** to **b**) corresponds to the oxidation spreading from the surface at 250ºC and 350ºC, to the bulk at 450ºC. The Mo content detected also decreases in the range 250-450ºC, meaning that the film thickness and/or density increases. [Cu]/[In] decreases as well, due to the increasing presence of In_2O_3 (XRD), which should be more important near the surface. The formation of In_2O_3 does not appear clearly in the SIMS data, but the In and O curves seem to be correlated, especially at 450ºC. The increased presence of Cu near the surface in all samples could be an artefact due to the increase of O, or be due to copper oxide. However, the [Cu]/[In] ratio decreases with temperature and the absence of such oxide in the XRD pattern contradict the latter possibility. At 530°C, most trends are reversed. Since increasing Mo content (EDS) and Mo peak height (XRD) can be correlated with a lower film thickness, a most likelyexplanation is that a superficial part of the film, containing mostly oxides and the element In (e.g. as In_2O_3), has evaporated. This scenario would account for the increase in [Cu]/[In] (EDS), the decrease in oxygen content (EDS), the decrease of In_2O_3 and In reflection intensities (XRD) and the increase of the molybdenum content (EDS) and peak intensity (XRD) observed between 450°C and 530°C.

7.3.2 Cu-In-Al precursor annealing

The same study as for the Cu-In precursors was carried out on Cu-In-Al precursors. In this study, the Cu-In-Al matrix was made of 47 at% of Cu, 36 at% of In and 17 at% of Al (x=[Al]/([Al]+[In])=0.32). According to the relationship 3.5 between band gap and x (section 3.5), the expected band gap obtained from such a composition is 1.41 eV, if Al is completely and homogeneously incorporated into the $CuInSe_2$ lattice.

7.3.2.1 Data

X-ray diffraction

The introduction of Al complicates the interpretation of the XRD patterns, because Al, belonging to the same column of the periodic table as In, can alloy into the different Cu_xIn_y phases, modifying the lattice parameters of these phases. This results in a continuous (as opposed to discrete) shift of the reflection angles. Therefore, some of the phases detected in the Cu-In-Al precursors were identified by comparison with the Cu-In precursor annealed at the same temperature. An example is shown in Figure 60, where the phases present in N591K5 (250°C) are identified by comparison with those in N623E5, annealed in the same run. Common reflections are found in the two samples: $Cu_{11}In_9$ (PDF 00-041-0883), In (PDF 00-005-0642) and Cu_2In (PDF 00-042-1475), but differences are also noticed:

(a) The peaks labelled ϕ' (e.g. at 42.52°), are shifted to higher angles compared to the overlapping α and ϕ peaks (42.24°), both present in Cu-In and Cu-In-Al.

(b) The peak labelled δ', at 43.76°, is absent from the Cu-In precursor.

These reflections could not be matched with any Cu_xIn_y or Cu_xAl_y phases, and are identified as alloyed phases of Cu, In and Al. The introduction of Al, which is a smaller atom than In, results, if the crystalline structure is preserved, in a decrease of the interplanar spacing d_{hkl} and therefore a shift of the diffraction peaks to higher 2θ angles, according to Bragg's law.
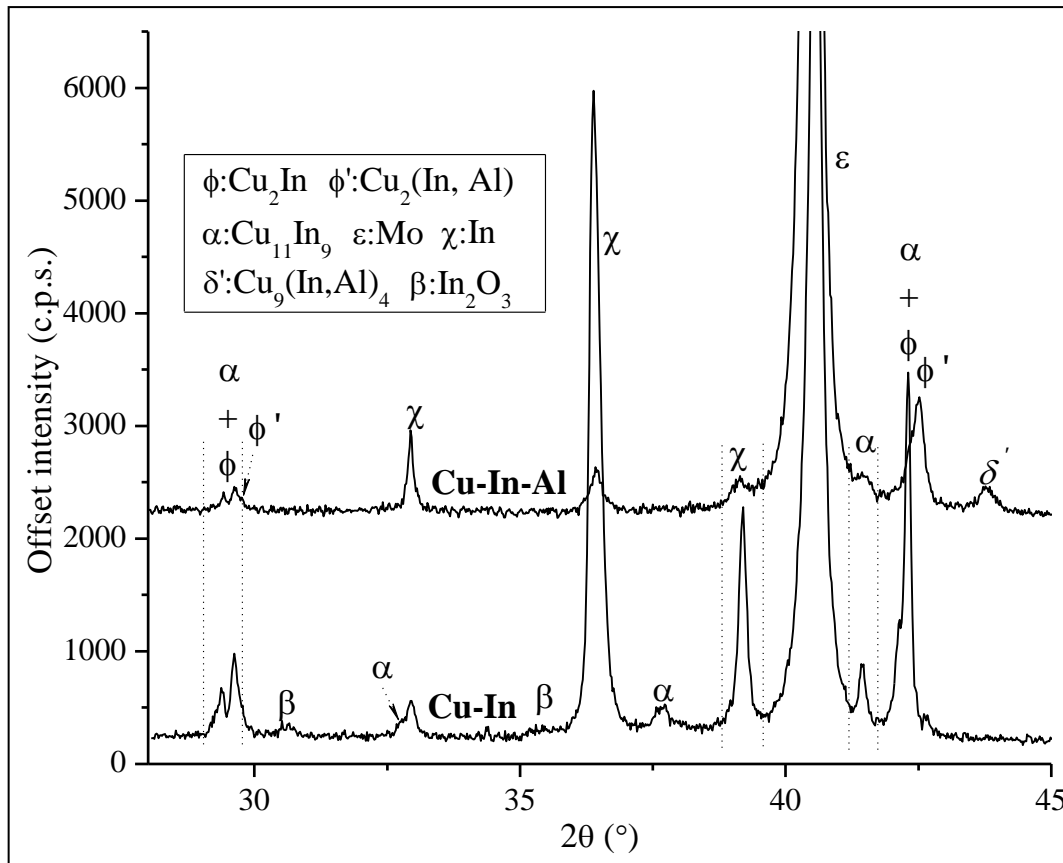
Figure 60: XRD patterns of N591K5 (Cu-In-Al precursor), and N623E5 (Cu-In precursor), annealed together at 250°C.

In his Ph.D dissertation on CIAS, Jost reported the presence of such alloyed phases in the metallic precursors and detailed their structures [66]. The software used for patterns analyses in the work presented here was used to "tune" the lattice parameters of the existing Cu_xIn_y and Cu_xAl_y standards in order to match the alloy phases between Cu, In and Al. The best matches with the phase labelled ϕ' were $Cu_{11}(In,Al)_9$ and $Cu_2(In,Al)$. $Cu_{11}(In,Al)_9$ could seem more logical since it only requires partial incorporation of Al into the already existing $Cu_{11}In_9$ phase (phase α in Figure 61), but $Cu_2(In,Al)$ is better supported by the analysis of N591K4 (350°C), where $Cu_2(In,Al)$ can be identified more unambiguously (Figure 61).

The phase δ' (43.88°) is believed to be $Cu_9(In,Al)_4$, matched by tuning of Cu_9In_4 (PDF 00-042-1476) and Cu_9Al_4 (PDF 01-071-0307). Cu_3Al_2 could also account for

140

δ' but the Cu-Al binary phase diagram [131] states a temperature of formation above 500°C. Finally, In_2O_3 (PDF 00-006-0416), present in the Cu-In precursor, is absent from the Cu-In-Al precursor annealed with it.
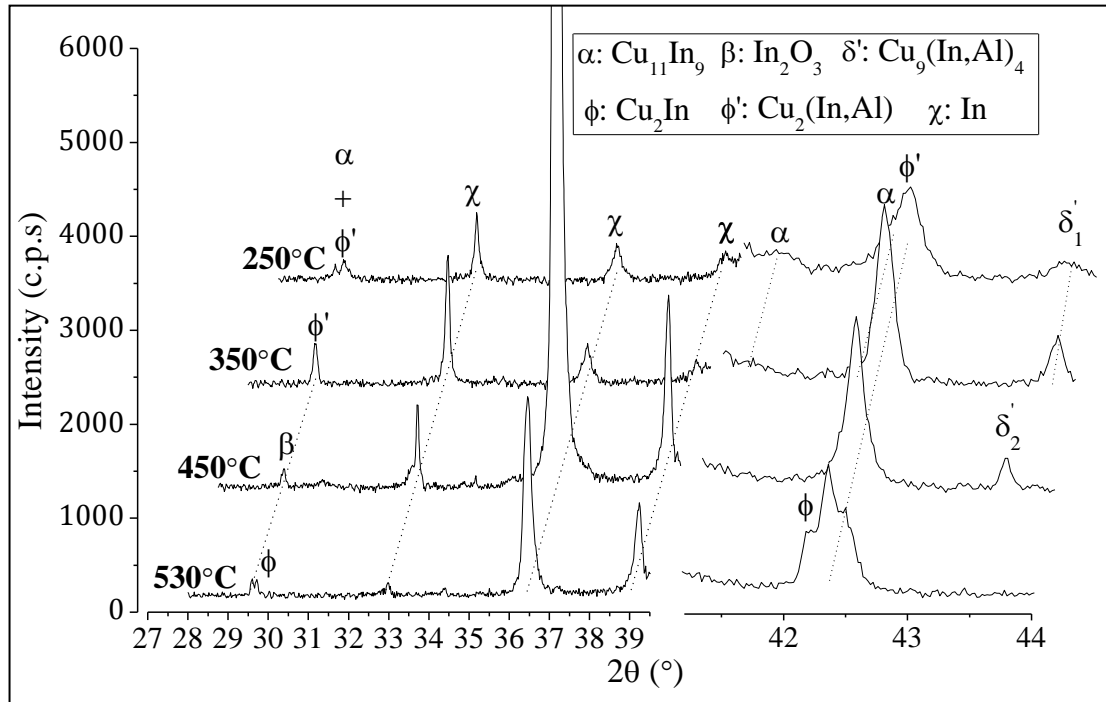
Figure 61: XRD patterns of four annealed pieces of N591K ([Cu]/([In]+[Al])=0.89, x=0.32), N591K5 (250°C), N591K4 (350°C), N591K3 (450°C) and N591K2 (530°C).

Figure 61 shows at 250°C (N591K) the phases $Cu_{11}In_9$, $Cu_2(In,Al)$ and $Cu_9(In,Al)$. $Cu_{11}In_9$ decreases between 250°C and 350°C, while In grows and $Cu_2(In,Al)$ and $Cu_9(In,Al)$ acquire a better crystallinity. $Cu_{11}In_9$ disappears at 450°C, and In aquires a strong (002) preferred orientation, similar to what happened at 250°C in N623E5. The intensity of the $Cu_2(In,Al)$ and $Cu_9(In,Al)$ reflections also decrease. At 530°C, finally, the In reflections weaken and $Cu_9(In,Al)$ disappears, while Al-free Cu_2In forms and $Cu_2(In,Al)$ is still present.

Energy dispersive spectroscopy

The EDS compositions of the samples were measured (Table 13).

Table 13: EDS composition of N591K5 (250°C), N591K4 (350°C), N591K3 (450°C) and N591K2 (530°C).

Sample ID	EDS composition (at %)					Cu/(Al+In)	Al/(Al+In)	O/(Cu+In+Al)
	Cu	In	Al	Mo	O			
N591K5 (250°C)	27.7	20.9	10.4	15.2	25.9	0.88	0.33	0.44
N591K4 (350°C)	22.4	19.0	9.7	11.3	37.7	0.78	0.34	0.74
N591K3 (450°C)	20.4	18.8	8.7	11.9	40.1	0.74	0.32	0.84
N591K2 (530°C)	20.7	16.9	8.1	13.2	41.2	0.83	0.32	0.90

[Cu]/([Al]+[In]) decreases between 250°C and 450°C (from 0.88 to 0.74) and then increases again at 530°C (0.83). [O]/([Cu]+[In]+[Al]), which measures the incorporation of oxygen into the thin film, increases with temperature from 0.44 at 250°C to 0.90 at 530°C. Unlike the Cu-In precursor, it does not decrease again at 530°C. The amount of Mo detected decreases from 250°C to 350°C and then increases again at 530°C. x=[Al]/([Al]+[In]) stays fairly stable through the four temperatures. Finally, the proportion of O detected increases sharply from 250ºC (0.44) to 350ºC (0.74), then more slowly up to 530ºC (0.90).

Secondary ion mass spectroscopy

SIMS was performed on the four samples (Figure 62).

142
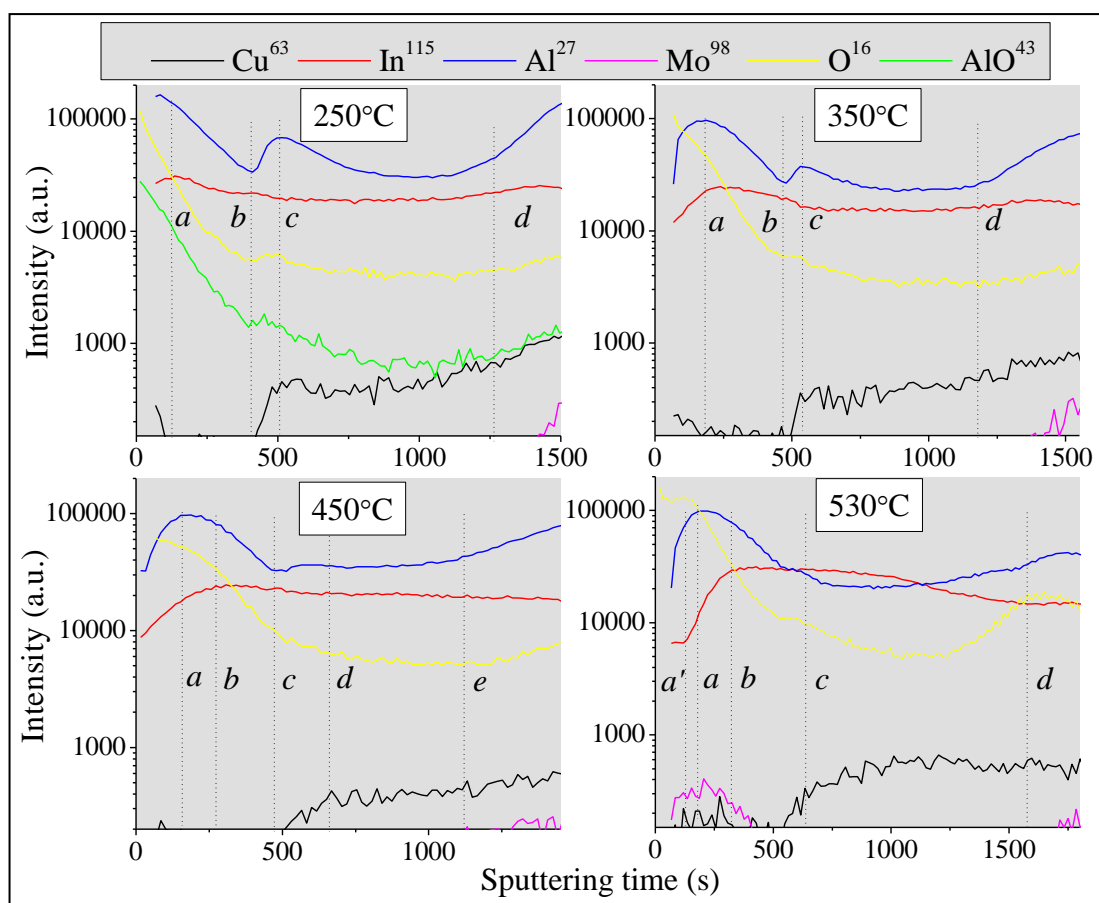
Figure 62: SIMS depth profiles of four pieces of the Cu-In-Al precursor N591K ([Cu]/([In]+[Al])=0.89, x=0.32) annealed for 1500 s, N591K5 (250°C), N591K4 (350°C), N591K3 (450°C) and N591K2 (530°C).

The results show the following features:

(a) O is maximal at the surface at all four temperatures, and then decreases in the bulk. The decrease is sharp from the surface down to a certain point (point *b* at 250ºC and 350ºC, point *c* at 450ºC and 530ºC), and then slighter.

(b) Al signal is more intense in a layer near the surface (up to *b* at 250ºC and 350ºC, up to *c* at 450ºC and 530ºC). Up to 350ºC, another increase is observed from *b* to *c*, before a relative stabilisation from *c* to *d*. Beyond 350ºC, this increase is absent or marginal.

(c) The mass of the compound AlO was also checked to determine whether some aluminium oxides could be present in the film. Its depth profile follows the

same trend as O and Al signals, with in particular the shoulder between ***b*** and

c and the increase towards the front. This was also true of the other samples,

but the line of AlO is not shown for clarity of the figures.

(d) Cu is absent from the regions between the surface and ***c*** at all temperatures. It

is then evenly distributed in the bulk.

(e) At 250ºC and 350ºC. In has a local maximum at ***a*** and is then even through

the bulk. At 450ºC and 530ºC, it has a minimum at the surface and then

increases until ***b***, where it stabilises. At 530ºC, however, In stays constant at

its minimum from the surface to ***a'***.

7.3.2.2 Discussion

The EDS results of N591K2-K5 (Cu-In-Al) can be compared to those of N623E2-E5

(Cu-In), since they were annealed together. The [O]/([Cu]+[In]+[Al]) ratio in N591K

(Table 13) increases sharply between 250°C and 350ºC, then more slowly up to

530°C. This departs from the trend observed in the Cu-In precursor (N623E), where

the sharpest increase was between 350ºC and 450ºC. This suggests that a different

oxide or combination of oxides might be involved in those two processes, with

different kinetics and thermodynamics. In_2O_3 is not detected in the Cu-In-Al samples

(XRD), in spite of an important presence of In. The oxygen detected in the film must

therefore be bound to another (other) element(s). Al is a likely candidate. Indeed,

although Al_2O_3 does not appear in the XRD patterns of the samples, it was reported

to be usually amorphous and very thin [132]. This oxide passivates the surface of

corrosion-sensitive materials by formation of a thin superficial layer that stops

deeper oxidation. The SIMS data supports this hypothesis, since the Al, AlO and O

profiles followed the same trends. Indium islands were observed in the SEM

micrographs, and an In phase visible in the XRD patterns up to 450ºC. However, the

fact that the abundant In phase is not oxidised suggests that the other(s) oxide(s) forming must be more reactive. The reported standard heat of formation of In_2O_3 is -923.5 kJ/mol [129] and that of Al_2O_3, -1676 kJ/mol [133], so that Al_2O_3 could explain the non-oxidation of In_2O_3 satisfactorily: Al captures the oxygen, either directly from the atmosphere or from In_2O_3, leaving an unoxidised In phase. Such a phenomenon is not unheard of, and it is to prevent Al from capturing oxygen from the transparent conductive oxide (TCO) that a Ni layer is interposed between the TCO and the Al contact grid in high efficiency devices [4, 30]. The SIMS data indicates that a surface layer more Al- and O-rich than the bulk is present, which could correspond to a surface Al_2O_3 layer. The O profile is clearly not correlated to the Cu and In profiles at 450°C and 530°C, since the signal does not increase in the bulk but only near the front. This superficial oxide would account for the more limited oxidation undergone by the Cu-In-Al, in comparison to Cu-In at 450°C. The oxygen contents are only similar at 530°C because some oxide evaporated in Cu-In but not in Cu-In-Al.

7.3.3 Cu-In-Al/Cu precursor annealing

As mentioned in the previous paragraph, aluminium seems to react strongly with oxygen to form Al_2O_3. This oxide is very resistive and not desirable in the film. Consequently, another precursor layout was tested to limit the contact of Al with the atmosphere, whether in air or in the annealing chamber. This layout included the same Cu-In-Al matrix as N591K, but with an additional 50 nm thick capping layer of copper.

7.3.3.1 Data

X-ray diffraction

The XRD patterns of N548L5 (250°C), N548L4 (350°C), N548L3 (450°C) and N548L2 (530°C) are shown in Figure 63.
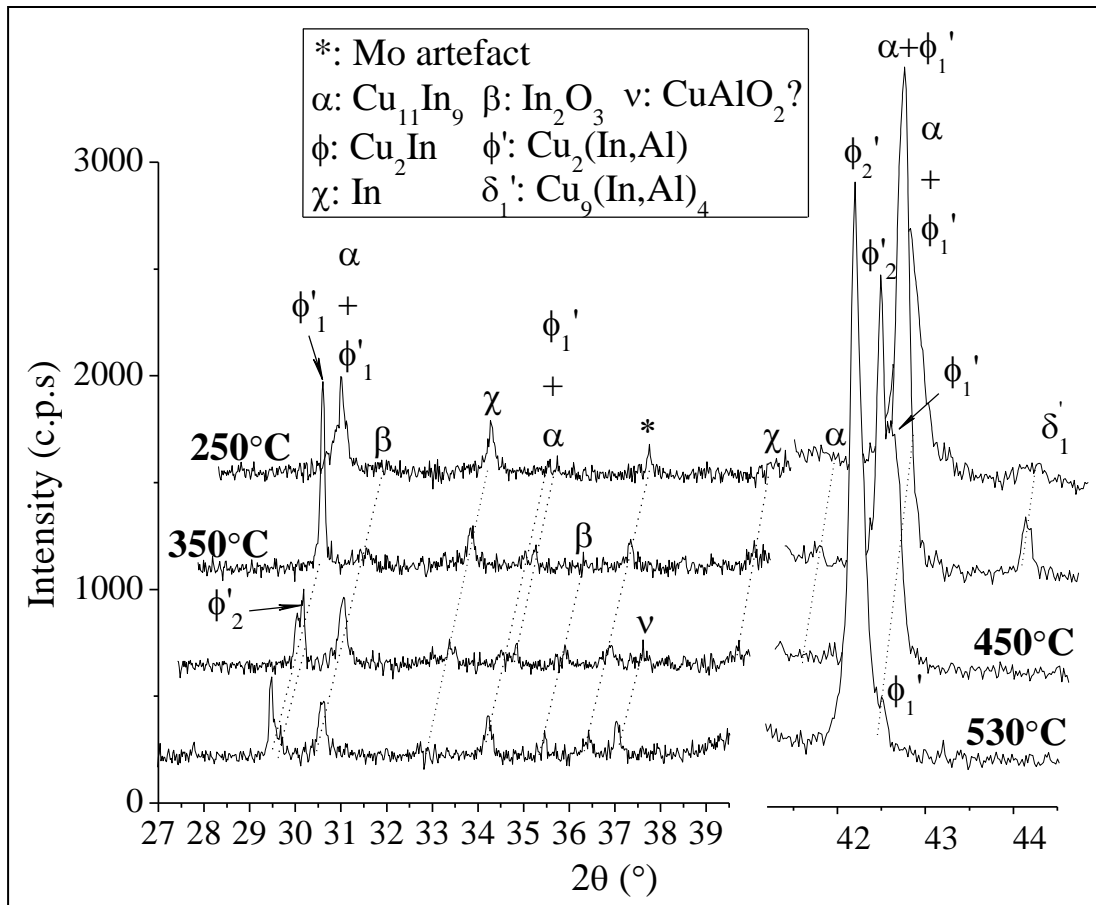
Figure 63: XRD patterns of four pieces of N548L (x=0.32, additional 50 nm thick Cu cap), N548L5 (250°C), N548L4 (350°C), N548L3 (450°C) and N548L2 (530°C).

Four notable differences are found between the Cu-In-Al/Cu patterns of Figure 63 and the Cu-In-Al patterns (Figure 61):

(a) The In phase does not grow but diminishes with increasing temperature.

(b) In_2O_3 is present. It forms at 250°C, grows up to 450°C and only decreases slightly at 540°C.

(c) An extra $Cu_2(In,Al)$ phase (ϕ_2') forms at 450°C and grows at 540°C. The $Cu_2(In,Al)$ phase present at lower temperatures (ϕ_1') decreases in parallel to this growth.

(d) Phase ν, that matches CuAlO$_2$, is detected in N548L3-L2 (450°C-530°C).

The Cu$_{11}$In$_9$ phase, unlike for Cu-In-Al, decreases from 250°C to 350°C and Cu$_2$(In,Al) (ϕ_1') grows. Cu$_9$(In,Al)$_4$ becomes more crystalline in this same range, but unlike Cu-In-Al, disappears at 450°C while a second Cu$_2$(In,Al) phase (ϕ_2') forms.

Energy dispersive spectroscopy

EDS analyses (Table 14) show that the oxygen content once again increases with increasing annealing temperature, and, like in Cu-In-Al, does not decrease at 530°C. [Cu]/([In]+[Al]) on the other hand, decreases slowly from 250°C to 450°C, and increases from 450°C to 530°C.

Table 14: EDS composition of four pieces of N548L (Cu-In-Al/Cu, x=0.32) selenised at different temperatures, N548L5 (250°C), N548L4 (350°C), N548L3 (450°C) and N548L2 (530°C).

Sample ID	EDS composition (at %)					Cu/(Al+In)	Al/(Al+In)	O/(Cu+In+Al)
	Cu	In	Al	Mo	O			
N548L5 (250°C)	36.6	23.3	8.2	10.7	21.2	1.16	0.26	0.31
N548L4 (350°C)	33.6	21.9	7.3	8.3	28.9	1.15	0.25	0.46
N548L3 (450°C)	29.4	19.5	7.7	6.6	36.7	1.08	0.28	0.65
N548L2 (530°C)	26.8	15.7	7.0	7.6	42.9	1.18	0.31	0.87

7.3.3.2 Discussion

Unlike the annealed Cu-In precursors N623E2-E5 (section 7.3.1), no oxide, and in particular no In$_2$O$_3$, was found in the XRD patterns of the Cu-In-Al precursors N591K2-K5 (section 7.3.2). This was in spite of a comparable amount of oxygen in the films (EDS) at the temperatures tested. In the Cu-In-Al/Cu samples N548L2-L5, however, In$_2$O$_3$ forms at 350°C, 450°C and 530°C, consuming the In phase and transforming Cu$_{11}$In$_9$ into Cu$_2$(In,Al) (ϕ_1') (Figure 63). The oxidation process involved in the Cu-In-Al precusors N591K5-K2 (section 7.3.2) is no longer as predominant, and some In$_2$O$_3$ is therefore free to form again. Furthermore, the In

islands are visible at 250°C at the surface of the Cu cap possibly remaining (SEM micrograph), so that the surface In could be isolated from the Al by Cu. $CuAlO_2$ formed in N548L3-L2 (450°C-530°C) because of the Cu cap. [O]/([Cu]+[In]+[Al]), indicative of the incorporation of O into the film, in the three types of precursors and at the two extreme temperatures tested, are summarised for better clarity in Table 15.

Table 15: Table summarising the oxygen contents of the films, assessed by the ratio [O]/([Cu]+[In]+[Al]), for the three types of precursors Cu-In, Cu-In-Al and Cu-In-Al/Cu, at 250°C and 530°C.

	N623E5 (250°C)	N548L5 (250°C)	N591K5 (250°C)
Precursor type	Cu-In	Cu-In-Al/Cu	Cu-In-Al
O/(Cu+In+Al)	0.22	0.31	0.44
	N623E2 (530°C)	N548L2 (530°C)	N591K2 (530°C)
Precursor type	Cu-In	Cu-In-Al/Cu	Cu-In-Al
O/(Cu+In+Al)	1.13	0.87	0.90

At 250°C, N548L5 contains a proportion of O about halfway between those of the Cu-In and Cu-In-Al. At 530°C (N548L2), however, this ratio becomes very close to that of Cu-In-Al (N591K2). One explanation for this trend is that Cu cap limits the formation of Al_2O_3 at 250°C, while the enhanced interdiffusion of this cap with the bulk at 530°C in the Cu-In-Al/Cu film results in Al oxide(s).

7.4   Selenisation study (RTP): effect of temperature

For this section, a study identical to that of section 7.3 was undertaken, although this time in the presence of Se. The results of selenisation of the Cu-In pecursors (N622C1-C4) were already discussed in section 6.4.3. As for the annealing study, the selenised Cu-In precursors, once analysed, were used as a standard to identify the phases present in the quaternary systems that are the selenised Cu-In-Al and Cu-In-Al/Cu precursors.

7.4.1 Experimental

After depositing the metallic precursors, the samples were loaded into the Nano 38 evaporation system and Se ($\approx$1.9 µm on N622C, $\approx$1.2 µm on N591K) was evaporated, and the samples cut. The experimental conditions were otherwise identical to section 7.3, and the precursors used originated from the same deposition batches. Note that a 10 mbar pressure was chosen to obtain similiar conditions to the tube furnace, where the only gauge available is unreliable for higher pressures than 10 mbar[15]. Note that for SIMS analyses, positive ions (i.e. from Cu, In, Al and Mo) were detected with an O ion beam, and negative ions (O and Se) with an Ar ion beam.

7.4.2 Cu-In-Al precursors Selenisation

Four pieces of N591R, from the same deposition batch as N591K (section 7.3.2), were selenised at different temperatures in the RTP, N591R4 (250°C), N591R3 (350°C), N591R2 (450°C) and N591R1 (530°C).

7.4.2.1 Data

X-ray diffraction

As in the precursor annealing study, the crystalline phases were identified by comparison with the selenised Cu-In precursors N622C1-C4. The XRD patterns of N591R1-R4 are displayed in Figure 64.

---

[15] The study showing the benefit of high pressures in the RTP had not yet been performed.

Figure 64: XRD patterns of four selenised pieces of the Cu-In-Al precursor N591R (x=0.32), N591R4 (250°C); N591R3 (350°C); N591R2 (450°C); N591R1 (530°C). The (hkl) indices belong to Cu0.938InSe2.

No Al-containing phase was detected in any of the four samples. All patterns reveal traces of the unconverted precursor phase $Cu_{16}In_9$ (PDF 00-026-0523), recognisable in particular by its (810) reflection. At 250°C, the binary selenides In_4Se_3 (PDF 01-083-0039), $CuSe_2$ (PDF 01-071-0046) and β-CuSe (PDF 00-027-0184) are observed. Trace $Cu_{0.938}InSe_2$ (PDF 01-078-2001) is also detected. At 350°C, no binary compounds remain except $Cu_{16}In_9$, and the CIS phase has grown (over 500% area increase) and become more crystalline (103 nm against 65 nm before). Low crystallinity In_2O_3 is also present. At 450°C, the same phases are present, with however more abundant and crystalline In_2O_3. Additional phases $Cu_{2-x}Se$ (PDF 00-006-0680) and κ are also found. κ was removed by KCN etch and is therefore a copper selenide. CIS is more abundant (20% area increase) and slightly more crystalline (113 nm against 103 nm before) than at 350°C. At 530°C (N591R1), In_2O_3 is less abundant, and deconvolution of the CIS peaks revealed κ', consistent

with trace CIAS. Finally, the Mo reflection intensity decreases from 250°C to 450°C and increases again at 530°C.

Energy dispersive spectroscopy

SEM imaging of N591R4 (250°C) shows two distinct regions stretching across the surface (Figure 65).
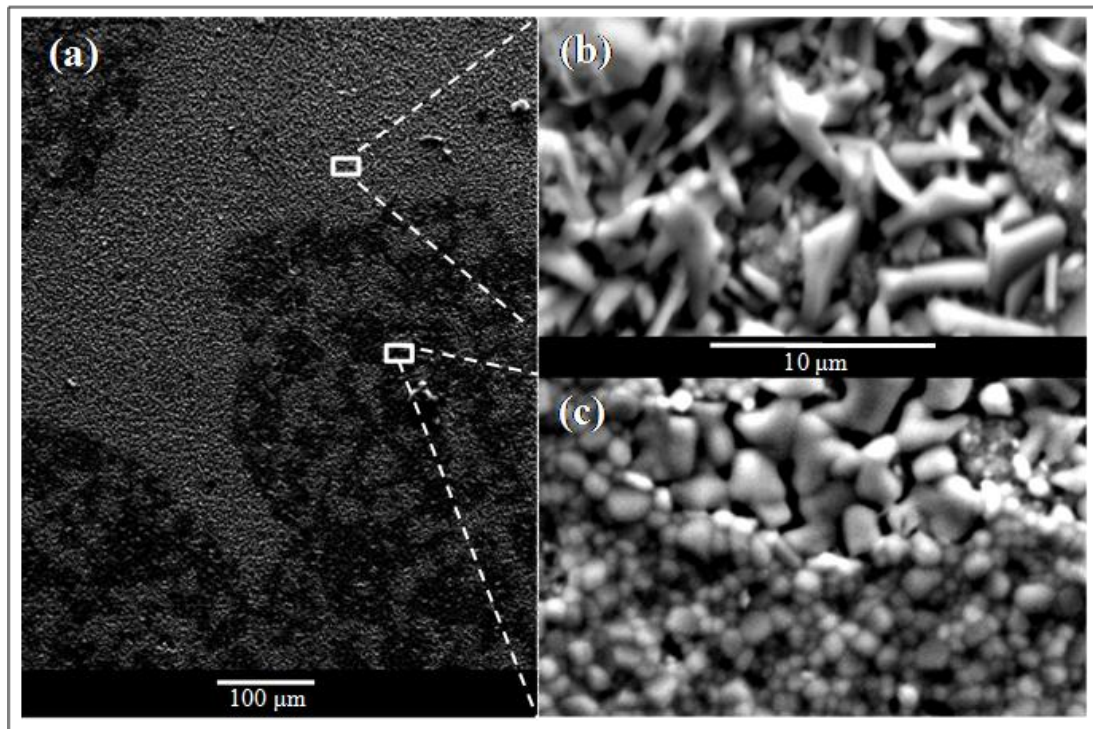
Figure 65: SEM micrographs of N591R4 (250°C selenisation) *(a)* **at low magnification, and zooming in on the two distinct regions,** *(b)* **one containing platelet-shaped features, and** *(c)* **the other containing two types of smoother features.**

Table 16: EDS atomic composition of N591R4 (250°C), N591R3 (350°C), N591R2 (450°C), and N591R1 (530°C). Note that there is partial energy overlap between Al K-transitions and Se L-transitions.

Sample ID	EDS composition (at %)						Cu/(Al+In)	Al/(Al+In)	Se/(Cu+In+Al)
	Cu	In	Al	Se	Mo	O			
N591R4 (250°C)	27.0	8.7	4.6	54.8	0.8	4.1	2.03	0.34	1.36
N591R4 (250°C) platelets region	29.0	12.4	4.8	46.8	1.0	6.0	1.68	0.28	1.01
N591R4 (250°C) round features region	25.9	7.8	5.0	56.8	0.8	3.7	2.02	0.39	1.47
N591R3 (350°C)	17.0	16.0	2.6	28.2	0.5	35.7	0.92	0.14	0.79
N591R2 (450°C)	15.9	15.8	5.3	26.0	0.6	36.4	0.76	0.25	0.70
N591R1 (530°C)	17.9	15.7	5.7	29.9	0.7	30.0	0.84	0.27	0.76

Zooming in on each of these regions and performing EDS (Table 16), it appears that:

(a) Region *(b)* is covered with platelet-like features. [Se]/[Cu]≈1.6[16] (2.0 for CIAS stoichiometry); [Cu]/([In]+[Al])≈1.7 (0.9 in as-deposited precursor); x=[Al]/([Al]+[In])≈0.3 (0.32 in as-deposited); [O]≈6 at% (26 at% in N591K5, section 7.3.2).

(b) Region *(c)* contains two types of features, some small and round-shaped, some bigger, smooth and of miscellaneous shapes. In this region, [Se]/[Cu]≈2.2; x≈0.4; [Cu]/([In]+[Al])≈2.0; [O]≈4 at%.

Note that the EDS measurements are this time affected by the partial energy overlapping between the Al K-transitions and Se L-transitions, so that the compositions, in Al and Se in particular, must only be taken as an indication. Still in N591R4, on a larger scale including regions *(b)* and *(c),* [O]≈4 at%, [Cu]/([In]+[Al])≈2.03 (0.89 in as-deposited), and [Se]/([Cu]+[In]+[Al])≈1.36 (1.0 in stoichiometric CIAS). In N591R3 (350°C), [O] increases sharply to ≈36 at%; [Cu]/([In]+[Al]) decreases to ≈0.92 (0.94 in as-deposited); [Se]/([Cu]+[In]+[Al])≈0.79; x≈0.14. N591R2 (450°C) has an equivalent oxygen

---

[16] The ratio is chosen between Se and Cu because Cu is the limiting element, the as-deposited precursor being Cu poor.

content ($\approx$36 at%); [Se]/([Cu]+[In]+[Al]) decreases to $\approx$0.70; [Cu]/([In]+[Al]) decreases to $\approx$0.76. In N591R1 (530°C) finally, the trends reverse slightly. [O]$\approx$30 at%; [Cu]/([In]+[Al])$\approx$0.84; [Se]/([Cu]+[In]+[Al])$\approx$0.76. A slightly increased x (0.27) was also measured.

Secondary ion mass spectroscopy

SIMS analyses (Figure 66) show the following results.

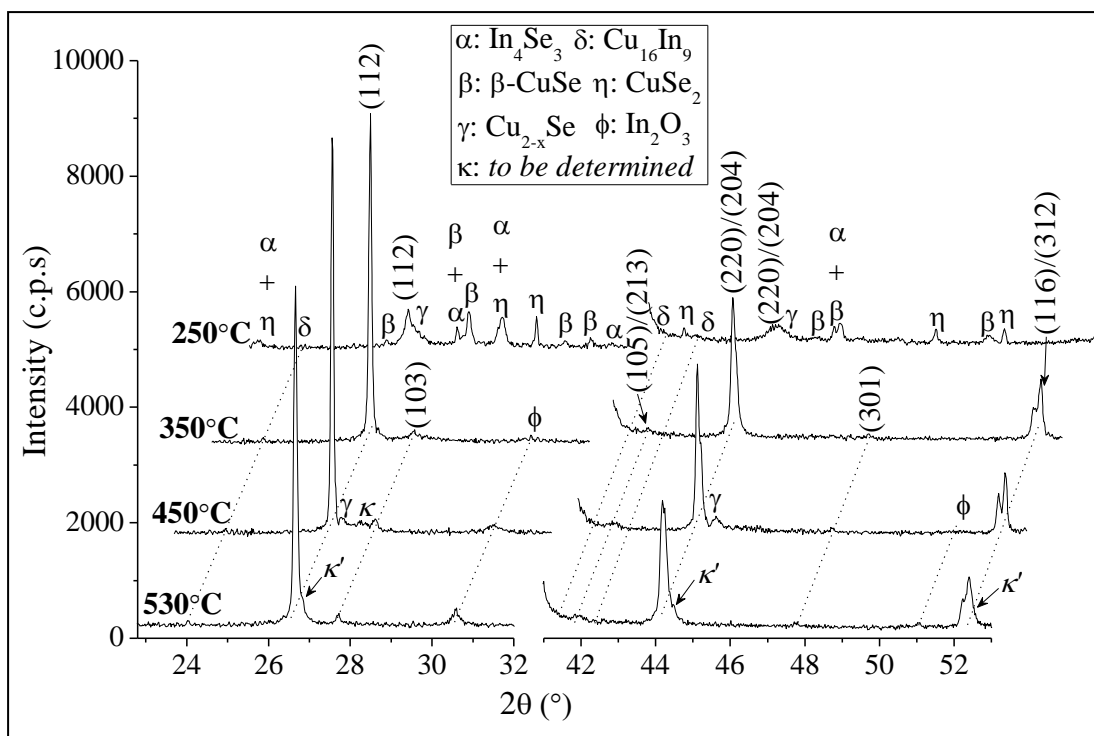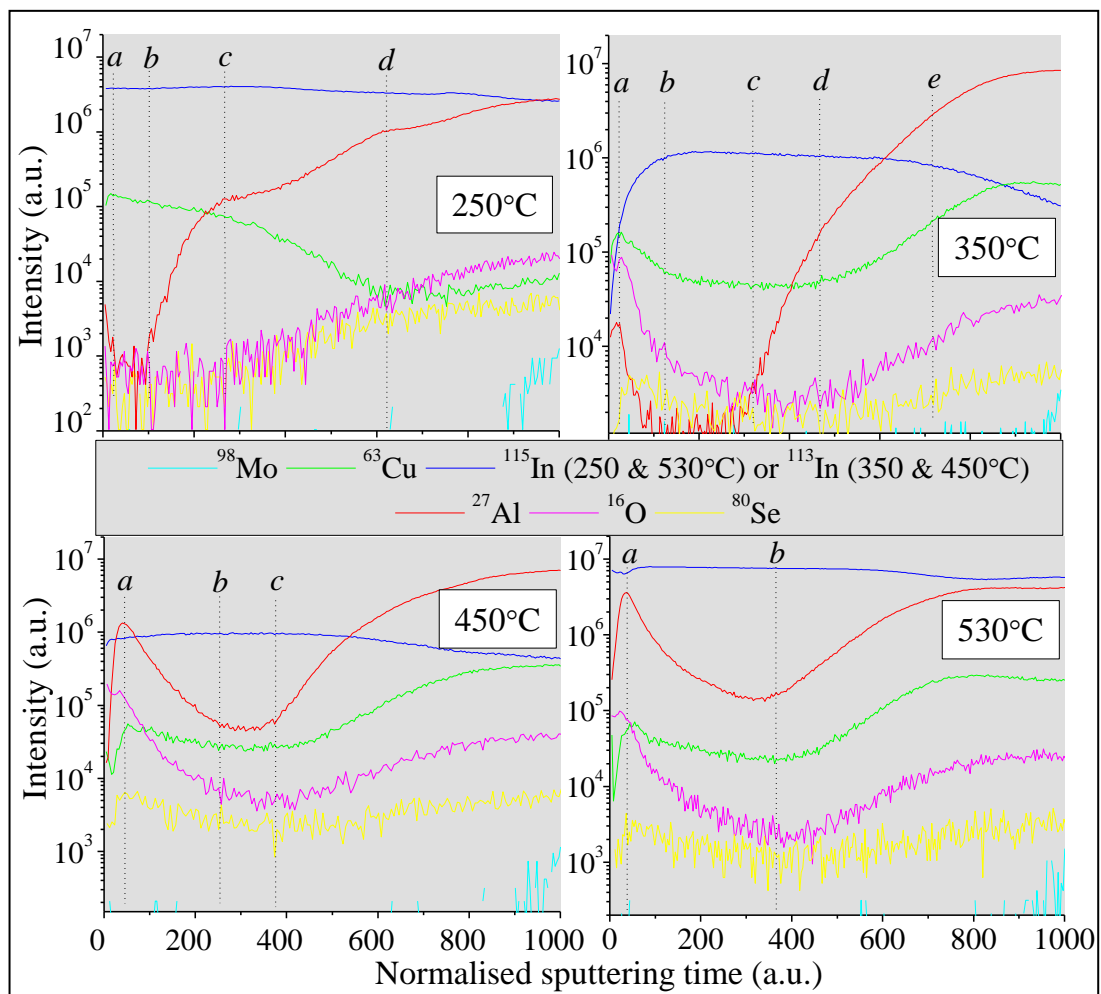**Figure 66: SIMS depth profiles of four selenised pieces of the Cu-In-Al precursor N591R (x=0.32), N591R4 (250°C), N591R3 (350°C), N591R2 (450°C) and N591R1 (530°C). Note that different isotopes of In were used for the detection at 250°C-530°C and 350°C-450°C (*see legend*).**

At 250°C (N591R4), Al is present as a thin layer extending from the surface to *a*, then absent from *a* to *b* (noisy signal associated with background noise), and the signal finally increases towards the back, sharply at first (*b* to *c*) and then more slowly. Se and O seem to follow a similar trend, with no signal at the front (up to *c*) and a gradual increase towards the back. Matrix effects[17] could be responsible, at least partly, for the increase of Se and O towards the back. Note that the O and Se signals stay noisy throughout the bulk, indicating that no more than a small amount is present. Cu, on the contrary, is more present at the front (up to *c*) and slopes down at the back. Indium, finally, is evenly distributed throughout the film.

At 350°C (N591R3), the Al signal starts low at the surface, reaches a maximum at *a* and a decrease and a zone of depletion from *b* to *c*. It then increases sharply towards the back. Indium is absent from the front[18] (up to *b*), evenly distributed from *b* to *e*, and decreases beyond *e*. O and Se peak near the surface (*a*), are then low from *b* to *d*, and increase again near the back. Note that O is maximum and Se depleted in a thin layer from the surface to *a*. Cu peaks at *a* and the back, and is otherwise uniformly distributed from *b* to *d*.

At 450°C, the Al profile is similar to that at 350°C, except for a thin Al-depleted layer from the surface to *a*, and a less Al-depleted region (the signal does not reach the background noise) from *b* to *c*. Cu and Se are both depleted in this same surface layer (up to *a*), evenly distributed from *b* to *c*, and increase gradually from *c* on. Oxygen shows a similar profile, but is once again present in a thin surface layer (up to *a*). Indium is evenly distributed throughout the film, with this time no clear

---

[17] Matrix effects can be due to a variety of phenomena such as charging of the matrix or variations in the bonding environment of the atom that is to be ionised (and detected). They result in the sputtering yield of a given ion to vary as the matrix changes (e.g. composition of the film).
[18] Note that a different isotope was used for the detection of In for N591R2-N591R3 (^{113}In) and N591R1-N591R4 (^{115}In), leading to a different intensity of signal.

depletion at the surface. At 530°C, all the features observed at 450°C are preserved except that In increases at the very surface.

7.4.2.2 Discussion

No Al was incorporated into the $CuInSe_2$ lattice at the four temperatures tested, and no Al-containing phase was visible in the XRD patterns either.

At 250°C (N591R4), the region **(c)** of Figure 65 (SEM) is more Se-rich than region **(b)**, and the [Cu]/([In]+[Al]) ratio higher. Therefore, a surface layer contains mostly Cu and Se. Indeed, such an inhomogeneous elemental distribution induces the EDS to overestimate the abundance of the elements in the superficial phases. This superficial layer can be identified with the overlaying layer made of small round features in Figure 65 (c). A likely candidate is $CuSe_2$, which is the only binary selenide that can form at 250°C [100, 109], is found in N591R4 (XRD Figure 64) and would account for the ratio [Se]/([Cu]+[In]+[Al])≈1.36 (with the error on Se due to Al). The apparent absence of Se near the surface in the SIMS spectrum of Figure 66 (250°C) is in contradiction with the EDS data. Surface roughness, which would induce different depths to be detected at the same time and therefore cause a loss of depth resolution near the surface, could account for this contradiction. However, the signal should in this case follow a slope, which does not happen here. Another noticeable feature of N591R4 is the oxygen content of 4 at%, compared to 26 at% in N591K5 (section 7.3.2.1). This clearly shows that the presence of Se or Cu_xSe_y phases at the surface of the film helped to prevent the oxidation of its bulk. The selenisation temperature, 250°C, is only slightly higher than 221°C, the melting point of Se (at 1 bar), and most of the Se must therefore have remained, as elemental Se or as copper selenide, on the film surface during the entire annealing process.

This superficial layer could have protected In and Al, which in this investigation seem to be the only two elements to form oxides, from a direct contact with O. As for Se, the SIMS depth profile of O is noisy and seems to be affected by matrix effects, which makes it difficult to interpret.

At 350°C (N591R3), the oxygen content shoots up at the surface (EDS, SIMS). This is due to some Se having diffused into the bulk to form CIS, leaving the surface exposed to oxidation. The consumption of the superficial copper selenide phases is supported by XRD and EDS data ([Cu]/([In]+[Al]) decreases). Furthermore, SIMS shows a more uniform distribution of Cu through most of the bulk (as opposed to the gradual decrease from front to back in N591R4) which also explains the [Cu]/([In]+[Al] decrease. In_2O_3 (XRD) certainly accounts for part of the oxygen increase. Al_2O_3 could also be present, since O and Al signals peak conjointly near the surface (SIMS). Besides, [O] is almost identical at 350°C and 450°C (EDS), in spite of the more abundant In_2O_3 phase at 450°C. Another oxide than In_2O_3 (allegedly Al_2O_3) must therefore be present at 350°C to account for the oxygen content. There could be residual superficial Cu_xSe_y phases, to account for Cu peaking at the surface (no $CuAlO_2$ detected). EDS also indicates that part of the Se has left the sample ([Se]/([Cu]+[In]+[Al])=0.79). At 450°C (N591R2), [Cu]/([In]+[Al]) decreases yet more (0.76). The superficial Cu depletion (SIMS) and/or the Al and Se energies overlap, could explain this variation. In the former case, superficial In_2O_3 (SIMS, XRD) could be screening the bulk, leading to an artificial decrease of [Cu] and [Al] and an increase of [In]. The presence of In_2O_3 has not found a satisfactory explanation. Al is present near the surface (SIMS), but absent from a thin region at the very front. This thin layer can be In_2O_3. However, the results of section 7.3.2 indicate that in this configuration the formation of Al_2O_3

156

should prevail over In_2O_3. This result might suggest that the Al is not, at this temperature, uniformly spread across the horizontal plane of the film, but aggregated in specific locations, the most plausible one being the grain boundaries. However, no data is available to test this hypothesis. The $Cu_{2-x}Se$ phase found in the XRD pattern is located near the front (SIMS), beneath or together with In_2O_3. At 530°C, evaporation of the surface oxides is suggested by the decreased presence of In_2O_3 (XRD) and lower [O] (EDS) compared to 450°C.

7.4.3 Cu-In-Al/Cu precursors Selenisation

7.4.3.1 Data

X-ray diffraction

N582L (Cu-In-Al/Cu) was cut and the pieces selenised. The XRD patterns of N582L4 (250°C), N582L3 (350°C), N582L2 (450°C) and N582L1 (530°C) are plotted in Figure 67. They are very similar to N591R4-R1 (Cu-In-Al), apart from these distinctive features:

(a) The copper selenide phases are more abundant in N582L4 than in N591R4.

(b) In_2O_3 appears at 350°C in Cu-In-Al/Cu (against 450°C in Cu-In-Al) and decreases at 450°C, to increase again at 530°C.

(c) Mo (110) decreases between 250°C and 350°C and increases again at 450°C already, while this trend reversal was taking place at 530°C only in Cu-In-Al.

(d) The κ type phases are present at 450°C and 530°C.

In order to remove the copper selenides and clarify the nature of the overlapping κ phases, the four selenised samples were submitted to 30 s etching in KCN and analysed by XRD once more (Figure 68). *K* was removed from N582L2 and N582L1, and the CIS (112) peak in N582L4 (250°C) remained.
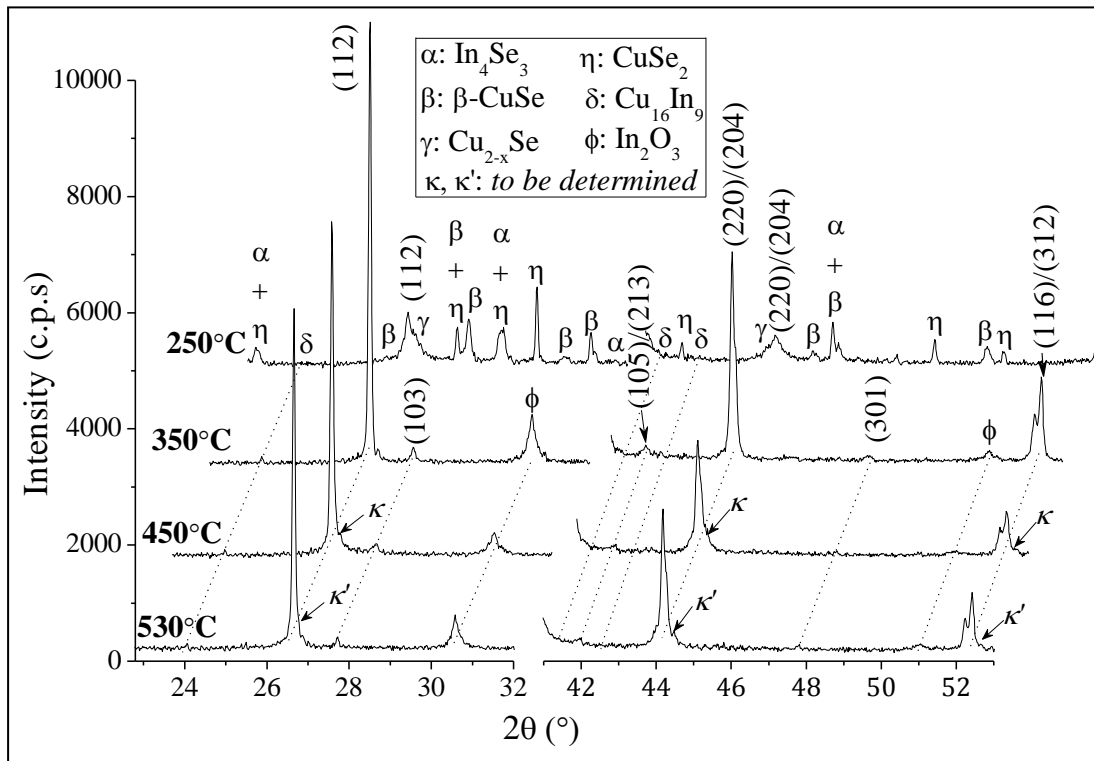
Figure 67: XRD patterns of four selenised pieces of the Cu-In-Al/Cu precursor N582L (x=0.31, 50 nm thick Cu cap), N582L4 (250°C), N582L3 (350°C), N582L2 (450°C), N582L1 (530°C).
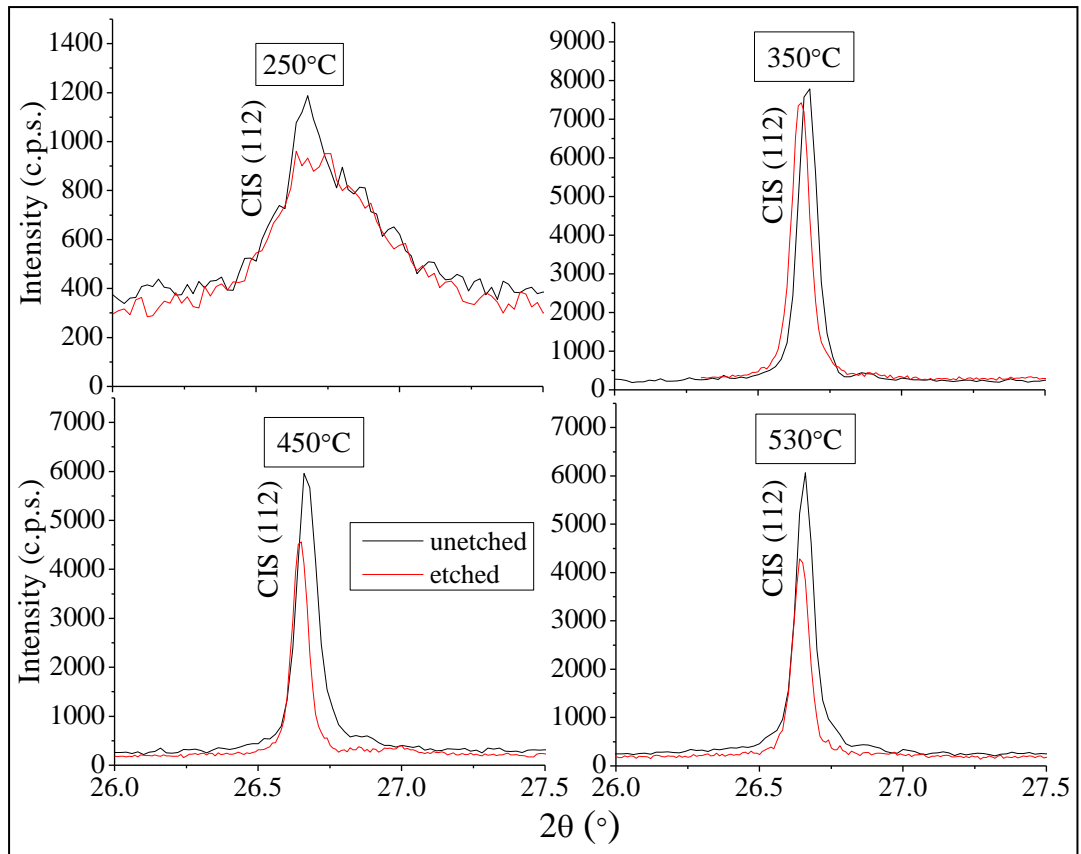
Figure 68: CIS (112) reflections of N582L4 (250°C), N582L3 (350°C), N582L2 (450°C) and N582L1 (530°C) before (*black line*) and after (*red line*) 30 s etching in KCN.

Energy dispersive spectroscopy

The elemental composition of the samples was measured before and after etching in KCN (Table 17), except for N582L1 for which the unetched part was missing.

Table 17: EDS compositions of N582L4 (250°C), N582L3 (350°C), N582L2 (450°C) and N582L1 (530°C). The darker cells contain the compositions after KCN etch.

Sample ID	EDS composition (at %)						Cu/(Al+In)	Al/(Al+In)	Se/(Cu+In+Al)
	Cu	In	Al	Se	Mo	O			
N582L4 250°C	30.4	3.4	3.1	61.0	0.2	2.0	4.69	0.47	1.65
	7.7	31.8	4.7	45.0	7.2	3.7	0.21	0.13	1.02
N582L3 350°C	20.3	15.1	1.8	26.7	0.4	35.7	1.20	0.11	0.72
	19.7	18.5	2.3	33.1	0.9	25.5	0.95	0.11	0.82
N582L2 450°C	19.0	13.9	3.1	22.9	0.4	40.8	1.12	0.18	0.64
	20.0	15.6	5.2	27.3	1.0	31.0	0.96	0.25	0.67
N582L1 530°C	N/A	N/A	N/A	N/A	N/A	N/A			
	16.0	18.1	4.1	28.2	0.8	32.8	0.72	0.19	0.74

In the unetched samples, [O] rises from 2 at% at 250°C to ≈36 at% at 530°C, in a similar way to Cu-In-Al (section 7.4.2.1), and more slowly between 350°C and 450°C. [Cu]/([Al]+[In]) falls between 250°C (4.69) and 350°C (1.20) and decreases slightly more at 450°C (1.12), as does [Se]/([Cu]+[Al]+[In]) (1.65, 0.72 and 0.64, respectively).

The KCN etching induces some changes to these compositions. At 250°C, the measured composition goes from Cu- and Se- rich before etching, to In- and Se- rich after etching. The Mo signal detected also greatly increases, from ≈0.2 at% to ≈7.2 at% after etching. This indicates an important thinning of the film. The etching also causes [Cu]/([In]+[Al]) and [O] to decrease at all temperatures tested.

Secondary ion mass spectroscopy

The SIMS depth profiles of the unetched samples are shown in Figure 69.
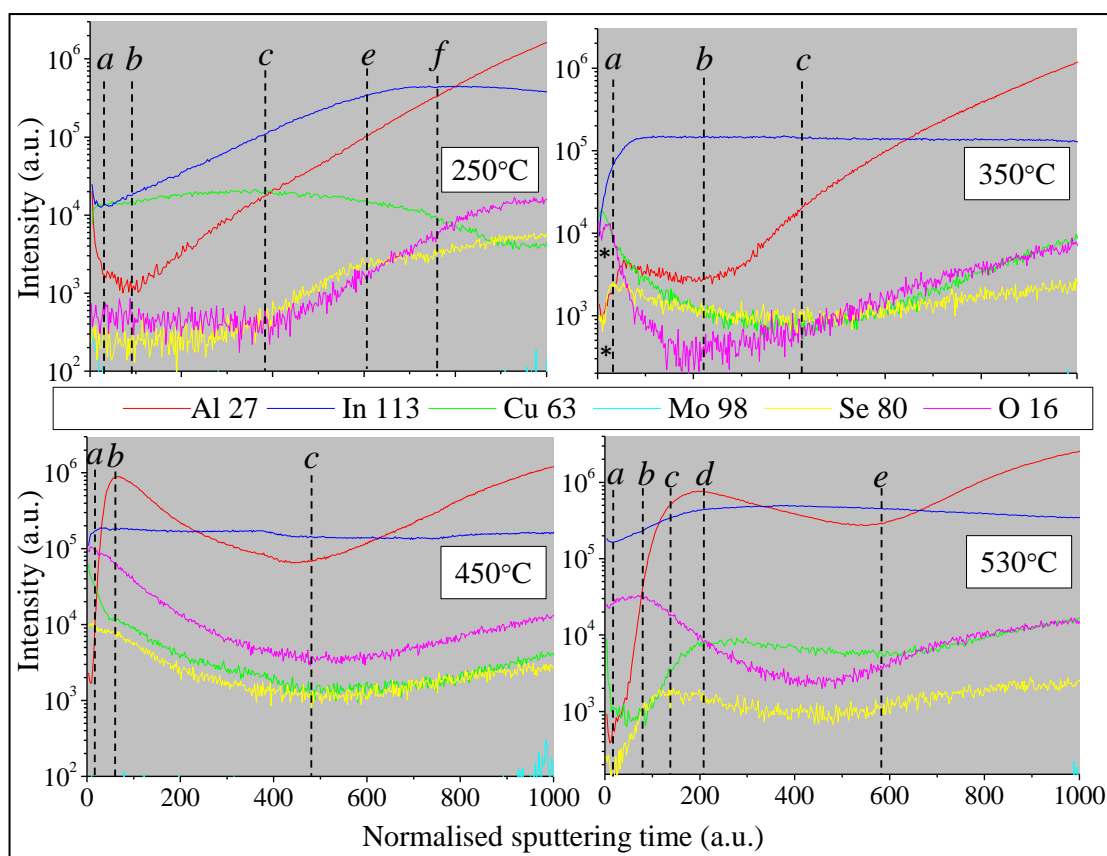
Figure 69: SIMS depth profiles of four selenised pieces of the Cu-In-Al/Cu precursor N582L (48 at% Cu, x=0.31 before adding the 50 nm thick Cu cap), N582L4 (250°C, 300 s ramp), N582L3 (350°C, 400 s ramp), N582L2 (450°C, 630 s ramp) and N582L1 (530°C, 750 s ramp).

At 250°C, the In and Al distributions both decrease sharply from the surface of the absorber, to reach a dip near the surface (In at *a*, Al at *b*), and then increase exponentially (logarithmic scale) towards the back. Cu is fairly uniform throughout, with however a decrease near the back. Se and O signals are affected with a noise corresponding to the background noise in a large part of the absorber (up to *c*) and can therefore be considered as non-existent in this region. They then slope up toward the back, but the signal stays noisy, suggesting matrix effect rather than a real increase.

At 350°C (N582L3), In becomes depleted in a thin layer at the front, undergoes a sharp increase (up to *a*) and is then uniformly distributed throughout the film. Al, O

161

and Se are present as a thin layer at the surface, before decreasing to a dip (marked *). O then decreases to reach the background noise (near *b*), while Se stays fairly constant throughout the bulk. Cu is also present at the surface, the signal then decreases up to *c* and increases again towards the back. The Al signal plateaus between *a* and *b* before increasing toward the back.

At 450°C (N582L2), the profile is very similar to N591R2 (section 7.4.2.1), except that the Se and Cu signals do not meet a dip near the surface.

At 530°C, the profile is similar to N591R1, but while Cu only met a narrow dip in Cu-In-Al, it is here completely absent from what seems a relatively thick region of the bulk (up to *b*), then increases till *d* and stays constant up to *e*.

7.4.3.2 Discussion

The aluminium was not incorporated into the chalcopyrite structure, and could not be detected in any other crystalline phase, in spite of it being present (although non-uniformly) throughout the bulk at 450°C and 530°C.

The same XRD phases are present in selenised Cu-In-Al and Cu-In-Al/Cu precursors, but the additional Cu capping layer leads to more abundant copper selenides at 250°C. Copper selenides (labelled κ), present at 450°C and 530°C, were removed by KCN etching.

The SIMS depth profiles however depart on several respects. At 250°C, the Cu cap partially diffuses through the bulk, yielding an increase of Cu and therefore a symmetrical decrease of In. In_2O_3 is also more abundant, in presence of the Cu cap, at 350°C, 450°C and 530°C. The following hypothesis can explain this observation:

(a) Without Cu cap (N591R1-R4), Al is present near the surface from the beginning of the selenisation process and therefore the oxygen bonds preferentially with this element.

(b) With the Cu cap, Al is no longer in direct contact with the atmosphere of the chamber, unlike In. Indeed, the In "islands", mentioned in 5.4, protrude from the Cu cap in the as-deposited precursor in spite of the Cu cap. In can therefore bond with O to form In_2O_3 without having to compete with Al.

The effect of etching on EDS compositions (Table 17) shows several trends. At 250°C, β-CuSe and $CuSe_2$, initially present as a relatively thick superficial layer, were removed by etching, while In_4Se_3 (EDS), located underneath, was preserved. This is supported by the substantial decrease of [Cu] and the parallel increase of [In] and [Mo], the latter being associated with film thinning.

The fact that [O] decreases after etching at all temperatures except 250°C indicates that some In_2O_3 was removed along with the copper selenides. This could happen if the copper selenides were located underneath the In_2O_3, their removal having led In_2O_3 to peel off. At 250°C, however, the oxygen detected originates from the as-deposited precursor. The removal of the superficial copper selenides therefore resulted in less screening of this bulk oxygen.

7.5 Selenisation study (TF): effect of temperature

A study similar to that of section 7.4 was carried out in a tube furnace (TF). Unlike the RTP, this furnace only permits slower heating (0.3°C/s against 9°C/s in the RTP) and cooling rates (0.015°C/s against 0.4°C/s). It was shown in section 7.4 that the main obstacles encountered in the RTP was an important presence of oxygen in the chamber, leading to oxygen contents in the sample up to >40 at%. The tube furnace,

on the other hand, yielded much lower levels of oxidation (typically <7 at%). The size of the tube furnace chamber also made it possible to anneal conjointly up to four full slides (26 mm by 76 mm) in the same run, which was later used for the study on cell fabrication (CHAPTER 9).

7.5.1 Introduction

As in the RTP (section 7.4.3), Cu-In-Al/Cu samples were selenised in the tube furnace at four different maximum temperatures, 250°C, 350°C, 450°C and 530°C. Two additional low temperature steps at 130°C and 250°C (for the 350 °C, 450 °C and 530°C samples) were introduced because those steps were reported in [134] to yield good crystallinity in CIS grown from stacked elemental layers.

7.5.2 Experimental

≈650 nm thick Cu-In-Al metallic precursors ([Cu]/([In][Al])≈1.00 and x=0.11 before Cu capping) were sputtered from elemental targets on Mo-coated SLG and a 100 nm thick Cu capping layer was added at the end of the sequence. Samples were subsequently coated with ≈2 μm of Se and selenised in 6 mbar of Ar. The heating profiles are described in Table 18. Unlike the previous study, the depth profiles were here characterised by glow discharge-optical emission spectroscopy (GD-OES) at Horiba Jobin Yvon. The measurement was not calibrated for quantitative analysis, but this technique provides more stability than quadrupole SIMS with respect to matrix effects and roughness. Indeed, it utilises a pulsed plasma and sputters atoms rather than ions. This eliminates local charging, an important cause of signal variation in SIMS. The atoms are collected over relatively large areas, typically 4 mm^2 (against 0.025 mm^2 in SIMS). This, associated with a lower depth resolution than the SIMS, results in a smoother signal, less influenced by local roughness.

Table 18: Selenisation steps summary for N582O, N582Q, N582K and N5325W. The average ramping rate was ≈18°C/min, and the cooling rate ≈0.9°C/min.

Name	Steps/Duration		
	Step 1	Step 2	Step 3
N582O	130°C (30 min)	250°C (30 min)	
N582Q	130°C (30 min)	250°C (30 min)	350°C (30 min)
N582K	130°C (30 min)	250°C (30 min)	450°C (30 min)
N535W	130°C (30 min)	250°C (30 min)	540°C (30 min)

7.5.3 Data

The XRD patterns of the samples are shown in Figure 70.
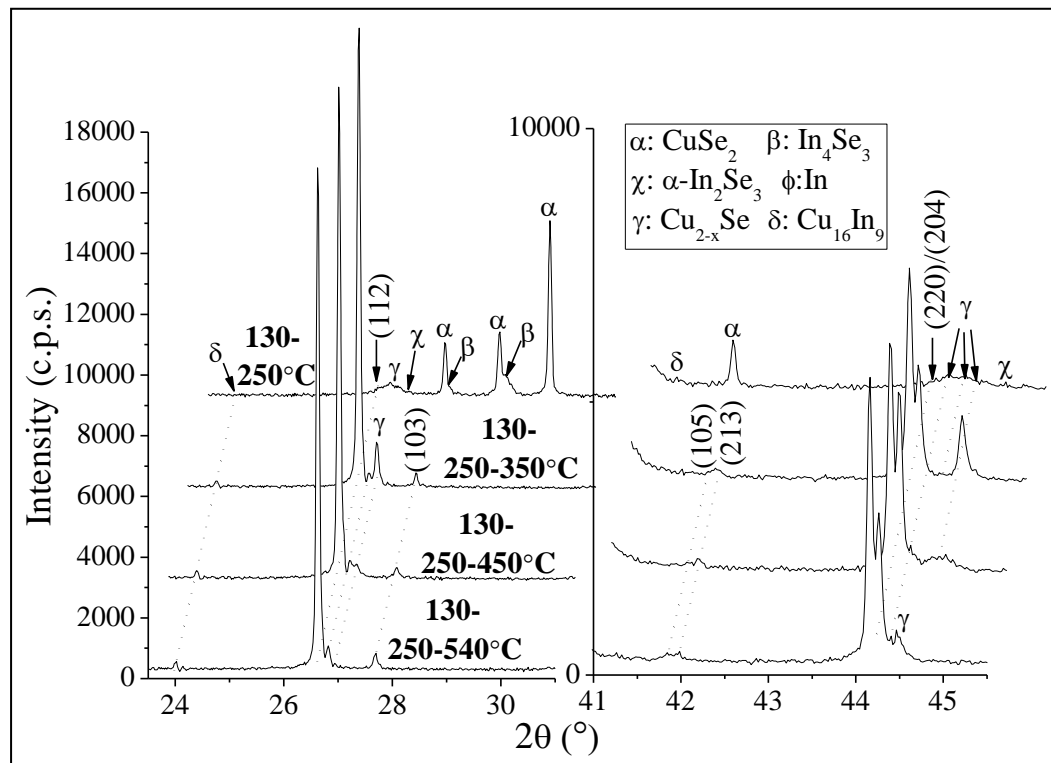
Figure 70: XRD patterns of four selenised Cu-In-Al/Cu precursors (x=0.11, 100 nm thick Cu cap), N582O (130°C-250°C), N582Q (130°C-250°C-350°C), N582K (130°C-250°C-450°C) and N535W (130°C-250°C-540°C).

The phases detected are summarized in Table 19, where are also indicated for comparison the phases detected in RTP samples from section 7.4.3 (*grey cells*).

Table 19: XRD crystalline phases in *third column* N582O (250°C), N582Q (350°C), N582K (450°C) and N535W (540°C), 3-steps processed in the TF; and *fourth column* samples N582L1 (250°C), N582L2 (350°C), N582L3 (450°C) and N582L4 (530°C), 1-step processed at an equivalent maximum temperatures in the RTP.

Name	Selenisation steps	XRD phases in TF	XRD phases in RTP
N582O	130°C-250°C	$CuInSe_2$*, $Cu_{2-x}Se$, $CuSe_2$, In_4Se_3, α-In_2Se_3*, $Cu_{16}In_9$*, In*	$CuInSe_2$, $Cu_{2-x}Se$*, $CuSe_2$ β-$CuSe$, In_4Se_3, $Cu_{16}In_9$*
N582Q	130°C-250°C-350°C	$Cu_{2-x}Se$, $CuInSe_2$, $Cu_{16}In_9$*, In*	$CuInSe_2$, $Cu_{2-x}Se$, In_2O_3, $Cu_{16}In_9$*
N582K	130°C-250°C-450°C	$Cu_{2-x}Se$, $CuInSe_2$, $Cu_{16}In_9$*, In*	$CuInSe_2$, $Cu_{2-x}Se$, In_2O_3, $Cu_{16}In_9$*
N535W	130°C-250°C-540°C	$Cu_{2-x}Se$, $CuInSe_2$	$CuInSe_2$, $Cu_{2-x}Se$, In_2O_3, $Cu_{16}In_9$*

*Traces only

The XRD analyses show that $Cu_{2-x}Se$ is present at all four temperatures, although only as trace and/or low crystallinity at 250°C. In N582O (maximal temperature 250°C), $CuSe_2$, In_4Se_3 (PDF 01-083-0039) and trace amounts of low crystallinity CIS were detected. Traces of indium (PDF 00-005-0642, not shown in the figure), $Cu_{16}In_9$ (PDF 00-026-0523) and α-In_2Se_3 (PDF 00-034-1279) were also present. At 350°C (N582Q), In_4Se_3 and $CuSe_2$ reflections are no longer present, while CIS is more abundant and crystalline. As a result, the CIS (103) peak has become visible and the (220)/(204) doublet resolved. Three distinct $Cu_{2-x}Se$ phases and traces of $Cu_{16}In_9$ and In are also present. The same phases were observed at 450°C (N582K), with however a dampening of one of the $Cu_{2-x}Se$ phases. Finally, at 540°C CIS, trace $Cu_{16}In_9$ and three $Cu_{2-x}Se$ phases were visible, with further dampening of the same $Cu_{2-x}Se$ phase that had decreased at 450°C. No Al-containing phase was observed in any of these samples. The crystallinity is better than in the RTP at all temperatures, and as a result the (204) and (220) peaks are resolved at temperatures as low as 350°C. The tetragonal distortion was found to be the same as in the RTP, i.e. -0.09, at 350°C (N582Q), 450°C (N582K) and 530°C (N535W).

Energy dispersive spectroscopy

EDS analyses are shown in Table 20.

Table 20: EDS composition of four selenised Cu-In-Al/Cu precursors, N582O (130-250°C), N582Q (130-250-350°C), N582K (130-250-450°C) and N535W (130-250-530°C+post selenisation annealing at 573°C).

ID	EDS composition (at %)						Cu/(Al+In)	Al/(Al+In)	Se/(Cu+In+Al)
	Cu	In	Al	Se	Mo	O			
N582O	28.3	1.8	2.9	66.7	0.0	0.4	6.09	0.62	2.02
N582Q	34.1	17.8	2.9	44.1	0.8	0.3	1.65	0.14	0.81
N582K	25.0	22.3	2.2	45.7	0.3	4.4	1.02	0.09	0.92
N535W	26.8	21.2	2.3	40.5	3.0	6.2	1.14	0.10	0.81

The oxygen content is much lower than in the RTP, with a maximum of 6 at% at 540°C (N535W). Note however that the composition of this last sample was only measured after an additional annealing process at 573°C (discussed in 8.4). The composition is very Cu- and Se-rich at 250°C (N582O), with $[Cu]/([Al]+[In]) \approx 6.1$ (1.0 in as-deposited) and $[Se]/([In]+[Al]) \approx 14.2$ (2.0 for stoichiometry), and still Cu-rich at 350°C (N582Q), with $[Cu]/([Al]+[In]) \approx 1.65$. At 450°C (N582K), $[Cu]/([In]+[Al]) \approx 1.02$, close to CIAS stoichiometry, although $[Al]/([Al]+[In]) \approx 0.09$ is lower than in the as-deposited precursor (0.11) and there is a slight deficit in Se ($[Se]/([Cu]+[In]+[Al]) \approx 0.92$). At 540°C (N535W), $[Cu]/([In]+[Al])$ increases and $[Se]/([Cu]+[In]+[Al])$ decreases once more (0.81), so that the overall composition appears Cu-rich and more Se-deficient than at 450°C.

Glow discharge optical emission spectroscopy

GD-OES was performed on the four samples (Figure 71).
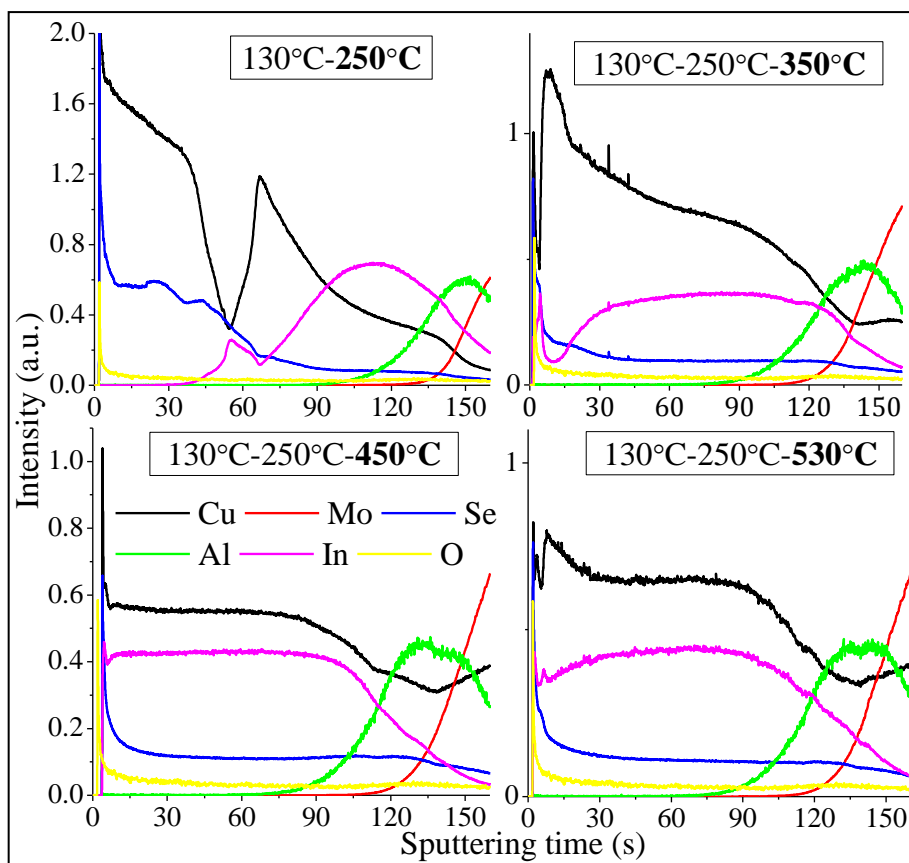
Figure 71: GD-OES depth profiles of four Cu-In-Al/Cu precursors ([Cu]/([In]+[Al])=1.0, x=0.11) selenised in the tube furnace, N582O (130°C-250°C), N582Q (130°C-250°C-350°C), N582K (130°C-250°C-450°C) and N535W (130°C-250°C-540°C).

In N582O (250°C, graph (**a**)), the Cu profile shows a decreasing slope from front to back, with however a "notch" around t=55 s. Indium is mostly present at the back, but a characteristic increase is also noted where the notch in Cu is observed. Finally, Al aggregates at the back of the film. N582Q (350°C, graph (**b**)) shows an enhanced interdiffusion of all the elements, except for Al, which remains located at the back of the film. The notch in the Cu profile is no longer present. In N582K (450°C, graph (**c**)) Cu, In and Se are distributed evenly, whereas Al shows an increased presence in the bulk compared to N582Q. In N535W (540°C, graph (**d**)), finally, a very similar depth profile to N582K is observed for all the elements, with however more Cu and possibly Se at the front.

168

7.5.4 Discussion

At 250°C and 350°C maximal temperatures, analyses (EDS, XRD, GD-OES) show that, as in 7.4.3, part of the Cu cap has bonded with Se to form superficial $CuSe_2$ and $Cu_{2-x}Se$ phases. GD-OES, in particular, shows that part of the Cu cap has diffused into the bulk at those temperatures. Two of the CIS formation paths reported in the literature [109] can apply to this study: reaction 6.6 and reaction 6.3 (pages 120 and 114, respectively). As mentioned before, reaction 6.6 starts at 221°C, with the formation of binary selenides, and is relatively slow. The required selenides can be formed via:

$$CuSe_2 + In_4Se_3 \rightarrow CuSe + 4InSe \tag{7.1}$$
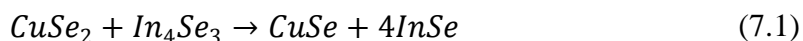
Reaction 6.3 starts at 370°C, and is faster than 6.6. It proceeds via the intermediary reaction:

$$2CuSe \rightarrow Cu_2Se + Se \tag{7.2}$$

These reaction pathways can be matched with XRD and GD-OES data in order to understand the trends observed. In N582O (250°C), only reaction 6.6 can account for the presence of CIS. The presence of In_4Se_3, $CuSe_2$ and only traces of CIS (XRD) indicate that reaction 7.1 has not occurred more than marginally. In Figure 72 are compared the XRD patterns obtained in the TF and in the RTP. The presence of β-CuSe in the RTP might have promoted the CIS growth observed in N582L4, since CuSe is a reactant of reaction 6.6. In N582O (TF), the incomplete consumption of In_4Se_3 by reaction 7.1 could be explained, as in section 6.4.1, by a too large crystallite size of $CuSe_2$ and/or In_4Se_3, slowing down reaction 7.1 and therefore reaction 6.6 (formation of CIS).
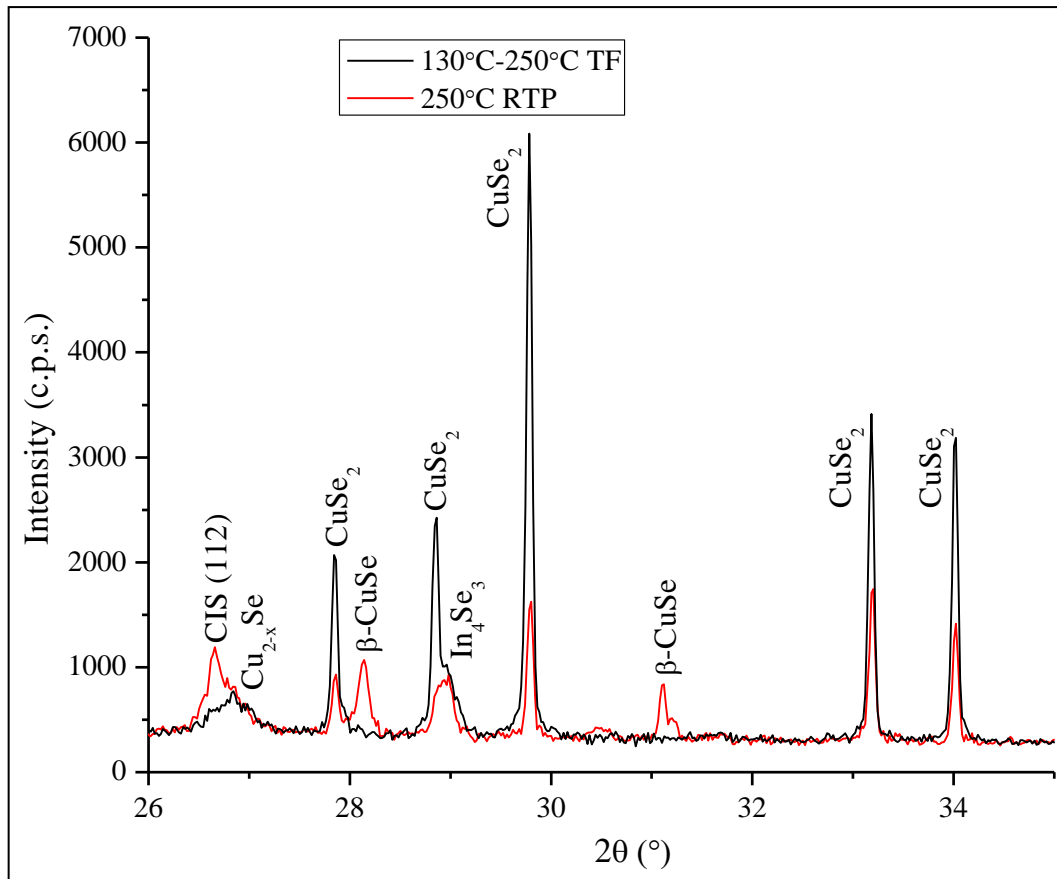
Figure 72: XRD patterns of N582O (TF, 130°C-250°C) and N582L4 (RTP, 250°C).

This hypothesis would accommodate the better growth of CIS in the RTP, since the ramping rate applied, almost three times faster, would have allowed less time for the phases to crystallise. However, the only crystallinity data accessible to us is the crystallinity after the entire process, which does not make it possible to check this hypothesis. Furthermore, GD-OES (Figure 71) reveals that the two phases are "geographically" distinct, with $CuSe_2$ located near the film surface (i.e. where the most Se is present), and In_4Se_3 deeper into the bulk. The notch observed in the Cu profile, concomitant with a spike in In ($t \approx 55$ s), most likely arises from the presence of In_4Se_3 in this region, formed from the In islands observed in Cu-In-Al as-deposited precursors (section 5.4). Normally present at the film surface, these islands are here buried underneath the 100 nm thick Cu cap (unlike results for N582L, where 50 nm were insufficient).

In N582Q (350°C), the CIS phase shows an important growth resulting from the total consumption of $CuSe_2$ and In_4Se_3, to form CIS. This was made possible by the peritectic decomposition of $CuSe_2$ into CuSe and a Se melt at 340°C, to form CIS via reaction 6.6. A better penetration of the Se from the front into the bulk is also an important factor in this enhanced growth.

In N582K (450°C), the maximum temperature was high enough to consume some of the Cu_2Se (high temperature form of $Cu_{2-x}Se$) to form CIS via reaction 6.3. This is supported by the dampening of the (111) reflections of the rightmost $Cu_{2-x}Se$ phase in the figure, and the slight growth of the CIS phase compared to N582Q.

N535W (540°C) is very similar to N582K, which makes sense since all the indium selenides had already been consumed at 450°C. The increased presence of Cu at the surface is indicative of an increased volume of $Cu_{2-x}Se$ in this region. Al is once again absent from the XRD phases at all temperatures tested. Its aggregation as amorphous Al_2O_3 is again the most likely explanation, although the oxygen level is much lower than in the RTP samples. The segregation of Al at the back (GD-OES) has already taken place at 250°C (N582O). This phenomenon is very similar to the observed segregation of Ga at the back of 2-stage processed CIGS [135]. The most commonly advanced cause is the relatively high temperature of formation of Ga selenides compared to In selenides [14, 135]. This hypothesis also applies for CIAS, since the only known selenide of aluminium is Al_2Se_3, which was reported to form at 480°C [100], against 221°C for the first In selenides. At the melting point of Se, In and Cu are driven towards the front by the formation of selenides with the liquid Se which started diffusing, while Al stays at the back since it cannot form any selenide. As the temperature increases, the binary selenides of In and Cu then go on to forming CIS, while Al stays at the back up to 480-490°C, when it starts forming

CIAS and/or CAS [100]. At this stage, only interdiffusion between the CIS at the front and the CAS (or low In-content CIAS) at the back can yield a single phase CIAS bulk. This interdiffusion clearly did not occur in the selenised samples. An important difference with N582L1, selenised at the same maximum temperature in the RTP, is that N535W shows a clear segregation of Al at the back in N535W, while it was present (although not uniformly distributed) throughout the bulk in N582L1. This supports the hypothesis of the earlier formation of In_xSe_y and Cu_xSe_y as the cause of this segregation, since the faster ramping rate applied in the RTP partially prevented it. However, neither in the RTP or the TF did any incorporation of Al into the chalcopyrite lattice seem to occur.

7.6 Selenisation study (TF): impact of the [Al]/([Al]+[In]) ratio

7.6.1 Data

X-ray diffraction

The effect of altering the x=[Al]/([Al]+[In]) ratio was tested on four samples, all selenised in similar conditions. The results are reported in Figure 73. The compositions x=0.11 (N591W) and x=0.31 (N587H) did not yield any incorporation of the aluminium, and the element was not present in any of the crystalline phases, or the degree of crystallinity was too low for them to be detected. For x=0.38, however, some Al-incorporation was observed in N394B4. The pattern of this sample shows that several overlapping phases are present, which remained after KCN etching. At x=0.51 (N783D1), some CIAS was also observed, but only as traces, and CAS was found as well. This last phase is visible in the increase of intensity and area, relative to the CIS (112) peak, of the peak normally assigned to CIS (103).
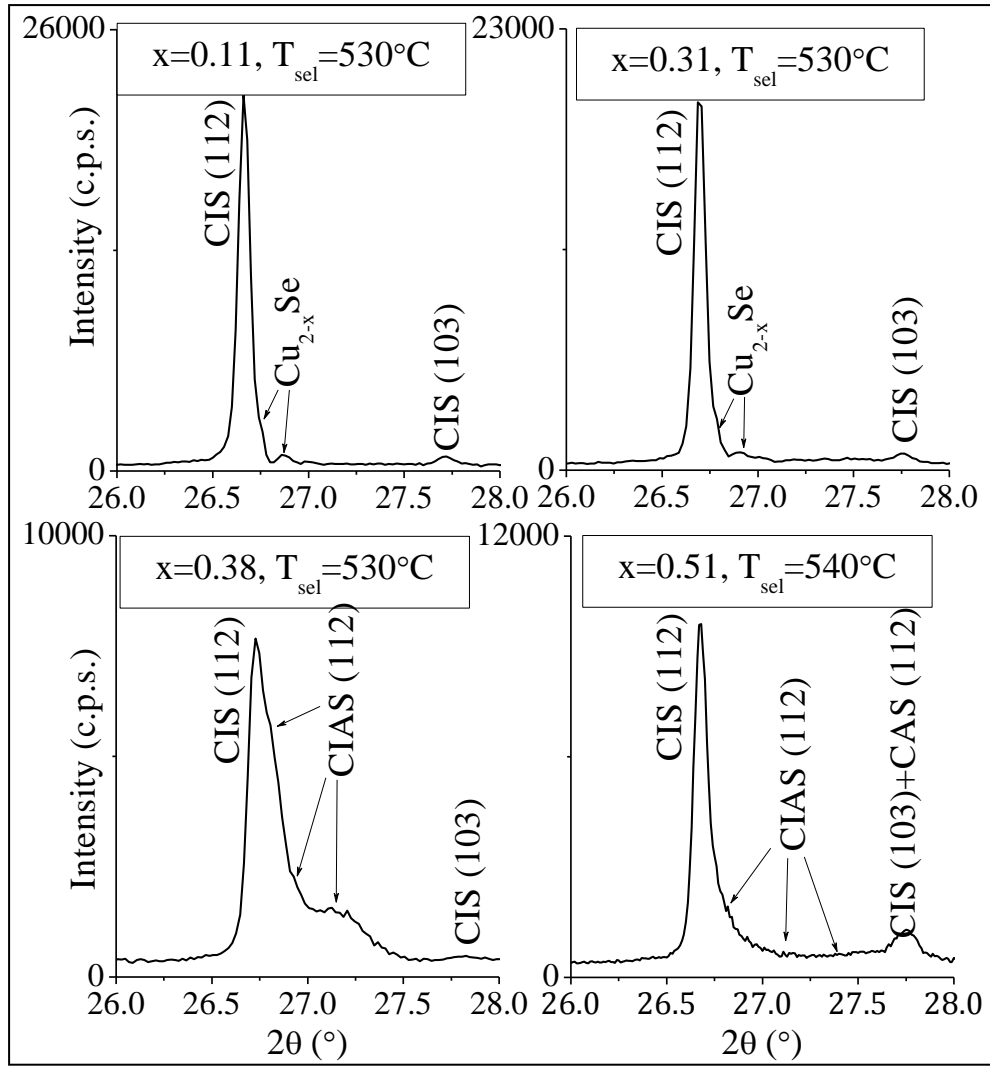
Figure 73: XRD patterns of four Cu-In-Al precursors of different x=[Al]/([Al]+[In]) ratios, N591W (x=0.11, 530°C), N587H (x=0.31, 530°C), N394B4 (x=0.38, 530°C) and N783D1 (x=0.51, 540°C).

Glow discharge optical emission spectroscopy

GD-OES was performed on N394B4 (Figure 74). As opposed to the results obtained at the same maximum temperature with x=0.11 in N535W (section 7.5), the Al did not here segregate entirely at the back, but instead decreases from the back to the front, before increasing again at **b**. Indium follows a reverse trend to Al, with a decreasing intensity from front to back, while Cu and Se are more evenly distributed through the bulk. Cu, Se and O are also seen to increase at the surface (**a**). The

increase of all elements at the back (*c*) is an artefact associated with the rise of the

Mo. The incorporation observed in N394B4 was not, however, a reproducible result.
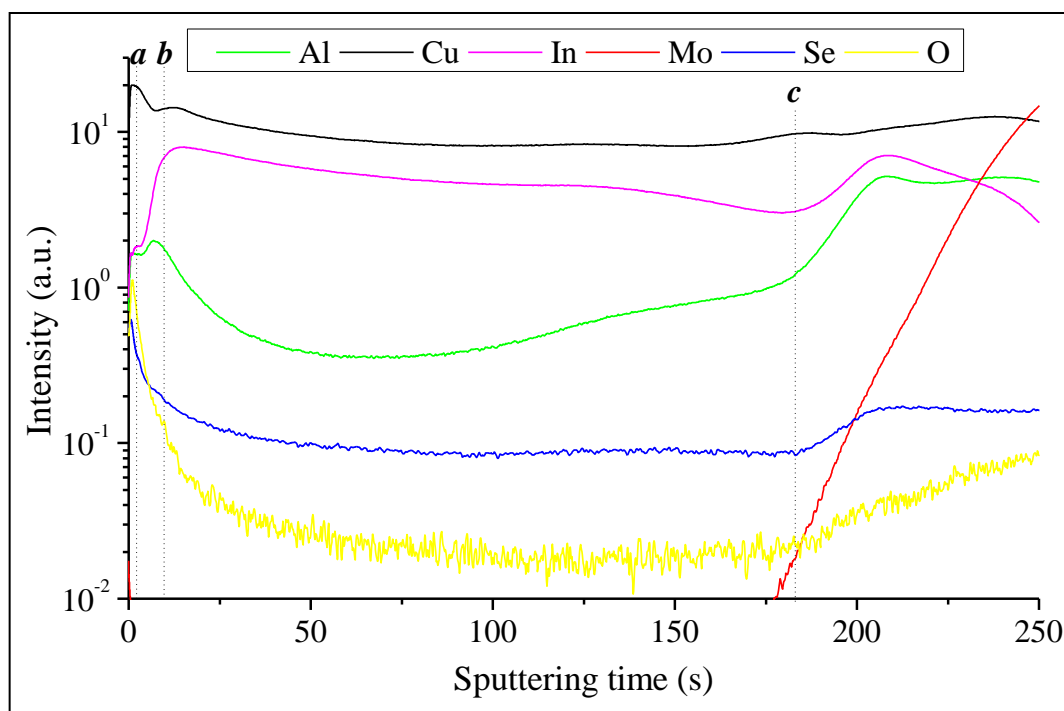
Figure 74: GD-OES depth profile of N394B4 (x=0.38, 530°C, 30 min, 10 mbar H2/N2).

N394C1, consisting of the same metallic precursor, and selenised together with

N394B4, also showed some incorporation of the Al, but the XRD pattern suggests a

different distribution of the Al incorporated (Figure 75), since the different

overlapping $CuIn_{1-x}Al_xSe_2$ (112) peaks have different shifts, and therefore different x

ratios. In particular, some Al seems to have segregated completely from the In,

leading the formation of a $CuAlSe_2$ phase.
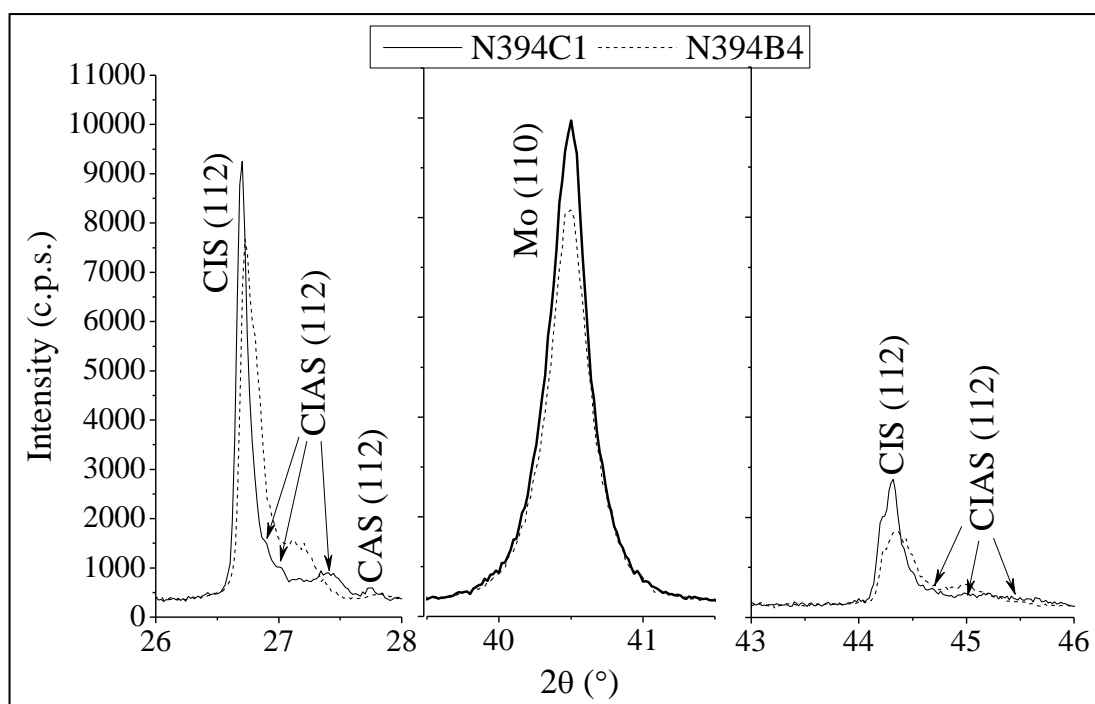
Figure 75: XRD patterns of N394C1 and N394B4, identical precursors (x=0.38) selenised together in the tube furnace (530°C, 30 min, 10 mbar H$_2$/N$_2$).

EDS/WDS cross section analysis

Conjoint EDS and WDS were carried out on the cross section of N394C1, in order to correlate the elemental distribution with particular features observed in the SEM micrograph of the cross section (Figure 76). WDS was used to measure the elements Al and Se, while EDS analysed Cu and In. No compositions could be extracted from the WDS/EDS linescan because WDS, unlike EDS, requires calibration for which the suitable standards were not available. This technique also suffers from inherently low spatial resolution, because of the size of the interaction volume between electron beam and the sample already mentioned. Therefore, the signal detected at each point can be seen as a weighted average of the signals emitted from a disk around the point scanned. The effect of this low resolution shows in the slope of the interface with the Mo. However, some valuable information can still be drawn from Figure 76 (a).
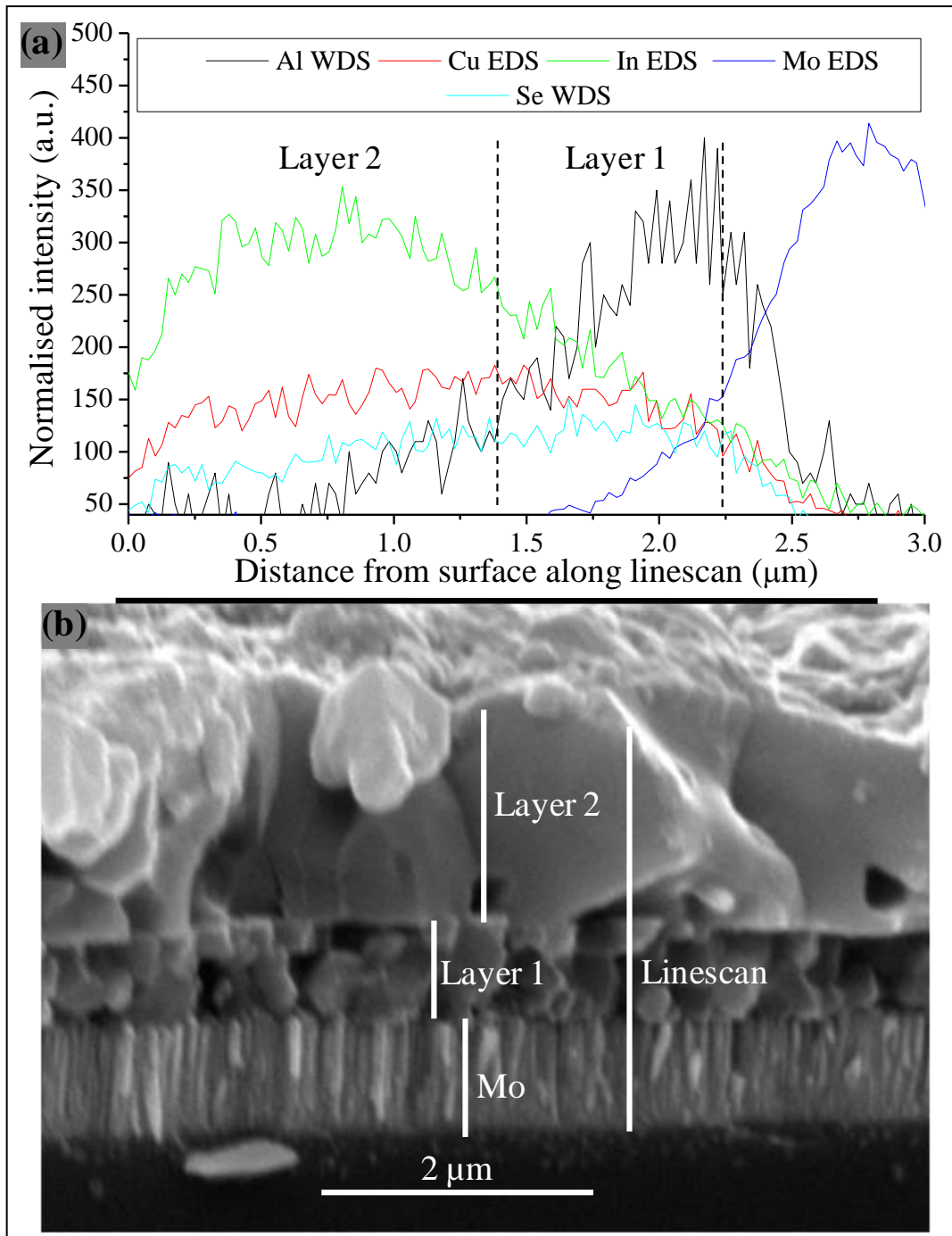
Figure 76: WDS/EDS linescan *(a)* performed along the cross section of N394C1 (x=0.38, 530°C, 30 min, 10 mbar H_2/N_2). Next to each element is indicated what detection technique was used. The linescan along which the measurement was done is shown on the SEM micrograph of the cross section *(b)*.

In particular, segregation is visible between Al, more present at the back, and Cu and In, more present in the body of the bulk. Two grain size regions are visible in Figure 76 (b): a small grained region at the interface with the Mo (***Layer 1***), and a large

grained region between this layer and the film surface (***Layer 2***). Therefore, *layer 1* is more Al-rich, while *layer 2* is more In-rich.

7.6.2 Discussion

No incorporation of the Al into the CIS lattice or any other crystalline phase is observed for compositions below x=0.38 (XRD). At this composition, although some CIAS formed, it is not single phase (i.e. only one x value throughout), but instead a grading of Al and In is present, leading to partial phase separation. The distribution observed (XRD, GD-OES) also varies from one sample to the next, for no discernable reason. Cross section WDS and EDS shows that the incorporation of Al into the chalcopyrite lattice yields smaller grain size, which ties up with the low crystallinity observed for the CIAS phases (XRD). It is unclear whether the different CIAS phases observed are a result of the sole depth distribution of the elements Al and In, or if they also result from variable degrees of incorporation of Al, or even from a non-homogeneous lateral distribution. At x=0.51, finally, almost complete segregation between CIS and CAS was observed, with only small or low crystallinity intermediary CIAS phases.

CHAPTER 8 ALTERNATIVE CuIn$_{1-x}$Al$_x$Se$_2$ PRECURSOR LAYOUTS AND POST SELENISATION ANNEAL IN THE TUBE FURNACE

In this chapter are reposted the results on alternative layouts of metallic precursors, designed to prevent the segregation of Al from In. A process which led, in the past, to reincorporation of segregated Ga in CIGS, is also tested on a sample which showed segregation after selenisation. Table 21, summarising the data on sample fabrication, can be found in section 8.1.

8.1 Fabrication data on the samples of the chapter

Table 21: Sample deposition and processing data summary. The compositions in italics are interpolated from single matrix precursors. In the "layout" column, the layers are indicated by order of deposition.

Page	ID	Substrate	Target	Layout	Comp. (at%)			Se?	Furnace	P^{re} (mbar)	Gas	Dwell T^{re} (°C)	Dwell dur. (s)	Ramp dur. (s)
					Cu	In	Al							
181	N510J	SLG/Mo	elem.	Cu-In/Cu-In-Al/Cu	*51.0*	*42.5*	*6.5*	Yes	TF	10	H_2/N_2	450	1800	≈1500
181	N557E	SLG/Mo	elem.	Cu-In/Cu-In-Al/Cu	*51.0*	*42.5*	*6.5*	Yes	TF	10	H_2/N_2	530	1800	≈1800
181-182	N557O	SLG/Mo	elem.	Cu-In/Cu-In-Al/Cu	*51.0*	*42.5*	*6.5*	Yes	TF	10	H_2/N_2	550	1800	≈1850
186-190,193	N782A	SLG/Mo	elem.	Cu-In/Al	*48.0*	*25.0*	*27.0*	Yes	TF	10	Ar	540	1800	≈1800
186-190	N782G	quartz/Mo	elem.	Cu-In/Al	*49.0*	*35.0*	*16.0*	Yes	TF	10	Ar	540	1800	≈1800
185-186	N783A	quartz/Mo	elem.	Cu-In-Al	48.0	25.0	27.0	Yes	TF	10	Ar	540	1800	≈1800
190-192,194,198-199	N782C1	SLG/Mo	elem.	In/Al/Cu	*48.0*	*25.0*	*27.0*	Yes	TF	10	Ar	540	1800	≈1800
186-187	N535K	SLG/Mo	elem.	Cu-In-Al	51.0	34.0	15.0		N/A					
188-190	N782E	SLG/Mo	elem.	In/Al/Cu	*48.0*	*25.0*	*27.0*		N/A					
190-199	N782B1	SLG/Mo	elem.	Cu-In/Al	*48.0*	*25.0*	*27.0*	Yes	TF	10	Ar	540	1800	≈1800
190-192,194-195,197-199,220	N782F1	SLG/Mo	elem.	Cu-In/Al	*49.0*	*35.0*	*16.0*	Yes	TF	10	Ar	540	1800	≈1800

8.2 Cu-In/Cu-In-Al/Cu

Since the depth distribution appeared to be a major hindrance to forming single phase CIAS in the tube furnace, alternative layouts were devised to overcome the tendency of Al and In to segregation.

8.2.1 Experimental

The first two layouts tested were:

(a) SLG/Cu-In/Cu-In-Al, where the Al was localised away from the back, to compensate for its diffusion.

(b) SLG/Cu-In/Cu-In-Al/Cu, identical to (a) but for an additional Cu layer at the surface.

However, layout **(a)** showed an important degree of evaporation, especially in the high temperature range (530-550°C), so that the study was carried on with layout **(b)** only. After depositing each layer of the stack (i.e. Cu-In and then Cu-In-Al), one platen containing a test sample was taken out, to measure the composition deposited. The Cu-In layer was of composition [Cu]/[In]≈0.92, and ≈300 nm thick. The Cu-In-Al layer, of similar thickness, was of composition x=0.27 and [Cu]/([Al]+[In])≈0.90. The Cu capping layer was ≈100 nm thick, and made the overall composition Cu-rich. The temperatures tested in the tube furnace were 450°C, 530°C and 550°C. Several selenisation runs were performed at each of the three temperatures, to make sure that the results were reproducible. All the results were found to be consistent, with only slight changes in the diffraction intensities of some copper selenide peaks.

8.2.2 Data

X-ray diffraction

The results obtained with 30 minutes dwell at the three temperatures, before and after etching in KCN, are summarised in Figure 77.
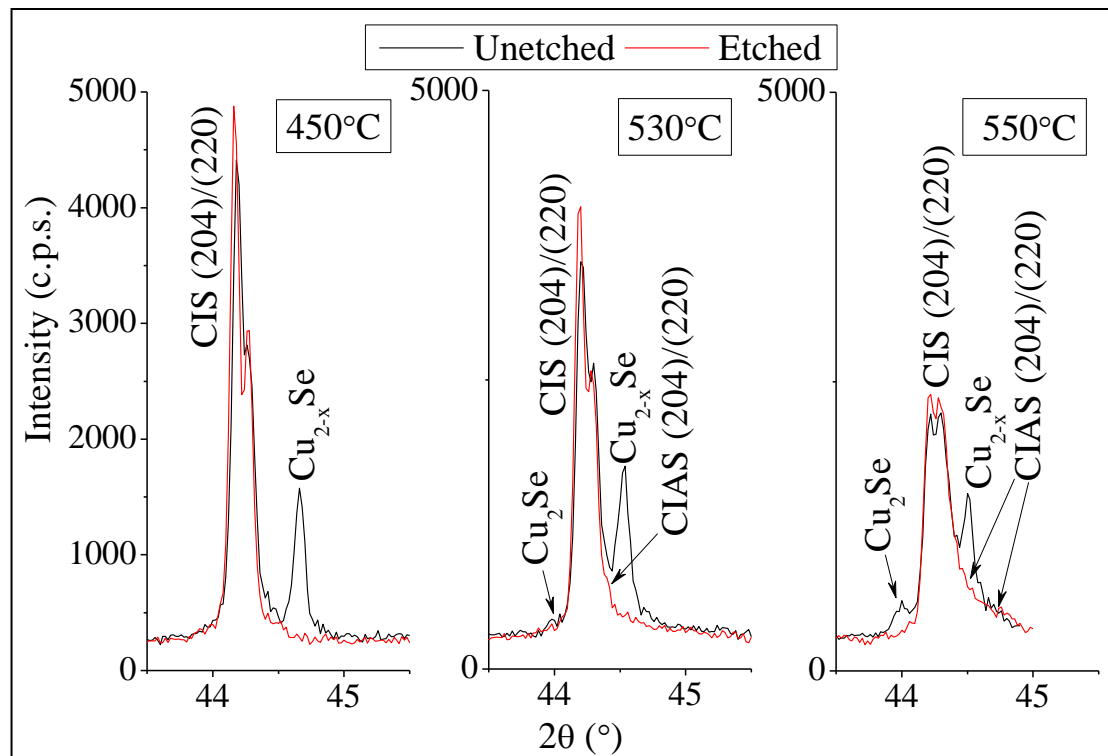
Figure 77: XRD patterns of three Cu-In/Cu-In-Al/Cu precursors selenised in the tube furnace (30 min dwell, 10 mbar H2/N2), N510J (450°C), N557E (530°C) and N557O (550°C). In each box, the unetched pattern (black line) is compared to the pattern obtained after the 30 s etching in 5 wt% KCN (red line).

The range of detection angles represented focuses around CIS (204)/(220) reflections instead of the (112) plane used before, in order to see more clearly the different phases present. The XRD patterns show that $Cu_{2-x}Se$ is present at all three temperatures, while the first phases identified as $CuIn_{1-x}Al_xSe_2$ only start forming at 530°C (N557E), as traces, and then develop at 550°C (N557O). At 450°C and 530°C, some Cu_2Se is also detected. Cu_2Se and $Cu_{2-x}Se$ are no longer found in the patterns of the etched samples. Between 530°C and 550°C, the CIS (204)/(220) peaks intensity decreases while that of CIAS increases. This is visible in the decreasing intensity of the leftmost peak of the CIS doublet (204)/(220). The

rightmost peak of the doublet decreases less because of the multiple overlapping CIAS peaks, which are growing. Although deconvolution is made difficult at 550°C by the presence of many overlapping CIAS (204)/(220) reflections, this trend seems to correspond to a decrease in CIS peak area and a concomitant increase of the CIAS peak area.

Energy dispersive spectroscopy

The sample N557O selenised at 550°C was etched in KCN. Its EDS composition was unfortunately not measured before etch, so another sample from the same deposition batch and selenised in the same conditions was used instead to assess the EDS composition of unetched sample (N557Y). The XRD patterns of the two samples prior to etching were very close, with only slight variations in the intensity of the peaks. In Table 22 are compared the compositions of the two samples.

Table 22: EDS composition of Cu-In/Cu-In-Al/Cu precursors selenised in identical conditions at 550°C before (N557Y) and after (N557O) etching in KCN.

Sample ID	EDS composition (at %)						Cu/(Al+In)	Se/(Cu+In+Al)
	Cu	In	Al	Se	Mo	O		
N557Y (unetched)	29.7	15.6	3.1	39.3	0.1	12.3	1.59	0.81
N557O (etched)	23.0	20.8	3.1	42.5	0.9	9.7	0.96	0.91

The relative O and Cu contents decrease after etching, while the relative In and Se contents increase.

8.2.3 Discussion

The abundance of $Cu_{2-x}Se$ is due to the overall Cu-rich composition induced by the Cu cap. The increasing formation of Cu_2Se at 530°C and then 550°C could be due to an increased diffusion of Se into the bulk. This hypothesis would account for the decrease of the amount of Se at the surface and lead some $Cu_{2-x}Se$ to convert into the more Se-deficient phase Cu_2Se. The absence of CIAS at 450°C was expected, since

the temperature of formation reported for CIAS by Jost *et al.* [100] is 490°C. The decrease of the CIS peak area and the conjointly increasing area of CIAS peaks as the maximum temperature is increased to 530°C and then 550°C can be understood as a transformation of CIS into CIAS, as more Al is incorporated into the CIS chalcopyrite structure. However, the tendency, already mentioned in section 7.4, of part of the sample to evaporate at 530°C could also explain part of the CIS decrease. EDS also shows a small increase of the Mo content detected (from 0.1% to 0.9%), which seems to confirm that some evaporation indeed happened.

8.3   Cu-In/Al and In/Al/Cu

Other layouts were tested near the end of this work:

(a) Cu-In/Al, to limit by diffusion the access of In to the selenium.

(b) In/Al/Cu, for the same reason as (a), but with the additional effect of the Cu capping layer.

The ideas behind these layouts were the following. In layout (a), In and Se would need to diffuse through the Al layer to meet.

This process could allow enough time for the process to reach 480°C, at which temperature Al_2Se_3 starts forming. Indeed, as demonstrated by the comparison between the results of sections 7.3 and 7.4, the formation of the In binary selenides at lower temperature than the Al selenides is the main cause of segregation. Less segregation would therefore be expected to occur in layout **(a)** before Al_2Se_3, and therefore CIAS, can form. Layout **(b)** aimed at producing the same delay in segregation, but with possible additional benefits of the Cu capping, namely:

(i)   Reduced exposure of Al to the oxygen present in the chamber.

(ii) Better capture of Se at low temperature, since CuSe$_2$ starts forming at 221°C, the melting point of Se.

Note that layout (**b**) is a type of design known as "stacked elemental layers" (SEL), commonly used in in-line deposition processes (see section 3.3.2).

8.3.1 Experimental

In order to be able to perform transmittance measurements on the films, a stripe of each substrate (SLG or Mo) was covered with a blank slide during Mo deposition. This covering slide was then removed for the deposition of the precursor layer, resulting in a portion of the film being deposited on the bare substrate, and the rest being deposited on the Mo-coated part of the substrate (see Figure 78). The samples were deposited from elemental targets of Cu, In and Al, and two x=[Al]/([Al]+[In]) ratios were tested: x≈0.31 and x≈0.52. However, the deposition of the layout In/Al/Cu failed at x=0.31, and only Cu-In/Al could be deposited at this x ratio. To determine the target powers and deposition times to apply, sets of powers that had produced the desired composition in the recent deposition history were applied on the three targets at the same time, so as to deposit a Cu-In-Al mixed matrix layer, on a test sample. The mass of metallic precursor deposited and the EDS composition were then measured, in order to check the deposition rate of each element, so that the powers could be adjusted when necessary. Once the sets of powers had been determined, the different layouts were deposited using these deposition parameters. For example, if the desired set of powers $P_{Cu}^{0.52}$, $P_{In}^{0.52}$ and $P_{Al}^{0.52}$, and deposition time $t^{0.52}$, had been determined to yield x=0.52 and the desired [Cu]/([In]+[Al]) ratio and thickness, then the Cu-In/Al layer was deposited by applying first $P_{Cu}^{0.52}$ and $P_{In}^{0.52}$ together for a duration $t^{0.52}$, and then $P_{Al}^{0.52}$ for $t^{0.52}$.
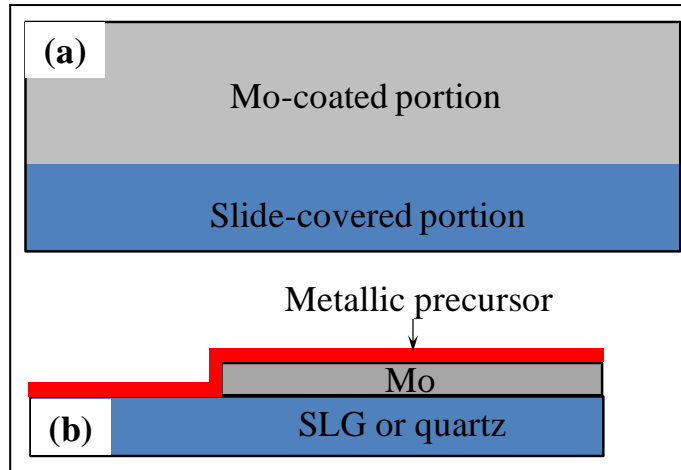
Figure 78: Illustration of the method used to obtain partial Mo coating of the substrate. *(a) top view of the slide after Mo deposition, (b) side-view along the width of the sample after metallic precursor deposition.*

In the same way, the layout In/Al/Cu was deposited by applying successively $P_{Cu}^{0.52}$, $P_{In}^{0.52}$ and $P_{Al}^{0.52}$ for the duration $t^{0.52}$ each time. The total amount of Cu deposited was kept constant, by adapting the deposition time, between the depositions at x=0.52 and x=0.31. This was done to make sure that a similar amount of material was present in both types of films, since EDS cannot determine the composition of such inhomogeneous layouts. The precursors, once characterised, were then selenised in the tube furnace for 30 minutes at 540°C in 10 mbar of Ar and characterised again (section 8.3.4). The amount of Se provided corresponded to about five times the amount required to reach stoichiometry.

8.3.2 Precursor data

Energy dispersive spectroscopy

The composition measured by EDS on the part of the precursor deposited on Mo was compared to that of the part deposited on the bare substrate (Table 23). On N783A, the measurements were performed near the edge between Mo-coated and uncoated part, to ensure that the variations were really due to the substrate. A higher Al

content was consistently observed on the bare substrate in all the precursors tested, and even more so on quartz substrates. The content in O, on the other hand, does not seem to vary considerably.

Table 23: EDS compositions of precursors N782A, N782G, N783D, N783A, measured on the Mo-coated part and the uncoated part.

N782A	EDS composition (at %)						Cu/(Al+In)	Al/(Al+In)
Cu-In/Al x=0.52	Cu	In	Al	Mo	Si	O		
Loc. 1 on Mo	32.2	17.5	40.0	6.2	0.3	3.8	0.56	**0.70**
Loc. 2 on SLG	33.1	17.6	43.7	-0.1	2.8	3.0	0.54	**0.71**
N782G	Cu	In	Al	Mo	Si	O	Cu/(Al+In)	Al/(Al+In)
(Cu-In/Al								
Loc. 1 on Mo	35.0	27.2	26.1	6.3	0.5	4.9	0.65	**0.49**
Loc. 2 on quartz	35.5	27.6	30.6	-0.1	2.7	3.7	0.61	**0.53**
N783D	Cu	In	Al	Mo	Si	O	Cu/(Al+In)	Al/(Al+In)
Cu-In-Al x=0.52								
Location 1 on	41.1	21.7	23.2	8.7	0.2	5.1	0.92	**0.52**
Loc. 2 on SLG	42.9	21.6	25.6	0.1	4.5	5.3	0.91	**0.54**
N783A	Cu	In	Al	Mo	Si	O	Cu/(Al+In)	Al/(Al+In)
(Cu-In-Al								
Loc. 1 on Mo	41.7	21.1	22.1	9.8	0.2	5.2	0.97	**0.51**
Loc. 2 on quartz	43.2	21.1	24.3	0.2	7.0	4.2	0.95	**0.54**

The measurements performed on the Mo side of all the precursors deposited are summarized in Table 24.

Table 24: EDS composition of the precursors tested. In bold is emphasized the element that should be the most overestimated by the EDS setup as a result of the layout.

Sample ID	EDS composition (at %)						Cu/In	Al/(Al+In)
	Cu	In	Al	Mo	Si	O		
N783D (Cu-In-Al x=0.52)	41.2	21.3	22.7	9.4	0.3	5.2	1.93	0.52
N782A (Cu-In/Al x=0.52)	32.2	17.5	**40.0**	6.2	0.3	3.8	1.84	**0.70**
N782C (In/Al/Cu x=0.52)	**48.6**	23.5	9.1	13.2	0.3	5.3	**2.06**	0.28
N535K (Cu-In-Al x=0.31)	49.1	32.9	14.6	0.2	0.0	3.2	1.49	0.31
N782G (Cu-In/Al x=0.31)	35.0	27.2	**26.1**	6.3	0.5	4.9	1.28	**0.49**

The compositions of the Cu-In-Al mixed matrices x=0.52 (N783D) and x=0.31 (N535K) are shown for comparison. Note however that the deposition parameters of

the x=0.31 samples were slightly altered compared to N535K, which was a test sample, in order to obtain a little less copper and a film thickness comparable to the x=0.52 films. Several comments can be made about this table. In the two Cu-In/Al layouts (N782A and N782G), the amount of Al detected is overestimated, because the Al layer is located at the top.

Furthermore, the ratios [Cu]/[In] in the Cu-In-Al matrix and in the Cu-In/Al layout can be compared. They are found to be 1.93 in N783D against 1.84 in N782A (x=0.52), and 1.49 in N535K against 1.28 in N782G (x=0.31). This seems to indicate that in both cases, the In composition is overestimated, although this is much more pronounced at x=0.31. In N782C (In/Al/Cu layout, x=0.52), [Cu] is overestimated because of the Cu layer present at the top. Another striking feature is the [Al]/([Al]+[In]) ratio of 0.28, in apparent contradiction with the fact that the Al was deposited on top of the In, and that x=0.52 was measured in the Cu-In-Al precursor.

Scanning electron microscope

The micrographs of the samples are shown in Figure 79. N782C (In/Al/Cu, x=0.52, image (a)) is covered with two types of features: one type small, and darker on the picture, the other type bigger, and brighter on the picture. The latter resemble the type of In islands reported by Chung *et al.* [118]. The surface of N782A (Cu-In/Al, x=0.52) is smooth, apart from small round features scarcely spread. N782G (Cu-In/Al, x=0.31) is covered with features very similar to the In islands observed in section 5.4.
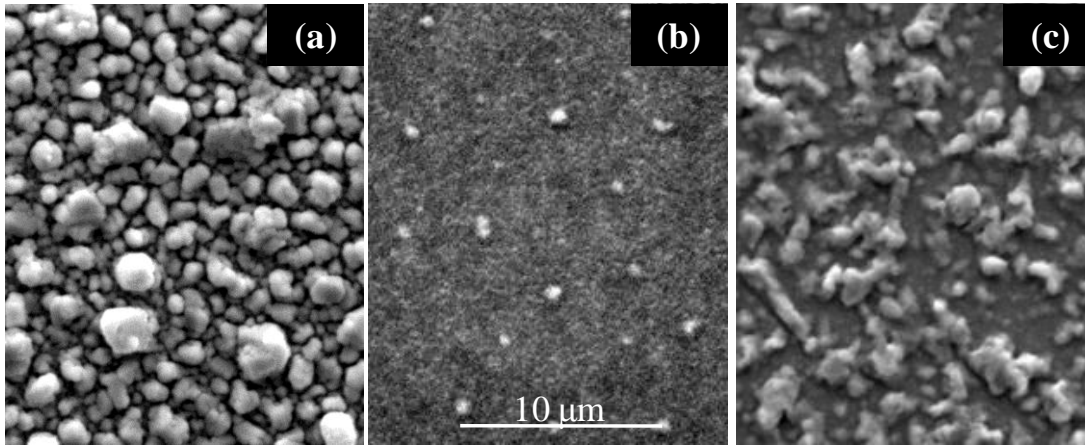
Figure 79: Scanning electron micrographs of *(a)* **N782C (In/Al/Cu, x=0.52),** *(b)* **N782A (Cu-In/Al, x=0.52) and** *(c)* **N782G (Cu-In/Al, x=0.31).**

X-ray diffraction

The XRD patterns obtained on the three alternative precursors, N782E (In/Al/Cu, x=0.52), N782A (Cu-In/Al, x=0.52) and N782G (Cu-In/Al, x=0.31) are shown in Figure 80.
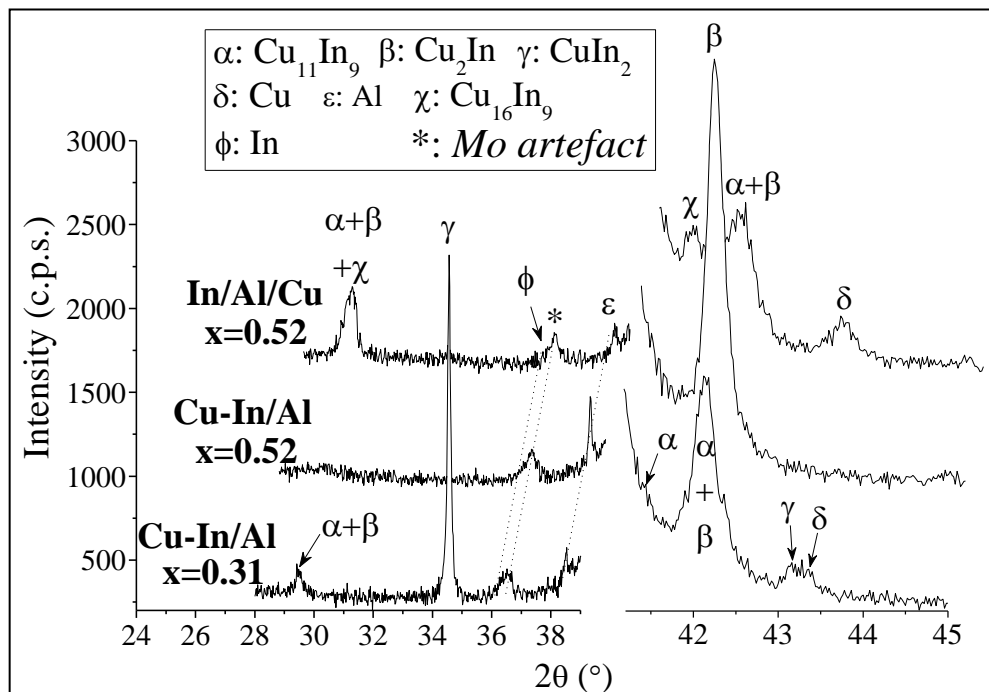
Figure 80: XRD patterns of the precursors N782E (In/Al/Cu, x=0.52), N782A (Cu-In/Al, x=0.52) and N782G (Cu-In/Al, x=0.31).

In N782E (In/Al/Cu, x=0.52) are found the phases $Cu_{11}In_9$ (PDF 00-041-0883), Cu_2In (PDF 00-042-1475) and $Cu_{16}In_9$ (PDF 00-026-0522), in spite of the fact that the In layer was meant to be separated from the Cu layer by the Al layer. Elemental Cu (PDF 00-004-0836), Al (PDF 00-004-0787) and traces of In (PDF 00-005-0642) are also detected. In N782A (Cu-In/Al, x=0.52), only Cu_2In, elemental Al and traces of In can be found. In N782G (Cu-In/Al, x=0.31), $Cu_{11}In_9$, Cu_2In, In, Al and Cu are present, along with the additional phase $CuIn_2$.

8.3.3 Discussion of the precursors

The EDS data suggests that a process drives some of the In above the Al layer in both Cu-In/Al and In/Al/Cu layouts. In/Al/Cu (N782E) is the most striking case, since the In mixed with the Cu even though the Al layer was deposited in between those layers. In this case, only a marginal presence of crystalline In is detected (XRD), which could mean that almost all the In has reached the Cu layer and mixed with it. Indeed, since no binary compound exists between In and Al, and In is known to form aggregates (islands) when on its own, it seems that, as Al was deposited, these In islands either extend throughout the Al layer and shoot up at its surface, or stayed "afloat" on top of the Al layer during the deposition. Furthermore, unlike N428Y (Cu-In-Al, x=0.56) studied in section 5.4, no Cu_4Al or any other Cu_xAl_y phase was formed, indicating limited contact between Al and Cu. The sputtering of Cu on top could therefore have caused the formation of Cu-In compounds.

In N782A (Cu-In/Al, x=0.52), the presence of Cu_2In and only a small amount of In (XRD) is compatible with the [Cu]/[In] ratio (EDS) of 1.84 (1.93 in the mixed matrix). The fact that no elemental Cu is left indicates that mixing of the two phases is complete, and the quasi absence of In "islands" on the film surface (SEM) shows

that the Al layer was thick enough to cover the surface completely. Unlike the case of N782E, the In was here already bound with Cu, which can explain that In didn't migrate on top of the Al layer.

In N782G (Cu-In/Al, x=0.31), finally, In is seen at the film surface (SEM), and the In phase is slightly more present (XRD) than in N782A, while the [Cu]/[In] ratio is considerably smaller than in the mixed matrix (1.28 against 1.49). This is most likely due to the lower [Cu]/[In] ratio in this film.

The XRD data confirms a change in stoichiometry, with the formation of $CuIn_2$, of higher In content than Cu_2In, which was the only Cu-In binary phase observed in N782A (x=0.52). The higher In content of the Cu-In matrix can have led to the formation of In islands, which ended up at the film surface. However, Chung *et al.* [118] reported the formation of In islands in co-sputtered Cu-In for [Cu]/[In]<0.61 only, a condition which is not satisfied here. The use of RF sputtering (as opposed to DC in the paper) and the power applied to the targets might influence the formation of islands as well, and explain the discrepancy. The higher Al content detected in the part of the precursor deposited on glass has not found an explanation. This does not seem to be related to a lower adhesion of Al onto this substrate, since the trend is observed even in Cu-In/Al, where only the adhesion of Al onto the Cu_xIn_y phases would matter.

8.3.4 Absorber data

The three alternative layout precursors N782C1 (In/Al/Cu, x=0.52), N782B1 (Cu-In/Al, x=0.52) and N782F1 (Cu-In/Al, x=0.31), and, for comparison, the mixed matrix N783D1 (Cu-In-Al, x=0.52), were selenised together in the tube furnace at 540°C. The XRD patterns obtained on the selenised samples are shown in Figure 81.

Figure 81: XRD patterns of the four types of precursor layouts selenised in the tube furnace (540°C, 30 min dwell, 10 mbar Ar), N783D1 (Cu-In-Al, x=0.52), N782C1 (In/Al/Cu, x=0.52), N782B1 (Cu-In/Al, x=0.52) and N782F1 (Cu-In/Al, x=0.31).

All samples contain CIS and CAS, as well as some CIAS phases in all except N782B1. N782B1 and N783D1 also contain $Cu_{2-x}Se$. N783D1 (Cu-In-Al) was already discussed in section 7.6. In the diffraction pattern of N782C1 (In/Al/Cu), both CIS and CAS seem relatively abundant, with (112) under-peak areas of 1440 and 560 respectively. The CIS (112) crystallites are of size $\geq$105 nm, while the CAS (112) crystallites are $\geq$50 nm. The most shifted CIAS (112) reflections correspond to x<0.19 (0.52 in the as-deposited precursor). In N782B1 (Cu-In/Al, x=0.52), the crystallinities of the CIS and CAS phases are very similar to N782C1, with $\geq$100 nm and $\geq$50 nm crystallites respectively, but the peak areas are smaller for both CIS (112) and CAS (112), with 530 and 220, respectively. No CIAS was present and $Cu_{2-x}Se$ was detected. The full scan of this sample (not shown) also revealed the presence of the phases $MoSe_2$, Cu_9Al_4, Al, CuSe and possibly traces of InSe. Finally, In N782F1 (Cu-In/Al, x=0.31), the crystallite sizes of the CIS and CAS phases are estimated as 100 nm and 140 nm respectively, and the peak areas 1200 and 12.

191

Furthermore, multiple CIAS phases are found, for which compositions range between x=0 and x=1. The cumulated areas of the fitted CIAS (112) peaks are estimated at 970 in N782F1 and 500 in N782C1.

SEM micrographs of these samples are displayed in Figure 82. Small regions of N782F1 have evaporated, resulting in multiple pinholes, on both the Mo-coated part and the non-coated part. For comparison, the standard Cu-In-Al layout (N783D1) only contains pinholes on the non-coated part. N782B1 shows big dark regions surrounded by bigger, shiny regions, as well as an important evaporation on the glass. N782C1, on the other hand, seems relatively preserved, and no sign of evaporation can be seen.

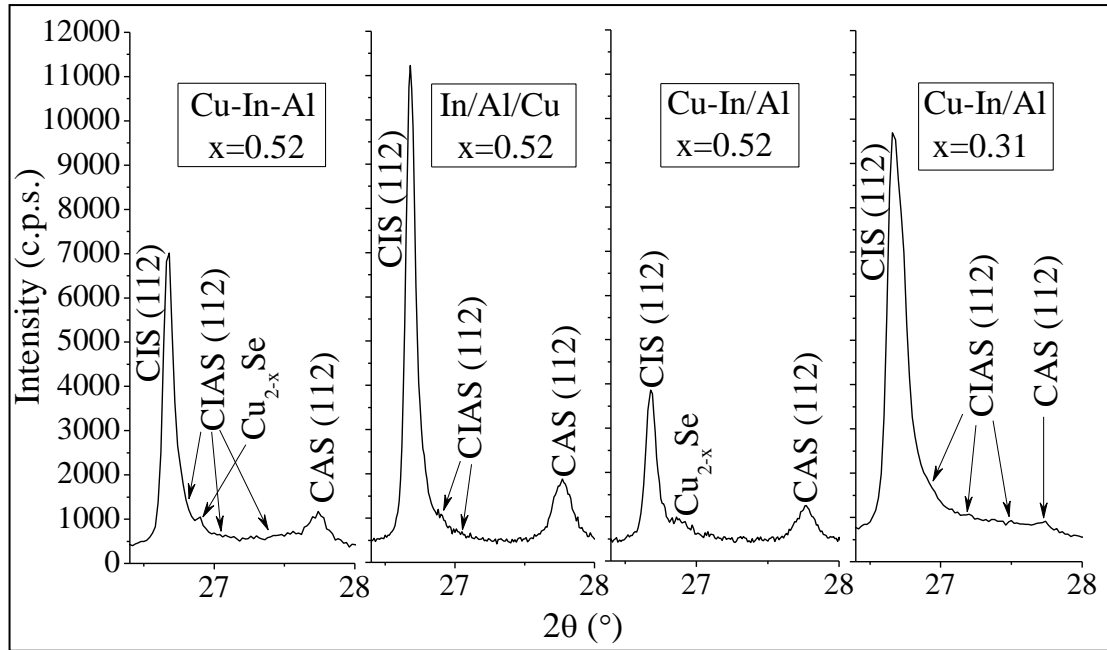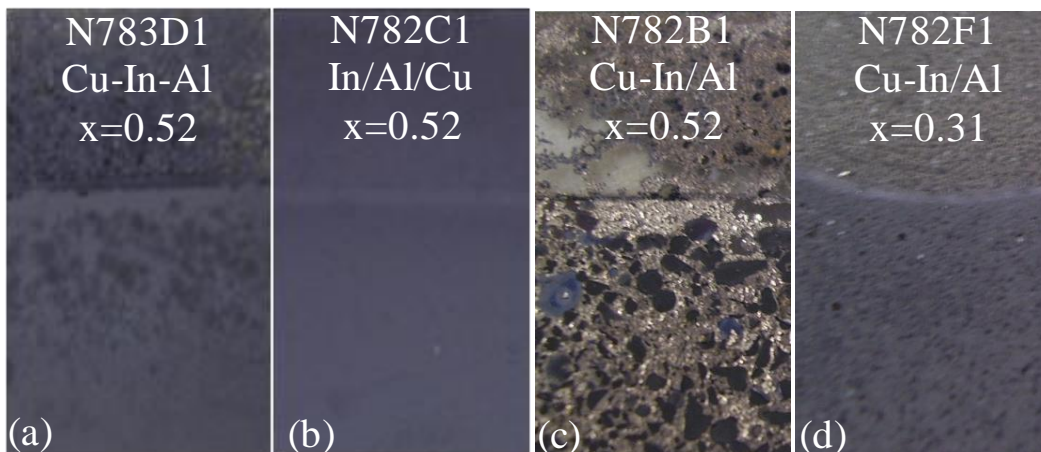**Figure 82: Photographs of the four types of precursor layouts selenised in the tube furnace (540°C, 30 min dwell, 10 mbar Ar),** *(a)* **N783D1 (Cu-In-Al, x=0.52),** *(b)* **N782C1 (In/Al/Cu, x=0.52),** *(c)* **N782B1 (Cu-In/Al, x=0.52) and** *(d)* **N782F1 (Cu-In/Al, x=0.31). The top part on the photographs is directly on glass, while the bottom part is on Mo-coated glass.**

SEM micrographs of N782B1 are shown in Figure 83.

Cu	In	Al	Se
41.0	2.6	25.5	1.8

Mo	Si	O
17.1	0.3	11.7

Cu	In	Al	Se
1.0	10.8	2.2	40.3

Mo	Si	O
38.9	0.4	6.5

10 μm   250 μm   10 μm
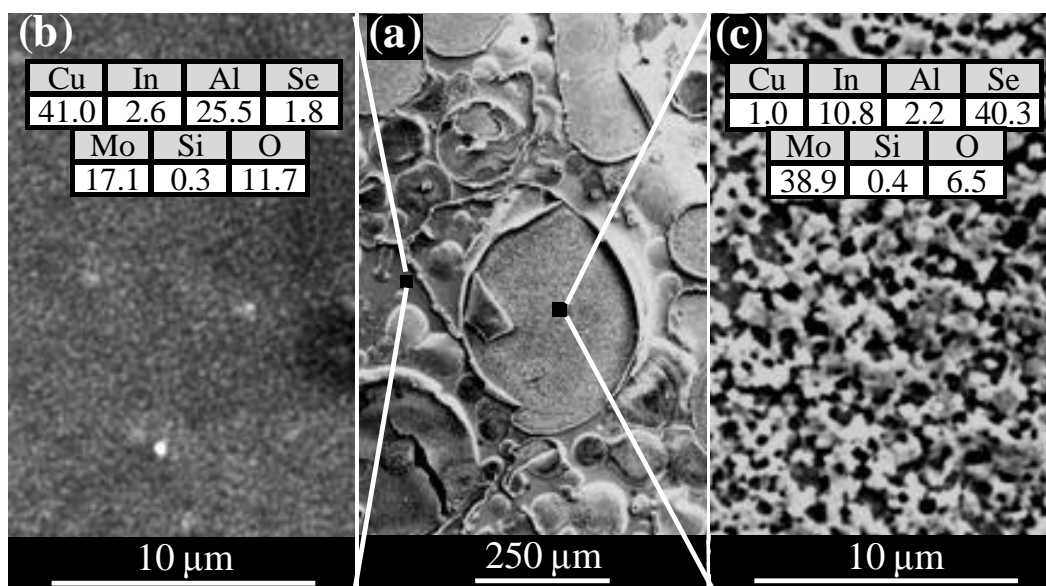
Figure 83: Scanning electron micrographs of N782B1 (Cu-In/Al, x=0.52, 540°C, 30 min, 10 mbar Ar). *(a)* **overview of the surface;** *(b)* **Zoom on a region of the superficial film;** *(c)* **zoom on a region where the superficial film has evaporated.**

The dark regions of Figure 82 correspond to the crater-like evaporated regions of Figure 83 **(a)** (zoomed on in **(c)**), while the shiny parts correspond to the non-evaporated superficial film in **(a)** (zoomed on in **(b)**). The EDS composition of the magnified regions **(b)** and **(c)** are inserted in the picture. The film nearest the surface is highly Cu and Al-rich compared to the as-deposited precursor, while the evaporated region contains mainly In, Se and Mo. Since the amount of Mo detected in **(c)** is very large (≈39%), the EDS composition is believed to be significantly affected. Note that the surface morphology of the superficial film **(b)** is very similar to that of the as-deposited precursor, shown in section 8.3.2 Figure 79 (N782A).

EDS analyses performed on the three alternative layouts and the Cu-In-Al reference are summarized in Table 25.

Table 25: Composition, determined by energy dispersive spectroscopy, of N783D1 (Cu-In-Al, x=0.52), N782C1 (In/Al/Cu, x=0.52), N782B1 (Cu-In/Al, x=0.52) and N782F1 (Cu-In/Al, x=0.31). The composition was measured on the Mo-coated part of the samples, except for N783D1, where it was also measured on the non-coated part for comparison.

Sample ID	EDS composition (at %)							Cu/(Al+In)	Al/(Al+In)	Se/(Cu+In+Al)
	Cu	In	Al	Se	Mo	Si	O			
N783D1 (Mo)	23.4	16.9	7.4	43.1	0.2	0.3	8.7	0.96	0.30	0.90
N783D1 (SLG)	18.7	13.3	4.5	32.4	0.2	7.7	23.3	1.05	0.25	0.89
N782B1 (Mo)	24.6	5.4	19.2	19.2	15.0	0.2	16.5	1.00	0.78	0.39
N782C1 (Mo)	24.0	19.8	4.7	43.8	0.5	0.3	6.9	0.98	0.19	0.90
N782F1 (Mo)	22.0	15.4	9.4	30.0	5.9	0.2	17.0	0.89	0.38	0.64

The part of N783D1 on Mo shows a higher Al content than on glass (x=0.30 against 0.25 on glass), which results in the ratio [Cu]/([Al]+[In]) being lower (0.96 against 1.05). The O content is also considerably higher on the glass part (23% against ≈9%). The EDS measurement of N782B1 (Cu-In/Al, x=0.52) shows a high Al content (x=0.78), and low In and Se contents. This measurement was performed at low magnification, unlike the measurements reported in Figure 83, so that a significant number of evaporated and preserved regions were included. In N782C1 (In/Al/Cu, x=0.52) on the contrary, x=0.19, which is lower than in the as-deposited precursor, while [Se]/([Cu]+[In]+[Al]) and [Cu]/([In]+[Al]) are close to stoichiometry. In N782F1 (Cu-In/Al, x=0.31) was detected a higher ratio x=0.38 than in the precursor, resulting in [Cu]/([In]+[Al])=0.89, and a low [Se]/([Cu]+[In]+[Al]) ratio of 0.69.

Spectrophotometry

The relationship between band gap E_G and absorption coefficient $\alpha(hv)$ in direct band gap semiconductors is reported in [17] as:

$$\alpha(hv) = A\sqrt{hv - E_G}$$ (8.1)

Therefore:

$$\alpha(hv)^2 = A^2.(hv - E_G)$$ (8.2)

With A a constant. $\alpha(hv)$ can be determined experimentally from the transmittance and reflectance spectra of a sample [136]:

$$\alpha = \frac{1}{t}.ln\left(\frac{\sqrt{(1 - R)^4 + 4T^2R^2} - (1 - R)^2}{2TR^2}\right)$$ (8.3)

With R the total reflectance, T the transmittance and t the sample thickness.

Therefore, the band gap of a direct semiconductor can be estimated by plotting $(\alpha hv)^2$ vs hv, for example, and a linear fit to the curve near the band edge will cut the abciss (i.e. α=0) at $hv = E_G$.

N782F1, which displayed the most promising XRD pattern in terms of incorporation of the Al into the CIS lattice, was characterised optically by spectrophotometry (Figure 84), and compared to N782B1 (Figure 85), which was less successful in achieving incorporation. The noisy region observed in the signal around 830 nm corresponds to the change of detector, from the photomultiplier (used for the range 310 nm-830 nm) to InGaAs detector (830 nm-1800 nm). Both samples exhibit an absorption edge at ≈0.90 eV (region between *a* and *b* in both figures), which was associated with CIS. This value is however lower than the values found in the literature, 1.0 eV [54], possibly due to the presence of some copper selenide phases.

The transmittance of N782F1 shows additional features to those observed in N782B1, with in particular a second set comprising a very soft shoulder (point *c*) and

elbow (point *d*). These inflexion points are not as sharp as *a* and *b* but the comparison with the tail of the plot *T vs λ* in N782B1 (Figure 85) confirms that their presence is real. In the $(\alpha h\nu)^2$ *vs hv* plot, only *a*, *b*, and *c* are still visible. *c* and *d* are believed to reflect the presence of additional, higher band gap phases in the film.
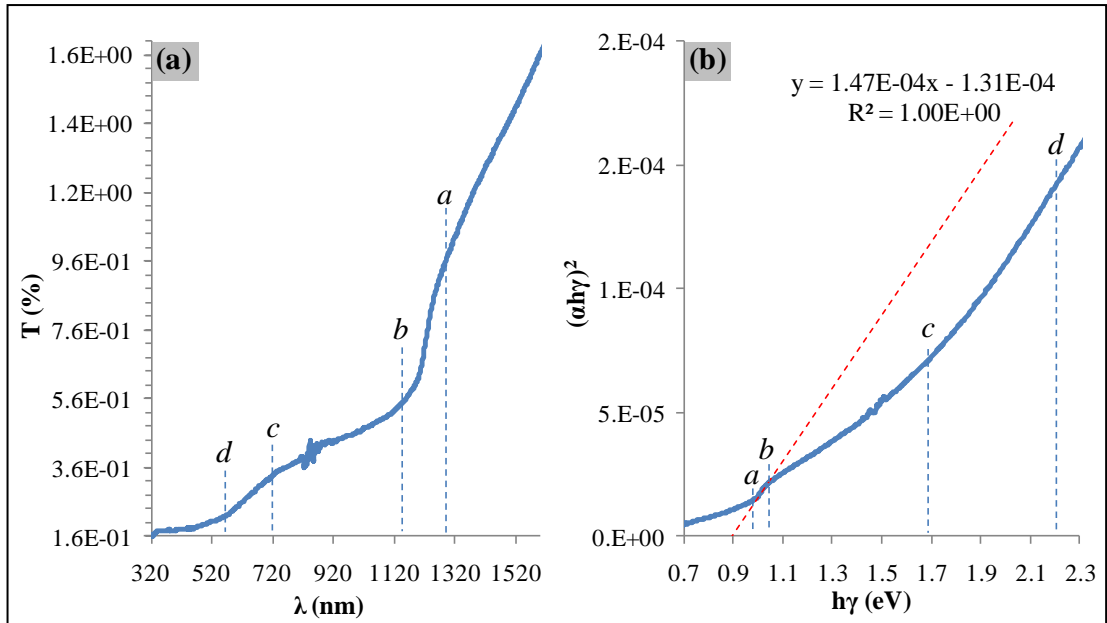
Figure 84: Transmittance measurement (a) and band gap assessment from the curve
(αhv)^2 vs hv **(b) in N782F1 (Cu-In/Al, x=0.31).**
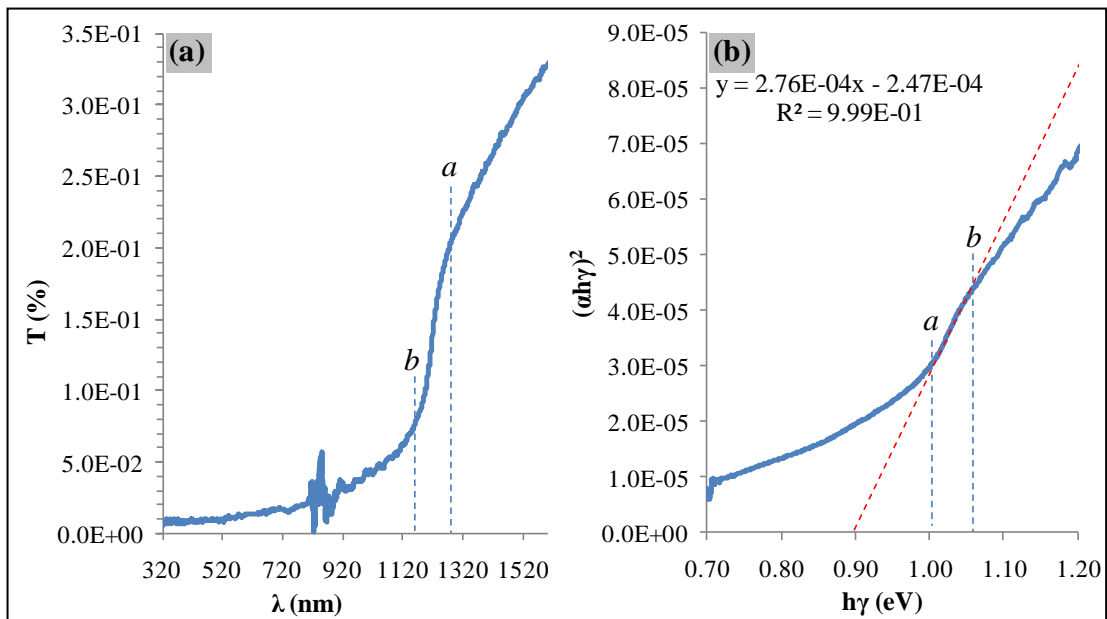
Figure 85: Transmittance measurement *(a)* and band gap assessment from the curve
(αhv)^2 vs hv (b) **in N782B1 (Cu-In/Al, x=0.52).**

8.3.5 Discussion of the absorbers

The comparative results of N782B1 (Cu-In/Al, x=0.52) and N782F1 (Cu-In/Al, x=0.31) indicate that the composition x=0.52 causes important stresses in the film that lead to the formation of blisters of important size and no or very little intermixing between CIS and CAS phases, while x=0.31 causes pinholes but a better intermixing, with almost no CAS and an important presence of CIAS phases. The reason behind these differences could be manifold. The SEM micrographs of the metallic precursors already emphasized an important difference: while absent from the higher x-content precursor, the phase In was present at the surface of the low content one. This would have allowed N782F1 (x=0.31) to capture more Se at low temperatures, before the stresses between the Cu-In layer and the superficial Al layer could cause certain regions to delaminate. Whether because the In seen at the surface was also in contact with the underlying layer of Cu-In or because the Cu diffused to the surface of the Al film, CIS formed in larger amount (or evaporated less) and CAS in smaller amount. The presence of relatively important amounts of CIAS in N782F1 (770 peak area) compared to N782C1 (In/Al/Cu, x=0.52, 500 peak area) and N782B1 (Cu-In/Al, x=0.52, no CIAS), and in spite of a lower initial Al content, seems to indicate a more efficient incorporation of Al into the CIS lattice. In N782B1, the phases formed are mostly Cu_9Al_4 and Al (XRD) at the unevaporated surface (Figure 83 (**b**)), which matches the EDS composition (41% Cu, 26% Al), and indicates that Cu diffused in the Al layer by forming compounds such as Cu_9Al_4 while In ($\approx$3%) did not. Under the 'blisters' (Figure 83 (**c**)) the Mo interface is exposed. There, $MoSe_2$ and small amounts of InSe are found (XRD). No depth profile is available for this sample, so that assumptions can only be made from the other data. It seems plausible that the Se was not incorporated via diffusion through

198

the Al layer, as intended, but rather directly at the back contact through the blisters where the film came off. The indium is expected to be located deeper in the bulk, and mostly present as CIS. CAS could be present near the back but on top of the CIS phase. The mechanism through which the Se was provided to form these phases is not clear from the data available.

The better Al incorporation in the CIS lattice of N782F1 (Cu-In/Al, x=0.31) could have been made possible by the presence of In islands in the Al-rich layer. The x ratio seems higher than in the precursor, which would mean that the Al has not completely migrated to the back, and is even slightly more present at the front. However, the data available does not provide direct information on the modalities of the Al-grading. Spectrophotometry seems to confirm the presence of a graded band gap material, with two inflexion points, at higher band gap than CIS, in N782F1, which are not present in N782B1 (Cu-In/Al, x=0.52). The presence of multiple $CuIn_{1-x}Al_xSe_2$ phases with grading x ratios, conjointly with a high film thickness, make the absorption edges associated with those CIAS phases less visible. Indeed, the former causes overlapping of the absorption edges and the latter results in most of the light above CIS band gap being absorbed by CIS, so that little light is left for absorption by the different CIAS phases.

The failure of the layout of N782C1 (In/Al/Cu, x=0.52) in preventing the segregation seems to arise from the fact that most of the In was present on top of the Al layer already in the as-deposited precursor, as demonstrated by the presence of compounds of Cu_xIn_y and the quasi-absence of In (XRD). This phenomenon, due possibly to the combination of the initial morphology of the In phase (islands) and the absence of existing In_xAl_y compounds, has resulted in the Al being isolated at the back from the very beginning. This is supported by the low x ratio measured by EDS (0.19, against

0.52 in as-deposited). The abundant CIS phase (XRD) therefore arises from the presence of Cu and In (at least partly as Cu_xIn_y compounds) near the surface from the beginning of the selenisation process, those two elements being capable of reacting with Se to form CIS at temperatures as low as Se melting point (221°C).

8.4   Post-selenisation anneal (PSA)

8.4.1   Introduction

In an attempt to obtain rediffusion of the Al in the bulk, an additional anneal of one hour was performed on N535W (SLG/Mo/Cu-In-Al/Cu), already selenised at 540°C, via a three-steps process in 6 mbar Ar (see section 7.5). This extra anneal, to which we will refer as post-selenisation anneal (PSA), was performed at 573°C in an Ar atmosphere of 10 mbar and without introducing any selenium source. This treatment was reported by Marudachalam *et al.* [135] to yield rediffusion of the Ga segregated at the back in 2-stage processed CIGS.

8.4.2   Data

The XRD pattern of N535W after the treatment is displayed in Figure 86. It shows a modified CIS phase which peaks are shifted towards higher angles. This suggests the incorporation of Al into the CIS lattice to form CIAS. A small CIS reflection is however still present. The reflectance measurement was performed on PSA N535W, and showed no change in the cutting wavelength, corresponding to CIS. Note that the same process was performed on N679B (quartz/Cu-In-Al), which had been previously selenised in a one-step anneal at 540°C and in the same conditions of pressure and dwell time as N535W, but showed no shift.
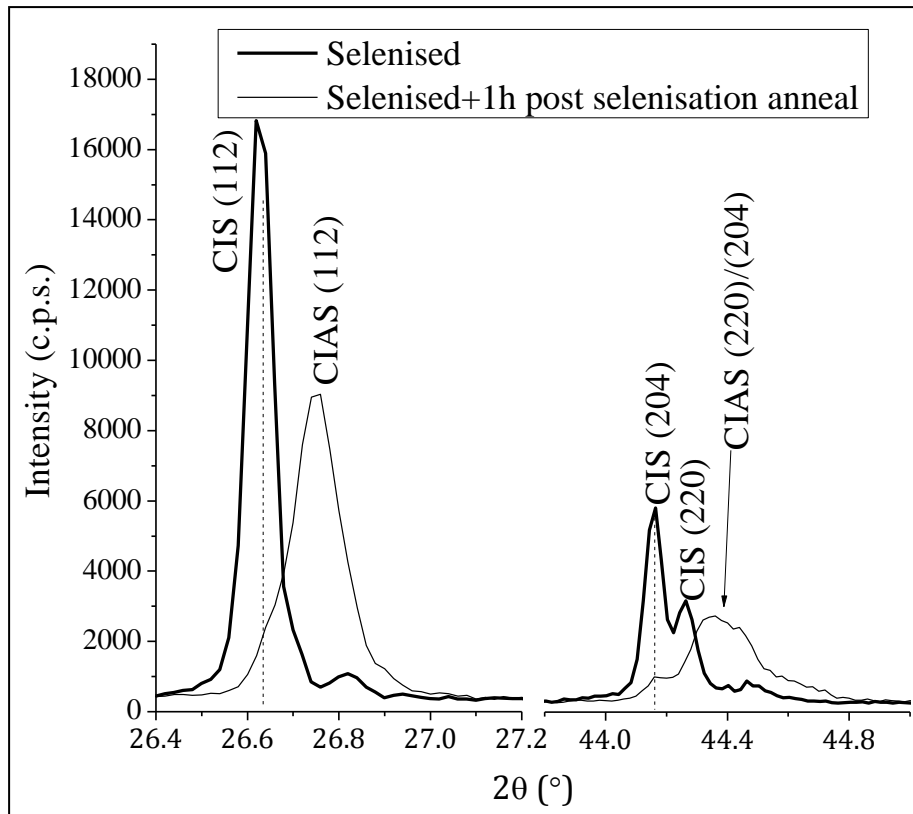
Figure 86: XRD patterns of N535W before (*thicker line*) and after (*thinner line*) 1h post-selenisation anneal at 573°C in 10 mbar Ar.

Glow discharge optical emission spectroscopy

GD-OES was performed on N535W after PSA, and is compared to the depth profile performed beforehand (Figure 87). The Al is still located at the back, and seems even further segregated. However, several other differences can be found from this figure:

(a) The Al maximum intensity, of ≈0.5 counts/extraction before PSA, is much lower after PSA, around 10^{-2} counts/extraction, while Cu and In show similar levels before and after PSA. The flat region of the Se signal is on the other hand higher than before PSA, with ≈0.3 counts per extraction, against 0.1 counts per extraction before PSA.

(b) The time required to reach the Mo back contact, of ≈100 s before PSA, is almost double that time after PSA (≈200 s).

The GD-OES measurements before and after PSA having been performed in the same conditions, these differences could be interpreted as an indication of a different bonding environment for the elements affected. Indeed, in the chalcopyrite lattice of CIAS, Cu, Al and In only bond with Se and do not bond together. The incorporation of Al into the lattice would therefore result in a different bonding environment for Al and Se, but not for Cu and In. The yield of the elements Al and Se could therefore have been affected by the incorporation of Al into the lattice of CIS.
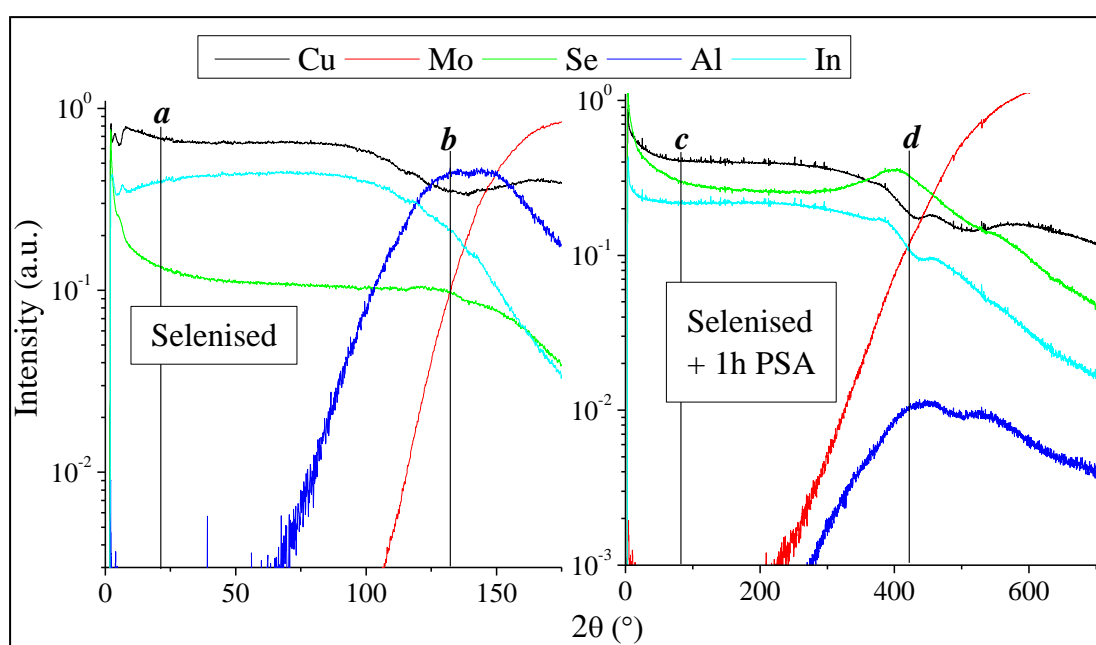
Figure 87: GD-OES depth profiles of N535W before (*left*) and after (*right*) 1h post-selenisation anneal without Se.

8.4.3 Discussion

When N535W is re-annealed without Se, its XRD spectrum appears to be containing two CIAS phases in addition to a small CIS phase. This seems to mean that Al has been incorporated into the CIS lattice. However, there is still a small reflection corresponding to pure CIS, which indicates that the incorporation is not complete, and some Al-free CIS is still present near the surface. The GD-OES depth profile after PSA indicates that Al has not rediffused into the bulk, but supports instead the

hypothesis of reincorporation of the Al into the CIS lattice where Al was already present, that is near the Mo back contact.

CHAPTER 9   CuInSe$_2$ AND CuIn$_{1-x}$Al$_x$Se$_2$ CELL FABRICATION

9.1   Experimental

Although no single phase CIAS could be achieved in this work, some layouts were tested for EQE in solution and the most promising ones made into devices. Indeed, CIGS devices with segregated Ga at the back were reported to perform better than CIS, including an improved open-circuit voltage [11, 47]. Three precursor layouts were tested for the CIAS absorbers: Cu-In-Al (N591Z1, [Cu]/([In]+[Al])=0.89, x=0.31), Cu-In-Al/Cu (N582F1, [Cu]/([In]+[Al])≈1.11, x=0.31), Cu-In/Cu-In-Al/Cu (N644R1, [Cu]/([In]+[Al])≈1.2, x=0.11)[19]. The Cu capping layer of N644R1 was 100 nm thick, while the one used on N582F1 was 50 nm thick. A CIS absorber (N623J1, [Cu]/[In]≈0.85) was also used in this study as a standard for comparison. The four types of layouts were selenised in the tube furnace at 530°C for 60 minutes in 6 mbar of Ar, and subsequently cut along the length as shown in Figure 88. This was done in order to be able to characterise[20] and test damaging processes (e.g. etching) on one half, while the other half was used for making complete devices. The direction of the cut aimed at obtaining two halves, of equivalent thickness at a given position along the length. Indeed, the thickness variation along the width was systematically lower than 5%, against ≈30% along the length (see section 7.1).

The half for characterisation was tested for photocurrent response to illumination by a white LED (see section 4.2.3) after several etching durations and, once the optimum etching duration defined, for EQE in electrolytic solution (4.2.4).

---

[19] The layouts In/Al/Cu and Cu-In/Al had not yet been devised at this stage of the investigation.
[20] This characterisation setup was shown to lead to performance degradation if the sample characterised was turned into complete cells, and therefore it was important that this step was not carried out on the half used for cell making.
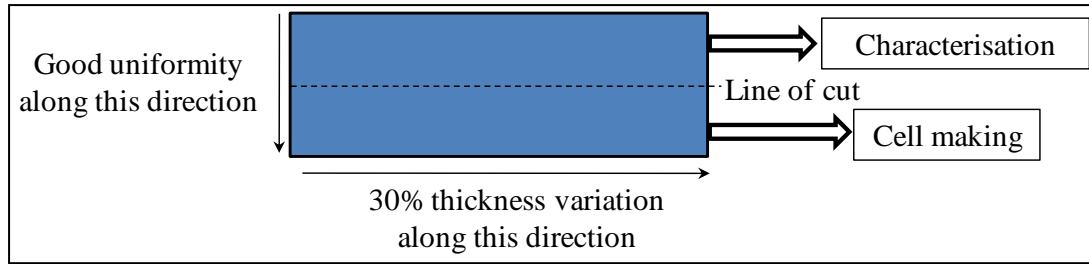
Figure 88: Sample cutting in preparation for characterisation and device making. For a given position along the length of the sample, the thickness variation of the metallic precursors between the half characterised and the half used for making cells was <5%.

The half of the sample kept for device making went through the steps described in section 4.1 to be turned into complete devices, and then tested for I-V characteristics at 25°C under AM1.5 illumination. Finally, EQE was also performed on some of the complete devices.

The sample fabrication data is summarised in Table 26 (section 9.2).

9.2 Fabrication data on the samples of the chapter

Table 26: Sample deposition and processing data for chapter 9. The compositions in italics are interpolated from single matrix precursors. In the "layout" column, the layers are indicated by order of deposition.

Page	ID	Subs-trate	Target	Layout	Comp. (at%)			Se?	Fur-nace	P^{re} (mbar)	Gas	Dwell T^{re} (°C)	Dwell dur. (s)	Ramp dur. (s)
					Cu	In	Al							
204,207-208,210-212,215 211	N591Z1 N591Z4	SLG/Mo	elem.	Cu-In-Al	47.0	36.0	17.0	Yes	TF	6	Ar	530	1800	≈1800
204,207-208,210-211,214 211	N582F1 N582F4	SLG/Mo	elem.	Cu-In-Al/Cu	*52.5*	*32.5*	*15.0*	Yes	TF	6	Ar	530	1800	≈1800
204,207-208,210,211,214,215 211	N644R1 N644R4	SLG/Mo	elem.	Cu-In/Cu-In-Al/Cu	*47.0*	*36.0*	*17.0*	Yes	TF	6	Ar	530	1800	≈1800
204,208,210 211-213	N623J1 N623J4	SLG/Mo	alloy	Cu-In	48.0	52.0	0.0	Yes	TF	6	Ar	530	1800	≈1800

9.3 Data on sample selection

Photocurrent vs etching time

KCN etching was observed in several occasions to damage the CIAS absorbers, causing in particular the film to peel off the substrate. Therefore, in order to avoid degradation, several etching durations were tested on each one of the three layouts. The concentration of the solution was 5 wt% KCN. To estimate the optimal etching time, the photocurrent generated under white LED illumination (we will refer to this process as "photoresponse") was assessed after each etching cycle. The accuracy of this technique is limited by the fact that the white LED, phosphor-based, does not produce the AM1.5 spectrum, but a peak of emission at ≈450 nm (blue) and two broader spectra around 525 nm and 575 nm (green-yellow), as shown in Figure 34. However, the spectrum is similar enough to assess important relative variations of photocurrent in a given sample. Examples of oscillograms for a sample similar to N644R1 before and after 30 s etch are displayed in Figure 89, and all the results obtained with the three layouts are summarized in Table 27. They indicate that optimum etching durations are 5 s to 15 s for N591Z1 (Cu-In-Al), 10 s to 15 s for N582F1 (Cu-In-Al/Cu), and 5 s to 10 s for N644R1 (Cu-In/Cu-In-Al/Cu). Furthermore, N644R1 is the only sample that shows a real degradation for a too prolonged etching, while in N582F1 and N591Z1 the photocurrent merely plateaus beyond the optimum etching duration. As already mentioned, the parts used for characterisation presented a thickness variation of about 30% along the length, and the photoresponse of the unetched thinner part was therefore compared to that of the unetched thicker part. Results show the thinner half yielded higher photocurrents, except for N582F1, where the signal was too low in both parts to make an accurate

comparison. N623J1 (Cu-In) was not etched since the measured composition was relatively Cu-poor.

Table 27: Summary of the photocurrents generated by N623J2, N591Z1, N582F1 and N644R1 under white LED illumination after different etching periods.

ID	Layout	Thickness	Part	Etching time	Bias	Photocurrent
N623J1	Cu-In	≈500nm	thin part	0s	0.71V	10 mA
N591Z1	Cu-In-Al	≈500nm	thin part	0s	0.50V	3 mA
			thick part	0s	0.50V	0.6 mA
			thick part	5s	0.73V	8 mA
			thick part	10s	0.80V	9 mA
			thick part	15s	0.75V	8 mA
N582F1	Cu-In-Al/Cu	≈550nm	thin part	0s	0.45V	<0.02 mA
			thick part	0s	0.45V	<0.02 mA
			thick part	5s	0.70V	2 mA
			thick part	10s	0.76V	6 mA
			thick part	15s	0.70V	6 mA
N644R1	Cu-In/Cu-In-Al/Cu	≈800nm	thin part	0s	0.70V	8 mA
			thick part	0s	0.74V	7 mA
			thick part	5s	0.76V	4 mA
			thick part	10s	0.76V	5 mA
			thick part	15s	0.70V	1 mA
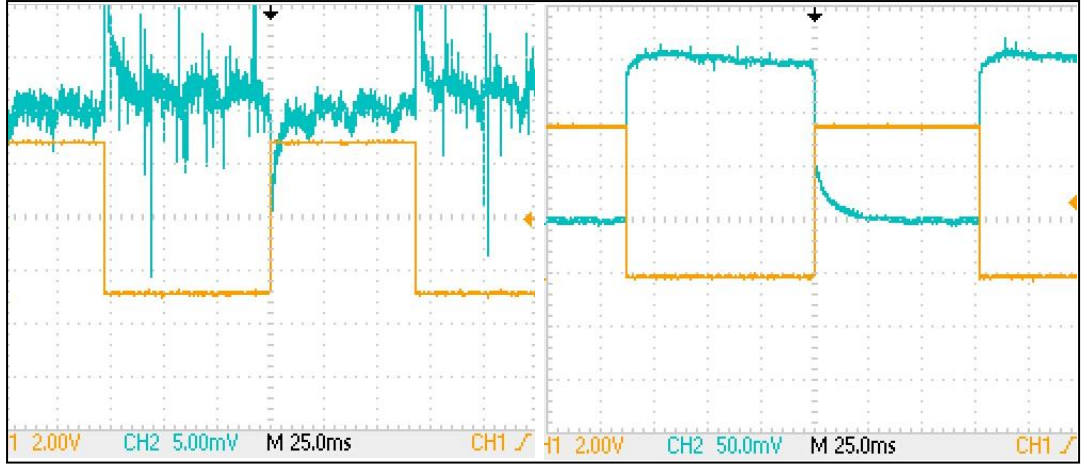
Figure 89: Oscillograms of N557V4 (Cu-In-Al/Cu, TF, 550°C, 30 min, 10 mbar H$_2$/N$_2$) with no etch at a bias of 0.39 V (*left*) and after 30 s etch at a bias of 0.51 V (*right*). The *yellow line* corresponds to the signal supplied to the white LED, and the *blue line* to the photogenerated signal of the sample.

External quantum efficiency

Once the optimal etching duration determined, EQE in electrolyte was measured. The band gap is determined from the EQE using an approximation of the Gärtner equation for short carrier diffusion lengths (usually met in polycrystalline films):

$$-\ln(1 - \Phi) = \alpha W \qquad (9.1)$$

with Φ the EQE, α the absorption coefficient and W the depletion width. Replacing α by its expression in equation 8.1 this yields:

$$-\ln(1 - \Phi) = AW\sqrt{h\upsilon - E_G} \qquad (9.2)$$

$$(\ln(1 - \Phi))^2 = AW(h\upsilon - E_G) \qquad (9.3)$$

and at the intersection between the curve *(ln(1-Φ))^2 vs hv* and the *hv*-axis, hv=E$_G$. The spike observed in all samples at 900 nm is due to a change of the detector, from Si to Ge, and the dip after this spike could be due to the absorption by the electrolyte traversed by the light to reach the sample. Special care was given to the contacting of

the Mo back contact, since the photocurrent response to the wavelengths scanned (named "spectroresponse" for the rest of this discussion) was highly dependent on the quality of the contact. The results, reported in Figure 90, indicate that all samples have a band gap at ≈1.0 eV.
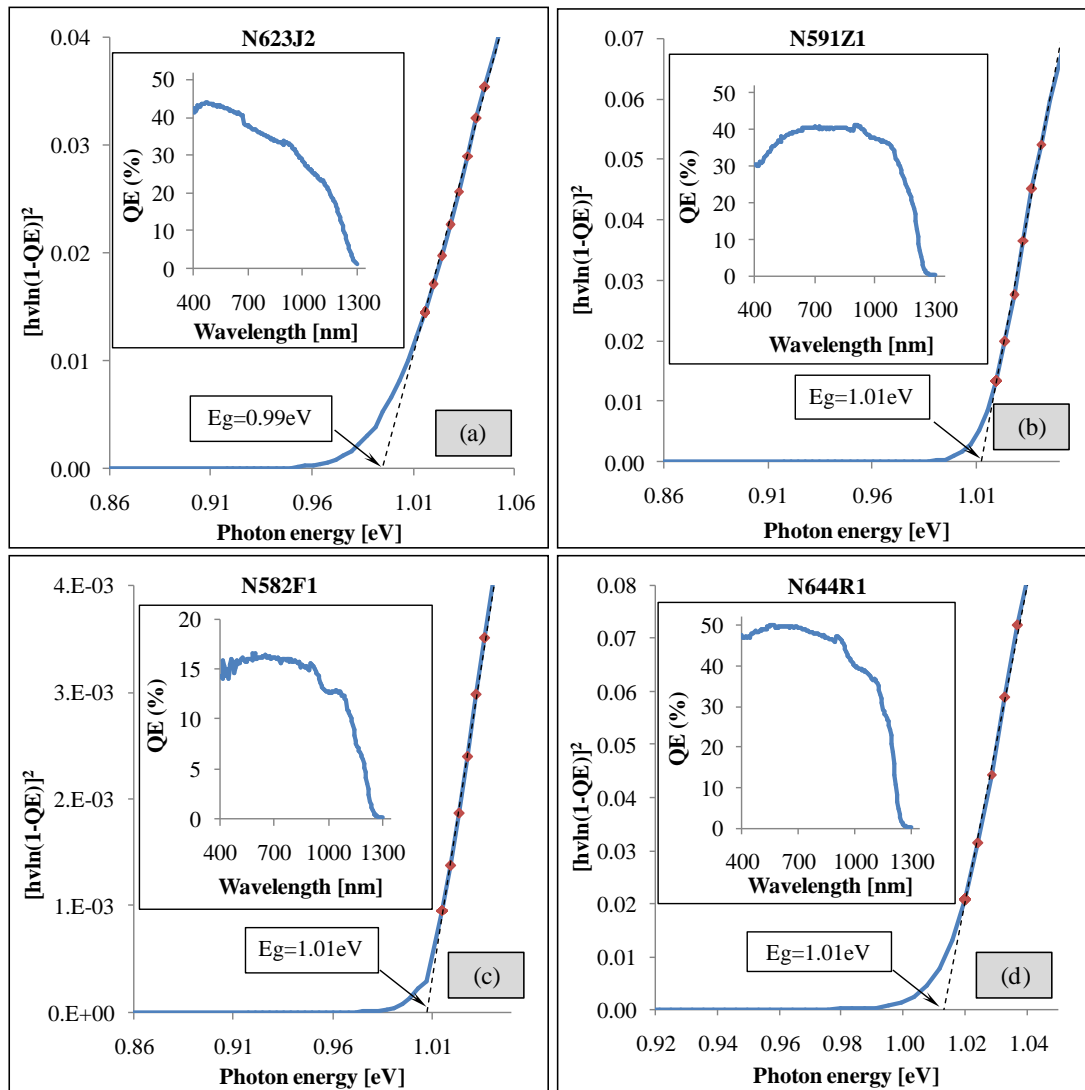
Figure 90: Plots of *(hv.ln(1-QE))²* ***vs hv*** **of** *(a)* **N591Z1 (Cu-In-Al),** *(b)* **N582F1 (Cu-In-Al/Cu),** *(c)* **N644R1 (Cu-In/Cu-In-Al/Cu), and** *(d)* **N623J1, selenised in the same conditions (TF, 530°C, 60 min dwell, 6 mbar Ar). A 0.70 V bias was applied for all four measurements.**

However, the maximum EQE values and the shape of the curves vary between samples. N644R1 **(d)** shows EQE values as high as 50% at 500-550 nm, N591Z1 **(b)** 40% at 700-800 nm, N582F1 **(c)** 16% at 550-750 nm. N591Z1 also displays a decrease in EQE in the range 400-600 nm EQE absent from the other three samples, while the CIS standard shows a steadily decreasing EQE as we move towards the higher wavelengths.

9.4   Data on devices

Complete devices were made with the other half of the samples tested above. I-V measurements were undertaken with four point of contact ('4 wires') rather than two ('2 wires'). This setup was used to limit carrier losses in the probes and wiring (see 4.2.8). The results of the characterisation were very poor for all the CIAS layouts (Table 28).

Table 28: I-V data for N623J4 (from Cu-In precursor), N591Z4 (Cu-In-Al), N644R4 (Cu-In/Cu-In-Al/Cu) and N582F4 (Cu-In-Al/Cu), all selenised in the TF (530°C, 60 min dwell, 6 mbar Ar).

cell #	N623J4 (CIS)		N591Z4 (CIAS)		N644R4 (CIAS)		N582F4 (CIAS)	
	Isc (mA)	Voc (mV)	Isc (mA)	Voc (mV)	Isc (mA)	Voc (mV)	Isc (mA)	Voc (mV)
2	-11.90	374	-1.00	6.0	-1.00	6.0	dead	
3	-11.40	363	-0.90	5.0	-0.90	5.0	dead	
4	-11.65	367	-1.80	5.0	-1.80	5.0	dead	
5	-11.95	370	-0.20	0.3	-0.20	0.3	dead	
6	-12.11	357	-0.04	0.1	-0.04	0.1	dead	
7	-9.73	352	-0.02	0.1	-0.02	0.1	dead	
9	-9.65	294	-0.60	1.3	-0.60	1.3	dead	
10	-9.62	297	-0.82	2.0	-0.82	2.0	dead	
11	-8.48	344	-0.70	1.9	-0.70	1.9	dead	
12	-9.80	373	-0.22	0.7	-0.22	0.7	dead	
13	-9.94	291	-0.06	0.2	-0.06	0.2	dead	
14	-9.14	340	-0.02	0.1	-0.02	0.1		

They showed only a slight response to light at no applied voltage (I_{SC}) and small V_{OC}, and exhibited fill factors of ≈25% (see example in Figure 91).
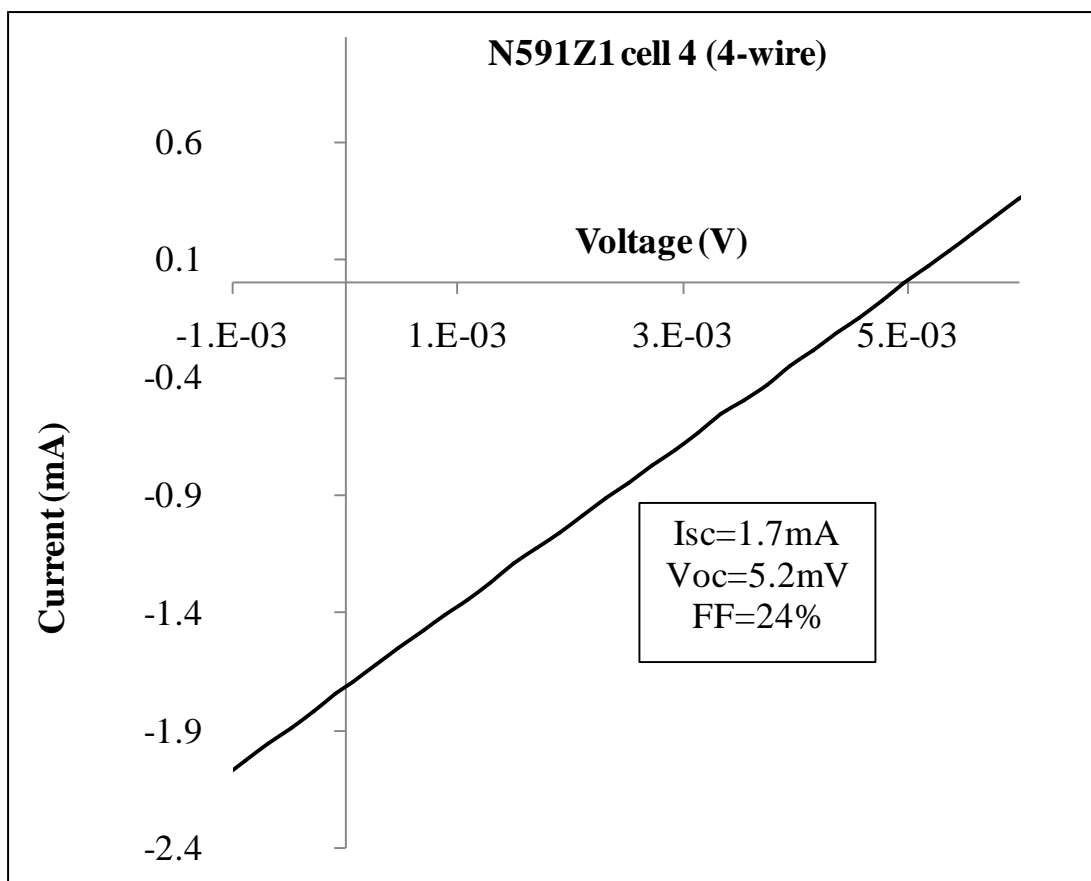
Figure 91: I-V characteristic of cell 4 of N591Z1 (Cu-In-Al, 530°C, 60 min dwell, 6 mbar Ar).

The CIS cells (N623J4), on the other hand, showed a diode-like behaviour (Figure 92). One row of cells displayed efficiencies >3% (cells 2 to 6), while the cells of the other row had lower efficiencies, typically 1% to 2%. The I-V characteristics of one typical cell obtained with a 4 wires setup, is compared to the I-V obtained with the 2 wires setup (Figure 92). Note that CIS devices prepared prior to those with a similar process (not reported here) yielded efficiencies up to 6.0%, with an average of 4.9%. The lower efficiencies measured in the CIS cells presented here are believed to arise from the absence of a KCN etching, and possibly from issues in the CdS deposition stage as well.
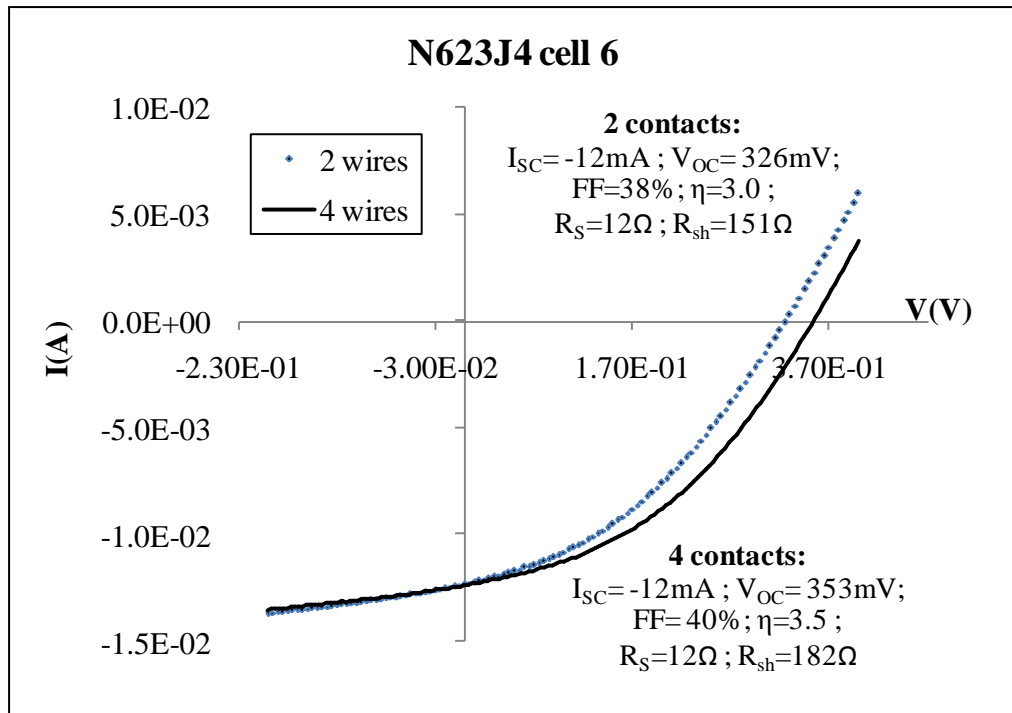
Figure 92: I-V characteristics of N623J4 cell 6, measured with the 2 wires method (*diamonds*) and the 4 wires method (*plain line*).

The extensive I-V data of three typical cells of N623J4 is reported in Table 29.

Table 29: Extensive I-V characterisation data of three representative cells in N623J4. The results obtained with '2 wires' (*white cells*) and '4 wires' (*grey cells*) are also compared.

	η(2 wires)	η(4 wires)	V_{OC} (2w)	V_{OC} (4w)	I_{SC} (2w)	I_{SC} (4w)
cell 3	3.4%	3.6%	340mV	359mV	-11.9mA	-11.8mA
	FF (2w)	FF (4w)	R_s (2w)	Rs (4w)	R_{sh} (2w)	R_{sh} (4w)
	42%	42%	11Ω	11Ω	162Ω	121Ω
cell 6	η(2 wires)	η(4 wires)	V_{OC} (2w)	V_{OC} (4w)	I_{SC} (2w)	I_{SC} (4w)
	3.0%	3.5%	326mV	354mV	-12.3mA	-12.4mA
	FF (2w)	FF (4w)	R_s (2w)	Rs (4w)	R_{sh} (2w)	R_{sh} (4w)
	38%	40%	12Ω	12Ω	151Ω	182Ω
cell 10	η(2 wires)	η(4 wires)	V_{OC} (2w)	V_{OC} (4w)	I_{SC} (2w)	I_{SC} (4w)
	1.5%	1.8%	268mV	292mV	-9.6mA	-10mA
	FF (2w)	FF (4w)	R_s (2w)	R_s (4w)	R_{sh} (2w)	R_{sh} (4w)
	29%	30%	14Ω	14Ω	45Ω	50Ω

Cells 3 and 6 belonged to the best performing row of cells, while cell 10 belonged to the lower efficiencies row. The results show an increase in V_{OC} in the 4 wires setup compared to the 2 wires.

9.5   Discussion

The results of photoresponse show that the maximum photocurrent in N644R1 (Cu-In/Cu-In-Al/Cu) is obtained in the unetched sample, while 10 s etching are required for N582F1 (Cu-In-Al/Cu). This is in spite of the fact that the Cu cap deposited on N644R1 was 100 nm thick, while the one deposited on N582F1 was only 50 nm thick, which should have made the former more Cu-rich overall and yielded more copper selenides by the end of the selenisation process. Besides, unlike the other two layouts, N644R1 shows degradation of the photocurrent for a too prolonged etching. Martín et al. [136] reported similar problems of adhesion with some CIAS films that were grown too Cu-rich. The composition of N644R1, although only inferred from previous depositions and not measured directly, is indeed expected to be the most Cu-rich of the three samples tested, which is in agreement with the authors' observation. This could suggest that the peeling of the film is due to a buried copper selenide phase. The removal of this buried layer by KCN would result in the film above being removed along with it. Why this phase would stay buried rather than end up at the film surface as is usually the case cannot be explained with the data available.

Regarding the increase of V_{OC} observed in four wire measurements, it does not seem to arise from an increase of the R_{sh}, as the results of cells 6 and 10 could suggest, since cell 3 shows both an increase in V_{OC} and a decreasein R_{sh}. Besides, only for relatively low values of R_{sh} (typically 30 Ω [137]) is the V_{OC} substantially affected

by a change in R_{sh}. Since the voltage was sourced and the current measured for all the measurements reported, the most sensible explanation of the V_{OC} increase is that, in the 2 wires setup, the voltage values set while sourcing are an underestimation of the actual voltages applied at the poles of the cells.

Indeed, the resistances of the two probes cause an additional voltage build up to the set one, and therefore the voltage applied to obtain open circuit conditions ($V=V_{OC}$) is an underestimation of the voltage (actual V_{OC} as measured with 4 wires) really applied to the poles of the cell. Alternately, saturation, known to increase V_{OC}, could account for the difference, although the shutter of the simulator was systematically shut between each cell measurement to limit this phenomenon.

The resistor-like I-V characteristics of the CIAS cells could mean that the p-n junction was not properly formed, or that the series resistance was too high, and the shunt resistance too low. Since the CIS cells were all active and of efficiencies >1%, the CdS cannot be the main reason for the poor performance. Dwyer et al. [107], who also obtained inactive CIAS devices from the 2-stage process, suggested that it was due to the presence of the highly resistive phase Al_2O_3 in the film. This hypothesis could hold for this work as well, since it was shown that Al_2O_3 was most likely present in the films. The absence of any activity in N583F1 (Cu-In-Al/Cu) could be due to the fact that this sample was the one that underwent the longest etching. The use of wet chemistry might have affected the junction formation, in addition to the losses already affecting N591Z1 and N644R1.

CHAPTER 10   CONCLUSION AND SUGGESTIONS FOR FUTURE WORK

10.1 Conclusion

Studies were carried out on as-deposited (section 5.4), annealed (sections 7.3.2-7.3.3) and selenised (section 7.4) Cu-In-Al metallic precursors. Progress was made towards the understanding of the physical causes preventing the formation of single phase CIAS. Solutions were devised, including the design of alternative precursor layouts (sections 0-8.3) and the testing of a post-selenisation anneal without Se (section 8.4). Some promising results were obtained but they would require a deeper exploration that was not possible in the time-frame of the project. CIS devices were also made, with efficiencies up to 5.8%, providing a proof of principle that the setup and parameters used for the entire device-making process were capable of producing good devices.

A special interest was first attached to comparing the as-deposited Cu-In, Cu-Al and Cu-In-Al precursors. This study was initially motivated by the observation that Cu-In-Al precursors display in profilometry measurements a surface roughness over five times higher than any Cu-In or Cu-Al precursor. In Cu-In-Al metallic precursors (section 5.4), the aluminium was observed to alloy with the Cu_9In_4 phase, to form $Cu_9(In,Al)_4$. The stoichiometry of this compound however leads to the formation of an In phase from the remaining indium. This phase, which either migrates to the film surface or protrudes from the bulk of the precursor, results in an important surface roughness in the Cu-In-Al precursors, observable in profilometry measurements. In the absence of Al (section 5.2), the In can bind with Cu to form Cu_2In and $CuIn_2$, and no or little In is left as an elementary phase. The roughness was consequently

much smaller in this type of precursor. The Cu-Al precursors were also relatively smooth.

It was equally important to find suitable growth parameters for both CIS and CAS, since those materials are two extreme compositions of $CuIn_{1-x}Al_xSe_2$ (x=0 and x=1, respectively), so that the results could be adapted and applied to CIAS. Both $CuInSe_2$ (CIS) and $CuAlSe_2$ (CAS) were successfully produced (CHAPTER 6). For CAS (section 6.3), the best results were obtained from a stoichiometric Cu-Al precursor selenised at 550°C, although traces of unconverted precursor were detected in the XRD pattern. A KCN etching was necessary for samples with this stoichiometry, although they seemed to remove a superficial part of the film. For CIS (section 6.4), a fast ramping rate and a dwelling temperature of 530°C yielded single phase material. An important presence of oxygen, which increased with the dwelling temperature, was also noticed in the samples selenised in the rapid thermal processor (RTP). This seems to be related to the setup, and could be minimised by establishing a high H_2/N_2 pressure in the chamber (close to 1 atm) before starting the process.

A study was then undertaken in the rapid thermal processor (RTP) to assess the evolution of the crystalline phase, bulk composition and depth profile of Cu-In-Al and Cu-In-Al/Cu precursors with the annealing temperature (without Se). Cu-In precursors were also used as a support for comparison. The primary aim of this investigation was to determine the unconverted phases that would be present at a given temperature in case of incomplete conversion of the film during selenisation. This annealing study was performed at temperatures ranging from 250°C to 530°C. Important amounts of oxygen were found, and increased with the maximal dwelling temperature. The modalities of oxidation of the Cu-In-Al precursors (evolution with temperature and total amount of oxygen) were different from Cu-In and Cu-In-Al/Cu

precursors. This fact was explained by the possible formation of an oxide of Al, allegedly Al_2O_3, which is either amorphous or of too low crystallinity to be detected by XRD. Al and In formed compounds, and no substantial segregation of those elements was observed.

The same study was subsequently carried out in the presence of Se. The results showed no incorporation of the Al into any crystalline phase (XRD), in spite of the element being present throughout the film at 450°C and 530°C (SIMS). This absence of incorporation is believed to be related to the high levels of oxidation observed in these films (EDS).

A similar study was then undertaken in the tube furnace (TF) on Cu-In-Al/Cu samples (section 7.5), at maximal temperatures ranging 250-540°C. The oxygen levels observed in the TF-selenised samples were much lower than in the RTP at the high temperatures expected to yield formation of CIAS (i.e. higher than 530°C). XRD analyses showed no formation of CIAS and GD-OES indicated that the segregation between Al and In was the main cause, rather than the absence of incorporation observed in the RTP-selenised samples. This segregation was due to excessive difference in formation temperature between the binary selenides of In and Al, conjointly with the ramping rates allowed by the TF being too slow. It was found to occur at all the temperatures tested. The effect of altering the ratio $x=[Al]/([In]+[Al])$ was also tested in the TF. The higher Al contents (>0.38) yielded some Al incorporation into a chalcopyrite lattice as either CIAS or CAS, although Al still presented a graded profile through the depth of the absorber layer.

To summarize, the Al did not seem to incorporate into the CIS lattice when selenised in the RTP, possibly because of oxidation. In the TF, although incorporation was

taking place when CIS and Al were both present and for sufficiently high x ratios, Al and In showed a tendency to segregate, the former migrating to the interface between the absorber and the back contact (Mo), and the latter migrating towards the film surface. As a result, distinct CIS and CAS phases and sometimes small CIAS phases of graded x ratios were formed. A large amount of time was spent trying to understand the causes and devise solutions to these two issues, that is the absence of incorporation of Al into the CIS lattice in the RTP and the segregation of Al and In in the TF. Alternative precursor layouts were then designed to overcome the segregation of Al at the back in the TF. The best results were obtained with x=0.31 and a Cu-In/Al stacked layout. An extra 1h annealing, at 573°C and without Se, was also tested on an absorber that initially showed no presence of CIAS. This extra annealing step seemed to yield formation of almost single CIAS phase, although the Al did not rediffuse to the front.

Finally, even though no single phase CIAS could be obtained and prior to the two findings mentioned in the previous paragraph, some CIAS absorbers were tested for quantum efficiency in solution and then made into complete devices, along with a CIS absorber used for comparison. CIGS absorbers with segregated Ga at the back had displayed in the past improved performances compared to CIS [48], and the driving idea was therefore that the segregation of Al at the back could have affected positively the performance of CIS cell. Although the results in solution were in some cases comparable or even better than those of the CIS absorber, the devices made from Al-containing absorbers showed no activity or very poor performances, whereas ≈3% efficient cells were made from CIS. It is possible that the p-n junction did not form properly or, alternately, that a too high series resistance and too low shunt resistance are responsible for these performances.

10.2 Suggestions for future work

Several of the results obtained during this project would deserve further investigation.

If the oxidation could be prevented in the RTP, this furnace should yield the best results, since the fast ramping rates it allows can prevent segregation between In and Al, as demonstrated by the depth profiles performed on RTP-selenised samples. It would be interesting to determine whether more incorporation occurs in the RTP if low oxidation levels can be achieved. If it was found not to be the case, a study of the grain boundaries would be relevant, since it is the most likely place where Al or some amorphous Al compound could aggregate.

If a tube furnace is used for the investigation, then the potential of precursor layouts such as N782F1 (Cu-In/Al, x=0.31) should be further explored. Martín-Gonzales *et al.* obtained some single phase material with In/Cu/In/Al stacked elemental layers [136], although their results did not seem totally reproducible. In our case, we observed that for high Al contents, depositing Al at the surface led to important stresses and degradation in the films selenised with a 1-step anneal. However, the additional steps performed by the authors of [136] at 130°C and 250°C could help to reduce those stresses by allowing diffusion of In to the surface. It is possible however that the ≈10 at% of oxygen present at 530°C in TF selenised samples is already too high to produce good devices, in which case a high vacuum process would be needed.

The post-selenisation anneal would also deserve more data. It would be interesting to determine whether the result observed is reproducible, whether it can lead to incorporation of Al for the samples selenised in the RTP, or if rediffusion of Al

towards the surface can be achieved in the TF. If this process did prove valuable, an annealing stage without Se could for example be incorporated at the end of the selenisation (by for example maintaining or increasing the temperature while pumping the gaseous Se from the chamber for this additional step).

If a single phase material could be obtained in a reproducible way, the absorbers should be made into cells with similar steps to those used in this work, and the performance assessed. If those devices still showed poor performance, an investigation should be carried out on the junction formation, using for instance electron beam induced current on the cross-section, and the defects possibly forming at its interface at one step or another of the process. It is also possible that CdS does not offer a favourable band line up with CIAS.

APPENDIX 1   Detailed balance and Shockley-Queisser limit

Detailed balance

When a photon of energy greater than the band gap is absorbed by an electron of a semiconductor, the electron is promoted from the valence band to the conduction band; it then very quickly (in $<10^{-13}$s) relaxes to the conduction band edge, in a process called *thermalisation*, losing the excess energy to the lattice, in the form of phonons [138]. Therefore, the higher the band gap, the less energy is lost by thermalisation[21]. On the other hand, a higher band gap means that less photons of the solar spectrum will have sufficient energy to be absorbed, so the energy of these photons will be lost to the photovoltaic process. From a qualitative point of view, it is already obvious at this point that these two competing processes will lead to an optimal band gap value.

A well established way to calculate the maximum attainable efficiency as a function of the absorber band gap is what is referred to as the *detailed balance*, first applied by Shockley and Queisser to solar cells [139]. It consists in detailing the different opto-electronic processes taking place in the cell, mainly carrier generation and radiative recombination. It allowed future research to concentrate on the most efficient band gaps and abandon absorbers like CdS, for example, which energy band gap was clearly not suitable. A rather simple description of the detailed balance of a photovoltaic device can be found in [28].

The model is based on the following assumptions:

---

[21] Collection of "hot carriers", that is before they thermalise, is also an active subject of research

(a) The *absorptance A(E)* is 0 for $E<E_g$ and 1 for $E>E_g$. Here, E is the energy of the photon passing through the absorber. The absorptance is defined as the probability of a photon reaching the absorber to be absorbed.

(b) All the electron-hole pairs generated are collected when the terminals are short-circuited.

(c) All the photogenerated carriers thermalise to the band edges (to the valence band edge for holes, and to the conduction band edge for electrons)

(d) The only loss mechanism taken into account for the photo-generated carriers is the radiative recombination process, whereby photoexcited electrons return to the valence band, filling holes and emitting photons of energy E_G. The lower limit for the recombination losses is dictated by the black body radiation $\Phi_{b.b}(E,T)$ of the cell, which is considered as a perfectly absorbing body in thermal equilibrium with its environment.

Since real devices do not necessarily meet these ideal criteria, the detailed balance described here sets an upper limit on the efficiency of a single junction cell. In summary of the assumptions made above, the only two processes that are being considered to define the output current generated are the photo-current and the recombination current.

The total generated *current density J_{gen}* by a material of given band gap depends on the incoming flux of photons $\Phi_{in}(E)$ and the probability of absorbing each of these photons *A(E)*. If broken down, $\Phi_{in}(E)$ contains two components: the cell is not only subject to the solar radiation $\Phi_{sun}(E)$, but also to the black body radiation from the environment in thermal equilibrium with it, $\Phi_{b.b}(E)$, and therefore,

$\Phi_{in}(E) = \Phi_{b.b}(E) + \Phi_{sun}(E)$. Regarding *A(E)*, it was assumed in (a) to be a sharp step from 0 to 1 at the band gap, and therefore:

$$J_{gen} = q. \int_0^\infty A(E). \Phi_{in}(E). dE \underset{(a)}{=} q. \int_{E_G}^\infty \Phi_{in}(E). dE \qquad \text{(A1.1)}$$

where q is the charge of the carrier.

The losses by radiative recombination are defined by the black body radiation $\Phi_{b.b}(E,T)$ that must be emitted (lost) by the solar cell in order to reach thermal equilibrium. This is expressed in Würfel's generalisation of Kirchhoff's law as follows [28]:

$$J_{rec} = q. \int_0^\infty A(E). \Phi_{b.b}(E,T). e^{\frac{qV}{kT}}. dE \underset{(a)}{=} q. \int_{E_G}^\infty \Phi_{b.b}(E,T). e^{\frac{qV}{kT}} dE \qquad \text{(A1.2)}$$

T is the temperature of the cell, and J_{rec} the recombination current density in the dark. If we use the assumption (c) that all the carriers have thermalised to the band edges and therefore have the same temperature *T*, the temperature becomes a constant in the black-body radiation term, and therefore $\Phi_{b.b}(E,T) \equiv \Phi_{b.b}(E)$. The total current generated at a voltage *V, is* obtained by adding up the recombination current in the dark (which increases with voltage) and the photogenerated current density (which is not affected by the voltage), i.e.:

$$J(V) = J_{rec}(V) - J_{SC} \underset{(c)}{=} q. \int_{E_G}^\infty \Phi_{b.b}(E). dE . e^{\frac{qV}{kT}} - q. \int_{E_G}^\infty \Phi_{in}(E). dE \qquad \text{(A1.3)}$$

At this stage, *$\Phi_{in}(E)$* needs to be detailed, and the expression of the current becomes after manipulation:

224

$$J(V) = q . \int_{E_G}^{\infty} \Phi_{b.b}(E) . dE . \left[e^{\frac{qV}{kT}} - 1 \right] - q . \int_{E_G}^{\infty} \Phi_{sun}(E) . dE \qquad \text{(A1.4)}$$

This expression is the equation of an ideal diode under illumination. It is often presented in its simplified form:

$$J(V) = J_0 . \left[e^{\frac{qV}{n_{id} kT}} - 1 \right] - J_{SC} \qquad \text{(A1.5)}$$

J_0 is the reverse saturation current density (due to recombination), n_{id} is the *ideality factor* of the diode, $J_{SC} = -J(V)|_{V=0} = -q . \int_{E_G}^{\infty} \Phi_{sun}(E) . dE$ and the *short-circuit current density.* $n_{id} = 1$ for the ideal case considered., Note that $n_{id} \neq 1$ in general in real devices. This is discussed in section 2.4.

At a certain voltage $V=V_{OC}$, the photogenerated current is exactly compensated by the recombination current and $J(V_{OC})=0$. V_{OC} is the *open-circuit voltage*. The expression of V_{OC} can be derived from equation A1.4:

$$V_{OC} = V(J)|_{J=0} = \frac{kT}{q} . ln \left(\frac{\int_{E_G}^{\infty} \Phi_{sun}(E) . dE}{\int_{E_G}^{\infty} \Phi_{b.b}(E) . dE} + 1 \right) = \frac{kT}{q} . ln \left(\frac{J_{SC}}{J_0} + 1 \right) \qquad \text{(A1.6)}$$

Both J_0 and J_{SC} depend on E_G, which is the lower limit of their integrals, therefore $J(V)$ can be expected to depend on E_g too. More precisely, when E_g increases, J_{SC} decreases, since less photons have enough energy to be absorbed, and J_0 increases, since more carriers are available at the electrodes for recombination.

Theoretical efficiency limits

The computed relationship between V_{OC} and E_g is almost linear [140]. This is due to the recombination current decreasing as E_g increases. A qualitative analogy can be done with the breakdown phenomenon observed in electrical boxes or the lightning

in a thunderstorm: when the voltage becomes too high, the accumulated charges "arc" through the medium separating the opposite poles (here the semiconductor).

The photovoltaic conversion efficiency η was defined in 2.1 as the ratio $= \frac{P_{MP}}{P_{in}}$.

P_{MP} is obtained by maximising the product $V.J(V)$. The efficiency can then be expressed as:

$$\eta = \frac{-\max(V.J(V))}{P_{opt}} = \frac{-\max(V.J(V))}{\int_{E_G}^{\infty} E.\Phi_{sun}(E).dE} \tag{A1.7}$$

If plotted against the energy band gap (Figure 93), η reaches a maximum of 33% at 1.35eV, with another local maximum of 32.8% at 1.15eV.
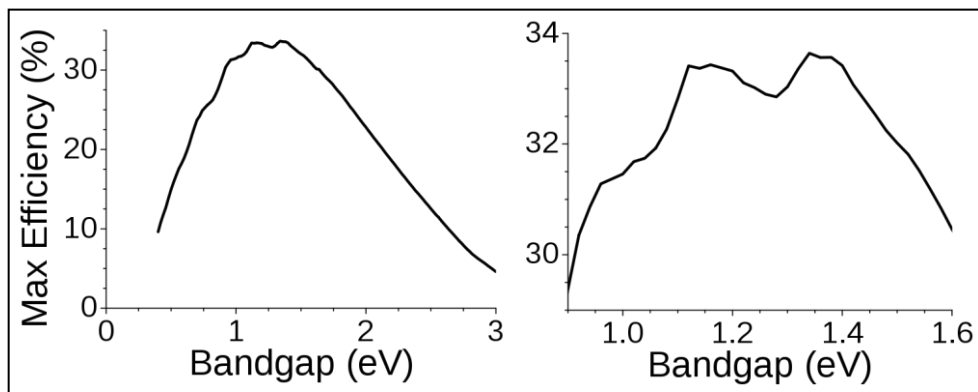
Figure 93: Shockley-Queisser limit calculated from the global AM1.5 solar spectrum.
Left: **large range;** *Right*: **zoom on the highest efficiency range.** *Source: [7, 141]*

Due to a defect-induced V_{OC} limitation, $E_G \approx 1.15$ eV, $\left(\frac{Ga}{In+Ga} \approx 0.3\right)$ is currently the average energy band gap used in the best performing CIGS devices [142].

As mentioned earlier, assumption (c) (losses by thermalisation to the band edges) could be removed if proper hot carrier collection could be achieved. Multi-junction devices aim at minimizing these losses by combining semiconductors with different band gaps. This route has already proved that devices with efficiencies above the 33% limit of single junction cells can be achieved in practice (e.g. a

226

GaInP/GaAs/GaInAs triple junction cell has been made by Sharp with an efficiency of 36.9% [143]). The maximum efficiency theoretically achievable if all the wavelengths of the solar spectrum are collected without thermalisation losses becomes 86% [138].

APPENDIX 2　　　　Ewald sphere and texture coefficient

Ewald sphere

Bragg's representation, although useful in terms of understanding, is not convenient to predict the exact diffraction pattern generated by a given crystal. To do this, a more useful tool was created, in 1913 as well, by the German physicist Ewald, named the *Ewald sphere* [144]. To build this representation, Ewald made use of a transformation of the real lattice into a so-called "reciprocal lattice" [145]. In the reciprocal lattice, the three vectors of the unit cell $\vec{a}, \vec{b}$ and $\vec{c}$ are replaced by $\vec{a}^*, \vec{b}^*$ and $\vec{c}^*$, which can be defined by:

$$\vec{a}^* = \frac{\vec{b} \times \vec{c}}{V}; \vec{b}^* = \frac{\vec{c} \times \vec{a}}{V}; \vec{c}^* = \frac{\vec{a} \times \vec{b}}{V} \tag{A2.1}$$

It can be shown from this definition that:

$$d^*_{hkl} = \frac{1}{d_{hkl}} \tag{A2.2}$$

$$|\vec{a}^*| = \frac{1}{a}; |\vec{b}^*| = \frac{1}{b}; |\vec{c}^*| = \frac{1}{c} \tag{A2.3}$$

with d^*_{hkl} the distance between two consecutive planes of the family (hkl). Ewald showed that diffraction phenomena could be represented by the construction given in Figure 94. If the wave vectors $\vec{k}_0$ and $\vec{k}_1$ are vectors, parallel to the incident and reflected beam, respectively, and of length:

$$|\vec{k}_0| = |\vec{k}_1| = \frac{1}{\lambda} \tag{A2.4}$$

The angle between $\vec{k}_0$ and $\vec{k}_1$ is *2θ* in the diagram used in Figure 10.
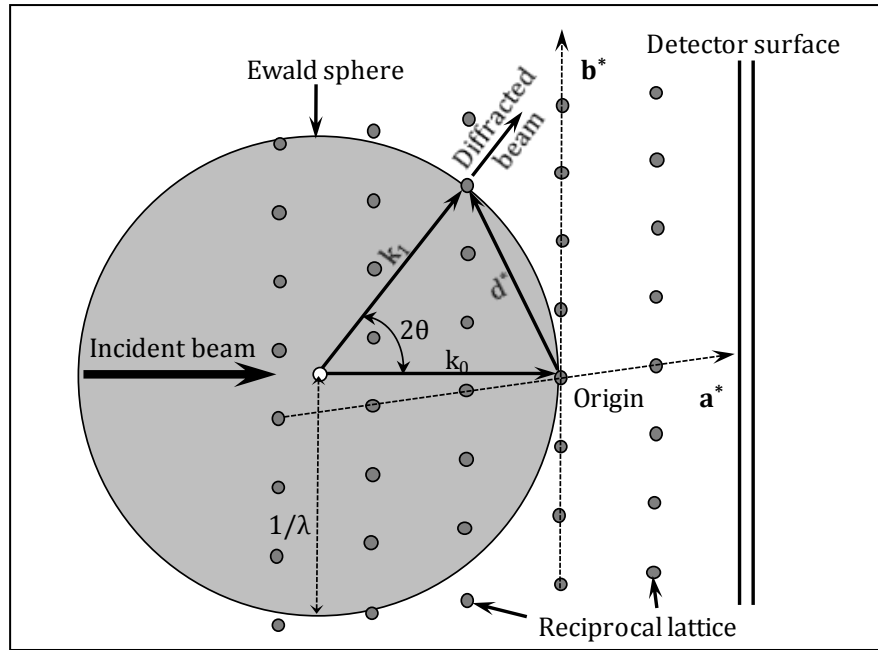
Figure 94: 2-dimensional diagram illustrating the use of the Ewald's sphere to predict the diffraction pattern formed on a flat detector by radiating X-rays onto a single crystal. Only the points of the reciprocal lattice coinciding with the surface of the Ewald's sphere will give rise to a diffraction spot. *Source: [146].*

Ewald showed that if the vector $\vec{k}_0$ is placed so that its end coincides with the origin of the lattice (Figure 94 and), then diffraction can only occur if $\vec{k}_1$ and $\vec{k}_0$ start at the origin and end on reciprocal lattice points. This can be understood if one considers that $\vec{k}_1$ must meet the condition $\left|\vec{k_0}\right| = \left|\vec{k_1}\right|$ and that the angle between the two vectors must be *2θ*. Therefore, the diffraction pattern observed on the detector will be the projection of the points of contact between the Ewald sphere and the reciprocal lattice, onto the detector surface. It must be pointed out that the reciprocal lattice does not correspond to any physical reality but is a valuable tool for the analysis of diffraction patterns. In the case of a single, non-rotating crystal, such as that represented in Figure 94, the diffraction pattern generated will be a series of bright points. Now in a powder, there are a multitude of small crystals, called crystallites, with each randomly oriented unit cell vectors.

In the ideal case of a perfect distribution of randomly oriented crystallites, the discrete points of the diffraction pattern become a series of concentric rings, called *Debye rings*. Indeed, the interplanar distance d_{hkl} (and therefore d_{hkl}^*) remains the same in a powder, but the random orientation of the crystallites yields this time a circle intersecting the Ewald sphere, perpendicular to $\vec{k}_0$. The projection of this circle onto the detector plane is a ring, only distorted by the tilt angle of the detector. This ring is called a *Debye ring*. For each value of d_{hkl} existing in the sample, which also corresponds to a *2θ* value, such a ring will be generated. The result is a pattern of concentric rings. An example, illustrating the generation of a diffraction pattern from a CuInSe$_2$ thin film on Mo, is shown in Figure 95.
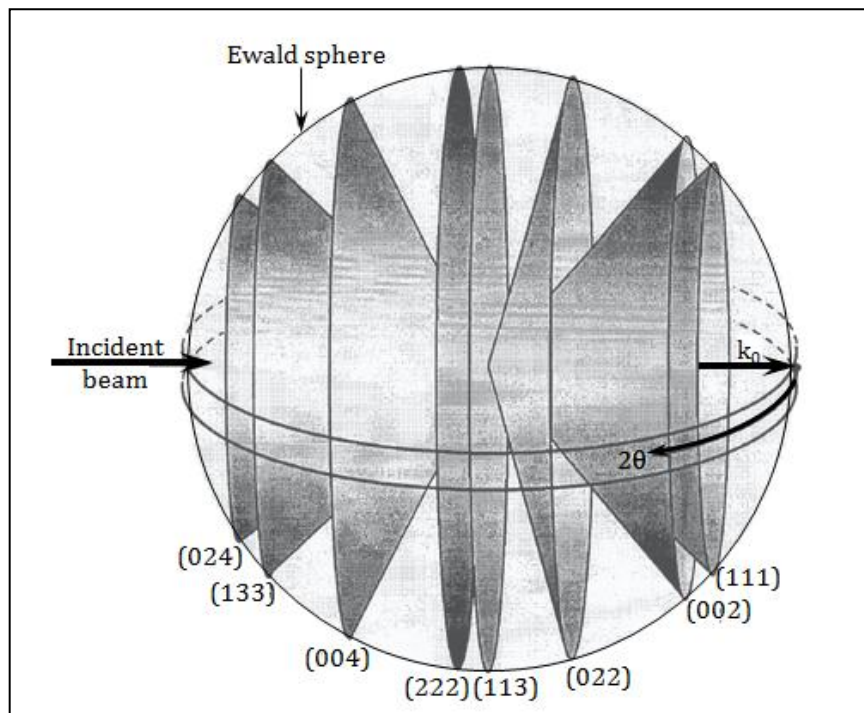
Figure 95: 3-Dimensional representation of the diffraction cones generated by a Cu polycrystalline powder under Cu Kα$_1$ radiation. *Source: [147].*

If a relatively narrow, rectangular detector is used to scan the *2θ* angles (symbolised by the equatorial ribbon in Figure 95), the result will be a spectrum with peaks of

intensity at the angles where the detector meets a cone, that is, at the d_{hkl} values specific to the crystal, as in the example shown in Figure 96.
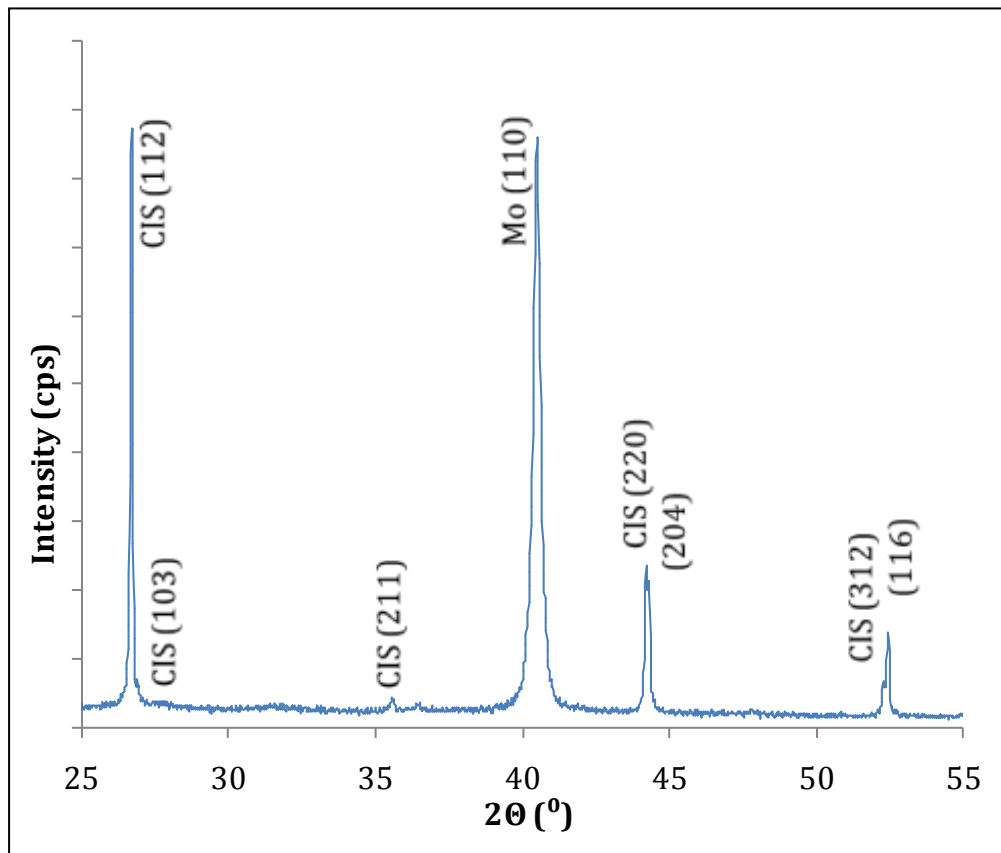
Figure 96: Example of an X-ray diffraction spectrum, here of a CuInSe2 sample on Mo, generated by a Cu Kα1 radiation.

In this spectrum, both the peaks positions and the ratio between the peak intensities will be characteristic of the sample analysed. Therefore, by comparing the peaks positions of a measured spectrum with the tabulated patterns produced from crystal powders, it is possible to identify the crystalline phases present in the sample analysed. Note that the separation of the (220)/(204) and (312)/(116) doublets is a characteristic of the tetragonal distortion.

Texture coefficient

The powder diffraction spectra used for phase identification are close to the ideal case where the crystal contains an infinite number of randomly distributed crystal orientations. However, this condition is generally only partly met in polycrystals: the orientations of the crystallites are generally not random. For instance, a platelet-like crystallite will tend to grow with its widest flat surface parallel to the substrate, and as a result the {hkl} planes that are parallel to the substrate will give rise to the most intense diffraction peaks compared to the other planes. The crystal will be said to have an <hkl> *texture*, or *preferred orientation* (as opposed to random orientation). Inversely, the reflections from the {h'k'l'} planes that are perpendicular to the surface will be the most attenuated. Therefore, the texture of a polycrystalline sample can be assessed by comparing the measured ratios between peaks, to the ratios reported for powder diffraction of the same crystalline phase. To determine a preferred orientation, a quantity called *texture coefficient,* C_{hkl}, is commonly used. It is defined as [148]:

$$C_{hkl} = \frac{\frac{I_{hkl}}{I_{r,hkl}}}{\frac{1}{n} \cdot \sum \frac{I_{h'k'l'}}{I_{r,h'k'l'}}} \tag{A2.5}$$

with I_{hkl} the intensity of the reflection from the family of atomic planes defined by the miller indices h, k, and l; $I_{r,hkl}$ the intensity of the peak in the reference spectrum, obtained from powders. A high texture coefficient for one family of Miller planes means that the polycrystal is preferentially oriented perpendicularly to this family of planes. Note that this expression is no longer accurate if the number of reflections is small. Besides, it is only valid for a moderate preferred orientation. If this is not the case, the luminosity varies locally along the Debye rings. Since the detector only

232

collects the diffracted light from a small portion of the Debye rings, the resulting intensity therefore depends on what portion of the ring is measured, and the results are no longer reliable.

Standard deviation of energy dispersive spectroscopy

(EDS) measurements

Standard deviation of the instrument

An experiment was devised to assess the stability of the compositions measured by

EDS for two different acquisition counts, 50,000 and 150,000 counts (Table 30).

Table 30: Stability of the EDS measurements obtained with 150,000 counts (top table)
or 50,000 counts (bottom table), on several locations, and twice on each location.

Elemental composition (atomic %)	Loc. 1 (150,000c)		Loc. 2 (150,000c)		Loc. 3 (150,000c)		Loc. 4 (150,000c)	
Cu	56.18	56.42	56.43	57.61	56.28	56.82	56.03	56.89
In	43.82	43.58	43.57	42.39	43.72	43.18	43.97	43.11

Elemental composition (atomic %)	Loc. 5 (50,000c)		Loc. 6 (50,000c)		Loc. 7 (50,000c)		Loc. 8 (50,000c)		Loc. 9 (50,000c)	
Cu	57.29	56.9	57.55	57.51	57.51	57.44	56.9	56.81	57.19	57.1
In	42.71	43.1	42.45	42.49	42.49	42.56	43.1	43.19	42.81	42.9

Composition measurements were performed in nine different locations of the same

sample, twice at each location. The difference measured within each couple was then

averaged over the nine locations, and a standard deviation on this composition was

extracted. This method permitted an assessment of the variation of the instrument

that was not affected by the variations in composition across the surface.

The average standard deviation on the measurements is therefore **0.06% for 150000**

counts and **0.4% for 50000 counts**. For the rest of this work, 0.4% was considered

accurate enough, and 50,000 counts was used for all EDS measurements.

Composition uniformity across the samples surface

As a routine, EDS measurements were performed on 5 standard locations of the samples: centre, centre left, centre right, top, bottom, using 50,000 counts. This made it possible to assess the standard deviation in composition (absolute value) across the surface. This standard deviation was measured on several Cu-In metallic precursors and $CuInSe_2$ absorbers, in order to assess the variation in composition across the sample's surface (Table 31).

Table 31: Standard deviation of the EDS composition in a set of precursors and converted layers (measured on 5 locations).

Sample	Standard deviation (%)		
	Cu	In	Se
Precursor 1	0.26	0.26	
Precursor 2	1.20	1.20	
Precursor 3	0.33	0.33	
Precursor 4	0.62	0.62	
Precursor 5	0.76	0.76	
Precursor 6	0.56	0.56	
Precursor 7	1.31	1.31	
Absorber 1	0.84	0.74	0.19
Absorber 2	2.39	1.60	0.84
Absorber 3	0.40	0.25	0.29
Absorber 4	0.55	0.24	0.37
Absorber 5	1.43	0.94	0.57
Absorber 6	0.84	0.41	0.54
Absorber 7	0.48	0.27	0.23
Absorber 8	0.65	0.39	0.34

Based on the results presented above, the average standard deviation measured with 50,000 counts in the precursors was therefore:

$$<\sigma_{Cu}> = <\sigma_{In}> = \mathbf{0.7\%}$$

and that of the selenised samples:

$$<\sigma_{Cu}> = 0.9\%; <\sigma_{In}> = 0.6\%; <\sigma_{Se}> = \mathbf{0.4\%}$$

In summary, the composition uniformity across the samples was found to be better than 1% on average for a 50,000 count measurement.

APPENDIX 4   Sputter targets calibration

The metallic precursors for CIAS and part of the CIS and CAS samples were deposited from elemental targets of Cu, In and Al. The first requirement was to determine what set of power had to be applied to the targets in order to obtain any desired composition. An initial calibration of the deposition rate of each target was performed, by placing SLG slides underneath a target with different powers applied. This was repeated for the three targets. It should be noted that the actual deposition of the metallic precursors was performed in the "dynamic mode", whereby the substrates were rotated underneath the targets, so as to deposit a succession of thin elemental layers. The results obtained from the static mode were therefore extrapolated to determine the power to apply in the dynamic mode.

Deposition rate

The **deposition rate** obtained from an elemental target i, S_i, is defined here as the average number of moles of element deposited from the target onto a 26 mm by 76 mm sample, each minute. It can be averaged over the duration of the deposition as:

$$S_i = \frac{\mathcal{N}_i}{T_{dep}} \qquad (10.1)$$

with $\mathcal{N}_i$ the number of moles of element i deposited over the entire course of the deposition, and T_{dep} the overall duration of the deposition, expressed in minutes. $\mathcal{N}_i$ was calculated in two different ways:

- $\mathcal{N}_i^t$ from the thickness of the film deposited and the tabulated density of the element. This route was only viable when the film contained a single element.

- $\mathcal{N}_i^m$ from the mass and the weight composition of the film, measured by EDS. This route applied also to films made of a homogeneous mixture of various elements.

For a single element, $\mathcal{N}_i^t$ can be determined as follows:

$$\mathcal{N}_i^t = \frac{\rho_i \cdot \mathcal{A}_s \cdot t_i}{\mathcal{M}_i} \tag{10.2}$$

ρ_i is the density of the element i, $\mathcal{M}_i$ its molar mass, t_i the thickness deposited and $\mathcal{A}_s$ the area of the substrate. $\mathcal{N}_i^m$, on the other hand, is obtained, in the general case where several elements can be present, from the following calculation:

$$\mathcal{N}_i^m = \frac{R_i^m \cdot \Delta m}{\mathcal{M}_i} \tag{10.3}$$

R_i^m is the weight percentage of element i as assessed by EDS, $\mathcal{M}_i$ its molar mass and Δm the total mass deposited.

Issues related to the use of thickness to assess the amount of material deposited

At this stage of the discussion, it is necessary to point out some inherent issues relating to the use of the film thickness as a figure of merit to estimate the deposition rate. In comparison to the mass variation method, the use of thickness can lead to two main types of error:

(a) If the identification of the phases in presence is erroneous, this can lead to relatively important errors on the density of the film, and therefore on the deposition rate S_i.

(b) If the film surface is rough, the error on the thickness increases and therefore so does the error on the deposition rate.

The impact of **(a)** is illustrated by the example below, where a selenised sample (absorber layer) is considered. Let us consider an absorber film of thickness *t*, deposited on a standard substrate of dimensions 26 mm by 76 mm, and two different phase compositions: a film containing a single $CuInSe_2$ phase or a film containing two phases, In and $CuSe_2$.

- Assuming a single phase of $CuInSe_2$. The unit cell volume of $CuInSe_2$ is $V^{cell}_{CuInSe_2}$=401.48 $Å^3$; and the number of $CuInSe_2$ molecules per unit cell α=4. The number of moles of $CuInSe_2$ present is therefore:

$$\mathcal{N}^t_{CuInSe_2} = \frac{\alpha_{CuInSe_2}}{\mathcal{N}_A} \times \frac{\mathcal{A}_s . t[cm]}{V^{cell}_{CuInSe_2}} = \mathbf{0.3269 \times t[cm]} \tag{10.4}$$

- Now, assuming two phases $CuSe_2$ and In, in the ratio 1:1. Cell volume of $CuSe_2$ $V^{cell}(CuSe_2)$ =229.11 $Å^3$, with $\alpha_{CuSe_2} = 4$ molecules per cell; $V^{cell}(In)$ =55.01 $Å^3$, with $\alpha_{In} = 2$ atoms per cell; The number of moles of $CuSe_2$ was defined as equal to that of In, so that:

$$\mathcal{N}^t_{CuSe_2} = \mathcal{N}^t_{In} = \frac{1}{\mathcal{N}_A} \times \frac{\mathcal{A}_s . t[cm]}{\frac{V^{cell}_{CuSe_2}}{\alpha_{CuSe_2}} + \frac{V^{cell}_{In}}{\alpha_{In}}} = \mathbf{0.3870 \times t[cm]} \tag{10.5}$$

The relative variation between these two values is:

$$\frac{\Delta \mathcal{N}^t}{\langle \mathcal{N}^t \rangle} = \frac{0.3870 - 0.3269}{0.35695} \approx 17\% \tag{10.6}$$

Thus, to work with thicknesses from films containing several elements, one has to know the atomic composition and the phases present. XRD, the main tool used for this purpose in this work, makes it possible to identify crystalline phase but does not detect amorphous phases. The identification of the phases based on XRD could

therefore be flawed. When working with mass variation instead of thickness, on the other hand, the knowledge of the phases present is not required.

Now, regarding the impact of **(b)**, one can compare the maximum relative error on $\mathcal{N}^{\mathrm{t}}$ and on $\mathcal{N}^{\mathrm{m}}$, and use the expression 5.2 for $\mathcal{N}^{\mathrm{t}}$. Considering a film made of a single element for simplicity, this yields:

$$\mathcal{N}_i^{\mathrm{t}} = \frac{\rho_i . \mathcal{A}_s . t_i}{\mathcal{M}_i} \rightarrow \frac{\sigma(\mathcal{N}_i^{\mathrm{t}})}{\mathcal{N}_i^{\mathrm{t}}} = \frac{\sigma(\rho_i)}{\rho_i} + \frac{\sigma(\mathcal{A}_s)}{\mathcal{A}_s} + \frac{\sigma(t_i)}{t_i} + \frac{\sigma(\mathcal{M}_i)}{\mathcal{M}_i} \tag{10.7}$$

$$\frac{\sigma(\rho_i)}{\rho_i} < 0.2\%; \;\; \frac{\sigma(\mathcal{A}_s)}{\mathcal{A}_s} < 0.3\%; \;\; \frac{\sigma(\mathcal{M}_i)}{\mathcal{M}_i} < 0.01\% \tag{10.8}$$

Where $\sigma(a)$ is the absolute error on the variable a. For the parameters found in the literature, σ was estimated from the number of digits provided. For the experimental data and when no other criteria of evaluation were available, σ was approximated to the standard deviation measured experimentally. Samples made of a pure element displayed a surface roughness typically in the range 10 nm to 30 nm, yielding

$$\frac{\sigma(t_i)}{t_i} < 3\% \rightarrow \frac{\sigma(\mathcal{N}_i^{\mathrm{t}})}{\mathcal{N}_i^{\mathrm{t}}} \approx \mathbf{3.5\%} \tag{10.9}$$

The roughness observed on a typical CuInAl precursor, however, was over 100 nm on a $\approx$600 nm thick precursor[22]. This yields

$$\frac{\sigma(t_i)}{t_i} = \frac{100}{600} \approx \mathbf{17\%} \rightarrow \frac{\sigma(\mathcal{N}_i^{\mathrm{t}})}{\mathcal{N}_i^{\mathrm{t}}} \approx \mathbf{17.5\%} \tag{10.10}$$

Therefore, the error on $\mathcal{N}^{\mathrm{t}}$ is largely dominated by the error on the thickness.

Using the mass variation technique, on the other hand, yields:

---

[22]**The higher roughness of CuInAl precursors and its possible cause are discussed in 5.4.**

$$\mathcal{N}_i^m = \frac{R_i^m \cdot \Delta m}{\mathcal{M}_i} \rightarrow \frac{\sigma(\mathcal{N}_i^m)}{\mathcal{N}_i^m} = \frac{\sigma(R_i^m)}{R_i^m} + \frac{\sigma(\Delta m)}{\Delta m} + \frac{\sigma(\mathcal{M}_i)}{\mathcal{M}_i}$$

$$\text{(10.11)}$$

$$\frac{\sigma(\mathcal{N}_i^m)}{\mathcal{N}_i^m} < 2.5\% + 5 \times 10^{-2}\% + 10^{-2}\% \approx \mathbf{2.6\%}$$

Therefore, the maximum error obtained by the mass variation method is lower than the one obtained from the thickness measurement, especially when a matrix of several elements is present in the film. As shown above, an erroneous identification of the phases in presence can lead to a substantial error when assessing $\mathcal{N}_i$ from thickness data. The amount of Cu, In and Al deposited in dynamic mode was consequently assessed using the mass variation technique rather than the thickness.

Plots for static depositions from single targets

For the initial static trials, a strip of each sample was covered with vacuum compatible tape, the samples to coat placed underneath the relevant target, and depositions at different powers with a static substrate table were performed. The tape was then removed and the thickness deposited, corresponding to the height of the step between the surface of the uncoated substrate and that of the precursor, was measured with a Talystep Taylor Hobson step profiler. The tabulated densities of each metal were then used to extract the deposition rates S_i from the thicknesses measured and the deposition time applied, and the graphs S_i vs P_{target}, where P_{target} is the power applied, were then plotted for each target. As mentioned before, the thickness deposited in static mode is highly non-uniform in both the radial direction of rotation of the substrate table, and its perpendicular direction. The thickness was therefore measured on the most central slide of the platen and at the same point, located approximately halfway along the slide's length (Figure 97).
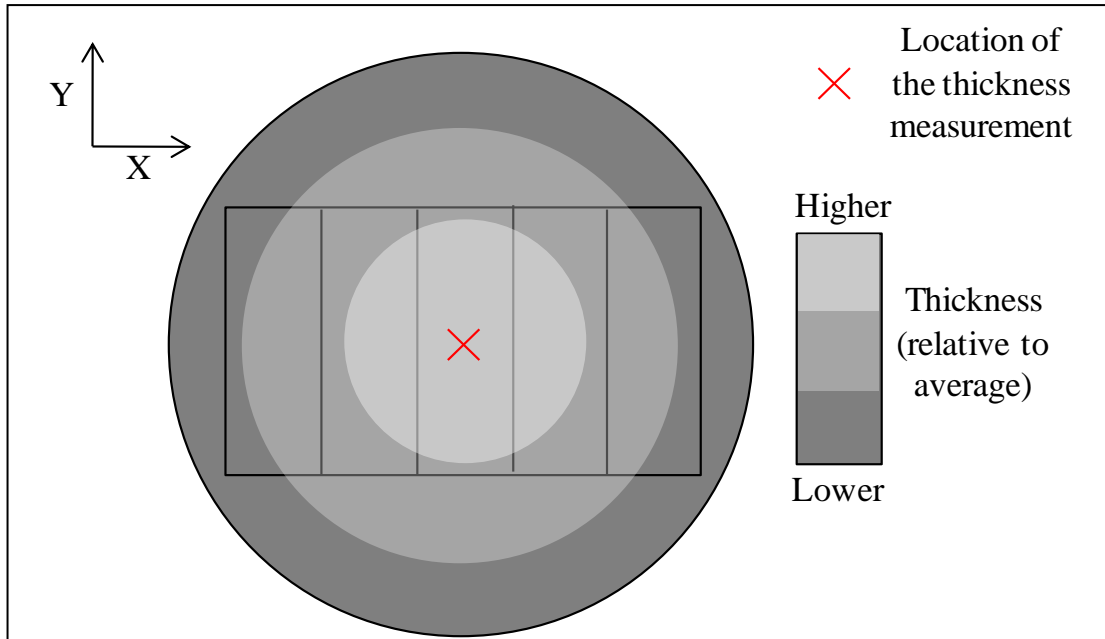
Figure 97: Location chosen for thickness measurement in static-deposited films.

Data

The plots S_{sput} vs P_{target} obtained for the Cu, In and Al target are represented in Figure 98, Figure 99 and Figure 100, respectively. The data points could be fitted approximately with a linear curve. The absolute errors used for each data point deposited in static were calculated from the following errors on the parameters:

$$\sigma_\rho < 10^{-2} \text{ g. cm}^{-3}; \ \sigma_\mathcal{M} < 10^{-2} \text{ g. mol}^{-1}; \ \sigma_{\mathcal{A}_s} < 2 \times 10^{-2} \text{cm}^2;$$

$$\sigma_t < 20 \text{ nm}; \ \sigma_{\Delta m} < 5 \times 10^{-5} \text{g} \tag{10.12}$$

The standard deviation on $\mathcal{N}_i^t$ was then calculated for all data points. It was found to be too low (typically below 0.1% of the data value) to be displayed on the plots. In particular, in the specific case where pure elements were deposited, the standard deviations obtained from mass variation were significantly lower (10 to 100 times lower) than those obtained from the thicknesses.
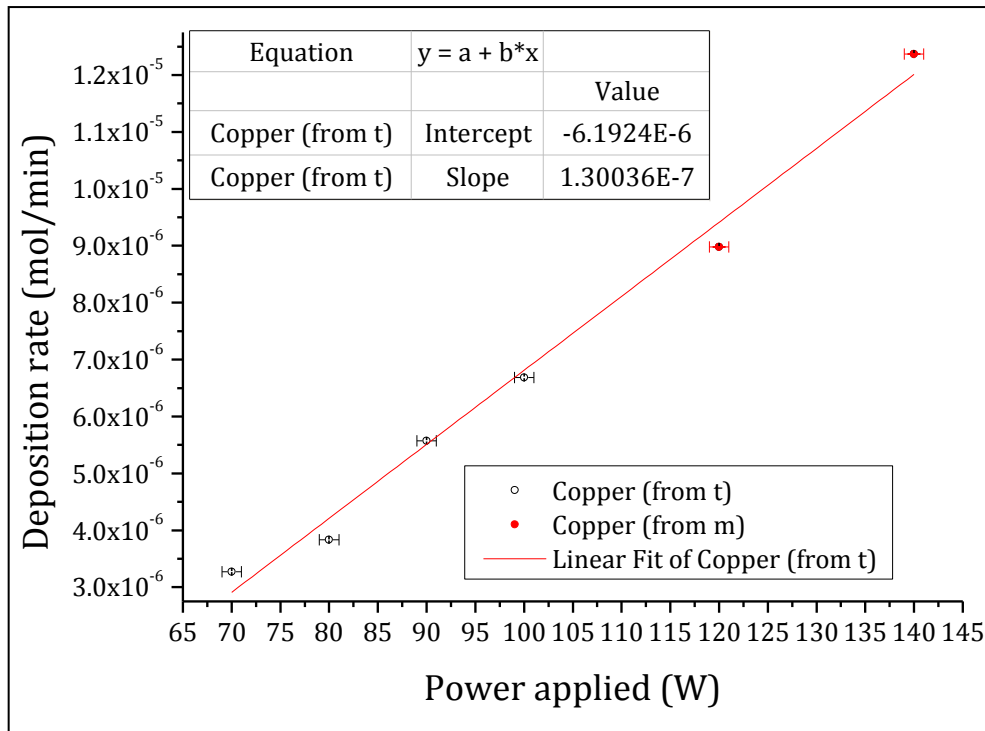
Figure 98: Cu target calibration curve from static deposition, assessed from thickness (empty black disks) or mass (full red disks).
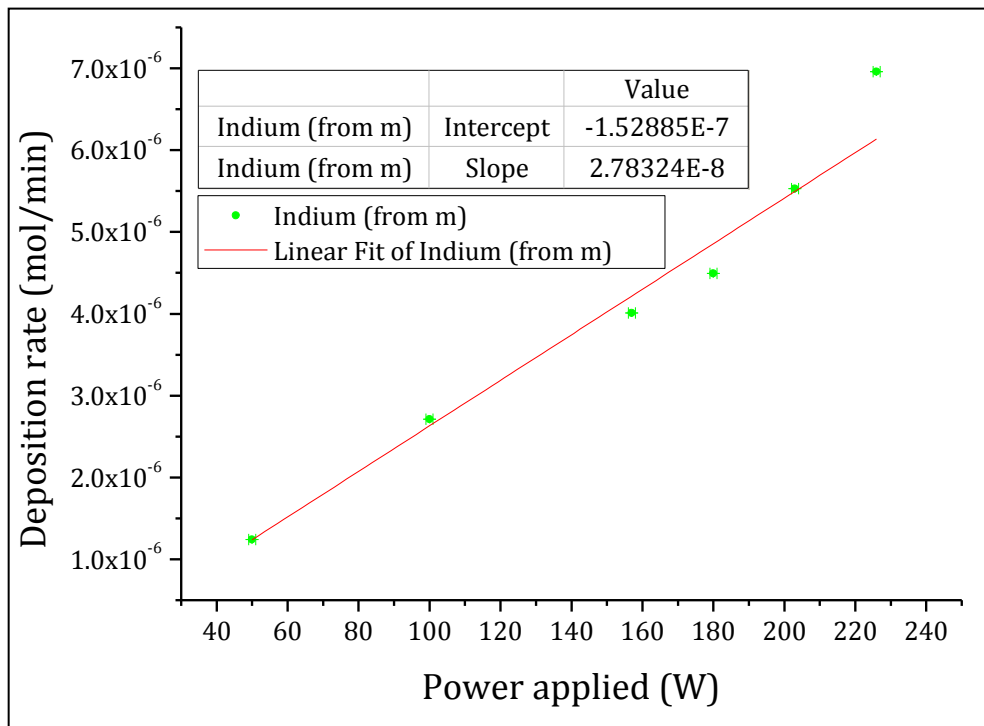
Figure 99: In target calibration curve from static deposition.
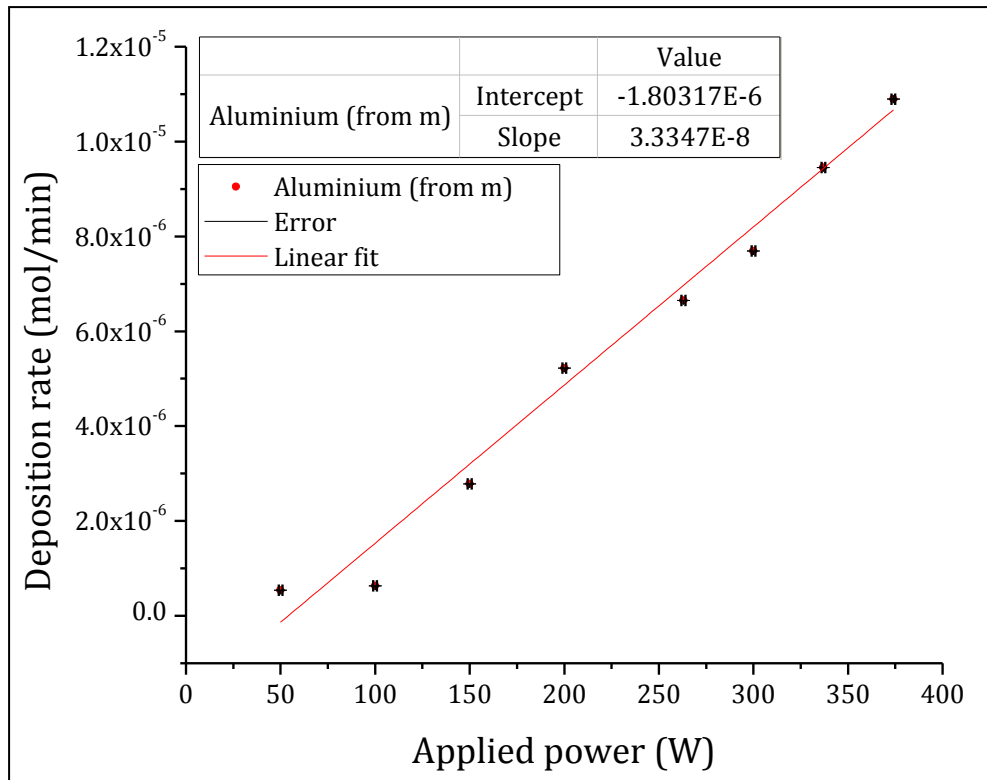
Figure 100: Al target calibration curve from static deposition.

Discussion

For the Cu calibration curve (Figure 98), two data points were assessed from mass variation, the rest being extracted from the thicknesses. The good match of these two points with the linear fit of the other points indicates a good compatibility of the two techniques.

Dynamic depositions from three targets

The equations of the linear fits were used to estimate approximately the set of powers to apply to obtain a given composition when moving to dynamic deposition from the three targets. From the plots in static and from single elemental targets, the powers to apply to approach a given composition could be extracted. To extrapolate the sets of power to apply in dynamic mode from the trials in static mode, the following assumptions were made:

(a) The average deposition rate of each target in dynamic depositions is proportional to the deposition rate in static.

(b) The deposition rates are stable through time.

(c) The proportionality coefficient is the same for all three targets.

Condition (a) is met if each target sputters over an area that corresponds to a constant portion of the rotation path of the substrates. Condition (c) means that all targets should sputter over the same area. This assumption was made as a starting point for dynamic depositions. However, the departure from it could then be assessed by the mass variation method and corrected. For dynamic depositions, the substrate table was rotating under the three targets Cu, In and Al. The slides were weighed before deposition on a precision scale (accuracy better than $5x10^{-5}$ g). After the metallic precursor deposition, the same samples were weighed again, and their weight composition measured by EDS. The deposition rates could then be extracted by the mass variation method and plotted against the power applied to each target.

Data

Deposition batches from three elemental targets were then started. The equations of the fitted lines in Figure 98, Figure 99 and Figure 100 were used to determine the sets of powers to apply to obtain aimed compositions. In practice, for an aimed composition x% of Cu, y% of In and z% of Al, the power applied to Cu was first chosen arbitrarily and the equation of the Cu fit in static was then used to determine what deposition rate to expect. The following relationship between the deposition rates S_i and the composition must be fulfilled:

$$x = \frac{S_{Cu}}{S_{Cu} + S_{In} + S_{Al}} ; y = \frac{S_{In}}{S_{Cu} + S_{In} + S_{Al}} ; z = \frac{S_{Al}}{S_{Cu} + S_{In} + S_{Al}} \qquad (10.13)$$

The power to apply to the In target is determined from the power applied to Cu, using once again the fitted equation, in order to get $S_{In} = \frac{S_{Cu} \times y}{x}$. The compositions expected from the fit of static data are compared to the data obtained in dynamic, by mass variation, in Table 32. In this table, samples deposited in different deposition batches are separated by thicker lines. Various sets of powers (not indicated in the table) were applied and resulted in various compositions. Results show that the compositions obtained in dynamic mode were in some cases significantly different from the expected values: up to ≈13% relative for In, or even ≈41% relative for Al, for example. However, percentages do not provide any real insight into the actual factors of variation because they are interdependent, i.e. if the deposition rate of one element changes, its percentage will change, and so will the others to ensure a constant total of 100%.

Table 32: Comparison of the compositions predicted from the fitted lines in static, and measured experimentally, for samples deposited in dynamic mode. The relative variation is indicated on the rightmost columns.

ID	Cu at% fit	In at% fit	Al at% fit	Cu at% real	In at% real	Al at% real	ΔCu/\<Cu>	ΔIn/\<In>	ΔAl/\<Al>
N420B	53%	38%	10%	45.2%	44.3%	10.5%	7.5%	7.8%	4.5%
N420D	53%	38%	10%	45.4%	43.5%	11.1%	7.3%	6.8%	7.5%
N394A	54%	26%	20%	49.2%	32.1%	18.7%	4.9%	11.2%	3.7%
N394B	54%	26%	20%	48.9%	32.8%	18.3%	5.2%	12.1%	4.5%
N426J	49%	21%	29%	45.3%	26.0%	28.7%	4.3%	10.0%	1.1%
N426K	49%	21%	29%	45.2%	25.8%	29.0%	4.4%	9.5%	0.5%
N428H	55%	19%	26%	51.3%	22.7%	26.0%	3.4%	9.0%	0.3%
N428I	55%	19%	26%	50.9%	22.5%	26.6%	3.8%	8.6%	0.9%
#557	35%	58%	6%	40.0%	44.5%	15.5%	6%	13%	41%

To explain the differences between measured compositions and expected ones, the mass variation method was applied to determine the deposition rates obtained in several dynamic depositions. These deposition rates are plotted against the power applied (Figure 101).

At least five samples from each deposition batch were weighed before and after deposition, and analysed by EDS. In Figure 101, the standard deviation on those results is represented by the error bars in both plots. This standard deviation is mostly influenced by the error on the measurement. One can notice a spread in the Cu deposition rate at powers higher than ≈140 W (there is not enough data at lower power to make any comment), and a more important spread of the deposition rate from the In target, with a variation as high as ≈46% at 160 W applied.

In Figure 102 are reported the different deposition rates obtained in a series of subsequent runs, in order to assess the stability of the deposition rates from one run to the next.

The plot shows that:

(a) The Al and Cu deposition rates are relatively stable in absolute terms, both from one run to the next and between "remote" deposition runs (e.g. Al deposition rates obtained at 160 W applied, or Cu at 130W-135W). However, Cu deposition rate changes abruptly between run #667 and #668, both performed at the same power, 142W.

(b) The deposition rate is relatively stable from one run to the next, but a more important variability between "remote" runs (e.g. 7.5×10^{-7} mol.min^{-1} in run #423 and 1.1×10^{-7} mol.min^{-1} in run #606) exists.
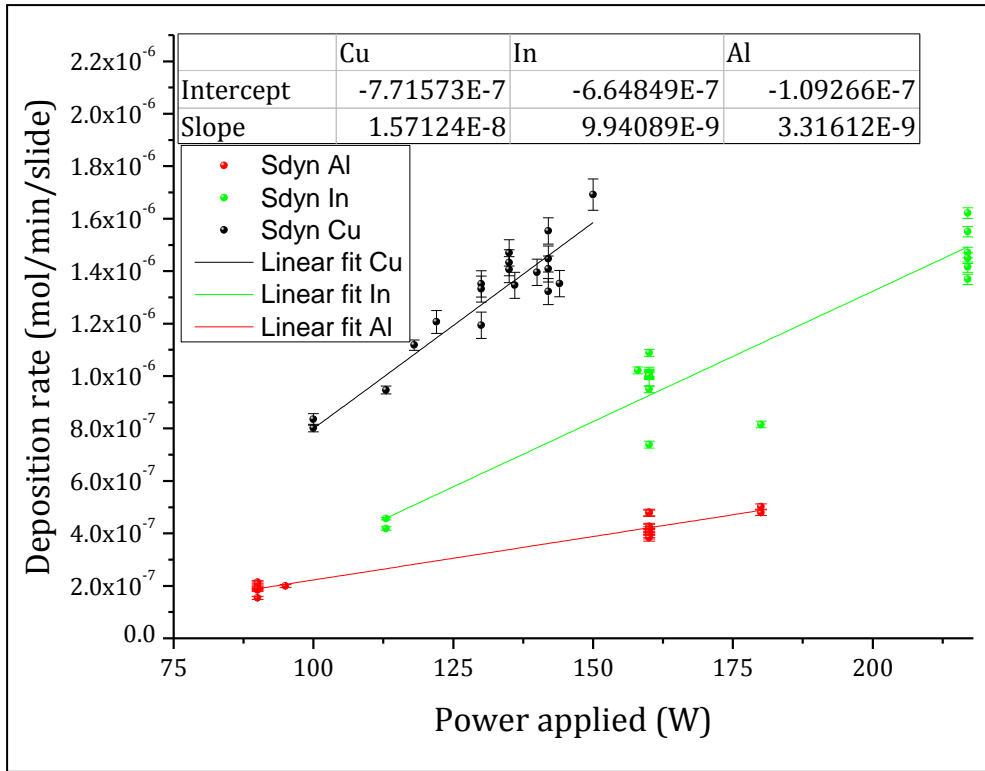
Figure 101: Deposition rates in dynamic depositions from the Cu, In and Al target, plotted against the power applied to the target.
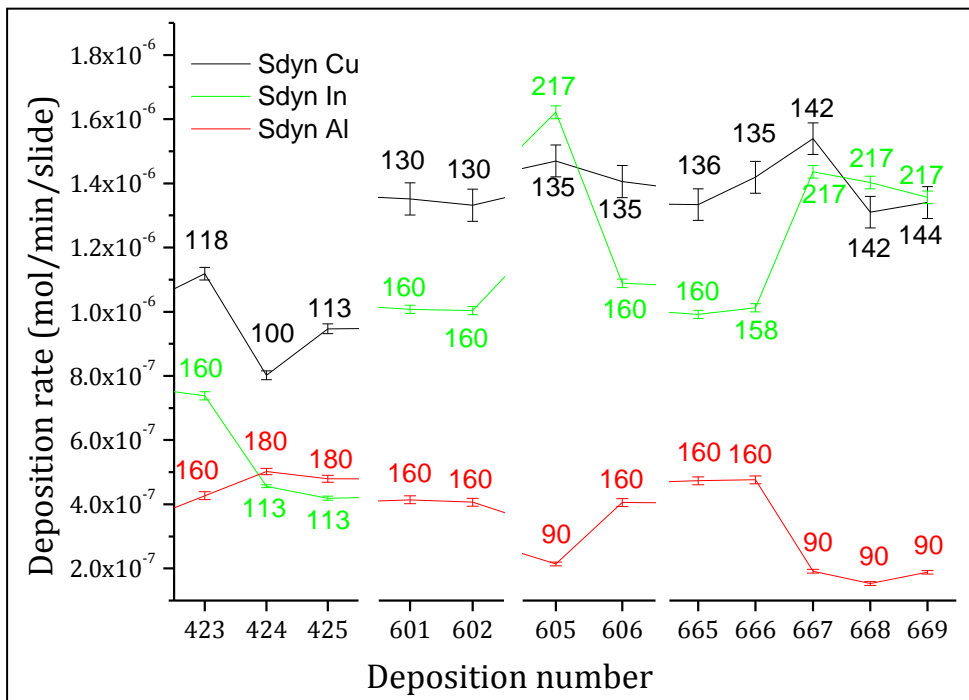

Figure 102: Deposition rates obtained in dynamic depositions from Cu, In and Al targets, plotted in the order of the depositions. Next to the points are indicated the powers applied to the targets.

247

Discussion

The important variability of In is likely to be the main cause for the observed discrepancy between the compositions extrapolated from the static measurements and the compositions measured after dynamic deposition. The fact that the spread in the In deposition rates did not appear clearly in static could be due to the lack of points, or rather to the fact that only a few depositions were performed, and one after another. Indeed, as Figure 102 indicates, as well as additional data points not shown in the figure, the major variations for this target seemed to appear over a great number of depositions. Oxidation of In targets was reported in the literature to cause a drop in sputtering rate. In particular is mentioned the necessity for pre-sputtering to remove the oxides that form during deposition. A 15 minutes pre-sputter was performed before each deposition in this work, but it is possible that some oxidation was still present in some cases. The calibration curves established in static and later dynamic (once enough data points populated the plots) could therefore only be used as a guide, and mainly when the set of powers was changed for previously untested values. These curves could lead to a ratio between [Cu] and [Al] close to the expected values, but the power to apply on In had then to be adjusted. When possible, using recently tested parameters proved a relatively safe way to obtain the wanted composition.

References

[1]   S. Marsillac, P. D. Paulson, M. W. Haimbodi, R. W. Birkmire, and W. N. Shafarman, "High-efficiency solar cells based on Cu(InAl)Se$_2$ thin films", *Applied Physics Letters,* vol. 81, pp. 1350-1352, 2002.

[2]   Solar Frontier, "Solar Frontier Sets New Efficiency World Record", *retrieved 29th February 2012*, http://www.solar-frontier.com/eng/news/ 2012/ C002980.html.

[3]   Miasole, "Miasole achieves efficiency milestone for panel production", *retrieved 16th February 2012*, http://www.miasole.com/sites/default/files/ MiaSole%2014%25%20efficiency-%20FINAL4.pdf.

[4]   P. Jackson, D. Hariskos, E. Lotter, S. Paetel, R. Wuerz, R. Menner, W. Wischmann, and M. Powalla, "New world record efficiency for Cu(In,Ga)Se$_2$ thin-film solar cells beyond 20%", *Progress in Photovoltaics: Research and Applications,* vol. 19, pp. 894-897, 2011.

[5]   PV news, "PV News Annual Data Collection Results: 2010 Cell, Module Production Explodes Past 20 GW", *retrieved 10th November 2011*, http://www.greentechmedia.com/articles/read/pv-news-annual-data-collection-results-cell-and-module-production-explode-p/.

[6]   U. Rau, M. Schmidt, A. Jasenek, G. Hanna, and H. W. Schock, "Electrical characterization of Cu(In,Ga)Se$_2$ thin-film solar cells and the role of defects for the device performance", *Solar Energy Materials and Solar Cells,* vol. 67, pp. 137-143, Mar 2001.

[7]   S. Siebentritt, "What limits the efficiency of chalcopyrite solar cells?", *Solar Energy Materials and Solar Cells,* vol. 95, pp. 1471-1476.

[8]   A. Luque and S. Hegedus, *History of photovoltaics*, in *Handbook of photovoltaics Science and Engineering*, 2005 ed, A. Luque and S. Hegedus, Eds.: John Wiley and sons ltd, 2003, pp. 11-15.

[9]   D. C. Reynolds, G. Leies, L. L. Antes, and R. E. Marburger, "Photovoltaic Effect in Cadmium Sulfide", *Physical Review,* vol. 96, pp. 533-534, 1954.

[10]   B. Tell, J. L. Shay, and H. M. Kasper, "Electrical properties, optical properties, and band structure of CuGaSe$_2$ and CuInSe$_2$", *Physical Review B,* vol. 4, pp. 2463-&, 1971.

[11]   J. R. Tuttle, M. Ruth, D. Albin, A. Mason, and R. Noufi, "Experiments on the modification of the bi-layer structure in CdS/CuInSe$_2$ devices", proceedings of *20th IEEE Photovoltaic Specialists Conference*, 1988, vol. 2, p.^pp. 1525-1530.

[12]   W. Gebicki, M. Igalson, W. Zajac, and R. Trykozko, "Growth and characterisation of CuAl$_x$In$_{1-x}$Se$_2$ mixed crystals", *Journal of Physics D: Applied Physics,* vol. 23, p. 964, 1990.

[13]   Solar Frontier, *retrieved 31st July 2012*, http://www.solar-frontier.com/eng/ cs/groups/co_de_corporate/documents/co_en_attachment/mdaw/mda1/~edisp /c005765.pdf.

[14]   B. M. Basol, V. K. Kapur, A. Halani, C. R. Leidholm, J. Sharp, J. R. Sites, A. Swartzlander, R. Matson, and H. Ullal, "Cu(In,Ga)Se$_2$ thin films and solar cells prepared by selenization of metallic precursors", *Journal of Vacuum Science & Technology a-Vacuum Surfaces and Films,* vol. 14, pp. 2251-2256, Jul-Aug 1996.

[15]   M. Marudachalam, H. Hichri, R. Klenk, R. W. Birkmire, W. N. Shafarman, and J. M. Schultz, "Preparation of homogeneous Cu(InGa)Se$_2$ films by selenization of metal precursors in H$_2$Se atmosphere", *Applied Physics Letters,* vol. 67, pp. 3978-3980, Dec 1995.

[16]   G. Zoppi, I. Forbes, P. Nasikkar, and R. W. Miles, *Characterisation of thin films CuIn$_{1-x}$Al$_x$Se$_2$ prepared by selenisation of magnetron sputtered metallic precursors*, in *Thin-Film Compound Semiconductor Photovoltaics - 2007.* vol. 1012, Warrendale: Materials Research Society, 2007, pp. 349-354.

[17]   J. L. Gray, *The Physics of the Solar Cell*, in *Handbook of photovoltaics Science and Engineering*, 2005 ed, A. Luque and S. Hegedus, Eds.: John Wiley and sons ltd, 2003, pp. 61-112.

[18]   R. C. Neville, *Energy needs-energy sources*, in *Solar Energy Conversion-The Solar Cell*, pp. 1-36.

[19]   Energy Information Administration, "International Total Primary Energy Consumption and Energy Intensity Available", http://www.eia.gov/emeu/international/energyconsumption.html.

[20]   World Bank, "Electricity consumption per capita", http://www.google.co.uk/publicdata/explore?ds=d5bncppjof8f9_&met_y=eg_use_elec_kh_pc&tdim=true&dl=en&hl=en&q=world+electricity+consumption.

[21]   NREL, *retrieved July 2010*, http://rredc.nrel.gov/solar/spectra/am1.5/.

[22]   C. Honsberg and S. Bowden, "PV CDROM", *retrieved 16th November 2011*, http://pvcdrom.pveducation.org/MANUFACT/FIRST.HTM.

[23]   Encyclopaedia Britannica, "Walter Schottky", *retrieved February 2012*, http://www.britannica.com/EBchecked/topic/528213/Walter-Schottky.

[24]   J. G. Korvink and A. Greiner, *Metal-Semiconductor Contacts*, in *Semiconductors for Micro and Nanotechnology—An Introduction for Engineers*: WILEY-VCH Verlag GmbH, 2002, pp. 313-324.

[25]   C. Honsberg and S. Bowden, "Formation of a P-N junction", *retrieved 16th November 2011*, http://www.pveducation.org/pvcdrom/pn-junction/formation-pn-junction.

[26]   R. T. Tung, "Free Surfaces of Semiconductors", *retrieved February 2012*, http://academic.brooklyn.cuny.edu/physics/tung/Schottky/surface.htm.

[27]   R. T. Tung, "Schottky Barrier Height Basics", *retrieved February 2012*, http://academic.brooklyn.cuny.edu/physics/tung/Schottky/index.htm.

[28]   T. Kirchatz and U. Rau, *Introduction to Thin-Film Photovoltaics*, in *Advanced Characterization Techniques for Thin Film Solar Cells*, D. Abou-Ras, U. Rau, and T. Kirchatz, Eds., pp. 1-35.

[29]   T. Kirchatz, K. Ding, and U. Rau, *Fundamental Electrical Characterisation of Thin-Film Solar Cells*, in *Advanced Characterization Techniques for Thin Film Solar Cells*, D. Abou-Ras, U. Rau, and T. Kirchatz, Eds., pp. 35-60.

[30]   I. Repins, M. A. Contreras, B. Egaas, C. DeHart, J. Scharf, C. L. Perkins, B. To, and R. Noufi, "19.9%-efficient ZnO/CdS/CuInGaSe$_2$ solar cell with 81.2% fill factor", *Progress in Photovoltaics,* vol. 16, pp. 235-239, May 2008.

[31]   The Chemical Database Service, *retrieved 26th January 2012*, https://cds.dl.ac.uk/.

[32]   M. A. Green, K. Emery, Y. Hishikawa, W. Warta, and E. D. Dunlop, "Solar cell efficiency tables (Version 38)", *Progress in Photovoltaics,* vol. 19, pp. 565-572, Aug 2011.

[33] S. Wagner, J. L. Shay, Migliora.P, and H. M. Kasper, "CuInSe$_2$-CdS heterojunction photovoltaic detectors", *Applied Physics Letters,* vol. 25, pp. 434-435, 1974.

[34] P. Migliora, B. Tell, J. L. Shay, and H. M. Kasper, "Junction electroluminescence in CuInSe$_2$", *Applied Physics Letters,* vol. 24, pp. 227-228, 1974.

[35] J. L. Shay, S. Wagner, and H. M. Kasper, "Efficient CuInSe$_2$/CdS solar cells", *Applied Physics Letters,* vol. 27, pp. 89-90, 1975.

[36] J. Hedstrom, H. Ohlsen, M. Bodegard, A. Kylner, L. Stolt, D. Hariskos, M. Ruckh, and H. W. Schock, "ZnO/CdS/Cu(In,Ga)Se$_2$ thin film solar cells with improved performance", proceedings of *23rd IEEE Photovoltaic Specialists Conference*, 1993, vol. 364-371.

[37] L. Kronik, D. Cahen, and H. W. Schock, "Effects of sodium on polycrystalline Cu(In,Ga)Se$_2$ and its solar cell performance", *Advanced Materials,* vol. 10, pp. 31-36, Jan 1998.

[38] M. Ruckh, D. Schmid, M. Kaiser, R. Schäffler, T. Walter, and H. W. Schock, "Influence of substrates on the electrical properties of Cu(In,Ga)Se$_2$ thin films", *Solar Energy Materials and Solar Cells,* vol. 41-42, pp. 335-343, 1996.

[39] A. Virtuani, E. Lotter, M. Powalla, U. Rau, J. H. Werner, and M. Acciarri, "Influence of Cu content on electronic transport and shunting behavior of Cu(In,Ga)Se$_2$ solar cells", *Journal of Applied Physics,* vol. 99, pp. 014906-11, 2006.

[40] D. Cahen and R. Noufi, "Surface passivation of polycrystalline, chalcogenide based photovoltaic cells", *Solar Cells,* vol. 30, pp. 53-59, 1991.

[41] V. Probst, F. Karg, J. Rimmasch, W. Riedl, W. Stetter, H. Harms, and O. Eibl, *Advanced stacked elemental layer process for Cu(InGa)Se$_2$ thin film photovoltaic devices*, in *Thin Films for Photovoltaic and Related Device Applications*. vol. 426, D. Ginley, A. Catalano, H. W. Schock, C. Eberspacher, T. M. Petersen, and T. Wada, Eds. Warrendale: Materials Research Society, 1996, pp. 165-176.

[42] R. Klenk, T. Walter, H. W. Schock, and D. Cahen, "A model for the successful growth of polycrystalline films of CuInSe$_2$ by multisource physical vacuum evaporation", *Advanced Materials,* vol. 5, pp. 114-119, Feb 1993.

[43] H. W. Schock and R. Noufi, "CIGS-based solar cells for the next millennium", *Progress in Photovoltaics,* vol. 8, pp. 151-160, Jan-Feb 2000.

[44] U. Rau and H. W. Schock, "Electronic properties of Cu(In,Ga)Se$_2$ heterojunction solar cells–recent achievements, current understanding, and future challenges", *Applied Physics A: Materials Science & Processing,* vol. 69, pp. 131-147, 1999.

[45] S. H. Wei and A. Zunger, "Band offsets and optical bowings of chalcopyrites and Zn-based II-VI alloys", *Journal of Applied Physics,* vol. 78, pp. 3846-3856, Sep 1995.

[46] M. Turcu, O. Pakma, and U. Rau, "Interdependence of absorber composition and recombination mechanism in Cu(In,Ga)(Se,S)$_2$ heterojunction solar cells", *Applied Physics Letters,* vol. 80, pp. 2598-2600, 2002.

[47] C. L. Jensen, D. E. Tarrant, J. H. Ermer, and G. A. Pollock, "The role of gallium in CuInSe$_2$ solar cells fabricated by a two-stage method",

proceedings of *23rd IEEE Photovoltaic Specialists Conference*, 1993, vol. 577-580.

[48]   T. Dullweber, O. Lundberg, J. Malmström, M. Bodegård, L. Stolt, U. Rau, H. W. Schock, and J. H. Werner, "Back surface band gap gradings in Cu(In,Ga)Se$_2$ solar cells", *Thin Solid Films,* vol. 387, pp. 11-13, 2001.

[49]   A. M. Gabor, J. R. Tuttle, M. H. Bode, A. Franz, A. L. Tennant, M. A. Contreras, R. Noufi, D. G. Jensen, and A. M. Hermann, "Band-gap engineering in Cu(In,Ga)Se$_2$ thin films grown from (In,Ga)$_2$Se$_3$ precursors", *Solar Energy Materials and Solar Cells,* vol. 41-42, pp. 247-260, 1996.

[50]   I. Repins, S. Glynn, J. Duenow, T. J. Coutts, W. Metzger, and M. A. Contreras, "Required Materials Properties for High-Efficiency CIGS Modules", NREL 2009, http://www.nrel.gov/docs/fy09osti/46235.pdf.

[51]   U. Rau and H. W. Schock, *Cu(In,Ga)Se$_2$ Thin-Film Solar Cells*, in *Practical Handbook of Photovoltaics*, U. Rau, H. W. Schock, M. Tom, and C. Luis, Eds. Amsterdam: Elsevier Science, 2003, pp. 367-413.

[52]   S. Lany and A. Zunger, "Limitation of the open-circuit voltage due to metastable intrinsic defects in Cu(In,Ga)Se$_2$ and strategies to avoid these defects", proceedings of *33rd IEEE Photovoltaic Specialists Conference*, San Diego, California, 2008, vol. 1-4, p.^pp. 1142-1144.

[53]   D. Schmid, M. Ruckh, F. Grunwald, and H. W. Schock, "Chalcopyrite/defect chalcopyrite heterojunctions on the basis of CuInSe$_2$", *Journal of Applied Physics,* vol. 73, pp. 2902-2909, 1993.

[54]   W. N. Shafarman and L. Stolt, *Cu(InGa)Se$_2$ Solar Cells*, in *Handbook of photovoltaics Science and Engineering*, 2005 ed, A. Luque and S. Hegedus, Eds.: John Wiley and sons ltd, 2003, pp. 567-616.

[55]   R. Herberholz, U. Rau, H. W. Schock, T. Haalboom, T. Godecke, F. Ernst, C. Beilharz, K. W. Benz, and D. Cahen, "Phase segregation, Cu migration and junction formation in Cu(In,Ga)Se$_2$", *European Physical Journal-Applied Physics,* vol. 6, pp. 131-139, May 1999.

[56]   F.-J. Haug, "Degenerate semiconductors", *retrieved 12th December 2011*, http://www.superstrate.net/pv/physics/degeneracy.html.

[57]   R. Klenk, R. Menner, D. Cahen, and H. W. Schock, "Improvement of Cu(Ga,In)Se$_2$ based solar cells by etching the absorber", proceedings of *21st IEEE Photovoltaic Specialists Conference*, 1990, vol. 1, p.^pp. 481-486.

[58]   T. Wada, Y. Hashimoto, K. Kusao, N. Kohara, T. Negami, and M. Nishitani, *Surface characterization of Cu(In,Ga)Se$_2$ thin films treated by various solutions*, in *Thin Films for Photovoltaic and Related Device Applications*. vol. 426, D. Ginley, A. Catalano, H. W. Schock, C. Eberspacher, T. M. Petersen, and T. Wada, Eds. Warrendale: Materials Research Society, 1996, pp. 291-296.

[59]   S. Menezes, H.-J. Lewerenz, and K. J. Bachmann, "Efficient and stable solar cell by interfacial film formation", *Nature,* vol. 305, pp. 615-616, 1983.

[60]   P. Fons, S. Niki, A. Yamada, M. Nishitani, T. Wada, and T. Kurafuji, *The effects of KCN etching on Cu-rich epitaxial CuInSe$_2$ thin films*, in *Thin Films for Photovoltaic and Related Device Applications*. vol. 426, D. Ginley, A. Catalano, H. W. Schock, C. Eberspacher, T. M. Petersen, and T. Wada, Eds. Warrendale: Materials Research Society, 1996, pp. 213-218.

[61]   B. Canava, O. Roussel, J. F. Guillemoles, D. Lincot, and A. Etcheberry, *Increasing solar cell efficiencies based on Cu(In,Ga)Se$_2$ after a specific chemical and oxidant treatment*, in *Physica Status Solidi C - Current Topics*

in Solid State Physics, Vol 3, No 8. vol. 3, M. Stutzmann, Ed. Weinheim: Wiley-V C H Verlag Gmbh, 2006, pp. 2551-2554.

[62]   R. Klenk, T. Walter, D. Schmid, and H. W. Schock, "Growth Mechanisms and Diffusion in Multinary and Multilayer Chalcopyrite Thin Films", *Japanese Journal of Applied Physics,* vol. 32-3, 1993.

[63]   R. A. Mickelsen and W. S. Chen, "High photocurrent polycrystalline thin-film CdS-CuInSe$_2$ solar-cell", *Applied Physics Letters,* vol. 36, pp. 371-373, 1980.

[64]   R. A. Mickelsen and W. S. Chen, "Methods for forming thin film heterojunction solar cells from I-III-VI$_2$ chalcopyrite compounds, and solar cells produced thereby". patent. 4335266, application. 221761, US, 1982.

[65]   M. A. Contreras, H. Wiesner, R. Matson, J. Tuttle, K. Ramanathan, and R. Noufi, *Defect chalcopyrite Cu(In$_{1-x}$Ga$_x$)$_3$Se$_5$ polycrystalline thin-film materials*, in *Thin Films for Photovoltaic and Related Device Applications.* vol. 426, Warrendale: Materials Research Society, 1996, pp. 243-244.

[66]   S. Jost, *The formation of CuInSe$_2$-based thin-film solar cell absorbers from alternative low-cost precursors*, PhD thesis: Universität Erlangen-Nürnberg, 2008

[67]   J. J. M. Binsma and H. A. van der Linden, "Preparation of thin CuInS$_2$ films via a two-stage process", *Thin Solid Films,* vol. 97, pp. 237-243, 1982.

[68]   V. K. Kapur, U. V. Chudary, and A. K. P. Chu, "Process of forming a compound semiconductive material". patent. 4,581,108, US: Atlantic Richfield Company (ARCO), 1986.

[69]   C. J. Hibberd, E. Chassaing, W. Liu, D. B. Mitzi, D. Lincot, and A. N. Tiwari, "Non-vacuum methods for formation of Cu(In, Ga)(Se,S)$_2$ thin film photovoltaic absorbers", *Progress in Photovoltaics: Research and Applications,* vol. 18, pp. 434-452.

[70]   D. B. Mitzi, "Solution Processing of Chalcogenide Semiconductors via Dimensional Reduction", *Advanced Materials,* vol. 21, pp. 3141-3158, 2009.

[71]   V. Alberts, M. Klenk, and E. Bucher, "X-ray fluorescence investigation of the Ga distribution in Cu(In,Ga)Se$_2$ thin films", *Solar Energy Materials and Solar Cells,* vol. 64, pp. 371-383, 2000.

[72]   V. Izquierdo-Roca, X. Fontane, J. Alvarez-Garcia, L. Calvo-Barrio, A. Perez-Rodriguez, J. R. Morante, C. M. Ruiz, E. Saucedo, and V. Bermudez, "Electrochemical synthesis of CuIn(S,Se)$_2$ alloys with graded composition for high efficiency solar cells", *Applied Physics Letters,* vol. 94, Feb 2009.

[73]   J. K. Van Duren, M. R. Robinson, and B. M. Sager, "High-throughput printing of semiconductor precursor layer from inter-metallic nanoflake particles", application. 11/394,849: NanoSolar inc., 2007.

[74]   W. N. Shafarman and J. Zhu, "Effect of substrate temperature and depostion profile on evaporated Cu(InGa)Se$_2$ films and devices", *Thin Solid Films,* vol. 361-362, pp. 473-477, 2000.

[75]   R. Scheer, A. Pérez-Rodríguez, and W. K. Metzger, "Advanced diagnostic and control methods of processes and layers in CIGS solar cells and modules", *Progress in Photovoltaics: Research and Applications,* vol. 18, pp. 467-480.

[76]   G. Voorwinden, R. Kniese, and M. Powalla, "In-line Cu(In,Ga)Se$_2$ co-evaporation processes with graded band gaps on large substrates", *Thin Solid Films,* vol. 431-432, pp. 538-542, 2003.

[77]   Q-Cells SE, "CIGS thin-film technology reaches world-record efficiency of 17.4%", http://www.q-cells.com/en/press/article//CIGS-thin-film-technology-reaches-world-record-efficiency-of-174.html.

[78]   S. Niki, T. Kurafuji, P. J. Fons, I. Kim, O. Hellman, and A. Yamada, *Growth and characterization of CuInSe2 epitaxial films for device applications*, in *Thin Films for Photovoltaic and Related Device Applications*. vol. 426, D. Ginley, A. Catalano, H. W. Schock, C. Eberspacher, T. M. Petersen, and T. Wada, Eds. Warrendale: Materials Research Society, 1996, pp. 233-241.

[79]   D. R. Hollars, "Manufacturing method for large-scale production of thin-film solar cells". patent. 7, 544, 884 B2, US: Miasole, Santa Clara, California (US), 2009.

[80]   Miasole, "MiaSolé Achieves 15.7% Efficiency with Commercial-Scale CIGS Thin-Film Solar Modules", http://www.miasole.com/technology.

[81]   S. Niki, M. Contreras, I. Repins, M. Powalla, K. Kushiya, S. Ishizuka, and K. Matsubara, "CIGS absorbers and processes", *Progress in Photovoltaics: Research and Applications,* vol. 18, pp. 453-466, 2010.

[82]   N. G. Dhere, "Present status and future prospects of CIGSS thin film solar cells", *Solar Energy Materials and Solar Cells,* vol. 90, pp. 2181-2190, Sep 2006.

[83]   Solibro GmbH, "CIGS thin-film technology reaches world-record efficiency of 17.4%", *retrieved 30th January 2012*, http://www.q-cells.com/en/press/article//CIGS-thin-film-technology-reaches-world-record-efficiency-of-174.html.

[84]   Q-Cells, "Q-Cells achieves with 13.4% new efficiency world record for CIGS thin film solar module out of mass production", *retrieved 16th February 2012*, http://www.q-cells.com/uploads/media/2011_0329_PR_QCE_CIGSrecord_ENG.pdf.

[85]   Nanosolar Communications, "Nanosolar Achieves 17.1% Aperture Efficiency Through Printed CIGS Process", http://www.nanosolar.com/company/blog.

[86]   Nanosolar Communications, "Nanosolar Confirms Factory Expansion and Financial Strength", http://www.nanosolar.com/company/blog.

[87]   M. Pinarbasi, S. Aksu, J. Freitag, T. Boone, H. Zolla, J. Vasquez, D. Nayak, E. Lee, T. Wang, J. Abushama, and B. Metin, "Flexible cells and modules produced using roll-to-roll electroplating approach", proceedings of *35th Photovoltaic Specialists Conference (PVSC)*, 2010, vol. 000169-000174.

[88]   T. K. Todorov, O. Gunawan, T. Gokmen, and D. B. Mitzi, "Solution-processed Cu(In,Ga)(S,Se)$_2$ absorber yielding a 15.2% efficient solar cell", to be published in *Progress in Photovoltaics: Research and Applications*, http://onlinelibrary.wiley.com/doi/10.1002/pip.1253/pdf.

[89]   J. H. Scofield, A. Duda, D. Albin, B. L. Ballard, and P. K. Predecki, "Sputtered molybdenum bilayer back contact for copper indium diselenide-based polycrystalline thin-film solar-cells", *Thin Solid Films,* vol. 260, pp. 26-31, May 1995.

[90]   G. Zoppi, N. Beattie, J. Major, R. Miles, and I. Forbes, "Electrical, morphological and structural properties of RF magnetron sputtered Mo thin films for application in thin film photovoltaic solar cells", *Journal of Materials Science,* vol. 46, pp. 4913-4921, 2011.

[91]   U. Schmid and H. Seidel, "Effect of substrate properties and thermal annealing on the resistivity of molybdenum thin films", *Thin Solid Films,* vol. 489, pp. 310-319, 2005.

[92]   D. Schmid, M. Ruckh, and H. W. Schock, "A comprehensive characterization of the interfaces in Mo/CIS/CdS/ZnO solar cell structures", *Solar Energy Materials and Solar Cells,* vol. 41-42, pp. 281-294, 1996.

[93]   T. Wada, N. Kohara, S. Nishiwaki, and T. Negami, "Characterization of the $Cu(In,Ga)Se_2$/Mo interface in CIGS solar cells", *Thin Solid Films,* vol. 387, pp. 118-122, May 2001.

[94]   N. Kohara, S. Nishiwaki, Y. Hashimoto, T. Negami, and T. Wada, "Electrical properties of the $Cu(In,Ga)Se_2/MoSe_2$/Mo structure", *Solar Energy Materials and Solar Cells,* vol. 67, pp. 209-215, 2001.

[95]   L. Assmann, J. C. Bernède, A. Drici, C. Amory, E. Halgand, and M. Morsli, "Study of the Mo thin films and Mo/CIGS interface properties", *Applied Surface Science,* vol. 246, pp. 159-166, 2005.

[96]   N. F. Cooray, K. Kushiya, A. Fujimaki, I. Sugiyama, T. Miura, D. Okumura, M. Sato, M. Ooshita, and O. Yamase, "Large area ZnO films optimized for graded band-gap $Cu(InGa)Se_2$-based thin-film mini-modules", *Solar Energy Materials and Solar Cells,* vol. 49, pp. 291-297, 1997.

[97]   B. C. Mohanty, D. H. Yeon, B. K. Kim, and Y. S. Cho, "Spatial Variation in Structural, Morphological and Optical Properties of Aluminum-Doped ZnO Thin Films Grown by 30°-Incident Radio Frequency Magnetron Sputtering", *Journal of the Electrochemical Society,* vol. 158, pp. P30-P35, January 1, 2011 2011.

[98]   J. Kim-Zajonz, S. Werner, and H. Schulz, *Zeitschrift fuer Kristallographie,* vol. 214, pp. 331-336, 1999.

[99]   P. D. Paulson, M. W. Haimbodi, S. Marsillac, R. W. Birkmire, and W. N. Shafarman, "$CuIn_{1-x}Al_xSe_2$ thin films and solar cells", *Journal of Applied Physics,* vol. 91, pp. 10153-10156, Jun 2002.

[100]   S. Jost, F. Hergert, R. Hock, M. Purwins, and R. Enderle, "Real-time investigations of selenization reactions in the system Cu-In-Al-Se", *physica status solidi (a),* vol. 203, pp. 2581-2587, 2006.

[101]   M. Sugiyama, A. Umezawa, T. Yasuniwa, A. Miyama, H. Nakanishi, and S. F. Chichibu, "Growth of single-phase $Cu(In,Al)Se_2$ photoabsorbing films by selenization using diethylselenide", *Thin Solid Films,* vol. 517, pp. 2175-2177, 2009.

[102]   T. Hayashi, T. Minemoto, G. Zoppi, I. Forbes, K. Tanaka, S. Yamada, T. Araki, and H. Takakura, "Effect of composition gradient in $Cu(In,Al)Se_2$ solar cells", *Solar Energy Materials and Solar Cells,* vol. 93, pp. 922-925, 2009.

[103]   D. Dwyer, I. Repins, H. Efstathiadis, and P. Halder, "Deposition of $CuInAlSe_2$ films using co-sputtered precursors and selenization", proceedings of *34th IEEE Photovoltaic Specialists Conference*, 2009, vol. 872-876.

[104]   Dhananjaya, J. Nagarajua, and S. B. Krupanidhi, "Structural and optical properties of $CuIn_{1-x}Al_xSe_2$ thin films prepared by four-source elemental evaporation", *Solid State Communications,* vol. 127, pp. 243-246, 2003.

[105]   T. Dullweber, U. Rau, M. A. Contreras, R. Noufi, and H. W. Schock, "Photogeneration and carrier recombination in graded gap $Cu(In,Ga)Se_2$ solar cells", *IEEE Transactions on Electron Devices,* vol. 47, pp. 2249-2254, Dec 2000.

255

[106] J. Olejnícek, C. A. Kamler, S. A. Darveau, C. L. Exstrom, L. E. Slaymaker, A. R. Vandeventer, N. J. Ianno, and R. J. Soukup, "Formation of $CuIn_{1-x}Al_xSe_2$ thin films studied by Raman scattering", *Thin Solid Films,* vol. In Press, Accepted Manuscript, 2011.

[107] D. Dwyer, I. Repins, H. Efstathiadis, and P. Haldar, "Selenization of co-sputtered CuInAl precursor films", *Solar Energy Materials and Solar Cells,* vol. 94, pp. 598-605, 2010.

[108] A. Umezawa, T. Yasuniwa, A. Miyama, H. Nakanishi, M. Sugiyama, and S. F. Chichibu, "Preparation of $Cu(In,Al)Se_2$ thin films by selenization using diethylselenide", *physica status solidi (c),* vol. 6, pp. 1016-1018, 2009.

[109] F. Hergert, R. Hock, A. Weber, M. Purwins, J. Palm, and V. Probst, "In situ investigation of the formation of $Cu(In,Ga)Se_2$ from selemsed metallic precursors by X-ray diffraction - The impact of Gallium, Sodium and Selenium excess", *Journal of Physics and Chemistry of Solids,* vol. 66, pp. 1903-1907, 2005.

[110] F. Hergert, S. Jost, R. Hock, and M. Purwins, "A crystallographic description of experimentally identified formation reactions of $Cu(In,Ga)Se_2$", *Journal of Solid State Chemistry,* vol. 179, pp. 2394-2415, 2006.

[111] E. Halgand, J. C. Bernède, S. Marsillac, and J. Kessler, "Physico-chemical characterisation of $Cu(In,Al)Se_2$ thin film for solar cells obtained by a selenisation process", *Thin Solid Films,* vol. 480-481, pp. 443-446, 2005.

[112] Carbolite, http://carbolite.thomasnet.com/browser?&plpver=1001&prodid=3001014&itemid=1101%20&assetid=1070.

[113] U. Malm and M. Edoff, "Influence from front contact sheet resistance on extracted diode parameters in CIGS solar cells", *Progress in Photovoltaics,* vol. 16, pp. 113-121, March 2008.

[114] J. J. Scragg, *Studies of Cu_2ZnSnS_4 films prepared by sulfurisation of electrodeposited precursors*: University of Bath, 2010.^May

[115] L. M. Peter, *Semiconductor electrochemistry*, in *Electrochemistry (Specialist Periodical Report)*. vol. 9 The Royal Society of Chemistry, Ed., 1984, pp. 66-100.

[116] Thorlabs, "Lamp specifications", http://www.thorlabs.de/NewGroupPage9.cfm?ObjectGroup_ID=2692.

[117] M. Gossla, H. Metzner, and H. Mahnke, "Coevaporated Cu-In films as precursors for solar cells", *Journal of Applied Physics,* vol. 86, pp. 3624-3632, 1999.

[118] C. H. Chung, S. D. Kim, H. J. Kim, F. O. Adurodija, K. H. Yoon, and J. Song, "Phase formation and control of morphology in sputtered Cu-In alloy layers", *Solid State Communications,* vol. 126, pp. 185-190, 2003.

[119] M. El-Boragy, R. Szepan, and K. Schubert, *Journal of the Less-Common Metals,* vol. 29, p. 133, 1972.

[120] S. Marsillac, T. B. Wahiba, C. El Moctar, J. C. Bernede, and A. Khelil, "Evolution of the properties of $CuAlSe_2$ thin films with the oxygen content", *Solar Energy Materials and Solar Cells,* vol. 71, pp. 425-434, 2002.

[121] C. O. El Moctar, S. Marsillac, J. C. Bernede, A. Conan, K. Benchouk, and A. Khelil, "Preparation of thin $CuAlSe_2$ films by annealing of stacked Cu/Al/Se/Al... layers, study of deposition conditions", *Physica Status Solidi a-Applied Research,* vol. 174, pp. 213-220, July 1999.

[122]	R. Bari, V. Ganesan, S. Potadar, and L. Patil, "Structural, optical and electrical properties of chemically deposited copper selenide films", *Bulletin of Materials Science,* vol. 32, pp. 37-42, 2009.

[123]	Y. B. K. Reddy and V. S. Raja, "Effect of Cu/Al ratio on the properties of $CuAlSe_2$ thin films prepared by co-evaporation", *Materials Chemistry and Physics,* vol. 100, pp. 152-157, 2006.

[124]	G. Zoppi, R. Aninat, I. Forbes, R. W. Miles, F. Luckert, P. Edwards, and R. W. Martin, "Rapid thermal processing of $CuAlSe_2$ ", in *PV-SAT 5*, 2009, http://nrl.northumbria.ac.uk/1629/.

[125]	National Physics Laboratory, "Determination of Residual Stresses by X-ray Diffraction – Issue 2", http://www.npl.co.uk/upload/pdf/Determination_of_ Residual_Stresses_by_X-ray_Diffraction_-_Issue_2.pdf.

[126]	A. Stevels and F. Jellinek, *Journal of the Royal Netherlands Chemical Society,* vol. 90, pp. 273-283, 1971.

[127]	A. M. Klimova, V. A. Ananichev, A. I. Demidov, and L. N. Blinov, "Investigation of the saturated vapor pressure of selenium and indium sesquiselenide $In_{0.4}Se_{0.6}$", *Glass Physics and Chemistry,* vol. 32, pp. 436-438, Jul-Aug 2006.

[128]	W. Borchert, *Zeitschrift fuer Kristallographie, Kristallgeometrie, Kristallphysik, Kristallchemie,* vol. 106, pp. 5-24, 1945.

[129]	E. H. P. Cordfunke, R. J. M. Konings, and W. Ouweltjes, "The standard enthalpy of formation of In_2O_3", *The Journal of Chemical Thermodynamics,* vol. 23, pp. 451-454, 1991.

[130]	H. J. Moore, D. L. Olson, and R. Noufi, "Use of the effective heat of formation model to determine phase formation sequences of In-Se, Ga-Se, Cu-Se, and Ga-In multilayer thin films", *Journal of Electronic Materials,* vol. 27, pp. 1334-1340, Dec 1998.

[131]	ASM, *Handbook: Alloy Phase Diagrams*, vol. 3, 1992.

[132]	T. Do and N. S. McIntyre, "Pressure effects on aluminium oxidation kinetics using X-ray photoelectron spectroscopy and parallel factor analysis", *Surface Science,* vol. 440, pp. 438-450, 1999.

[133]	S. Zumdahl, *Chemical Principles*: Houghton Mifflin 2004.

[134]	R. Caballero and C. Guillén, "$CuInSe_2$ Formation by selenization of sequentially evaporated metallic layers", *Solar Energy Materials and Solar Cells,* vol. 86, pp. 1-10, February 2005.

[135]	M. Marudachalam, R. Birkmire, J. M. Schultz, and T. Yokimcus, "Characterization of Cu-In-Ga precursors used to form $Cu(In,Ga)Se_2$ films", proceedings of 24th *IEEE Photovoltaic Specialists Conference* 1994, vol. 1, p.^pp. 234-237 vol.1.

[136]	S. Martín and C. Guillén, "Study of the chalcopyrite $Cu(In,Al)Se_2$ crystalline growth by selenization of different evaporated precursors ratios", *Journal of Crystal Growth,* vol. 336, pp. 82-88, 2011.

[137]	C. Honsberg and S. Bowden, "Impact of Both Series and Shunt Resistance", *retrieved 16th November 2011*, http://www.pveducation.org/pvcdrom/solar-cell-operation/impact-of-both-resistances.

[138]	A. Luque and A. Marti, *Theoretical Limits of Photovoltaic Conversion*, in *Handbook of photovoltaics Science and Engineering*, 2005 ed, A. Luque and S. Hegedus, Eds.: John Wiley and sons ltd, 2003, pp. 113-153.

[139]	W. Shockley and H. Queisser, "Some theoretical aspects of the physics of solar cells", *Solar Energy,* vol. 5, pp. 34-34, 1961.

[140] C. Honsberg and S. Bowden, "Open-circuit voltage", *retrieved 16th November 2011*, http://www.pveducation.org/pvcdrom/solar-cell-operation/open-circuit-voltage.

[141] Wikipedia, http://en.wikipedia.org/wiki/First_Solar#Market_history.

[142] I. Repins, M. Contreras, M. Romero, Y. Yan, W. Metzger, S. J. J. Li, B. Egaas, C. DeHart, and J. Scharf, "Characterization of 19.9%-Efficient CIGS Absorbers", proceedings of *33rd IEEE Photovoltaics Specialists Conference*, San Diego, California, 2008, vol. 1-6.

[143] M. A. Green, K. Emery, Y. Hishikawa, W. Warta, and E. D. Dunlop, "Solar cell efficiency tables (version 39)", *Progress in Photovoltaics: Research and Applications,* vol. 20, pp. 12-20, 2012.

[144] http://reference.iucr.org/dictionary/Ewald_sphere, *retrieved 24th January 2012*, http://reference.iucr.org/dictionary/Ewald_sphere.

[145] V. K. Pecharsky and P. Y. Zavalij, *Reciprocal lattice*, in *Fundamentals of Powder Diffraction and Structural Characterization of Materials*: Springer, 2005, pp. 50-52.

[146] V. K. Pecharsky and P. Y. Zavalij, *Reciprocal lattice and Ewald's sphere*, in *Fundamentals of Powder Diffraction and Structural Characterization of Materials*: Springer, 2005, pp. 149-152.

[147] V. K. Pecharsky and P. Y. Zavalij, *Origin of the powder diffraction pattern*, in *Fundamentals of Powder Diffraction and Structural Characterization of Materials*: Springer, 2005, pp. 153-171.

[148] C. S. Barrett and T. B. Massalski, *Structure of Metals, Third Edition: Crystallographic Methods, Principles and Data*: Pergamon, 1980.